Epsilon-Near-Zero metamaterials applied to mid-infrared optoelectronic devices

Tuan Nghia Lê

université
PARIS-SACLAY

Epsilon-Near-Zero metamaterials applied to mid-infrared optoelectronic devices

Métamatériaux à fonction diélectrique proche de zéro appliqués à des dispositifs optoélectroniques dans l'infrarouge moyen

Thèse de doctorat de l'université Paris-Saclay

École doctorale n° 572, Ondes et Matière (EDOM)
Spécialité de doctorat : Physique
Graduate School : Physique. Référent : Faculté des sciences d'Orsay

Thèse préparée dans les unités de recherche **SPEC** (Université Paris-Saclay, CEA, CNRS) et **C2N** (Université Paris-Saclay, CNRS),
sous la direction de **Fabrice CHARRA**, Directeur de Recherche CEA
et le co-encadrement de **Simon VASSANT**, Chercheur CEA

Thèse soutenue à Paris-Saclay, le 21 février 2022, par

Tuan Nghia LÊ

Composition du jury

Delphine MARRIS-MORINI Professeure, C2N, Université Paris-Saclay	Présidente
Jean-François LAMPIN Directeur de Recherche, IEMN, Université de Lille	Rapporteur & Examinateur
Thierry TALIERCIO Directeur de Recherche, IES, Université de Montpellier	Rapporteur & Examinateur
Yannick DE WILDE Directeur de Recherche, Institut Langevin, ESPCI Paris	Examinateur
Fabrice CHARRA Directeur de Recherche, CEA, Université Paris-Saclay	Directeur de thèse

Thèse de doctorat

NNT : 2022UPASP020

université PARIS-SACLAY

ÉCOLE DOCTORALE
Ondes et matière
(EDOM)

Titre : Métamatériaux à fonction diélectrique proche de zéro appliqués à des dispositifs optoélectroniques dans l'infrarouge moyen.

Mots clés : ENZ, fonction diélectrique, MIM, modulateur, QCD

Résumé : Les matériaux Epsilon-near-zero (ENZ) appartiennent aux branches plasmonique et métamatériaux de la nanophotonique. La fonction diélectrique proche de zéro induit une exaltation intrinsèque et un confinement des ondes électromagnétiques dans une fine couche ENZ très sub-longueur d'onde, augmentant ainsi l'interaction lumière-matière. Dans ce travail, nous avons appliqué le concept ENZ à des dispositifs optoélectroniques dans le moyen infrarouge, traditionnellement limités par une faible interaction lumière-matière : un modulateur électro-optique (EOM) ENZ et un détecteur à cascade quantique à période unique (QCD) ENZ, fonctionnant autour de 10μm. Le mécanisme de l'ENZ-EOM consiste à déplacer la résonance d'un mode ENZ, couplé avec un mode de cavité, en appliquant une tension. Quant à l'ENZ-QCD, il bénéficie de l'exaltation de la composante normale du champ électrique dans la couche puits quantique (QW) unique, favorisant son absorption intersousbande.

La démarche de ces études consiste en plusieurs étapes : caractérisations des matériaux, simulations électromagnétiques des dispositifs, fabrication et caractérisations de la réponse des dispositifs. Dans les deux cas, de l'InGaAs fortement dopé est utilisé pour atteindre le régime ENZ grace à des électrons libres ou des transitions intersousbandes (TISB), et une cavité MIM est utilisée pour coupler la lumière de l'espace libre vers le dispositif. Pour le dispositif ENZ-EOM, avec la configuration finale de type MOSFET, un nouveau mécanisme de modulation utilisant un régime de couplage à trois modes est exploré et une profondeur de modulation expérimentale d'environ 0.5-1.2dB est atteinte vers 7.5μm. Concernant le dispositif ENZ-QCD, une signature optique de la TISB d'un puits quantique unique est clairement observée à basse température et une efficacité quantique externe d'environ 0.057% est atteinte. Les résultats expérimentaux sont plus petits que les valeurs simulées et celles de l'état de l'art, actuellement limités par des propriétés électriques complexes dans ces systèmes. Ces études contribuent à une meilleure compréhension de la physique des dispositifs et ouvre la voie vers des dispositifs de haute performance si le verrou des limitations électriques est relevé.

Title : Epsilon-Near-Zero metamaterials applied to mid-infrared optoelectronic devices.

Keywords : ENZ, dielectric function, MIM, modulator, QCD

Abstract : Epsilon-near-zero (ENZ) materials belong to the plasmonics and metamaterials branches of nanophotonics. The near-zero dielectric function offers intrinsic enhancement and confinement of electromagnetic waves in highly sub-wavelength ENZ layer, thus increases light-matter interaction. Here, we applied the ENZ concept to mid-infrared optoelectronic devices, traditionally limited by weak light-matter interaction : an ENZ electro-optical modulator (EOM) and an ENZ single-period quantum cascade detector (QCD), operating around 10μm. The ENZ-EOM's mechanism is based on detuning an ENZ mode - coupled to a cavity mode - by applying a bias. The ENZ-QCD benefits from the enhancement of electric field's normal component, favorizing the intersubband absorption in a single active quantum well.

This work consists of several main steps : material characterizations, electromagnetic simulation of device's response, device's fabrication and characterizations. In both cases, highly doped InGaAs is used to reach ENZ regime via free electrons or strong intersubband transition (ISBT) and a MIM cavity is used to couple light from free space into the device. For the ENZ-EOM device, in the final MOSFET-like structure, a new modulation mechanism using a three-mode coupling regime was explored for the first time and an experimental modulation depth of about 0.5-1.2dB at around 7.5μm was reached. For the ENZ-QCD device, an optical signature of a single quantum well ISBT was clearly observed at low temperature and an external quantum efficiency of about 0.057% was reached. These experimental results are smaller than values from simulations and the state of the art, at the moment mainly limited by complex electrical properties in these systems. These studies contribute to a better understanding of the devices' physics and promise high performance devices in case of improvement of the electrical properties.

Résumé de la thèse

Les matériaux Epsilon-near-zero (ENZ) appartiennent aux branches plasmonique et métamatériaux de la nanophotonique et ont été activement étudiés au cours de la dernière décennie. La fonction diélectrique proche de zéro induit une exaltation intrinsèque et un confinement des ondes électromagnétiques dans une fine couche ENZ très sub-longueur d'onde, augmentant ainsi l'interaction lumière-matière. Dans ce travail, nous avons appliqué le concept ENZ à des dispositifs optoélectroniques dans le moyen infrarouge, traditionnellement limités par une faible interaction lumière-matière. Plus précisément, nous avons conçu et essayé de réaliser un modulateur électro-optique (EOM) ENZ et un détecteur à cascade quantique à période unique (QCD) ENZ, fonctionnant autour de 10μm. Le mécanisme de l'ENZ-EOM consiste à déplacer un mode ENZ, qui est initialement en couplage fort avec un mode de cavité. La fréquence du mode ENZ peut être déplacée par déplétion d'électron en appliquant une tension. Ce mécanisme offre théoriquement une modulation d'amplitude importante, mais n'a pas été utilisé jusqu'à présent dans cette gamme de longueur d'onde. Quant au QCD, il appartient à la famille des dispositifs intersousbandes, qui souffre généralement d'une faible absorption dans les structures classiques, du fait de la règle de sélection. L'ENZ-QCD bénéficie de l'exaltation de la composante normale du champ électrique - la composante utile pour l'absorption intersousbande.

Les fonctions diélectriques des matériaux utilisés ont une place centrale dans la conception optique de ces dispositifs, nous avons donc commencé par les étudier expérimentalement et théoriquement. Le régime ENZ est atteint dans les dispositifs EOM et QCD, en utilisant respectivement une couche InGaAs de type Drude fortement dopée (N~1×10^{19}cm^{-3}) et une transition intersousbande forte dans un puits quantique unique en InGaAs/InAlAs (N~0.5-1×10^{18}cm^{-3}). Nous avons également caractérisé la contribution des phonons optiques dans l'InGaAs dans la fonction diélectrique infrarouge, qui restait encore mal décrit dans la littérature. Ensuite, j'ai réalisé la conception optique des dispositifs, leur microfabrication, suivie par des caractérisations optiques, électriques et optoélectroniques.

Pour le dispositif ENZ-EOM de type HEMT (empilement InP/InGaAs dopé/InP inséré dans une cavité MIM en Au/Ti), à tension nulle, nous avons observé expérimentalement le régime de couplage fort entre le mode ENZ et le mode de cavité, en accord avec la simulation optique. Cependant, l'isolation électrique dans cette structure est faible, nous ne pouvons pas appliquer une tension suffisamment grande pour dépléter les électrons. Avec le dispositif ENZ-EOM de type MOSFET dans lequel une couche de 5nm de SiO_2 est ajoutée, l'isolation électrique est amélio-

rée. Nous avons exploré pour la première fois un nouveau mécanisme de modulation utilisant un couplage à trois modes (ENZ Drude dans l'InGaAs, ENZ du phonon optique du SiO_2 et le mode de cavité MIM) dont le mode de type phonon optique est modulable. Avec cette structure de type MOSFET, une profondeur de modulation expérimentale d'environ 0.5-1.2dB est atteinte vers 7.5μm, comparable à des dispositifs similaires dans l'état de l'art. Une déplétion significative des électrons pour moduler davantage le mode ENZ paraît difficile expérimentalement, limitée par la tension de claquage et par écrantage dû à des charges piégées dans les défauts d'interface. En perspective, d'autres systèmes de matériaux avec un offset de bande de conduction plus élevé sont considérés : InGaAs/InAlAs, GaAs/AlGaAs, GaN/AlGaN. Le mécanisme de modulation dans la structure de type HEMT peut être appliqué à la gamme THz dans laquelle une plus faible densité d'électron suffit pour atteindre le régime ENZ, donc la modulation de densité d'électron est a priori plus simple. Nous allons également explorer davantage le régime de couplage à trois modes.

Concernant le dispositif ENZ-QCD, nous avons étudié le rôle du *depolarization shift* dans l'absorption des transitions intersousbande et sa relation avec le concept ENZ, nous permettant de correctement prendre en compte ce phénomène dans nos simulations électromagnétiques. La simulation électromagnétique indique une grande absorption utile dans le puits quantique actif unique, jusqu'à 50-60% du flux incident, tandis que des structures QCD conventionnelles sont souvent limitées avec une absorption utile de moins de quelques pourcents par période active. Expérimentalement, des mesures de réflectivité des dispositifs ENZ-QCD en fonction de la température montre une transition d'un régime de couplage faible à un régime de couplage fort de la transition intersousbande avec le mode de cavité. A partir des mesures du photocourant et de la réponse spectrale, nous estimons une efficacité quantique externe d'environ 0.057%, environ un ordre de grandeur inférieur à l'état de l'art. Considérant qu'il s'agit de la première génération de l'ENZ-QCD, les résultats obtenus sont encourageants et nous pensons que d'autres améliorations dans les prochaines générations sont réalistes. La physique dans le système ENZ-QCD est riche et constitue donc un sujet intéressant pour de futures études.

Contents

List of abbreviations and notations

EM: Electromagnetic
ENZ: Epsilon-Near-Zero
EOM: Electro-Optical Modulator
EQE: External Quantum Efficiency
FSOC: Free-Space Optical Communication
FTIR: Fourier Transform Infrared Spectroscopy
HEMT: High-Electron-Mobility Transistor
IQE: Internal Quantum Efficiency
LWIR: Longwave Infrared (typically defined as the 8.0 – 14.0 μm wavelength range)
MOSFET: Metal-Oxide-Semiconductor Field-Effect Transistor
MCT: Mercury Cadmium Telluride
METIS: Modelling of the Electronic Transport of Intersubband Structures
ISB: Intersubband
ISBT: Intersubband Transition
QCD: Quantum Cascade Detector
QCL: Quantum Cascade Laser
QW: Quantum Well
QWIP: Quantum Well Infrared Detector
RCWA: Rigorous Coupled-Wave Analysis
SNR: Signal over Noise Ratio

Acknowledgements / Remerciements

Ce travail de doctorat est une aventure inoubliable pendant laquelle j'ai pu rencontrer et travailler avec plusieurs personnes. J'aimerais remercier à tous ceux qui m'ont aidé à arriver au bout de cette aventure:

D'abord, je tiens à remercier particulièrement mes encadrants Fabrice Charra et Simon Vassant. Merci à Fabrice pour ta gentillesse extrême, pour ta disponibilité à tout moment pour une discussion, pour tes remarques pertinentes et constructives sur mon travail et sur la compréhension physique en générale! Merci à Simon pour tout le travail qu'on a réalisé ensemble, pour m'avoir appris plein de choses pendant cette thèse, la physique, la techno, mais aussi les interactions humaines! Merci pour avoir été très patient avec moi pendant la période compliquée de rédaction! Et je me souviendrai évidemment du 'Le mieux est l'ennemie du bien'!

J'aimerais remercier aux membres du jury de thèse, Mme. Delphine Marris-Morini, M. Jean-François Lampin, M. Thierry Taliercio, M. Yannick De Wilde pour la relecture et l'examination de mon travail de thèse. J'ai beaucoup apprécié les échanges intéressants avec le jury ainsi que vos remarques et vos questions pertinentes pour avoir un point de vue objectif sur ce travail et des perspectives pour la suite.

Merci à l'équipe des permanents du LEPO: Simon, Fabrice, Ludovic, Céline qui m'ont beaucoup appris en nanophotonique et qui sont toujours disponibles pour m'aider pendant ces trois années. Merci à Ludo pour les discussions scientifiques et pour tes anecdotes intéressantes. Merci à Céline pour tes encouragements et aussi tes conseils d'orientation professionnelle. Un grand merci à tous les thésards, postdocs et stagiaires de notre groupe! À Sarra, William et Quanbo pour m'avoir accompagné quand j'étais encore tout nouveau à Saclay, je me rappelle toujours des midis d'observation de poissons chromatiques géants. Merci à Sarra pour toujours être attentionnée et pour tes messages encourageant! Merci à Edouard pour tes blagues de qualité que je saisissais rarement dès le premier coup. Merci à Hung Ju et Mansour pour vos bonnes humeurs. A big thank to Remik for being a 'sweetheart', your favorite word ;)! You can count on me for lunch bread to save money for your heart operation!!

Au SPEC, merci à la direction et le secrétariat pour vos aides. Merci à M. Ladieu pour vos encouragements pendant des périodes difficiles de ma thèse. Merci à Pief, Sébastien et Aurélie pour vos aides techniques en salle blanche. Merci à tous mes amis thésards du labo, et parmi eux: Paul, Anas, Cyril, Binh, Eric, Myriam! Merci à Paul pour tes échantillons qui m'étaient bien utiles

pour la calibration des mesures Hall. Merci à Eric pour m'avoir introduit au club du kb, j'ai beaucoup apprécié les séances de discussion sur l'écologie, les questions de climat et des ressources. Un très grand merci à Myriam pour tous ces moments qu'on a partagés: la piscine, les sorties, le covoiturage et des discussions intéressantes ;)... Merci pour avoir été présente pour moi quand j'avais le plus besoin!

Au C2N, merci à Jean-Luc Pélouard pour m'avoir permis de venir travailler au C2N et pour de longues discussions sur des dispositifs et des process. Merci à Fabrice Pardo pour venir en aide rapidement et toujours d'une efficacité remarquable quand j'ai rencontré des problèmes de montage ou de mesure. Merci à Shatha pour avoir pris le relais de la suite du travail, pour ton soutien et tes conseils quand j'étais au C2N. Merci à Christophe, Nathalie et Abdou pour vos aides précieuses en salle blanche, vos disponibilités et la bonne humeur! Merci à mes amis Linh Nguyen, Linh Tran, Duong, Romain, Bérengère pour de superbes moments aux cafés, aux déjeuners et en salle blanche, pour remonter le moral ensemble des jours difficiles où le process ne marchait pas! Merci également à tous les deux Linh pour vos aides en techno et au MEB!

Au III-V lab, merci à Alexandre Delga et à Virginie Trinité pour les discussions théoriques très intéressantes sur les QCDs, à Jean-Luc Reverchon pour son aide sur des tests de bonding. Un grand merci à Mathurin, Grégory et Thomas pour de nombreux échanges, pour vos aides, pour vos résultats qui sont importants dans le projet Metanizo, et aussi pour des sorties ensemble!

A l'ONERA, merci à Julien Jaeck et à Baptiste Fix pour m'avoir accueilli au labo pour les caractérisations électro-optiques ainsi que de longues discussions sur des instruments de caractérisation. Merci à Clément V. pour ton aide sur le montage de mesure FTIR à froid qui a donné de beaux spectres. Merci à Baptiste, Laura, Clément, Clément, Claire, Cécile et tous les autres membres du groupe qui m'ont accompagné tous les jours pour l'entrée et la sortie du site pendant 2 mois, des repas et des pauses de jeux ensemble!

A l'IOGS, un grand merci à Jean-Paul pour ton aide précieuse sur le code Reticolo. Merci à M. Greffet pour le cours Nanophotonique, un des meilleurs cours que j'ai particulièrement appréciés.

Enfin, un très grand merci à tous mes amis hors des labos et à ma famille qui m'ont toujours soutenu pendant ces trois ans de thèse. Thanks Marija, you are my best coloc ever! Con cảm ơn ba má và anh Nhân luôn bên cạnh và nhắc nhở, ủng hộ con!

Some citations as a reminder to myself and to my friends:

"The secret to happiness in life: low expectations"

Geography Club, Hartinger Brent

De Martha Boeglin, Scriptoria. Et j'ajouterais: penser à reculer pour avoir une perspective plus large.

General introduction

Electromagnetic radiations, or light in a broad definition, surround us in many forms: radio waves, microwaves, infrared, visible light, ultraviolet, X-rays and gamma rays. Using light, we can probe, image, interact and transform matters at various scale, both in daily life applications and in fundamental research. When it comes to probe or interact with microscopic objects (cells, micro-crystals,...), optical lenses are very handy and commonly used to focus an incident lightbeam into a tiny light spot on the object of interest. We want the light spot typically to be as large as the object's size. Without the help of such optical lens, the incident beam is usually too large, and a majority part of light just passes by without 'seeing' the object. Focalization of the incident beam to the object's size allows the entire beam to interact with the object (that means being absorbed or scattered, triggering electronic transition for instance).

Nowadays, progresses in science and technology push our exploration further down to the nanoscale. A lot of new properties and potential applications can be uncovered by studying light-matter interaction at the nanoscale - near the atomic limit of matters. However, the well-known fundamental law of diffraction states that dielectric lenses can not focus light to a spot smaller than half of the wavelength of light in air. Because of this diffraction limit, it is challenging if we want to use light to probe or interact with deeply sub-wavelength objects. The nanophotonic (or nano-optic) field investigates new structures and concepts allowing deeply sub-wavelength light confinement and enhancing light-matter interaction at nanoscale. Nanophotonics includes several domains: near-field microscopy (exploiting evanescent waves in near field that are not subject to the diffraction limit in far field), photonic crystals (creating periodic structures of high and low index materials that create photonic bandgap for light confinement [1]), plasmonic (using electrons and electromagnetic oscillations combinations called surface plasmon polariton to strongly confine light), metamaterials (exploiting special values of optical index of materials to manipulate light, the special optical indices can usually be obtained by engineering the structure of different compounds). Nanophotonics is a flourishing field and has opened new paths to study light emission, sensing, harvesting, guiding and modulating.

Epsilon-Near-Zero (ENZ) materials are a family of materials with dielectric constant close to zero (compared to a dielectric constant of unity for vacuum or several unities for usual dielectrics). This family of materials - having been actively studied for the last ten years - belongs to the meta-

1. Conventional photonic structures are limited by diffraction limit, but new structures offer deeply sub-wavelength confinement [1].

materials and plasmonic branches of nanophotonics. An ENZ medium offers an 'intrinsic' normal electric field enhancement thanks to the material's dielectric constant being close to zero. This unique 'intrinsic' field enhancement can be combined with other 'extrinsic' field enhancements (due to structuration for example), to create a greater total field enhancement. When structured into highly sub-wavelength thin slab, ENZ materials can confine a majority of electric field inside the slab thanks to the apparition of an optical mode called the ENZ mode. ENZ medium also offers a quasi-constant wave's phase in the medium, a diverging phase velocity and a zero group velocity. These properties confer to ENZ media several fascinating phenomena such as: non-linearities boosting, slow light, photon tunneling (full light transmission through narrow arbitrary shape tunnel), highly directive light emission... In recent years, ENZ materials are the subject of numerous experimental studies on light modulation, perfect absorber, directional thermal emitter, second harmonic generation,... where ENZ materials proved their role. New applications of ENZ materials are awaiting to be demonstrated, and my PhD work is dedicated to this goal. My study focuses on two kinds of optoelectronics devices, an Electro-Optical Modulator (EOM) and a Quantum Cascade Detector (QCD), where we think ENZ materials bring their new features into contribution. These devices are designed at the longwave infrared range (around 10 μm) due to their potential applications (rapid detector and modulator for Free Space Optical Communication, gaz spectroscopy using dual-comb spectroscopy,...).

Regarding the EOM, it is an important component playing the role of an electrical-to-optical transducer - the optical output beam intensity of EOM is controlled and modulated by an electrical source. One common role of optical modulation is to encode information, e.g. in optical communication. For fiber-optic communication in the telecom wavelength range (1.55μm), the optical signal of a transmitter can be modulated at moderate frequency (up to several GHz) directly by switching the current supply of the light source (LED, laser diode). This approach is however limited by the rise and fall time of the source, and the signal is usually distorted at modulation frequency ranges higher than 10 GHz [2]. External optical modulators are employed for high speed modulation. For telecom wavelength range, several kind of modulators exist: electro-optic modulators (exploiting optical index change under an applied electric field to change the light's phase, e.g. Lithium Niobate is frequently used), electro-absorption modulators (using Quantum-confined Stark effect to reduce the absorption bandgap of an absorbing quantum well, changing the absorption level of the wavelength of interest), acousto-optic modulators (using acoustic waves to deflect the incident beam and modulate its intensity). However, these solutions are either not adapted or not well developed in the LWIR wavelength range. Indeed, few studies are found on electro-optical modulation around 10 μm, and very rare commercial devices based on acousto-optic or electro-optic are narrow bandwidth or have a low modulation efficiency [3]. An efficient broadband modulator is missing at LWIR range, even though this wavelength range has promising potential for free space optical communication. In this work, we want to apply the ENZ concept to realize a modulator at LWIR range. We use a thin ENZ layer embedded in an optical cavity to create an EOM in which a transition between strong coupling and weak coupling regimes modulates the optical output. ENZ materials are indeed employed in numerous studies on optical modulation, mostly around the telecom wavelength. The ENZ property allows to confine light in a deeply sub-wavelength layer. Our goal of modulating the optical properties of this thin layer is facilitated compared to a thick layer. The concept of strong-to-weak coupling regime, not commonly explored yet in the literature, is an elegant way to modulate optical signal and also interesting to understand in term of physics.

QCD belongs to the intersubband devices family. They emerged in early 2000s as a combination of two older technologies: Quantum Well Infrared Photodetector (QWIP) and Quantum

Cascade Laser (QCL). QCD employs an asymetric band structure scheme, allowing it to generate a photocurrent response without applying a voltage bias. Thanks to this property, QCD offers a lower dark current compared to its predecessor QWIP, which is beneficial for the device's signal over noise ratio (SNR). However, a polarization selection rule imposes to intersubband devices: QCD are only sensitive to the normal component of the electric field. This normal component is usually very small when light comes to the detector at quasi-normal incidence. Special coupling schemes (Brewster angle, 45° facet coupling) are needed in conventional QCD structures, and these coupling schemes are not pratical in real devices applications. In addition, there is a huge spatial mismatch between the detected wavelength (usually severals μm in infrared range) and a quantum well (typically 10nm thick) where infrared photons are absorbed. The small overlap between the infrared photon and the quantum well means low light-matter interaction, and a small intersubband absorbtion per quantum well. To counter this problem, QCD are usually made of tens of active quantum wells, but this in turn also reduces the signal over noise of the device according to reference [4]. An application of ENZ medium in case of QCD offer two advantages. The normal electric field is enhanced which is beneficial for the intersubband absorption. The infrared light can be squeezed and confined at deeply sub-wavelength scale, increasing the light-matter interaction and rendering possible a QCD structure with a single active quantum well - having better SNR. These ENZ contributions can help to improve QCD's performance and increase the device's operating temperature.

My work is a part of the mEtaNiZo ANR project (Matériau anisotrope à fonction diélectrique proche de zéro pour la photodétection), which aims to apply ENZ properties to enhance light-matter interaction in new structures of infrared photodetector. Five research groups with different expertises brought together their skills in the project:

- SPEC of CEA Saclay as my home institution, with my advisor Simon Vassant,
- III-V lab with Alexandre Delga, Virginie Trinité as researchers and Mathurin Lagrée as PhD student,
- NEO of C2N with Jean-Luc Pelouard, Fabrice Pardo as researchers, Shatha Kaassamani as Postdoc,
- LCF of IOGS with Jean-Jacque Greffet and Jean-Paul Hugonin as researchers,
- ONDA of ONERA with Julien Jaeck and Baptiste Fix as researchers.

The III-V lab was in charge of the electronic transport modeling for QCD structures and substrates epitaxial growth. C2N participated in the design discussions of the devices and provided their expertises in fabrication processes as well as in electrical characterizations. IOGS provided their expertise in electromagnetic computation and precious theoretical discussions on nanophotonics. ONERA provided their expertise in optoelectronic characterizations of final devices. SPEC group with my advisor and myself participated in most parts of the project: we were in charge of the optical conception and modeling of both devices, materials' preliminary optical characterizations, samples' microfabrications and characterizations. I spent my three years of PhD between three labs, at SPEC to learn and apply electromagnetic computation, optical characterizations and clean room fabrication, at C2N to realize most of my samples in clean room as well as some characterizations, and at ONERA to realize final optoelectronic characterizations.

My work, even though not having reached the project's ultimate goal of demonstrating new ENZ optoelectronics devices with performances at the state of the art, has contributed to build some fundamental understandings on the subject. On materials' properties, we offered a new way to measure optical phonons in InGaAs thin film using a detuned Salisbury screen scheme to enhance it's optical response. A Gaussian lineshape model was used to model optical phonon's

contribution to the InGaAs dielectric function, in order to correct a non-causal error commonly seen in the literature. We also understood better the origine of the depolarization shift usually mentioned in QCD's conception, which is in fact a dielectric contrast effect, directly linked to the ENZ effect. One of its consequence is that this term should not be included in the dielectric function of intersubband quantum well in an electromagnetic computations where this effect is already taken into account by boundary conditions.

Concerning real devices, for the EOM HEMT-like, we observed experimentally a strong coupling regime between an ENZ mode and a cavity mode. However, the transition to weak coupling regime by depleting free electron in the ENZ highly doped layer appreared to be challenging. Materials' interface electrical behavior appears to be crucial and needs to be better controlled. In the final MOSFET-like structure, a new modulation mechanism using a three-mode coupling regime was explored for the first time. An experimental modulation depth of about 0.5-1.2dB at around 7.5μm was reached and is comparable to the modulation depth of similar devices in the state of the art.

As for QCD, electromagnetic computations show a large useful absorption in the quantum well, up to about 60% of the incident flux for the chosen doping level of the quantum well, and even larger for higher doping. The ENZ effect in the QCD system is quite modest as we chose to limit the doping level due to noise considerations, but still contributes to the overall field enhancement and confinement. The understanding of the depolarization shift helps to choose optimized parameters for the optical cavity. Optical reflectivity characterization at cryogenic temperatures shows the intersubband transition of a single quantum well, in a strong coupling regime with the cavity mode. Interestingly, the system transits from strong coupling at cryogenic temperature to weak coupling regime at room temperature, even though this was not our first intention. This evolution merits further investigation to better understand our system. Photocurrents and spectral responses of our first generation QCDs were realized. The external quantum efficiency of my best sample currently is about 0.057%, about an order of magnitude smaller than the state of the art. Considering this is the first time we realize a single active quantum well QCD in the project, this result is encouraging and we believe further improvements in future generations to be realistic.

This dissertation is organised into four chapters:
In the first chapter, I will introduce the ENZ concept and a brief state of the art on ENZ applications. Then I will present different the physical contributions to the dielectric function that allow to reach ENZ regime, along with some figures of merit. After that, I introduce the interface polariton mode and ENZ mode notions.

The second chapter centers on characterizations of the dielectric function of our material of interest InGaAs. Van der Pauw - Hall effect, Raman and Fourier Transform Infrared (FTIR) spectroscopies will be introduced. Then I will discuss how to reach ENZ regime in InGaAs, the material of choice for our devices.

In the third chapter, I will present the epsilon-near-zero electro-optical modulator (ENZ-EOM). I will give some elements on the state of the art and describe the working principle of the device. Then I will show our procedures of electromagnetic and electronic conception and modelization. Next, I will present the samples' fabrication and characterization through two generations of ENZ-EOM, with band structures inspired from High-Electron-Mobility Transistor (HEMT) and Metal-Oxide-Semiconductor Field-Effect Transistor (MOSFET). I will finish this chapter with some discussions on current results and further perspectives.

In the last chapter, I will present our work on single active quantum well QCD benefiting from an ENZ field enhancement effect. The chapter is organized in the same manner as the third chap-

ter. I will present the state of the art and the working principle of the device. Then I will show the electromagnetic computation to optimize the useful absorption in the device, as well as the device's band structure computed by our project partner. Then I will present the sample fabrication process and different characterizations of these QCD. I will finish with some discussions about future perspective for these QCD.

1

Introduction to ENZ effect

This chapter introduces briefly the concept of the Epsilon-Near-Zero (ENZ) materials and the state of the art. I will explain the field enhancement in ENZ materials that will be studied in this work. Then I will present different contributions to the infrared dielectric function in a material, corresponding to different paths to reach the ENZ regime. Finally, I will introduce the notions of surface plasmon polariton, the ENZ mode and the Berreman mode.

1.1 State of the art and theories of the ENZ effect

1.1.1 Generalities on the dielectric function

At low frequency, the permitivity or dielectric constant ϵ is a familiar physical quantity, characterizing how a dielectric medium opposes to an external electric field by polarizing itself. The figure 1.1 illustrates this phenomenon. Under the action of an external electric field, charges in the medium move as a response to the Lorentz force. Microscopically, electric dipole moments are formed and their electric field opposes to the external electric field. The net electric field (local electric field) is the sum of the external field and all the dipoles' field. Compared to the external electric field, the net electric field inside the dielectric medium is reduced by a factor of ϵ - the dielectric constant. The larger the dielectric constant is, the smaller the local electric field will be.

The dipoles formation in the medium is characterized by the polarization vector **P** (dipole moment density) and the electric susceptibility χ as:

$$\mathbf{P} = \epsilon_0 \chi \mathbf{E}, \tag{1.1}$$

where **E** is the internal electric field and ϵ_0 is the vacuum permittivity. The electric displacement field **D** is defined from the polarization vector as:

$$\begin{aligned} \mathbf{D} &= \epsilon_0 \mathbf{E} + \mathbf{P} && (1.2)\\ &= \epsilon_0 \mathbf{E} + \epsilon_0 \chi \mathbf{E} && (1.3)\\ &= \epsilon_0 (1+\chi) \mathbf{E} && (1.4)\\ &= \epsilon_0 \epsilon \mathbf{E}. && (1.5) \end{aligned}$$

The dielectric constant ϵ is defined as the sum χ+1.

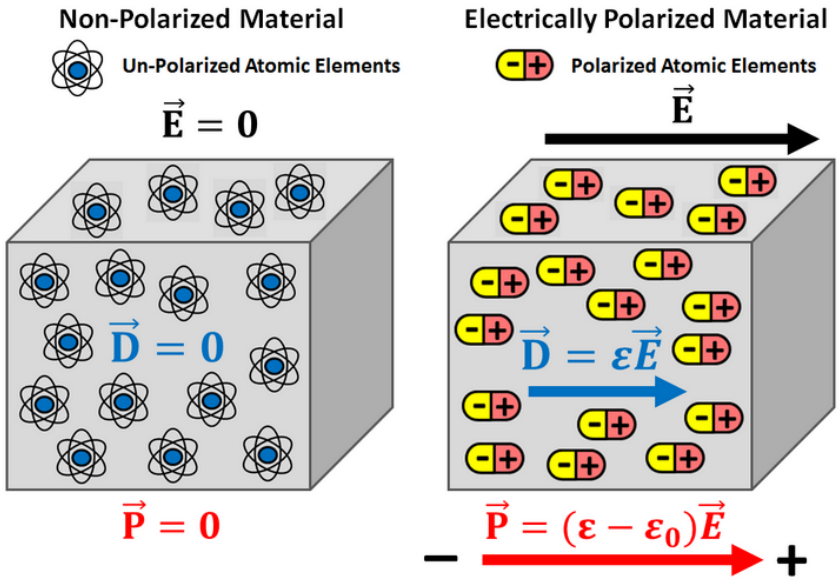

Figure 1.1 – Material's polarization under external electric field [5]

When we shine the light on a medium, similar phenonomenon happens because of the oscillating electric field of light. Charges (both free and bound ones) start to oscillate at the same frequency as the incident electromagnetic (EM) waves. The medidum is once again polarized. The biggest difference with the low frequency regime is that the optical frequency can be close to the natural frequency of charges oscillation. The resonance of charges oscillation with the driving force of the EM field makes the medium's response to the EM field highly frequency dependent.
Similar to forced oscillation of a mechanical spring, when the light frequency becomes larger than the natural frequency of charges oscillation, the electric field oscillation and charge oscillation are out-of-phase by π. One consequence of this out-of-phase movement is that the polarization no longer opposes to the incident field but instead enhances it. The susceptibility χ becomes negative and the dielectric constant ϵ can get smaller than 1.
The full analysis is a bit more complex since the internal electric field is used in the definition of the polarization vector **P**. As a consequence, the polarization vector changes direction when the susceptibility χ is negative, then it changes direction again when the dielectric constant ϵ gets negative. Hence, the polarization's contribution to the internal electric field must be analyzed with care. What we can keep in mind is that around charges oscillation resonance, the susceptibility is strongly dependent on frequency, and so does the dielectric constant ϵ. Also because of this reason, the name dielectric function $\epsilon(\omega)$ is more adapted to express the frequency dependence and it will be employed in this work.
Another point to keep in mind is that there are different kind of charges oscillation happening at different frequency ranges in a material. The dielectric function can be rewritten as:

$$\epsilon(\omega) = 1 + \chi_{oscillation\,1}(\omega) + \chi_{oscillation\,2}(\omega) + ... \tag{1.6}$$

Because these resonances generally have very distinct frequency ranges, we can suppose that non resonant contributions are non dispersive background contribution and rewrite the expression of

the dielectric function as:

$$\epsilon(\omega) = 1 + \chi_{background} + \chi_{resonant}(\omega) = \epsilon_\infty + \chi_{resonant} \tag{1.7}$$

Further discussions about the different kind of charges oscillation contribution to the dielectric function will be developped in section 1.2. The dielectric function contains all the information about how the material reacts to electromagnetic waves.
It should be noticed that, in this work, it is the relative dielectric function that we are talking about when I mention 'the dielectric function' and use the notation $\epsilon(\omega)$ or just ϵ. [1]
The dielectric function $\epsilon(\omega)$ usually has complex value:

$$\epsilon(\omega) = \epsilon'(\omega) + i\epsilon''(\omega), \tag{1.8}$$

where the real part $\epsilon'(\omega)$ describes the usual meaning of ϵ for charge screening and the imaginary part $\epsilon''(\omega)$ accounts for optical losses in the material.
The dielectric function is related to the complex refractive index as: $n = n' + in'' = \sqrt{\epsilon}$. The real part $n' = \sqrt{\frac{|\epsilon| + \epsilon'}{2}}$ is related to the phase velocity of electromagnetic waves in the material $v_p = c/n'(\omega)$. The imaginary part $n'' = \sqrt{\frac{|\epsilon| - \epsilon'}{2}}$ is related to the decay length of EM wave's amplitude during propagation in the medium: $\delta = \frac{\lambda_0}{2\pi n''(\omega)}$, where λ_0 is the wavelength in vacuum.
The materials' optical response regarding electromagnetic waves can be categorized in two families:

- Metal-like behavior: the real part of the dielectric function is negative $\epsilon' < 0$, the refractive index is mostly imaginary. The EM wave decays rapidly when entering metal-like medium and can not propagate further.
- Dielectric-like behavior: the real part of the dielectric function is positive $\epsilon' > 0$, the refractive index is mostly real. EM wave doesn't decay rapidly and can propagate inside dielectric-like medium.

Some materials can have both behavior depending on the frequency range. Interesting properties emerge at the transition wavelength between metal-like and dielectric-like, where the real part of the dielectric function crosses zero.

1.1.2 State of the art of ENZ

In the last two decades, a class of materials called 'Epsilon-Near-Zero' has emerged in numerous studies. These materials possesses a dielectric function with the real part passing by zero and the imaginary part smaller than unity (low loss). This family of materials belongs to the metamaterials and plasmonic branches of nanophotonics which investigate new structures and concepts allowing deeply sub-wavelength light confinement and enhanced light-matter interaction at the nanoscale. An ENZ medium offers an 'intrinsic' normal electric field enhancement thanks to the materials' dielectric constant being close to zero. When structured into highly sub-wavelength thin slab, ENZ materials can confine a majority of electric field inside the slab thanks to the apparition of an optical mode called the ENZ mode. ENZ medium also offers a quasi-constant wave's

1. The notation ϵ_r can be used in other works to indicate the relative dielectric function, however, I prefer omitting the index 'r' to simplify the notation.

phase in the medium, a diverging phase velocity and a zero group velocity. Pioneering works (Engheta [6], Enoch [7]) shown that ENZ materials offer the possibility to realize photon tunneling / perfect light coupler (full transmission of electromagnetic waves through deeply sub-wavelength tunnel of arbitrary shape) and highly directive antenna's emission. The photon tunneling effect was experimentally demonstrated in microwave regime [8] [2], and can be understood by impedance matching arguments. Indeed, ENZ medium has larger light impedance than usual materials (defined as $\sqrt{\mu_0\mu/\epsilon_0\epsilon}$). Narrow width tunnel of large impedance ENZ materials has a total impedance of the same order of magnitude as free space. The impedance matching assures the full transmission of light through the channel. The photon tunneling through an arbitrary shape tunnel is unique to ENZ materials and offers a new technique to make waveguides with arbitrary shape. Highly directive antenna's emission of ENZ materials, on the other hand, comes from the fact that EM wave's phase in ENZ materials is almost constant. A well controlled pattern of wave's phase results in directional emission thanks to interferences.
These works have stimulated a lot of new investigations on materials with ENZ properties. Later on, ENZ materials were employed to experimentally demonstrate nonlinear effect enhancement [10], optical modulators [11, 12], perfect absorbers [13], broadband directional thermal emission [14].
There are two approaches to obtain an ENZ medium. A homogeneous medium having an intense and narrow linewidth charge oscillation resonance creates a large polarization vector **P**. If the corresponding susceptibility is negative enough to counter other non resonant contributions, the dielectric function can cross zero and reach ENZ regime. The Figure 1.2a depicts the ENZ regime in a phononic material and in doped oxides.
A second approach consists of inhomogeneous medium made of a mix of metal-like and dielectric-like materials, in forms of spheres, rods or thin films, as illustrated in Figure 1.2b. Metal-like materials have negative ϵ' while dielectric-like materials have positive ϵ'. Their mixture results in a medium with an effective dielectric function close to zero when carefully designed. However, the effective dielectric function approximation only holds for wavelength larger than the inclusions' size (as discussed the review article by Kinsley et al. [15]), equivalent to an upper bound to the wave vector k. Therefore, the interpretation of electromagnetic properties in ENZ inhomogeneous media must be done while keeping this limit in mind. In this thesis, I will only concentrate on the continuous medium approach.

The beauty of the homogeneous ENZ materials lies in its intrinsic electric field enhancement happening naturally at the material's boundary. This happens without the need of complex structure and is well appreciated for its simplicity in fabrication. This intrinsic electric field enhancement due to the materials's property can also be combined with other extrinsic field enhancement factors (e.g. optical resonators) for a greater enhancement level by inserting ENZ materials in these structures.

ENZ materials are predicted to increase light-matter interaction, strongly enhance and confine light in very sub-wavelength structures. These properties can be beneficial to optoelectronics devices like optical modulator and photodetector. Indeed, ENZ materials are employed in numerous studies on optical modulation, mostly around the telecom wavelength [11, 12, 16, 17]. The ENZ property allows to confine light in a deeply sub-wavelength layer whose optical properties' modulation is facilitated compared to a thick layer. For general photodetectors, optical field confinement means device's size reduction, which generally improves the device speed (smaller capacitive effect) and reduces device's power consumption. For interband photodetectors where electrons and holes are generated, separated and collected, thinner absorber layer also eases the charge collec-

2. Also demonstrated in mid-IR range in reference [9] but the transmission is limited due to larger loss.

tion when the charge's free path is larger than the absorber's thickness. In the case intersubband devices using quantum well, the devices are only sensitive to the normal electric field component which is generally small without special collection scheme. ENZ effect enhances this normal electric field component which is much appreciated in these intersubband devices. To our knowlegde, only a few experimental demonstrations of light modulator in near IR range using ENZ materials have been realized up to now. There is no application of ENZ effect in photodetection or optical modulation in the Longwave Infrared (LWIR) range around 10μm.

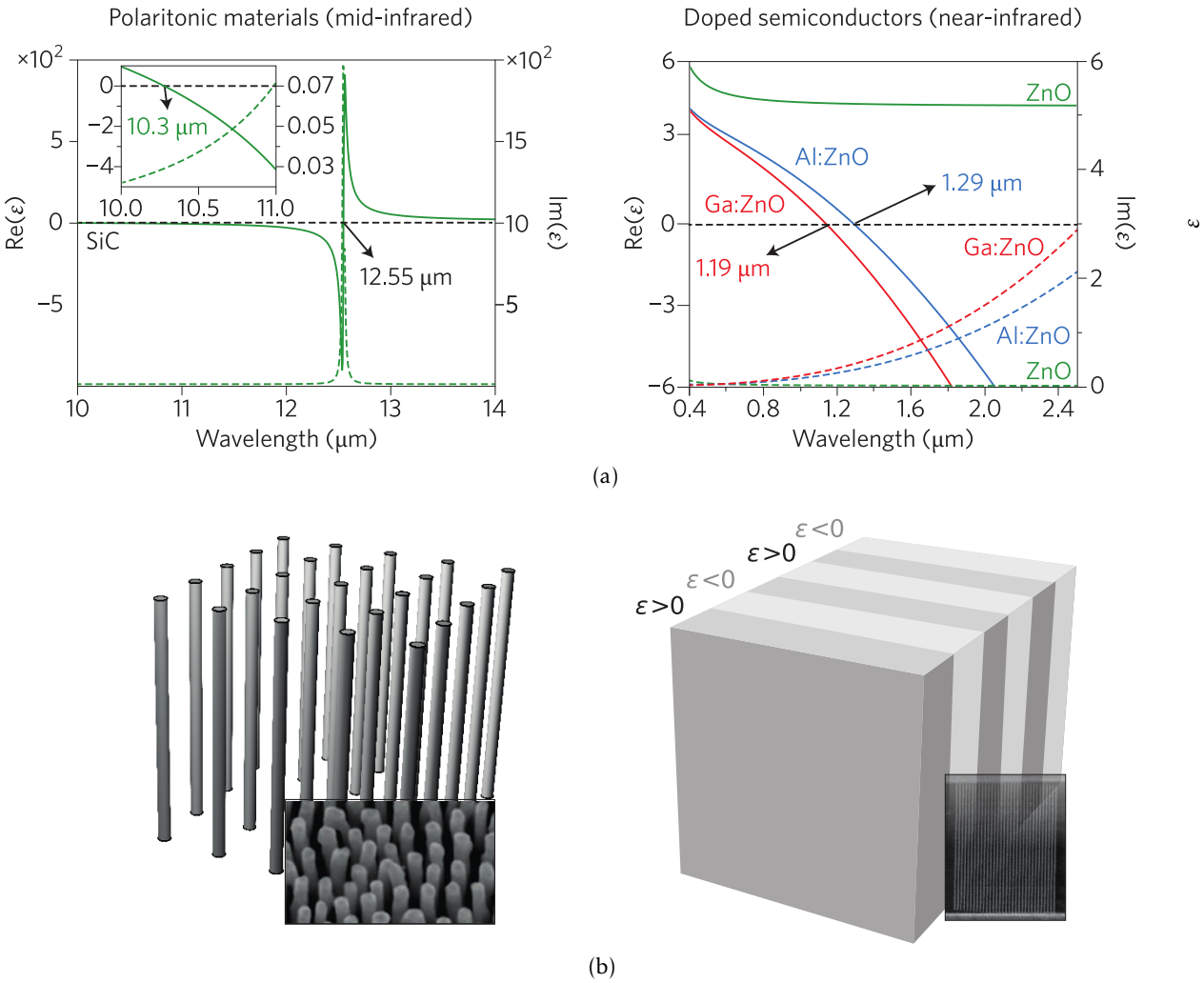

Figure 1.2 – ENZ materials: continuous and inhomogeneous media, figure adapted from reference [18]. Top figures illustrate the dielectric functions of continuous ENZ media: Phononic materials SiC, λ_{ENZ} ~10.3μm; doped oxide ZnO, $\lambda_{ENZ} \sim 1.3\mu m$. Bottom figures illustrates inhomogeneous ENZ media: metallic nanorods (gold) in dielectric medium (air); metallic-dielectric multilayer made of Ag-SiN

1.1.3 Electric field enhancement with ENZ materials

Let's consider the interface between two media (1) and (2) as depicted in figure 1.3, with the dielectric function of the medium (2) close to zero.

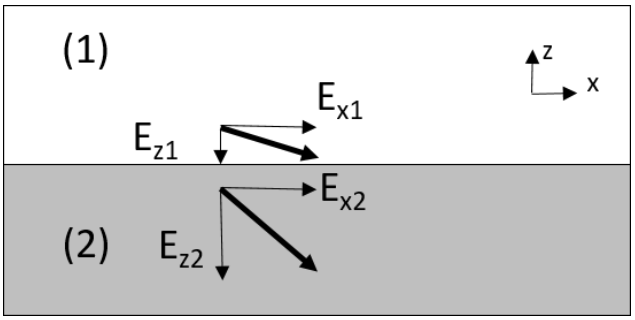

Figure 1.3 – Interface between two media (1) and (2)

For linear optics, the general form of the dielectric function is a 2^{nd} rank tensor that connects the electric field **E** to the electric dispacement field **D** in a medium:

$$\mathbf{D} = \epsilon_0 \overline{\overline{\epsilon}} \mathbf{E} = \epsilon_0 \begin{pmatrix} \epsilon_{xx} & \epsilon_{xy} & \epsilon_{xz} \\ \epsilon_{yx} & \epsilon_{yy} & \epsilon_{yz} \\ \epsilon_{zx} & \epsilon_{zy} & \epsilon_{zz} \end{pmatrix} \mathbf{E}. \tag{1.9}$$

For optically isotropic materials (cubic crystals) and anisotropic orthorhombic materials, the dielectric tensor is respectively simplified as:

$$\overline{\overline{\epsilon}}_{iso.} = \begin{pmatrix} \epsilon & 0 & 0 \\ 0 & \epsilon & 0 \\ 0 & 0 & \epsilon \end{pmatrix} \text{ and } \overline{\overline{\epsilon}}_{aniso.\ ortho.} = \begin{pmatrix} \epsilon_x & 0 & 0 \\ 0 & \epsilon_y & 0 \\ 0 & 0 & \epsilon_z \end{pmatrix}, \tag{1.10}$$

$$\mathbf{D}_{iso.} = \epsilon_0 \epsilon \mathbf{E}, \tag{1.11}$$

$$\mathbf{D}_{aniso.\ ortho.} = \epsilon_0 (\epsilon_x \mathbf{E}_x + \epsilon_y \mathbf{E}_y + \epsilon_z \mathbf{E}_z). \tag{1.12}$$

Due to near zero dielectric function of the medium (2), the normal component of the electric field to the interface in this the medium can be strongly enhanced. This enhancement is called the ENZ field enhancement effect. In fact, the continuity conditions oblige the continuity at the interface of the normal component of electric displacement field D_z:

$$D_{z1} = D_{z2}, \tag{1.13}$$

$$\epsilon_{z1} E_{z1} = \epsilon_{z2} E_{z2} \tag{1.14}$$

$$|E_{z2}| = |E_{z1}| \frac{|\epsilon_{z1}|}{|\epsilon_{z2}|} \tag{1.15}$$

When $|\epsilon_{z2}|$ tends towards zero, $|E_{z2}|$ can become very large. However, $|E_{z2}|$ won't diverge, because losses are always present and hence the imaginary part of ϵ_{z2} is always strictly positive (in a passive medium). Non negligeable optical loss, meaning a large imaginary part dielectric function, is indeed one of the main fundamental limits to many ENZ materials for their wider uses. A small imaginary part of ϵ is necessary to achieve a large electric field enhancement, we put a threshold of $\epsilon''_{ENZ} < 1$ to define an ENZ medium.

We introduce the ENZ factor K_{ENZ} as a figure of merit to characterize the intensity enhancement:

$$K_{ENZ} = \left|\frac{E_{z2}}{E_{z1}}\right|^2 \tag{1.16}$$

$$= \left|\frac{\epsilon_{z1}}{\epsilon_{z2}}\right|^2 \tag{1.17}$$

$$= \left|\frac{\epsilon_{z1}}{\epsilon''_{z2}(\omega_{ENZ})}\right|^2. \tag{1.18}$$

The ENZ factor depends on $\epsilon''(\omega_{ENZ})$ but also strongly on ϵ_{z1} the dielectric function of the boundary material. From now on, we reserve the notation K_{ENZ} for the cases where ϵ_{z1}=1 as in vacuum. In practice, in this work, ENZ layer is sandwiched by other boundary materials of large dielectric function of about 10 (ϵ_{InAlAs} ~10.24, ϵ_{InP} ~9.38 around the wavelength 9μm of interest). I will add a subscript to the ENZ factor when the boundary medium is not vacuum:

$$K_{ENZ} = \frac{1}{|\epsilon_{z2}(\omega_{ENZ})|^2} \tag{1.19}$$

$$K_{ENZ,\,InP} = \frac{9.38^2}{|\epsilon_{z2}(\omega_{ENZ})|^2} \tag{1.20}$$

$$K_{ENZ,\,InAlAs} = \frac{10.24^2}{|\epsilon_{z2}(\omega_{ENZ})|^2}. \tag{1.21}$$

In more general cases, we can also have a field enhancement even if the real part of the dielectric function doesn't cross zero, but the dielectric function $|\epsilon_{z2}|$ has a local minimum or $|\epsilon_{z1}|$ has a local maximum. In those cases, we will replace the name ENZ factor of field enhancement by a dielectric constrast field enhancement factor, with the notation $K_{dielectric}$.

The field enhancement in ENZ media can be interpreted by slow light phenomenon. Indeed, as mentioned above, light's group velocity in an ENZ medium tends towards zero, light's power flux propagates slowly in the medium and builds up. This is the origin of the electric field enhancement. The order of magnitude of the field enhancement factor K_{ENZ} typically changes from 10^{-1} to 10^2 with air as boundary material. When usual boundary materials of large dielectric function are considered, the field enhancement factor increases by two orders of magnitude (10^1-10^4). Compared to other electric field enhancement schemes like a Fabry-Perot cavity (field enhancement can reach for example 10^6 [3]) or photonic crystal structures (enhancement factor of 10^5 for instance, in reference [19]), the field enhancement factor in ENZ is more modest , mainly limited by material's intrinsic loss. On the other hand, ENZ enhancement is an intrinsic effect due to material's properties that can be added up to other enhancement schemes, as discussed in section 1.1.2. ENZ enhancement is not as sensitve to the geometry fluctuation as in the case of Fabry-Perot cavity or photonic crystal.

3. With highly reflective mirrors R_1=1, R_2=99.8%, the field enhancement factor of a Fabry-Perot cavity is $[1/\left(1-\sqrt{R_1R_2}\right)^2] \sim 10^6$).

1.2 Physical means to reach ENZ regime in homegeneous media

The dielectric function of a material is the response of charges in a medium to the electromagnetic wave. Hence, to reach the ENZ regime in homegeneous media, we have to play with different kinds of charges in the materials: free electrons or holes, intersubband transitions, optical phonons. We also have the interband transitions contribution to the dielectric function in the VIS-NIR range. However, the interband transition is usually accompanied by large optical losses. In this thesis I am mostly interested in the LWIR range, so we won't detail the interband contribution here.

1.2.1 Free charge carriers contribution

The Drude model [20] is usually used to describe the optical response of free charges carriers. Let a free electron of mass m_0 move under an optical electric field $\mathbf{E}(t)= \mathbf{E}_0 \exp(-i\omega t)$. A damping parameter Γ is introduced to take into account scattering events that induce losses. The equation of motion of the electron is written as:

$$m_0\ddot{\mathbf{r}}(t) + m_0\Gamma\dot{\mathbf{r}}(t) = -e\mathbf{E}_0 \exp(-i\omega t) \tag{1.22}$$

We want to find a solution in the form of $\mathbf{r} = \mathbf{r}_0 exp(-i\omega t)$. The equation of motion becomes:

$$\begin{aligned} m_0\omega^2\mathbf{r} + i\omega m_0\Gamma\mathbf{r} &= e\mathbf{E} && (1.23)\\ \mathbf{r} &= e\mathbf{E}/(m_0(\omega^2 + i\Gamma\omega)) && (1.24) \end{aligned}$$

This motion of electron leads to a polarization

$$\mathbf{P}_{free\ charges} = -Ne\mathbf{r}, \tag{1.25}$$

where N is the number of electron per unit volume, and –e**r** the dipole moment of one electron. By definition we have:

$$\mathbf{P}_{free\ charges} = \epsilon_0\chi_{free\ charges}\mathbf{E}. \tag{1.26}$$

This leads to:

$$\begin{aligned} \epsilon &= 1 + \chi_{background} + \chi_{free\ charges} && (1.27)\\ &= \epsilon_\infty - \frac{Ne^2}{m_0\epsilon_0}\frac{1}{\omega^2 + i\Gamma\omega}. && (1.28) \end{aligned}$$

Here we introduce other background contributions as $\chi_{background}$, that translates into ϵ_∞ – the high frequency dielectric constant. In solids, the lattice periodicity interacts with its electrons, an effective mass of electron m_0^* is used instead of m_0 to take this interaction into account. In the end we get:

$$\begin{aligned} \epsilon &= \epsilon_\infty - \frac{Ne^2}{m_0^*\epsilon_0}\frac{1}{\omega^2 + i\Gamma\omega} && (1.29)\\ &= \epsilon_\infty - \epsilon_\infty\frac{\omega_p^2}{\omega^2 + i\Gamma\omega} && (1.30)\\ & && (1.31) \end{aligned}$$

where $\omega_p = \sqrt{\frac{Ne^2}{m_0^* \epsilon_0 \epsilon_\infty}}$ is the screened plasma frequency [4].

With the Drude model, the real part of epsilon crosses zero at:

$$\epsilon'(\omega_{ENZ}) = 0 \tag{1.32}$$

$$\epsilon_\infty(1 - \frac{\omega_p^2}{\omega_{ENZ}^2 + i\Gamma\omega_{ENZ}}) = 0 \tag{1.33}$$

$$\omega_{ENZ} = \sqrt{\omega_p^2 - \Gamma^2} \tag{1.34}$$

$$\tag{1.35}$$

We usually have $\Gamma \ll \omega_p$, so $\omega_{ENZ} \sim \omega_p$. Therefore, ω_{ENZ} depends mostly on free charge concentration N, the effective mass m_0^* and ϵ_∞ that appear in the expression of ω_p.

Figure 1.4 shows plots of the free charges' contribution to the dielectric function by Drude model. ω_{ENZ} is blueshifted and the loss ϵ'' increases at larger electron concentration.

We also want to derive the condition for low loss ENZ medium $\epsilon''(\omega_{ENZ}) < 1$:

$$\epsilon''(\omega_{ENZ}) = \epsilon_\infty \frac{\Gamma}{\sqrt{\omega_p^2 - \Gamma^2}} < 1 \tag{1.36}$$

$$\iff \Gamma < \frac{\omega_p}{\sqrt{\epsilon_\infty^2 + 1}} \sim \frac{\omega_p}{\epsilon_\infty} \tag{1.37}$$

From the condtion (1.37), and with all other parameters staying constant, the smaller Γ be, the better the ENZ properties will be. Nevertheless, Γ and other parameters can be dependent on the same variable (e.g: both Γ and ω_p increase with doping), so we can not make a quick assumption without this point in mind.
Metals like gold, silver or tungsten exhibit zero crossing of the real part of epsilon at wavelengths in UV-VIS range, but usually have large ϵ'' due to interband absorption happening in the same range. Transparent doped oxides like ITO, AZO usually offer ENZ behavior in near IR range. For LWIR range, heavily doped semiconductors are common candidates.

4. Not to be confounded with the plasma frequency $\omega_p = \sqrt{\frac{Ne^2}{m_0^* \epsilon_0}}$ found in some other works. In solids, ϵ_∞ is usually larger than unity. If we consider lossless medium ($\Gamma = 0$), the screened plasma frequency indicates the frequency limit of the metal-like ($\omega < \omega_p$) or dielectric-like ($\omega > \omega_p$) behavior.

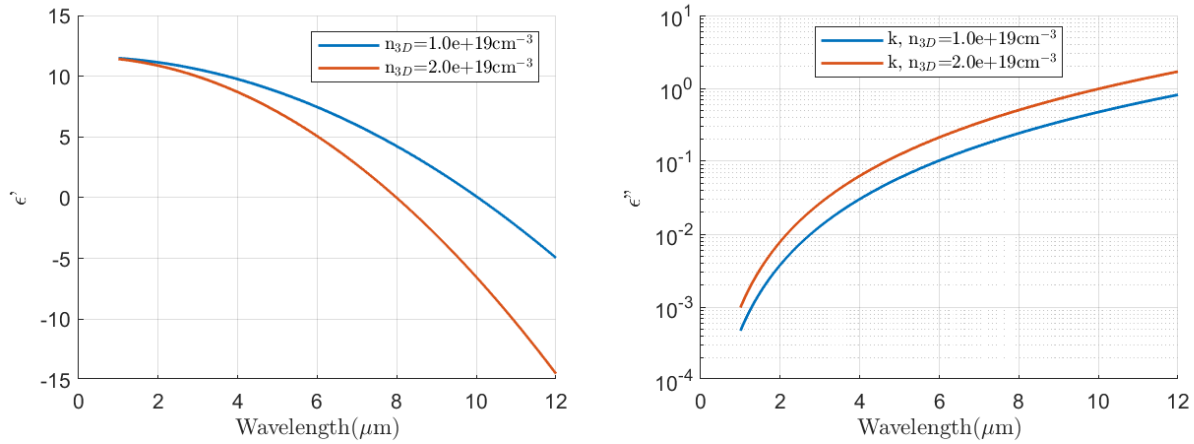

(a) (b)

Figure 1.4 – Drude's model of free charges contribution to the dielectric function, with $\epsilon_\infty = 11.6$, $m_0^* = 0.08m_0$.

1.2.2 ISB transition contribution

Band structures of semiconductors' heterostructures are engineered to create quantum wells (QW), bands and subbands structures, having numerous applications in optoelectronics. The intersubband (ISB) transition corresponds to an optical transition between two subbands states of a QW, as illustrated in Figure 1.5. ISB transition is accompanied with a charge displacement between two subband wave functions, and is characterized by a dipole moment along the confinement direction of the QW (z direction). Therefore, an ISB transition interacts only with the E_z component of the electromagnetic field. The intersubband transiton's contribution to the dielectric function is discussed in different papers and textbooks by Ando [21], Zaluzny [22], Helm [23], Rosencher [24], Fox [25].

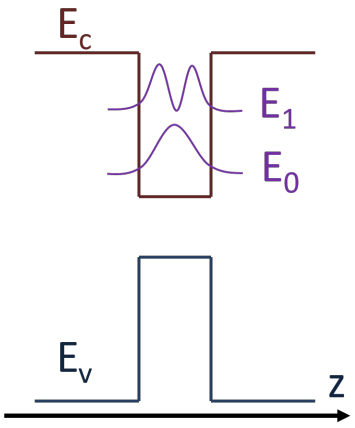

Figure 1.5 – A schematic of a quantum well band diagram with conduction band edge E_c and valence band edge E_v. The QW has two intersubband states of energy E_0 and E_1.

1.2.2.1 Drude-Lorentz model

In a classical approach, we can describe the ISB transition by the motion of a bound electron in a harmonic potential, with a damping term accounting for dissipation [25]. This is the Drude-Lorentz model. The reasoning is similar to the Drude model, with a restoring force term $m_0\omega_0^2\mathbf{r}$ in addition, accounting for the harmonic potential:

$$m_0\ddot{\mathbf{r}}(t) + m_0\Gamma_{ISB}\dot{\mathbf{r}}(t) + m_0\omega_0^2\mathbf{r} = -e\mathbf{E}_0\exp(-i\omega t) \tag{1.38}$$

$$\begin{aligned} \mathbf{P}_{ISB} &= -Ne\mathbf{r} && (1.39)\\ &= -\frac{Ne^2}{m_0(\omega^2-\omega_0^2+i\Gamma_{ISB}\omega)}\mathbf{E} && (1.40)\\ &= \epsilon_0\chi_{ISB}\mathbf{E} && (1.41) \end{aligned}$$

$$\begin{aligned} \epsilon &= 1+\chi_{background}+\chi_{ISB} && (1.42)\\ &= \epsilon_\infty - \frac{Ne^2}{m_0\epsilon_0}\frac{1}{\omega^2-\omega_0^2+i\Gamma_{ISB}\omega} && (1.43) \end{aligned}$$

This formula can be generalized when we have more than one ISB transition by summing over their contributions. In this work, we choose to limit ourselves to the case of only one ISB transition from ground state (0) to first excited state (1) for simplicity and because it is enough to satisfy our device's design. We also introduce an oscillator strength factor f_{01} to account for the transition probability, an effective mass m_0^*, an effective length L_{eff} and a 2D charge density N_{2D} to take into account the 2D dimensionality of the electron gaz in QW:

$$\begin{aligned} \epsilon &= \epsilon_\infty - \frac{N_{2D}e^2}{m_0^*\epsilon_0 L_{eff}}\frac{f_{01}}{\omega^2-\omega_0^2+i\Gamma_{ISB}\omega} && (1.44)\\ &= \epsilon_\infty - \epsilon_\infty\frac{\tilde{\omega}_p^2}{\omega^2-\omega_0^2+i\Gamma_{ISB}\omega}, && (1.45) \end{aligned}$$

where $\tilde{\omega}_p^2 = \dfrac{f_{01}N_{2D}e^2}{m_0^*\epsilon_0 L_{eff}}$.

We want to look for general conditions for ϵ' to pass by zero, this is satisfied when:

$$\tilde{\omega}_p^2(\omega^2-\omega_0^2) = (\omega^2-\omega_0^2)^2 + \Gamma_{ISB}^2\omega^2 \tag{1.46}$$

This equation admits solutions when:

$$\Gamma_{ISB} \leq \sqrt{\tilde{\omega}_p^2+\omega_0^2} - \omega_0 \iff \tilde{\omega}_p \geq \sqrt{\Gamma_{ISB}(2\omega_0+\Gamma_{ISB})} \tag{1.47}$$

For ISB transition, a rule of thumb says that Γ_{ISB} is about 10% ω_0 [26]. The condition above becomes $\tilde{\omega}_p \geq 0.46\omega_0$. This is a fast approximation to estimate the doping level to so that ϵ' crosses zero.
Figure 1.6 shows an example of the contribution of ISB transition to the dielectric function (N =1 $\times 10^{18} cm^{-3}, \Gamma_{ISB} = 6meV$).

The electron concentration N and the damping factor Γ_{ISB} are two key parameters which pilot the ISB dielectric function. Figure 1.7 illustrates the evolution of the real part and imaginary part

of the ISB dielectric function as a function of electron concentration, at a constant damping factor Γ_{ISB}=6meV. The amplitude of both ϵ' and ϵ'' changes proportionally to the electron concentration. The real part of dielectric function ϵ' starts to cross zero at N $\approx 1\times10^{18}cm^{-3}$, and becomes negative down to about -30 for N $\approx 4\times10^{18}cm^{-3}$. At the same time, when N increases from $5\times10^{17}cm^{-3}$ to $4\times10^{18}cm^{-3}$, λ_{ENZ} blueshifts from about 9.5μm to about 8.3μm, and $\epsilon''(\omega_{ENZ})$ stays larger than 1. In Figure 1.8, the ISB dielectric function is computed with a constant electron concentration N=$1\times10^{18}cm^{-3}$ while the damping factor Γ_{ISB} increases from 3meV to 12meV. In the Drude Lorentz model, the damping factor Γ_{ISB} is also the full width at half maximum (FWHM) of the lorentzian lineshape [5]. The smaller Γ_{ISB} is, the sharper the resonance is.

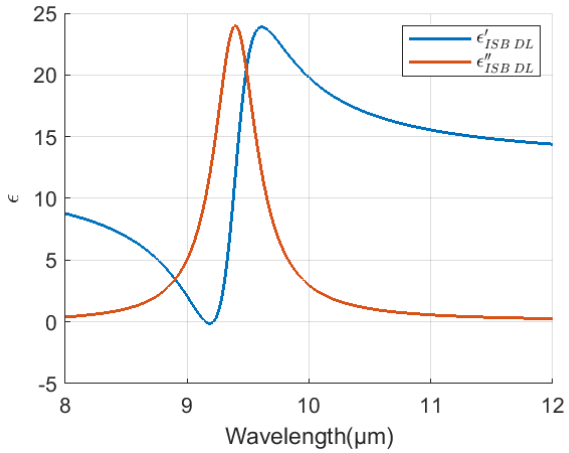

Figure 1.6 – Drude-Lorentz ISB transition dielectric function, N=$1\times10^{18}cm^{-3}$, Γ_{ISB}=6meV, ϵ_∞=11.6

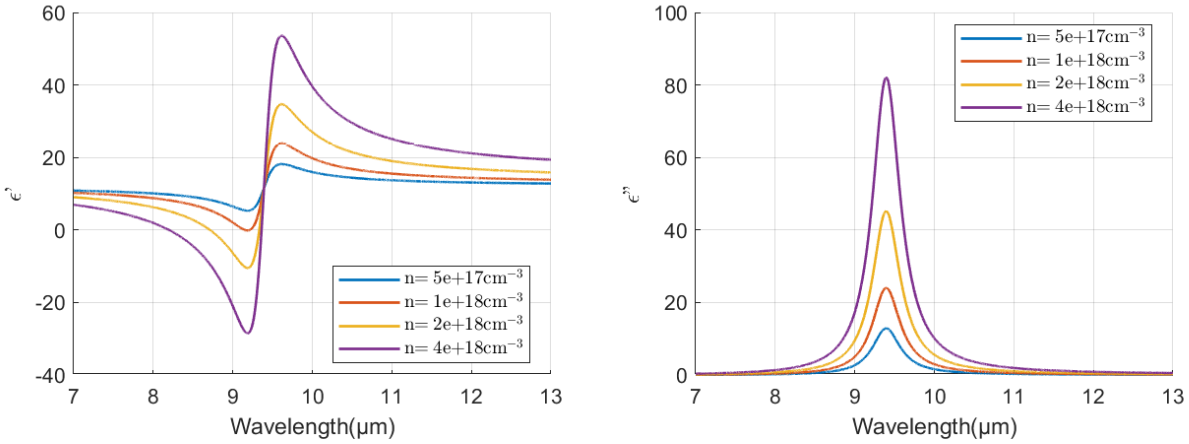

(a) (b)

Figure 1.7 – Evolution of ISB transition contribution as a function of doping

5. Be careful, the lorentzian in this case have ω^2 as variable instead of only ω as in usual lorentzian lineshape definition.

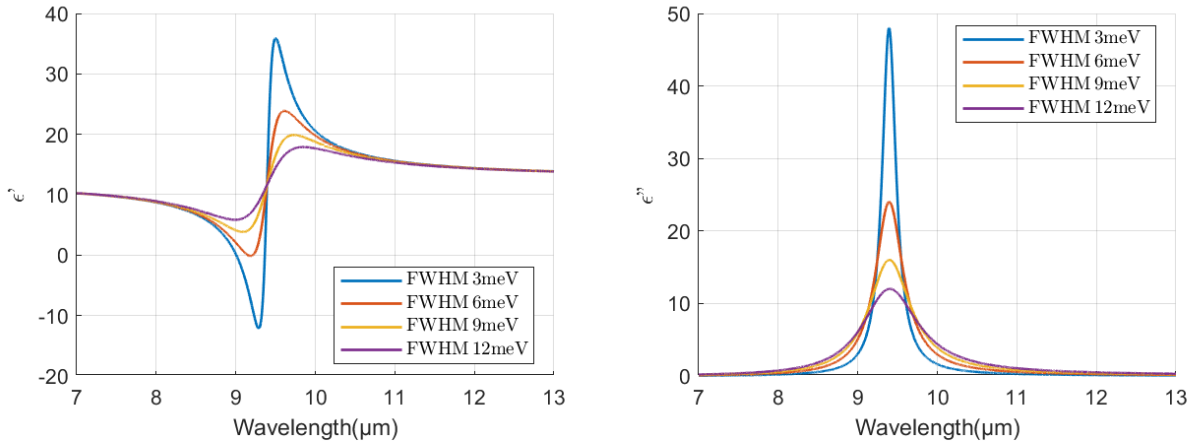

(a) (b)

Figure 1.8 – Evolution of ISB transition contribution as a function of damping factor

1.2.3 Optical phonon contribution

In polar materials (constituted of atoms with different electronegativities), optical phonons induce oscillating dipoles of bound charges, and thus contribute to the dielectric function of the materials. Let's consider a binary polar crystal made of A and B atoms. In a similar manner to the ISB transition's case, the contribution of optical phonon can be described by a Drude-Lorentz model as follows:

$$\epsilon = \epsilon_\infty \left(1 - \frac{e^{*2}N}{m_{red}\epsilon_0\epsilon_\infty} \frac{1}{\omega^2 - \omega_T^2 + i\Gamma_{ph}\omega}\right) = \epsilon_\infty \left(1 - \frac{\tilde{\omega}_p^2}{\omega^2 - \omega_T^2 + i\Gamma_{ph}\omega}\right). \tag{1.48}$$

More developed demonstration can be found in Rosencher's textbook (chapter 6.B and equation 6.B.30), where:

- e^* is the effective charge transfer of neighboring atoms A and B,
- $m_{red} = \dfrac{m_A m_B}{m_A + m_B}$ is the reduced mass,
- $\omega_T = \sqrt{\dfrac{2K}{m_{red}}}$ is the transverse optical (TO) phonon frequency
- K is the stiffness constant representing interatomic force between A and B,
- Γ_{ph} is the phonon's damping factor,
- N is the volumic density of A-B in the crystal,
- $\tilde{\omega}_p = \sqrt{\dfrac{e^{*2}N}{m_{red}\epsilon_0\epsilon_\infty}}$ is the plasma frequency equivalent for phonon.

In his textbook, Rosencher also discussed about the origin of the longitudinal optical (LO) phonon frequency shift with respect to transverse optical phonon frequency. In polar crystal, LO phonon vibrations induce an effective charge concentration [6]. The frequency shift results from the induced

6. Because of divergence's vectorial properties, TO phonons do not induce effective charge.

polarization field of the net bound charge concentration in the LO phonon's case:

$$\omega_L^2 = \omega_T^2 + \tilde{\omega}_p^2. \tag{1.49}$$

Therefore, equation 1.48 can be re-written as follows:

$$\epsilon = \epsilon_\infty \left(1 - \frac{\omega_L^2 - \omega_T^2}{\omega^2 - \omega_T^2 + i\Gamma_{ph}\omega}\right). \tag{1.50}$$

This is a more common form in literature (Born and Huang [27]) for optical phonon dielectric function. The formula 1.50 with one oscillator is applicable to binary materials with single optical phonon mode, like GaAs, SiC. Others ternary or anisotropic materials require more complex models that we will discuss later in chapter 2. For the sake of simplicity, this model is enough at the moment to discuss the influence of optical phonons on the dielectric function.
Figure 1.9 shows the behaviors of the dielectric functions of optical phonon for GaAs and SiC. The damping factor of optical phonons can be very small (Γ_{GaAs}=2.4cm^{-1} [28], Γ_{SiC}=4.76cm^{-1} [29] so the associated resonances are sharp. In these two cases, for frequencies in range of $[\omega_T, \omega_L]$, the real part of the dielectric function is negative, the materials are metal-like optically.
GaAs reaches ENZ regime at ~34.2μm and SiC at ~10.3μm, close to their LO phonons. However, the LO phonon frequency is intrinsic to each materials, therefore the phonon contribution is very material-dependent. It's worth noticing also that the phonon frequency is directedly linked to the atomic masses of atoms forming the material. The heavier these atoms are, the smaller the corresponding phonon frequency will be (indeed, when constituent atoms get heavier, the reduced mass m_{eff} increases, while the stiffness constant K of the interatomic force does not change much).

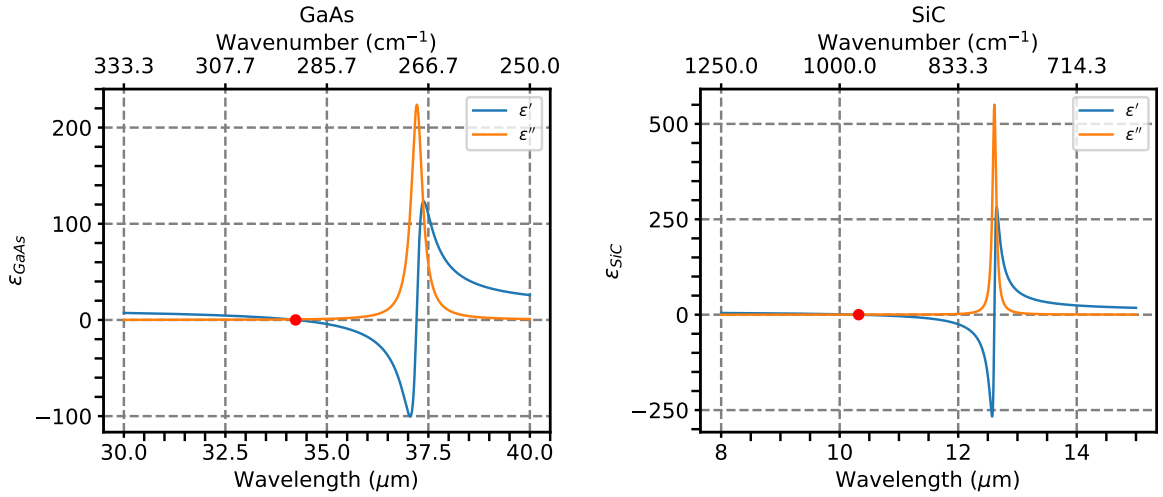

(a) (b)

Figure 1.9 – Contribution of optical phonons to the dielectric function in GaAs (left) and SiC (right). The red dots indicate the zero crossing of ϵ', respectively at 34.2μm and 10.3μm for intrinsic GaAs and SiC.

1.2.4 Figure of merit

In Figure 1.10 from Ref. [15], authors show a figure of merit for ENZ materials: the imaginary part of ϵ at the ENZ wavelength (note that in this case, the smaller $\epsilon''(\omega_{ENZ})$ is, the stronger the ENZ effect will be). As commented earlier, each family of materials corresponds to a certain range of wavelength for the ENZ effect. Some materials are noticeable for low loss at their ENZ frequency: Al, Dy:CdO, hBN, GaN, SiC. III-V semiconductors generally have lower loss for lower doping level, with $\epsilon'' \sim 0.3$-1 around 10μm.

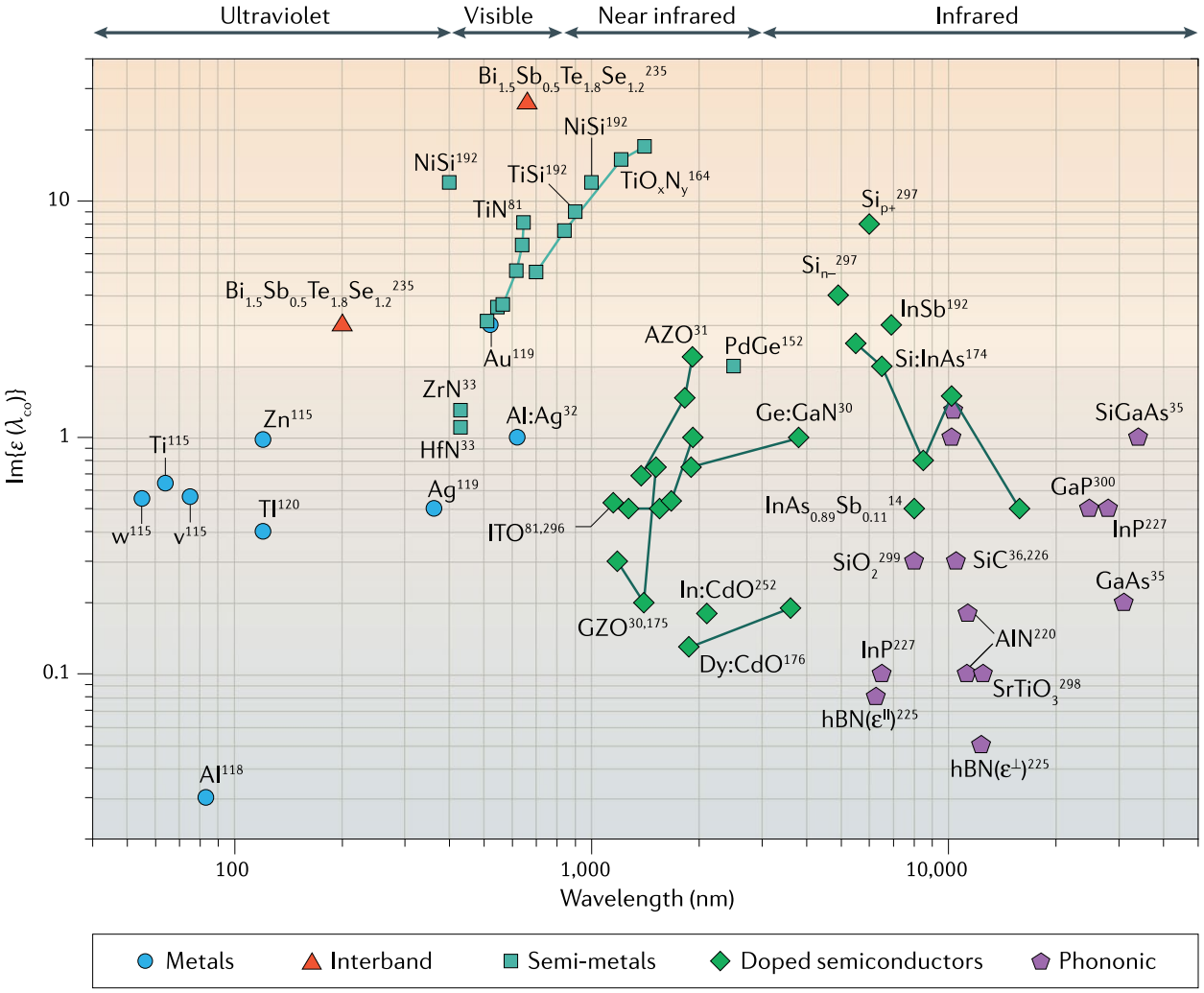

Figure 1.10 – ENZ materials in continuous media [15]

Figure 1.11 depicts the ENZ factor K_{ENZ} of several popular materials or some that will be studied later on in this work: phononic materials GaAs, SiC, GaN, InGaAs; doped semiconductor Dy:CdO, InGaAs; ISB transition in InGaAs/InAlAs quantum well. The boundary material used for this computation is air. In absolute value, the ENZ factors K_{ENZ} in InGaAs used in this work are smaller than in other materials. However, as will be discussed in section 2.2.3, when the real barrier material are taken into account, the ENZ factors becomes considerable.

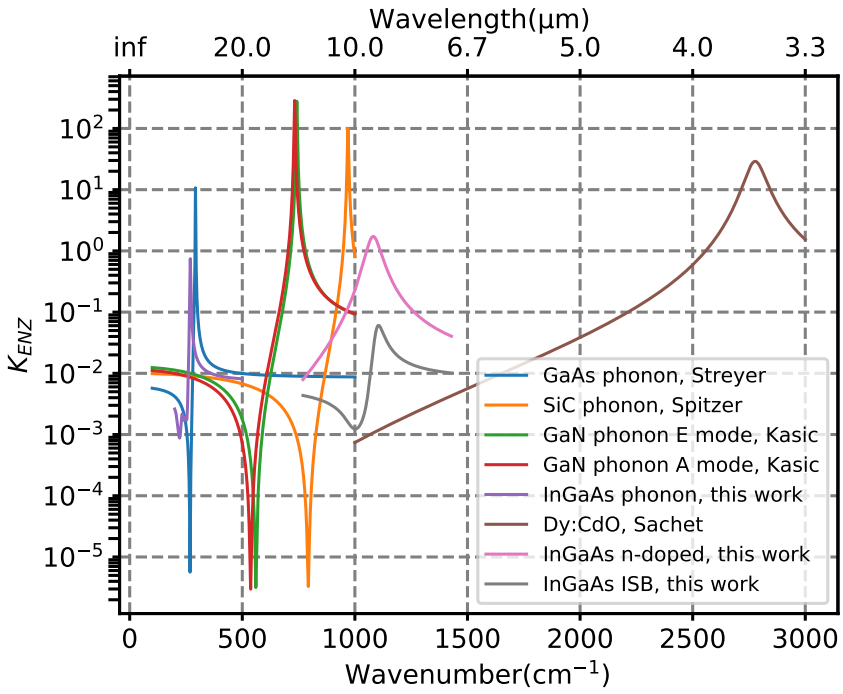

Figure 1.11 – FOM K_{ENZ} in different materials: phonon GaAs [30], phonon SiC [29], phonon GaN [31], phonon InGaAs (this work), Dy:CdO n-doped [32], InGaAs n-doped (this work), InGaAs ISB transition (this work).

1.3 ENZ mode and Berreman mode

We have discussed about ENZ materials. We will now focus on the bound optical modes that can be supported by these materials. We will first derive some useful relations to describe single interface polariton modes, and then move to slab modes, where ENZ modes can appear. The ENZ mode is a Long Range Surface Polariton (LRSP) in a thin slab of an ENZ material.

1.3.0.1 Interface polariton mode

An interface polariton is a mixture of electromagnetic field oscillation and mechanical charge oscillation that occurs at the interface of two media. It is a solution of the Helmholtz's equation – the electromagnetic wave equation without the source term. In fact, the solution of the EM wave equation without source is the natural frequency/eigenfrequency of the considered system. When we turn on then turn off an EM source, the system is perturbed and will oscillate at this natural frequency, similarly to the excitation of a mechanical spring's oscillation.
First, let's consider the interface of two semi-infinite non magnetic media: a dielectric medium (1) ($\epsilon_1' > 0$) and a metal-like medium (2) ($\epsilon_2' < 0$), under an incident tranverse magnetic (TM) wave. The Helmholtz equation is written as:

$$\nabla^2 \mathbf{E}_j + \epsilon_j \frac{\omega^2}{c^2} \mathbf{E}_j = 0, \tag{1.51}$$

where j=1,2, ϵ_j is the dielectric function in medium j. Each medium is homogeneous and so admits solutions in form of plane wave:

$$\begin{aligned} E_{x1} &= E_0 exp(ik_x x + ik_{z1} z) \text{ for } z > 0 \\ E_{x2} &= E_0 exp(ik_x x - ik_{z2} z) \text{ for } z < 0 \end{aligned} \tag{1.52}$$

where, where k_x is the in-plane wave vector component (same value in two media), $k_{zj} = \sqrt{\epsilon_j \frac{\omega^2}{c^2} - k_x^2}$ is the normal wave vector component.

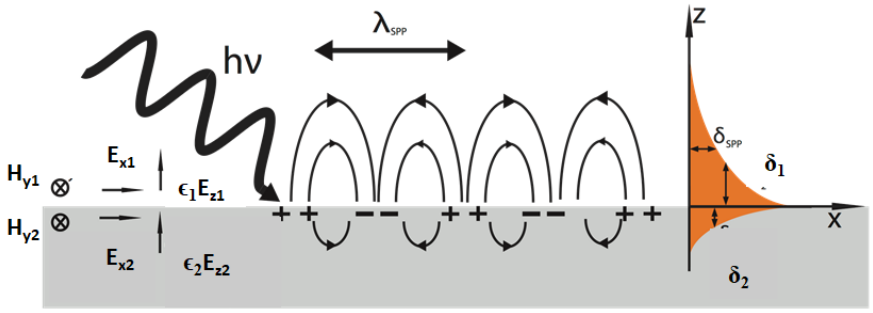

Figure 1.12 – SPP

We look for transverse wave solution, so $\nabla.\mathbf{E} = 0$, $\mathbf{k}_j.\mathbf{E} = 0$ (homogeneous media) where $\mathbf{k}_1 = (k_x, 0, k_{z_1})$; $\mathbf{k}_2 = (k_x, 0, -k_{z_2})$. It follows that:

$$E_{z1} = \frac{-k_x E_0}{k_{z1}} exp(ik_x x + ik_{z1} z), \text{ for } z > 0 \tag{1.53}$$

$$E_{z2} = \frac{k_x E_0}{k_{z2}} exp(ik_x x - ik_{z2} z), \text{ for } z < 0 \tag{1.54}$$

Applying the continuity of electric displacement at the interface, $D_{z1}(z = 0) = D_{z2}(z = 0)$ we have:

$$-\epsilon_{z1} k_{z2} = \epsilon_{z2} k_{z1} \tag{1.55}$$

Replacing k_{z1} and k_{z2} in the equation above, we finally obtain:

$$k_x^2(\omega) = \frac{\omega^2}{c^2} \frac{\epsilon_1 \epsilon_2}{\epsilon_1 + \epsilon_2}. \tag{1.56}$$

The solution is a surface wave when the wave decreases exponentially away from the interface. For simplicity, let's consider media (1) and (2) without losses (ϵ_1 and ϵ_2 are real). The evanescent wave condition is satisfied when k_{zj} are imaginary and $Im(k_{zj}) > 0$. This means that k_{zj}^2 have to be negative, from the equation 1.56 we have:

$$k_{x1}^2 > k_1^2 = \frac{\omega^2}{c^2} \epsilon_1, \tag{1.57}$$

$$k_{x2}^2 > k_2^2 = \frac{\omega^2}{c^2} \epsilon_2. \tag{1.58}$$

Because $\epsilon_1 > 0$ and $\epsilon_2 < 0$, this condition is equivalent to:

$$\Leftrightarrow \frac{\epsilon_2}{\epsilon_1+\epsilon_2} > 1 \; and \; \frac{\epsilon_1}{\epsilon_1+\epsilon_2} < 1 \tag{1.59}$$

$$\Leftrightarrow \epsilon_2 < -\epsilon_1 \tag{1.60}$$

So the surface wave solution is finally written as follow:

$$E_{x1} = E_0 exp\left(i\frac{\omega}{c}\sqrt{\frac{\epsilon_1\epsilon_2}{\epsilon_1+\epsilon_2}}x - \frac{\omega}{c}\sqrt{\frac{-\epsilon_1^2}{\epsilon_1+\epsilon_2}}z \right) for\ z>0 \tag{1.61}$$

$$E_{x2} = E_0 exp\left(i\frac{\omega}{c}\sqrt{\frac{\epsilon_1\epsilon_2}{\epsilon_1+\epsilon_2}}x + \frac{\omega}{c}\sqrt{\frac{-\epsilon_2^2}{\epsilon_1+\epsilon_2}}z \right) for\ z<0 \tag{1.62}$$

$$E_{z1} = i\sqrt{\frac{-\epsilon_2}{\epsilon_1}}E_{x1}\ for\ z>0 \tag{1.63}$$

$$E_{z2} = -i\sqrt{\frac{-\epsilon_1}{\epsilon_2}}E_{x2}\ for\ z<0 \tag{1.64}$$

This solution is an interface polariton mode. If the medium (2) is a metalic medium with free electrons, the interface polariton mode is called Surface Plasmon Polariton (SPP). Other materials like phononic materials which are metal-like in the range of $[\omega_{TO}, \omega_{LO}]$, also support an interface polariton mode called interface phonon polariton. More extensive description about interface polaritons can be found in textbooks like [33].
The dispersion relation of an SPP at an air-metal interface is depicted in figure 1.13. The SPP mode is beyond the light cone, and the energy of an SPP mode has a upper bound. Using a Drude model, the upper bound is $\omega_p/\sqrt{2}$.

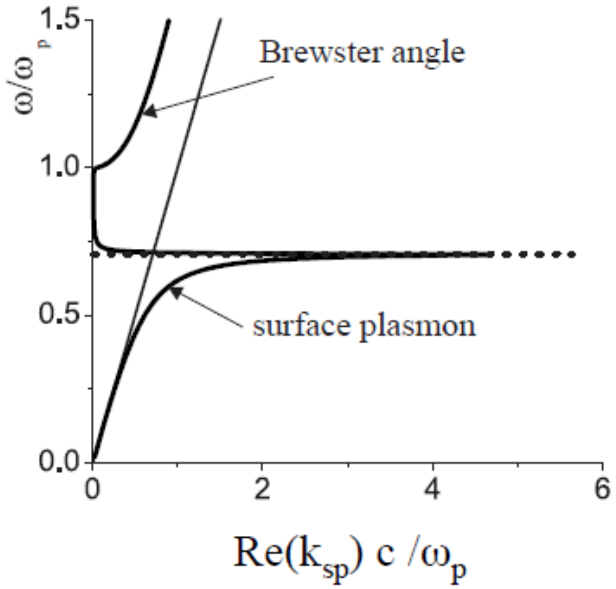

Figure 1.13 – Dispersion relation of SPP at an interface of vacuum-Drude metal is illustrated by the bold line below the dash line (SPP's upper bound $\omega_p/\sqrt{2}$).

The electric field of SPP mode is generally enhanced with respect to the incident field. We would like to apply the ENZ effect to enhance further the electric field of the SPP mode. However, the ENZ frequency ω_{ENZ} is out of the frequency range of SPP's existence (in this case $\omega_{ENZ} = \omega_p > \omega_p/\sqrt{2}$). Therefore, a single interface SPP mode can not benefit from ENZ field enhancement. The situation is different when we consider two SPP modes in interaction in a thin slab.

1.3.0.2 ENZ mode

Let's consider a thin slab of metal (2) surrounded by a dielectric medium (1). Two interface polariton modes exist at the two interfaces. When the thickness d of the metal slab (2) is small enough for the evanescent parts in the metal of the two modes to overlap, they start to interact with each other. The interactions of these two modes results in two new hybrid modes, called Long Range SPP and Short Range SPP, whose dispersion relations change with the slab's thickness d [34], [35]. The thinner the slab is, the more the two new dispersions repel each other further from the original semi-infinite media SPP mode close to $\omega_p/\sqrt{2}$.

Vassant *et al.* [36], [37] in 2012 and Campione *et al.* [38] in 2015 introduced the concept of ENZ mode, which is a LRSPP mode supported by a thin ENZ slab. In very thin ENZ layer ($d \lesssim \lambda/50$ is a good rule of thumb according to reference [38]), the LRSPP mode dispersion branch enters in a frequency range close to ω_{ENZ} (equivalent to ω_p in case of Drude's free carriers). Therefore, the LRSPP mode now benefits from the material ENZ properties and is named the ENZ mode.

The figure 1.14a illustrates the dispersion relation and the normal electric field profile of LRSPP mode in metal slabs of different thicknesses, $\lambda_p = 1\mu m$, $\Gamma = 100cm^{-1}$ (λ_p is the wavelength correspond to the plasma frequency ω_p). The ENZ upper limit in this case is $\lambda_p/50 = 20nm$. Compared to a classic LRSPP mode as in the 150-nm slab case, the E_z component is strongly enhanced in a 2-nm slab due to the ENZ effect. Indeed, the E_z field is proportional to $1/d$ [38] as depicted in figure 1.14b. The field profile is almost constant inside the slab, and decreases abruptly at the metal-dielectric interfaces. The mode's energy is therefore strongly confined in the slab. In addition, the ENZ mode dispersion relation is almost flat for thin slabs, reducing its angular dependency. These characteristics make ENZ mode an interesting way to confine and enhance light.

Similar analysis can be applied to the case of an ENZ phononic slab, where the ENZ behavior is due to the optical phonon contribution. Figure 1.15 illustrates this situation in a system made of a thin slab of GaAs sandwiched between two $Al_{0.33}Ga_{0.67}As$ semi-infinite layers. The dielectric functions of GaAs and AlGaAs are plotted in the first figure to the left. GaAs behaves like a metal optically in the interval $[\omega_{TO\,GaAs}, \omega_{LO\,GaAs}]$ of about [270-290]cm^{-1}. GaAs shows ENZ properties around longtitudinal phonon $\omega_{LO\,GaAs}$. The gray zone corresponds to the frequency range of existence of a single interface phonon polariton mode. The green zone marks the range where the ENZ factor $K_{ENZ\,AlGaAs}$ is larger than 50. The dipersion relations of the GaAs slab's interface modes are depicted in the figure in the middle, with different slab's thicknesses. We observe one more time similar behavior of the long range mode (illustrated with full lines, denoted with 'sym') compared to a Drude metal slab. When the thickness of the slab decreases, the long range mode gets out of the existence zone of single interface polariton (gray) and enters the the ENZ zone (green). Short range modes dispersions(illustrated with broken lines and denoted by 'antisym') are also plotted. The last figure on the right illustrate the normal electric field profile of the ENZ mode in a 22nm-thick GaAs slab, which is almost constant in the slab and decreases abrubtly in the AlGaAs barriers.
These two examples show very general behaviors of ENZ mode. ENZ mode is recently employed in

different works ([39], [36]). The strong electric field enhancement and confinement are interesting for non-linear optics, Second Harmonic Generation (SHG) for example. The normal component of electric field is enhanced, which is very interesting for phenomena like ISB transition - only sensitive to this normal component of light.

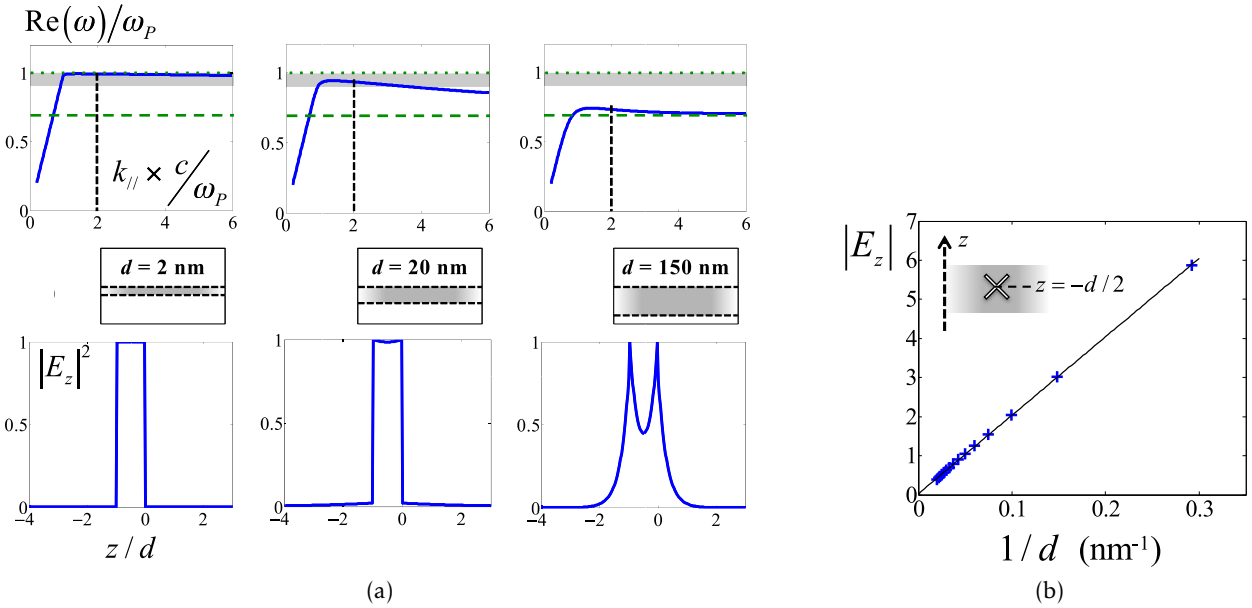

Figure 1.14 – ENZ mode field distribution and dispersion behaviors in a Drude metal slab [38]

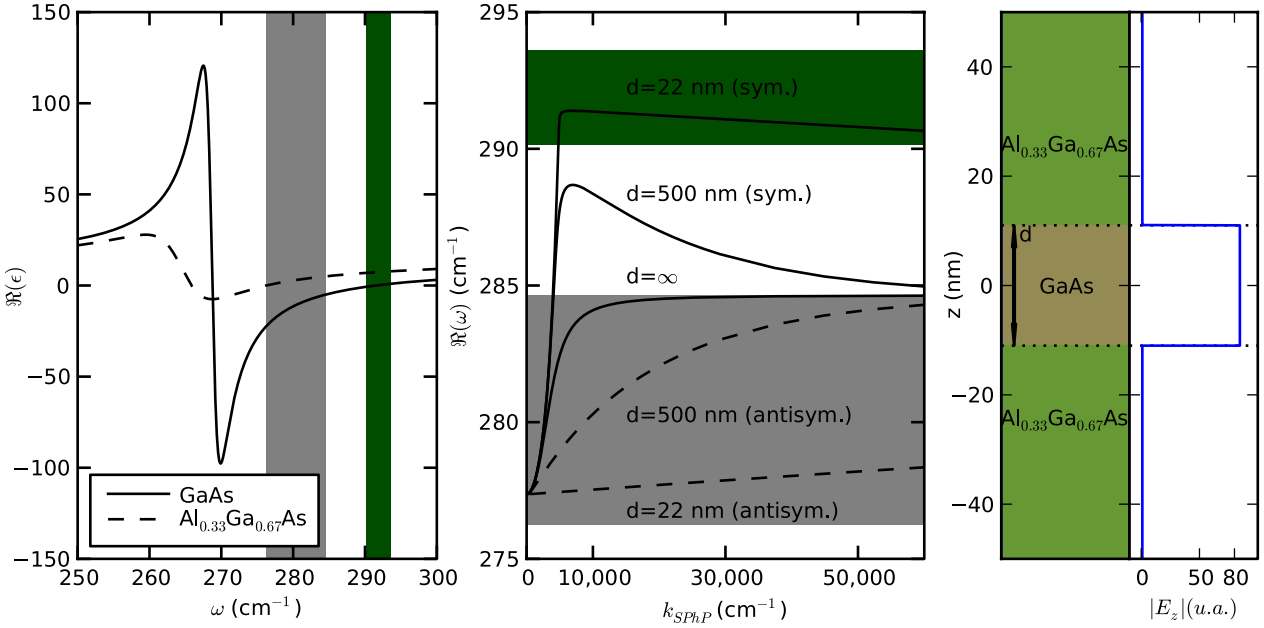

Figure 1.15 – ENZ mode field distribution and dispersion behaviors in a phononic slab GaAs embedded in AlGaAs [36]

It is important to notice that the dispersion relations of SPP, LRSP, ENZ mode are all beyond the light cone. Therefore, these resonances can not be excited with light coming directly

from free space due to wavevector mismatch. The excitation of ENZ mode can be realized with help of evanescent waves having a matched wavevector value, using prism configurations (Otto, Kretschmann), scatterers or diffracting grating. This part will be discussed in the section 3.1.2, where we use MIM cavity within a 1D grating to excite and interact with the ENZ mode.

1.3.0.3 Berreman mode and generalized plasma shift (depolarization shift) concept

In thin ENZ slab, there exists a counterpart of the ENZ mode with the dispersion relation staying inside of the light cone. This mode is usually called the Berreman mode, studied in reference [37] (also refered to as Brewster mode [40]). Historically, 'Berreman mode' name is used to refer to the optical phonon case in a phononic slab, whereas 'Brewster mode' name is used for free electrons in Drude metal slab. The physics in these systems are the same and can be generalized to other ENZ materials. An example of the dispersion relations of the Berreman mode along with the ENZ mode is given in Figure 1.16 for a Drude metal slab. The Berreman mode frequency is close to ENZ frequency, especially for very thin slab. The Berreman mode can be directly coupled with light coming from vacuum, this constitutes a path to experimentally investigate the ENZ frequency in ENZ materials.

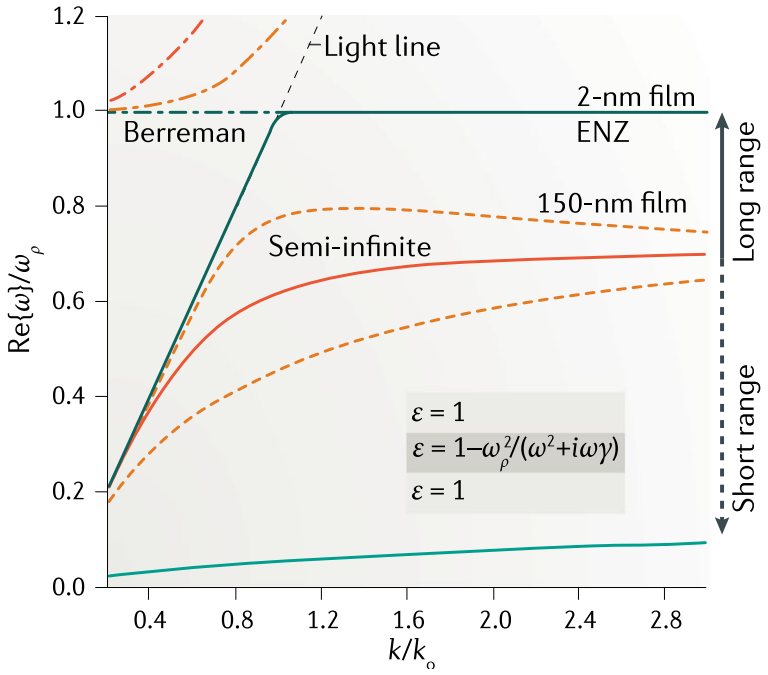

Figure 1.16 – Berreman mode and ENZ mode in a thin Drude metal slab [15]

Let's have a closer look at the experimental description of the phenomenon in case of optical phonon. When we excite a thin slab of a phononic material deposited on metal with a TM polarized light, an absorption peak is observered at the longitudinal optical phonon frequency (ω_{LO}) of the material, and the peak's amplitude increases with increasing incident angle. It is called the Berreman mode. This absorption peak was first assigned to the excitation of the longitudinal optical phonon, but this interpretation appears later to be incorrect (Agranovich [41], Schubert [42], Vassant [37]). Vassant *et al.* [37] attributed this absorption to the excitation of a 'leaky mode', which is also a solution of the same dispersion equation as the ENZ mode, but having wavevector

k_x value in the light cone. Because the Berreman mode happens at ω_{LO} where the dielectric function tends towards zero, it benefits from the normal electric field enhancement just like the ENZ mode. This normal electric field enhancement is the physical origin of Berreman's absorption.
To better understand this point, let's consider a slab of an ENZ medium (2) surrounded by a medium (1). A TM-polarized light beam of incidence θ and of electric field E_1 is sent on the ENZ slab of thickness d as illustrated in Figure 1.17:

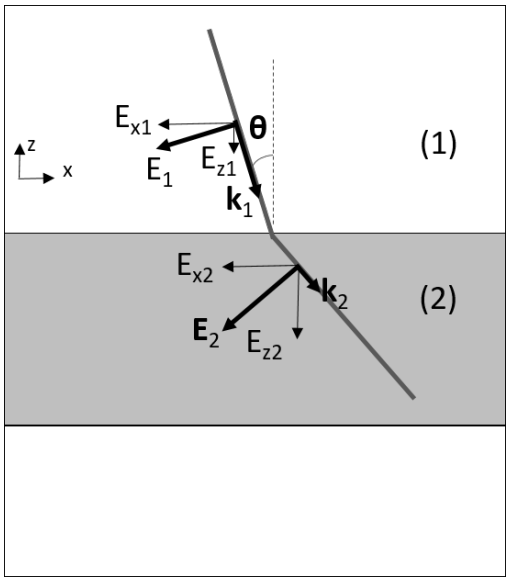

Figure 1.17 – TM wave is incident on a thin film interface

As dicussed in reference [43], for thin film, the reflectance is quadratic in film's normalized thickness $\delta = d\omega/c$ while the transmittance (and thus the absorption) shows a linear dependence. In other words, for very sub-wavelength thickness where $\delta \ll 1$, the reflectance is negligeable. Therefore, here we can consider the transmitted field and neglect the reflected field. The continuity of the normal electric displacement field at the interfaces imposes:

$$\epsilon_{z1} E_{z1} = \epsilon_{z2} E_{z2} \tag{1.65}$$

$$|E_{z2}| = |E_{z1}| \frac{|\epsilon_{z1}|}{|\epsilon_{z2}|} \tag{1.66}$$

$$= |E_1 sin\theta| \frac{|\epsilon_{z1}|}{|\epsilon_{z2}|}. \tag{1.67}$$

The normal electric field contribution to the absorption of the ENZ slab is written as:

$$A_{z2} = \frac{Absorbed\ power}{Incident\ flux\ power} \tag{1.68}$$

$$A_{z2} = \frac{\frac{\omega\epsilon_0}{2} \int \epsilon''_{z2} |E_{z2}|^2 dxdydz}{\int \frac{c\epsilon_0 |\epsilon_1|}{2} |E_1|^2 cos\theta dxdy} \tag{1.69}$$

Berreman mode's normal electric field profile is also almost constant inside the slab. In addition, the slab is flat along x and y direction. Using these considerations and the expression of E_{z2}, equation 1.69 can be simplified as:

$$A_{z2} = \frac{\omega |E_{z2}|^2 S d}{c|\epsilon_1||E_1|^2 cos\theta S} \tag{1.70}$$

$$= \frac{\omega}{c}\frac{sin\theta^2}{cos\theta}\frac{\epsilon''_{z2}}{|\epsilon_{z2}|^2}|\epsilon_{z1}|d, \tag{1.71}$$

where S and d are respectively the slab's surface area and thickness. We can also write:

$$\frac{\epsilon''_{z2}}{|\epsilon_{z2}|^2} = \frac{Im(-\epsilon^*_{z2})}{|\epsilon_{z2}|^2} \tag{1.72}$$

$$= Im\left(\frac{-\epsilon^*_{z2}}{|\epsilon_{z2}|^2}\right) \tag{1.73}$$

$$= Im\left(\frac{-\epsilon^*_{z2}}{\epsilon_{z2}\epsilon^*_{z2}}\right) \tag{1.74}$$

$$= Im\left(\frac{-1}{\epsilon_{z2}}\right), \tag{1.75}$$

where Im denotes the imaginary part of a complex number, and ϵ^*_{z2} denotes the complex conjugate of ϵ_{z2}. The absorption expression in equation 1.71 can be rewritten as follows:

$$A_{z2} = \frac{\omega}{c}\frac{sin\theta^2}{cos\theta} Im\left(\frac{-1}{\epsilon_{z2}}\right)|\epsilon_{z1}|d \tag{1.76}$$

This result is in good agreement with references [43] and [44]. In the equations 1.69 and 1.76, we see clearly that the field enhancement due to ENZ effect is reflected in the normal field contribution to the absorption of the ENZ slab with the ϵ_{z2} term appearing at the denominator. Indeed, when ϵ_{z2} tends towards zero, the imaginary part ϵ_{z2} is reduced which seems to reduce the absorption. However, the normal electric field is enhanced in square of $1/\epsilon_{z2}$, so overall the absorption A_{z2} increases proportionally to Im(-1/ϵ_{z2})! It is also worth noticing that the barrier dielectric function ϵ_{z1} appears at the numerator of the absorption expression. We already saw that a large ϵ_{z1} increases the ENZ factor. Here indeed it also increases the absorption of the ENZ layer (e.g. a resonance in the medium (1) has a great impact on the absorption of the slab (2)).

Getting back to the equation 1.76, we can develop it further by substituing a Drude-Lorentz dielectric function to ϵ_{z2}: Using :

$$\epsilon_{z2} = \epsilon_\infty\left(1 - \frac{\omega_p^2}{\omega^2 - \omega_0^2 + i\Gamma_{ISB}\omega}\right) \tag{1.77}$$

$$= \epsilon_\infty\left(\frac{\omega^2 - (\omega_0^2 + \omega_p^2) + i\Gamma_{ISB}\omega}{\omega^2 - \omega_0^2 + i\Gamma_{ISB}\omega}\right) \tag{1.78}$$

We get :

$$\omega Im\left(\frac{-1}{\epsilon_{z2}}\right) = \frac{\omega}{\epsilon_\infty} Im\left(-\frac{\omega^2-\omega_0^2+i\Gamma\omega}{\omega^2-(\omega_0^2+\omega_p^2)+i\Gamma\omega}\right) \quad (1.79)$$

$$= \frac{\omega}{\epsilon_\infty} Im\left(-1-\frac{\omega_p^2}{\omega^2-(\omega_0^2+\omega_p^2)+i\Gamma\omega}\right) \quad (1.80)$$

$$= \frac{-\omega\omega_p^2}{\epsilon_\infty} Im\left(\frac{1}{\omega^2-(\omega_0^2+\omega_p^2)+i\Gamma\omega}\right) \quad (1.81)$$

$$= \frac{-\omega\omega_p^2}{\epsilon_\infty} Im\left(\frac{1}{\omega^2-\tilde{\omega}_0^2+i\Gamma\omega}\right) \quad (1.82)$$

$$= \frac{\omega_p^2\Gamma}{\epsilon_\infty}\frac{\omega^2}{(\omega^2-\tilde{\omega}_0^2)^2+\Gamma^2\omega^2}, \quad (1.83)$$

where $\tilde{\omega}_0^2 = \omega_0^2 + \omega_p^2$.

The function $\frac{\omega^2}{(\omega^2-\tilde{\omega}_0^2)^2+\Gamma^2\omega^2}$ behaves similarly to a Lorentzian function, and reaches its maximum $\frac{1}{\Gamma^2}$ at $\omega = \tilde{\omega}_0$. Therefore, if we ignore the frequency dependence of ϵ_{z1}, the Berreman absorption will have a lorentzian lineshape with the maximal value given by:

$$A_{z2\,max} = \frac{sin\theta^2}{cos\theta}\frac{\omega_p^2}{c\epsilon_\infty\Gamma}|\epsilon_{z1}|d, \quad (1.84)$$

The absorption peak of the Berreman mode happens at $\omega = \tilde{\omega}_0 = \sqrt{\omega_0^2+\omega_p^2}$. Due to the ENZ normal electric field enhancement, the Berreman absorption of a thin ENZ slap is actually shifted to $\sqrt{\omega_0^2+\omega_p^2}$ whereas the original bulk material absorbs the most at ω_0 where the imaginary part of its dielectric function ϵ''_{z2} is maximized. The peak shift depends on the plasma frequency ω_p in the Drude-Lorentz function. Two assumptions we made are a constant field profile of the Berreman mode (valid in thin ENZ slab) and a frequency independent barrier's dielectric constant ϵ_{z1}. The reasoning above is very general and can be applied to different situations:

- For a Drude metal ENZ slab, $\omega_0 = 0$, the Berreman mode absorption peak happens at $\omega = \omega_p$ as expected.
- For a phononic ENZ slab, $\omega_0 = \omega_T$ the tranverse optical phonon, the Berreman mode absorption peak happens at $\omega = \sqrt{\omega_T^2+\tilde{\omega}_p^2} = \omega_L$ the longitudinal optical phonon, with $\tilde{\omega}_p$ defined in section 1.2.3 .
- For an ISB ENZ slab, $\omega_0 = \omega_{ISB}$ the intersubband transition, the Berreman mode absorption peak happens at $\omega = \sqrt{\omega_{ISB}^2+\tilde{\omega}_p^2} = \tilde{\omega}_{ISB}$ with $\tilde{\omega}_p$ defined in section 1.2.2.1. In case of ISB transition, the peak shift is usually mentioned as 'depolarization shift' or 'plasma shift' [21] and it is truely the consequence of the normal electric field enhancement due to dielectric contrast.

1.4 Chapter conclusion

In this chapter, I introduced the notion of Epsilon-Near-Zero (ENZ) materials and their ability to enhance and confine light in deeply sub-wavelength structures. ENZ regime can be reached with free charges carriers, ISB transition or optical phonons in different kind of materials. An optical resonance called ENZ mode can be excited in a thin ENZ slab. It is a LRSP mode in nature, with the electric field profile strongly modified due to the ENZ characteristic of the slab. The strong enhancement and confinement of the electric field, as well as the relatively flat angular dispersion of the ENZ mode can be beneficial in new optoelectronic device structures. The Berreman mode is the counterpart of the ENZ mode inside the light cone and can be used to probe the ENZ properties of a thin film. Berreman absorption, initially studied in phononic ENZ slabs, can be generalized to other ENZ systems with Drude or ISB transition.

ENZ materials are characterized by their ENZ frequency ω_{ENZ}, and the material's optical loss at this frequency $\epsilon''(\omega_{ENZ})$. These two parameters are directly linked to the dielectric function of the materials, so mastering the dielectric function of the material is essential. In the next chapter, I will study in detail the dielectric function of InGaAs - the material of choice in this work.

2

Study of InGaAs dielectric function

In this work, I aim to apply the ENZ concept to electro-optical modulation and photodetection in the LWIR range. There is a large range of ENZ materials as introduced in chapter 1: metal, doped oxides, doped semiconductors, phononic materials. However, we need a material compatible with electronic transport properties in our optoelectronic devices, as well as relatively well-known materials for growth and fabrication process.

Our choice is oriented to InGaAs. This ternary alloy belongs to the III-V semiconductor family, with zinc-blende structure. It can be grown epitaxially by Molecular Beam Epitaxy (MBE) or Metalorganic Vapour-Phase Epitaxy (MOVPE) on InP substrate with high crystallinity, good thickness control and low mechanical stress. Its optical and electrical properties, as well as fabrication process are relatively well-known thanks to numerous applications in mid-IR optoelectronics. Advantages of InGaAs are the low electron effective mass, high electron mobility, and the possibility to grow quantum heterostructures (InGaAs/InP or InGaAs/InAlAs). These systems can also be chemically etched with a high selectivity. As mentioned above, the doped III-V semiconductor family can also give access to ENZ regime in LWIR range. Therefore, InGaAs is our material of choice in this thesis. The alloy $In_{0.53}Ga_{0.47}As$ is lattice-matched to InP, frequently used in many application and will be the only alloy composition that I study in this work. Without other precision, the notation InGaAs corresponds specifically to $In_{0.53}Ga_{0.47}As$ in this dissertation.

Despite being a commonly used material, different parameters in the dielectric function of InGaAs are still missing from the literature. In this chapter, I will study InGaAs's dielectric function in detail. I used Fourier Transform Infrared spectroscopy (FTIR), Raman spectroscopy and Van der Pauw method to characterize different parameters of the material.

2.1 Introduction to experimental setups

2.1.1 Van der Pauw - Hall effect

Free charge carriers concentration is an important parameter in the dielectric function of InGaAs. The experimental value of charges concentration can vary typically by several tens of percentage with respect to the nominal value of the growth process. The experimental value of charge concentration are usually determined electrically by Hall effect measurement.

The Van der Pauw method [45] is an effective and commonly used method to measure the re-

sistivity and Hall coefficients in thin film samples. The method amounts to making four ohmic contacts on the edge of a thin film sample and measuring current-voltage I(V) characteristic between different contacts's couples. From these measurements, we can compute the dopant's type and concentration, the sheet resistance of the thin film and the mobility of the majority carrier [1].

In theory, Van der Pauw method is adapted to sample of arbitrary shape, provided that there is no isolated hole in the sample. In practice, symmetrical square-like configurations are preferable [2].

The configuration usually used in this work for the Van der Pauw measurement is presented in Figure 2.1b. The sample is process into a center square with four contact pads labelled (1), (2), (3), (4) [3].

I use the notations as follow: the current I_{24} is a current entering the circuit at contact (2) and getting out at contact (4), the voltage V_{13} is equal to $V_{(3)}$ - $V_{(1)}$. The positive **B** field is oriented perpendicular to the sample plane, pointing towards the reader, as indicated in Figure2.1c.

With these conventions, when a current I_{24} is injected into the sample under a positive B field, a Hall voltage is developed in the perpendicular direction (1)$\longrightarrow$(3): $V_H = V_{13(I_{24},+)} < 0$ (as illustrated in Figure2.1c, +/- stands for positive or negative B field). The sign of the Hall voltage V_H corresponds to the majority charge's sign (electrons if $V_H < 0$, holes if $V_H > 0$). To reduce the influence of the sample's asymmetry and increase the accuracy of the measurement, we switch the measurement between different contacts couples and also reverse the magnetic field orientation. V_H is then averaged over all the possibles configurations:

$$V_H = \frac{V_{13(I_{24},+)} + V_{31(I_{42},+)} + V_{24,(I_{31},+)} + V_{42(I_{13},+)} - V_{13(I_{24},-)} - V_{31(I_{42},-)} - V_{24(I_{31},-)} - V_{42(I_{13},-)}}{8} \tag{2.1}$$

We need to be careful with the order of contacts in these measurements to avoid sign problem. For example, if the sample is perfectly symmetric, the invariance by rotation implies that $V_{13,(I_{24},+)}$ is equivalent to $V_{24,(I_{31},+)}$ and not to $V_{24,(I_{13},+)}$.

The surface charge density is computed as follows:

$$n_S = \left| \frac{IB}{qV_H} \right|, \tag{2.2}$$

where I is the injected current, B is the applied magnetic field, q is the elementary charge.

1. Some conditions need to be satisfied so that the Van der Pauw measurement is valid: the four probe points have to be on the edge of the sample, and the contact size must be at least one order of magnitude smaller than the samples size [46]. Otherwise, we can encounter non-linear I(V) characteristic, as well as a reduced accuracy of the measurement.

2. In Hall effect measurement, if two contact couples are not disposed perpendicularly, the measured voltage can have a large longitudinal voltage contribution with respect to Hall transverse voltage. In some case, the Hall transverse voltage can be submerged in noise fluctuation due to a large longitudinal voltage.

3. It is important to follow the notation rule, with (1), (2), (3), (4) counter-clockwise and (1) is the top left contact as depicted in Figure 2.1c. In this convention, Hall voltage's sign give the majority charge's sign.

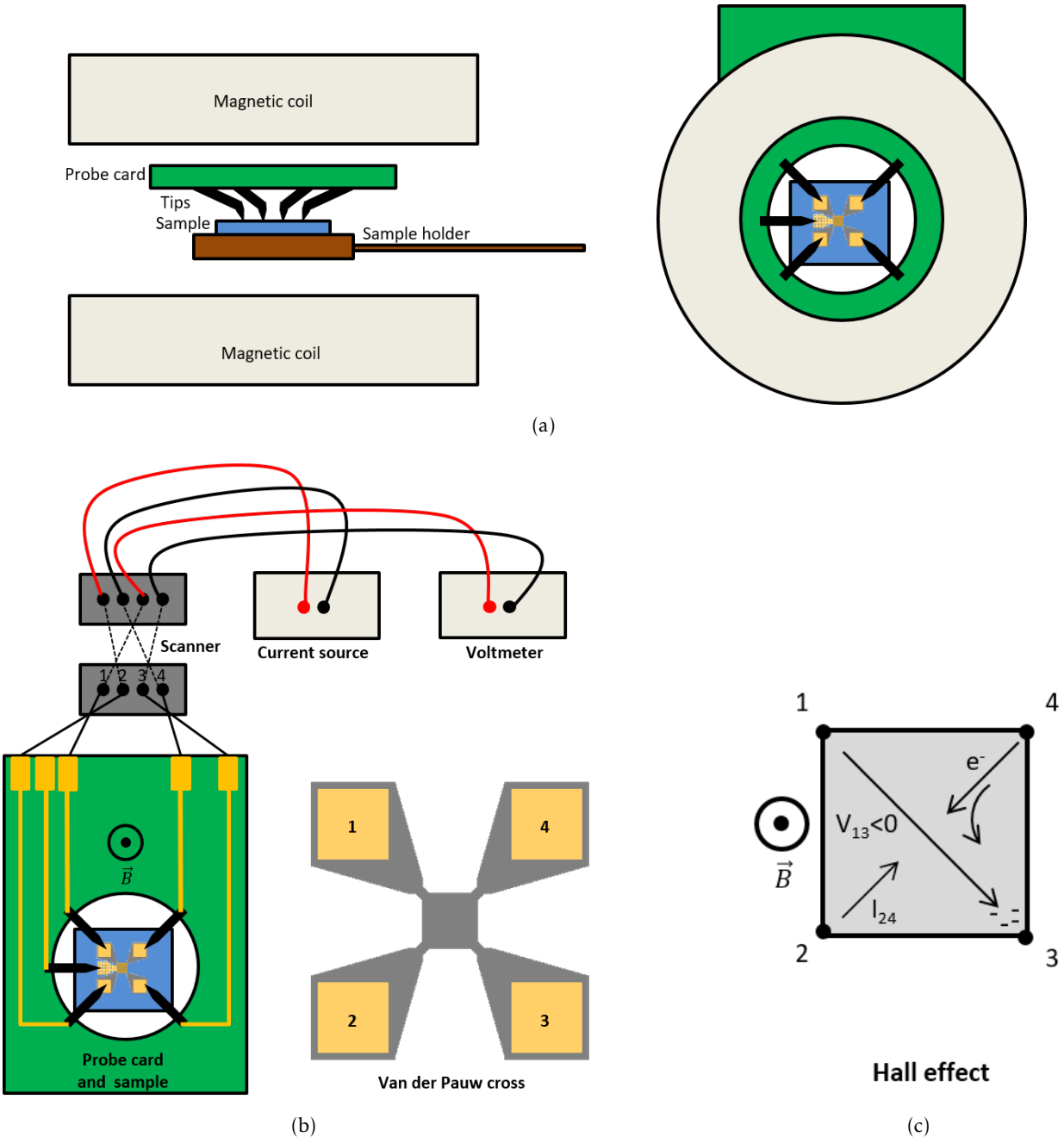

Figure 2.1 – Van der Pauw - Hall effect probe station setup. a) Left: side view, right: top view of Hall setup schematic b) Full electrical setup and Van der Pauw cross; c) Hall effect measurement

We use a homemade probe station to perform the Van der Pauw measurement. The setup is illustrated in Figure2.1. A sample with a Van der Pauw cross is electrically connected to a current source (*Keithley220*) and a voltmeter (*Multimeter Keithley 2000*) with the help of a probe cards and metallic tips (*SynergyCad*). The sample is fixed on a sample holder floating in the air by means of an air suspension system. The air suspension system allows the probe card with multiple tips to approche the sample gently without pressing strongly on fragile samples. A scanner containing a set of relays allows each output connector of the probe card to be freely matched to an input

connector of the current source or the voltmeter, without manually rewiring. The magnetic field B up to ±0.4T is applied perpendicularly to the sample's plan with the help of a Helmholtz coil (*DRUSCH et Cie*) powered by a three-phase power supply (*Danfysik7000*).

This setup was not functional prior to my PhD because of broken/missing pieces and the move of the C2N from Marcoussis to the Saclay Plateau. During my PhD, I remounted the setup, created a computer-apparatus interface in Python to control and automatize the Van der Pauw measurement using GPIB connections. The magnetic field output was calibrated as a function of the power supply current using a magnetic probe. The Van der Pauw measurement was tested with metallic thin film and gave satisfying results, proving its capability to measure charge concentration in thin film samples.

2.1.2 Raman spectroscopy

Raman spectroscopy is an elegant way to probe the vibrational states of materials non-destructively. In this work, I used Raman spectroscopy to probe the phononic properties and the doping level of InGaAs in our structures.
Raman scattering was experimentally observed for the first time in 1928 by C.V. Raman in organic liquid using sunlight [47]. Raman effect is an inelastic light scattering process, produced by the interaction of light with matter's molecular vibrations in general and with optical phonon modes in the specific case of polar semiconductor. Usually, only a small fraction of the incoming light undergoes the Raman scattering process, producing outgoing light with shifted frequencies from the initial incoming light. In particle point of view, the outgoing photons either lose or gain a quantum energy of the vibrational mode (respectively corresponding to Stokes and anti-Stokes Raman scattering, described in figure2.2).
For Stokes Raman scattering, the Raman shift is defined as $\delta = 1/\lambda_{laser\ peak} - 1/\lambda_{Stokes\ peak}$, corresponding to the vibrational mode's energy.

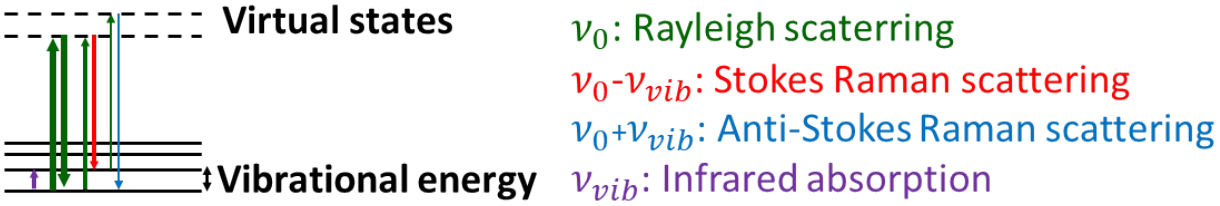

Figure 2.2 – Light-matter interaction processes: Rayleigh scattering is the dominant elastic scattering, the photon's energy is conserved. Stokes Raman scattering corresponds to an excitation of an electron from the ground state to a virtual state, followed by a relaxation of the electron to a vibrational state and an emission of a photon of lower energy. Anti-Stokes Raman scattering also concerns photon absorption and emission of an electron, but the initial state is a vibrational state and the final state is the ground state. Emitted photons have higher energy. Finally, infrared absorption corresponds to photon absorption and electron excitation from the ground state to a vibrational state.

Not all vibrational modes give a Raman scattering response. The Raman activity of a material depends on how the vibrational mode modifies the polarizability of the matetrial and can be

predicted by group theory. More details about Raman scattering's theory can be found in references [48], [49], [50], [51].

In our lab, we mounted a system in backscattering configuration as illustrated in Figure2.3 to perform Raman micro-spectroscopy. A 532nm, continuous wave laser (*Excelsior*) provides a linearly polarized excitation, with a power of 1mW at the entrance of the microscope objective. Excitation is cleaned with a 532nm line-filter (*Semrock 532 nm MaxLine laser clean-up filter*). Backscattered light, including Rayleigh and Raman scattering photons, is collected with the same objective and is oriented into the detection path. Two sharp long-pass filters(*Semrock RazorEdge532nm*) are used to stop laser photons (Rayleigh scattering) while allowing Stokes Raman photons of above 66cm^{-1} (534.3nm) to pass through. We then use a wire-grid polarizer(*Thorlabs WP25M-VIS*) to analyze the polarization of the Raman scattered signal. We focus the Stokes light from the sample with a 50cm lens on the 10μm wide entrance slit of an Andor Schamrock spectrometer, equipped with a blazed diffraction grating (1200 lines/mm). We collect the dispersed light with an air cooled Andor iDUS401-BVF CCD camera. The detection path is also equipped with a Thorlabs camera, a system of telescope and a pinhole positioned at a conjugate plane of the objective's front focal plane. This system allows us to limit the size of the probed zone and hence realize Raman micro-spectroscopy.

Dispersive Raman has a disadvantage of uncertainty on the absolute value of the Raman shift. Indeed, a small change of 0.1nm in the laser wavelength from 532nm to 532.1nm results in a change of about 3.5cm^{-1} in Raman shift. Therefore, the value of the laser's wavelength has to be determined precisely. Also, the grating's light dispersion is not totally linear, so the system needs to be calibrated carefully in order to give highly accurate Raman shift. I calibrated the Raman system using organic compounds like toluene and paracetamol's Raman signal, as well as a Neon calibration lamp. With these calibration, we achieve a ± 1cm^{-1} accuracy.

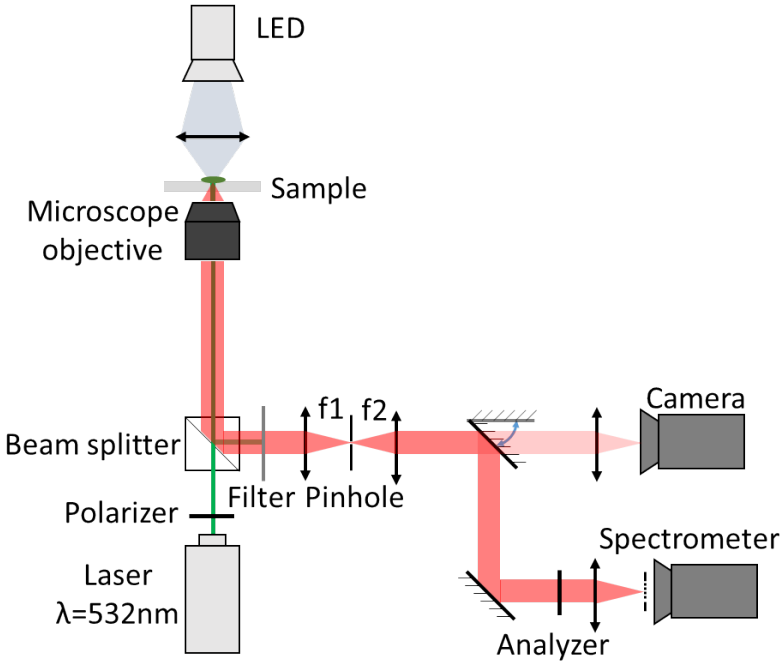

Figure 2.3 – Micro-spectroscopy Raman setup.

2.1.2.1 Notation and selection rules in polarized Raman

Longitudinal and transverse phonon modes of semiconductors can be excited selectively with different states of light polarization in Raman measurement. This is a handy tool to distinguish and assign different phonon modes. Now I will introduce the Porto's notation [52] commonly used in polarized Raman measurement. We note configuration **a(bc)d** where:
- **a** is the direction of propagation of incident exciting laser.
- **b** is the direction of polarization of incident exciting laser $\hat{\boldsymbol{e}}_i$.
- **c** is the direction of polarization of scattered beam to be analyzed $\hat{\boldsymbol{e}}_s$.
- **d** is the direction of propagation of scattered beam to be analyzed.

a, b, c, d are defined in a certain coordinate system (lab's coordinate system), usually chosen according to the probed crystal axes. For example: the configuration Z(XY)$\bar{Z}$ corresponds to a backscattering measurement, with propagation direction $\vec{k}//\vec{Z}$, the incident laser is polarized in the direction of $\vec{X}$, the scattered light is detected in polarization $\vec{Y}$.

In semiconductors with zinc-blende structure, if (X, Y, Z) = ([1$\bar{1}$0], [110], [001]) where [001] is the growth direction, then TO phonon modes are always forbidden for face (001). LO phonon modes are Raman active in Z(XX)$\bar{Z}$ or Z(YY)$\bar{Z}$ configurations, but inactive in Z(XY)$\bar{Z}$.
On the other hand, if (X, Y, Z) = ([1$\bar{1}$0], [00$\bar{2}$] , [110]) (backscattering on sample's edge), LO modes are always forbidden. TO modes are allowed in Z(XY)$\bar{Z}$, Z(YX)$\bar{Z}$, Z(XX)$\bar{Z}$ configurations, and forbidden in Z(YY)$\bar{Z}$. These selection rules are given in reference [51] and illustrated in Figure2.4.

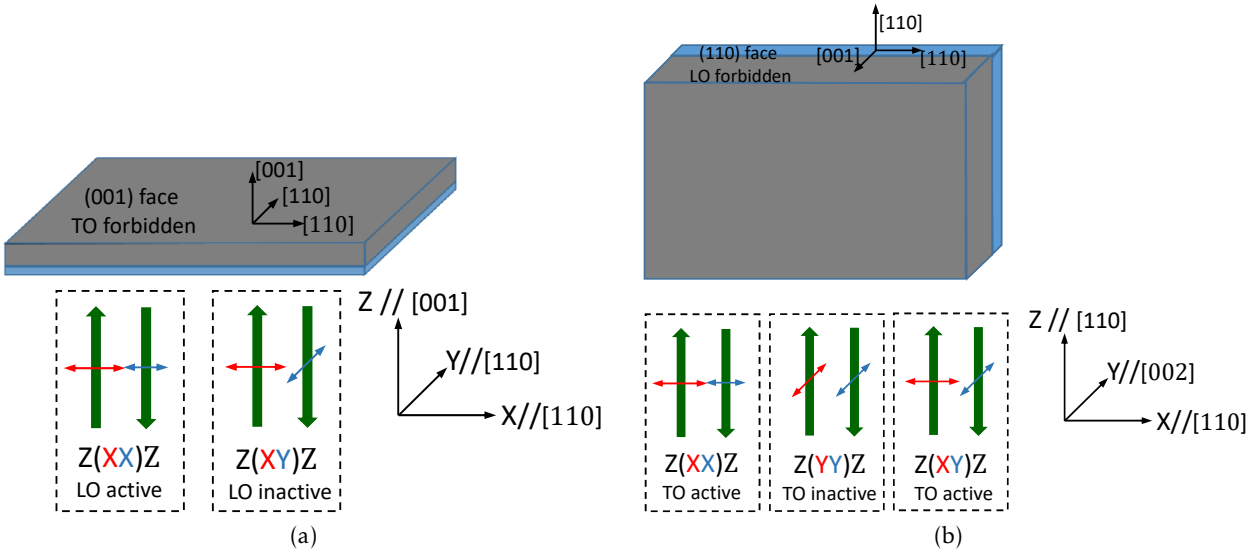

Figure 2.4 – Raman selection rule for zinc-blende structure.

2.1.2.2 Plasmon-phonon coupling

When a polar semiconductor is doped, free charges interact with lattice vibrations, the charges' screening effect modifies the LO phonon frequency. This phenonmenon is referred to as plasmon-phonon coupling and was described by Varga *et al.* in 1965 [53]. The frequencies of the new longitudinal modes are the roots of the total dielectric function. Varga explained that the polarizabilities of free charges and ions are additive (there is no correction term in the total dielectric

function due to their interaction). For instance, in case of GaAs n-doped, the total dielectric function is:

$$\epsilon(\omega) = \epsilon_\infty \left(1 - \frac{\omega_L^2 - \omega_T^2}{\omega^2 - \omega_T^2 + i\Gamma_{ph}\omega}\right) - \frac{Ne^2}{m_0^*\epsilon_0}\frac{1}{\omega^2 + i\Gamma\omega}. \tag{2.3}$$

By setting both damping factors to zero, then searching for positive roots of this dielectric function, we find the two new modes L_+ and L_-. Figure 2.5 from the reference [54] illustrates the evolution of L_+ and L_- as functions of the electron concentration. Like the initial LO phonon mode, L_+ and L_- modes are Raman-active. At large electron concentrations (10^{18}-10^{19}cm^{-3}), the L_+ frequency changes significantly with the electron concentration. Thus, via L_+ mode's determination, Raman spectroscopy offers a non-destructive way to probe the electron concentration in doped polar seminconductors.

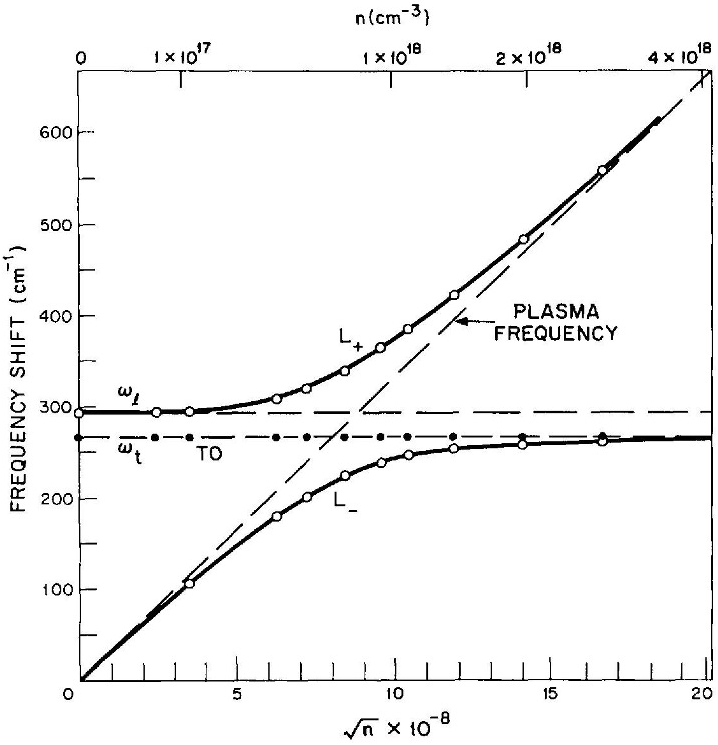

Figure 2.5 – Plasmon - LO phonon coupling in GaAs [54]. Horizontal dashed line and dashed-dotted line correspond respectively to ω_{LO} and ω_{TO} energies. Oblique dash line corresponds to the plasma frequency. Solid dotted branches correspond to the plasmon-phonon modes L_+ and L_-, displaying anti-crossing at electron concentrations around N=1×10$^{18}cm^{-3}$. Beyond N=3×10$^{18}cm^{-3}$, L_+ mode almost superimposes the plasma frequency line, its frequency changes significantly with the electron concentration and can be used to probe the electron concentration via Raman measurement.

2.1.3 FTIR spectroscopy

Fourier Transform Infrared spectroscopy (FTIR) is a Fourier spectroscopy technique, widely used to study infrared absorption of solid, liquid or gas by measuring the sample's response in re-

flection or transmission. In this work, we study semiconductors in thin film or bulk, the reflection configuration is the most adapted.

A scheme of a basic FTIR in reflection configuration is depicted in Figure2.6b. The heart of the system is a Michelson interferometer, made of a fixed mirror and a movable mirror. A light source sends light through a beamsplitter towards the two mirrors. The output light's intensity is modulated as a function of the displacement of the movable mirror, as a result of interference between the two light beams. Using a polarizer, the beam can be polarized into transverse magnetic light (TM or p-polarisation, with the electric field vector parallel to the incident plane) or transverse electric light (TE or s-polarisation, with the electric field perpendicular to the incident plane). Then the output beam arrives on the sample's surface and reflects towards a detector. This output beam's intensity is acquired as a function of the movable mirror's displacement, giving an interferogram. The Fourier transform of this interferogram gives the spectral response of the measurement which is a product of different elements:

$$H_{total}(\lambda) = S_{source}(\lambda).T_{path}(\lambda).R_{sample}(\lambda).D_{detector}(\lambda), \tag{2.4}$$

where $S_{source}(\lambda)$ is the source's spectrum, $T_{path}(\lambda)$ is the optical path's transmission , $R_{sample}(\lambda)$ is the sample's reflectance and $D_{detector}(\lambda)$ is the detector's spectral response.

To obtain the reflectance of a sample, we start by acquiring a reference spectrum $H_{ref}(\lambda)$ using a highly reflective mirror where $R_{ref}(\lambda)$ is very close to unity in the wavelength range of interest. Then we acquire the sample's spectrum $H_{sample}(\lambda)$ by replacing the mirror with the sample while keeping other elements unchanged.

The sample's reflectance is obtained by making the ratio:

$$\frac{H_{sample}(\lambda)}{H_{ref}(\lambda)} = \frac{R_{sample}(\lambda)}{R_{ref}(\lambda)} \sim R_{sample}(\lambda), \tag{2.5}$$

where we make the assumption that $S_{source}(\lambda)$, $T_{path}(\lambda)$ and $D_{detector}(\lambda)$ are unchanged between the two acquisitions.

This assumption is usually valid, with some exceptions which induce errors in the reflectance spectrum. Indeed, blackbody sources like globar, frequently used in FTIR, needs time to heat up and stabilize, its spectrum can also drift after long acquisition time. To limit this problem, I turn on the source at least 30 minutes before measurements to stabilize its response. Room temperature can also be controlled to limit drift and thermal fluctuations.

Regarding $T_{path}(\lambda)$, I try to keep the optical path identical between two acquisition by not rotating the polarizer and putting the sample at the same position and orientation as the reference. It happens that the mirror and the sample do not have the same height or are tilted a bit differently when put in the FTIR. These variations (change in tilt angle in particular), are usually sources of error, easily giving a baseline shift in the sample's reflectance spectrum of about 5-10% and sometime leading to a reflectance larger than 1! Ideally, we should have the sample and the mirror reference on the same substrate, so that we only need to translate from one to the other between two acquisitions and limit tilt angle and height variation.

As for the $D_{detector}(\lambda)$ term, the detector's response can be non-linear as a function of the input light intensity at a given wavelength, which deforms the spectral response. A detector with linear response is well appreciated.

As a Fourier method, FTIR has the advantages of high accuracy in wavenumber, thanks to the use of a stable He-Ne laser at 632.99nm to determine accurately the displacement of the mov-

able mirror. Calibration with well-known samples are not necessary, as opposed to the dispersive spectroscopy like our dispersive Raman setup.

I use a gold mirror whose reflectance is almost unity in the mid and far infrared range. Thin film semiconductor samples are transferred on highly reflective substrate (gold) in order to deliver a larger signal level in the reflection configuration. I worked with different FTIR setups, having different ranges of wavelength, with different source, detector and beamsplitter adapted to each range:

- For optical phonon measurements in the far-IR range, we used a FTIR system in IOGS's lab adapted to large samples (about 1-2cm width): a Vertex 70 FTIR (*Bruker*) under dry air flow (to minimize water absorption in the spectrum), with a globar source, a Deuterated, L-alanine doped TriGlycine Sulfate (DLaTGS) thermal detector and a Si beamsplitter. A linear wire-grid THz polarizer (*Tydex*) is used to define an incident polarization. The angle-resolved A513/Q reflectivity accessory gives access to incident angles between 15° and 65°. For Berreman mode measurement of a flat ENZ sample in mid-IR range, we used the same system with a KBr beamsplitter.
- For small samples (e.g. devices of about 150μm width), I used two FTIR systems quite similar from C2N and ONERA labs. These samples are measured in the mid-IR range. A FTIR (Vertex 70, *Bruker*) is coupled to an infrared microscope (Hyperion 2000, *Bruker*), allowing to measure the reflectance of small sample, as illustrated in Figure 2.6c. After passing through the Michelson interferometer, the light beam is sent through an external windows to the microscope, focused on the sample thanks to a Cassegrain objective x15. This objective is made of reflective mirrors, which is more adapted to broadband measurements in mid IR range (conventionnal refractive objectives are wavelength-dependant in mid IR range). The light beam is focused on the sample under a range of incident angle spreading from 12° to 24°. The FTIR system in ONERA's lab can also be coupled with a temperature control stage Linkam THMS600, where the sample can be heated up to 600 Kelvin or cooled down to 80 Kelvin. The optical path of the microscope is equipped with a polarizer to define light polarization and a knife-edge aperture located in the conjugated plane of the sample's plane, allowing to limit the probed zone. For mid IR range, I used a globar as light source, a KBr beamsplitter and a Mercury-Cadmium-Telluride (MCT) photodetector. MCT photodetectors offer higher detectivity compared to DLaTGS thermal detectors, which reduces considerably the acquisition time needed for the same signal over noise (SNR) level. On the other hand, MCT detectors need to be cooled down by liquid nitrogen while DLaTGS detectors work at room temperature. MCT detectors are also known for being non-linear, which can induce a shift in the spectrum's baseline [55], [56], [57].

(a)

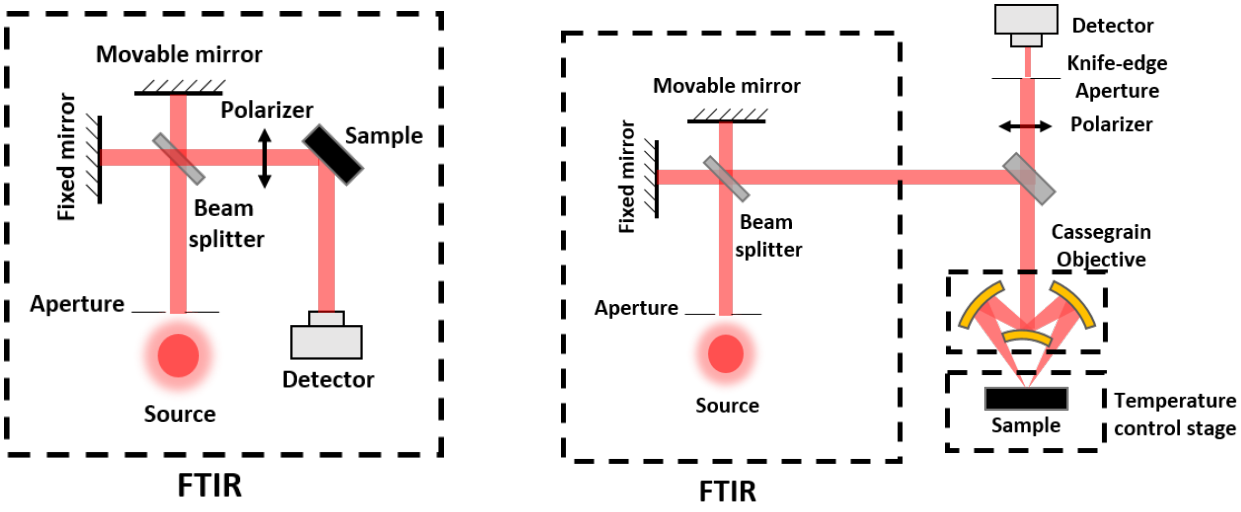

(b) (c)

Figure 2.6 – FTIR setup. a) FTIR and microscope, b)Standalone FTIR scheme, c) FTIR coupled to microscope scheme

2.2 Study of different physical parameters in InGaAs dielectric function

In this section, I will present the study of different physical parameters to the dielectric function of InGaAs, either determinated experimentally with measurement methods introduced here above or extracted from literature review. I estimated the ENZ factor in different scenarios.

2.2.1 Phonon contribution

Optical phonons in InGaAs are in 30 to 50μm range, and their contribution can also make InGaAs an ENZ material in this wavelength range. Furthermore, phonon contribution can give a non negligible contribution to the dielectric function in shorter wavelength range. In this section, we will study this contribution in detail.

The dielectric function of InGaAs is more complex than the single oscillator Drude-Lorentz model presented in section 1.2.3. InGaAs is not a binary like GaAs or SiC but a ternary compound. It presents a multiple-phonon behavior, with InAs-like and GaAs-like phonon modes. Multiple-phonon modes can be described optically by a sum of Lorentzians, however this form fails to render fine details and asymetric lineshapes experimentally observed in InGaAs as well as in some other materials.
To better fit the experimental data, a factorized form was suggested by Lowndes [58] for binary compound, and was extended to the case with more than one oscillator by Gervais [59]:

$$\epsilon = \epsilon_\infty \prod_j \frac{\omega^2 - \omega_{Lj}^2 + i\Gamma_{Lj}\omega}{\omega^2 - \omega_{Tj}^2 + i\Gamma_{Tj}\omega}. \tag{2.6}$$

But this factorized form can result in a negative imaginary part of the dielectric function. A negative ϵ'' means that the medium creates more electromagnetic energy when light propagates through it - a gain medium. This is not physical because InGaAs alone is a passive medium. Tedious behaviors like a computed reflectivity larger than unity can be observed with this error.
For InGaAs, most studies use the factorized form. In the papers where all parameters are provided to calculate the dielectric function [60–63], there is almost systematically a frequency range, either before or after the phonon resonances where $\epsilon'' < 0$.
Fortunately there are alternatives to the factorized form. Certain classes of materials, especially glasses, are difficult to describe with pure gaussian or pure Lorentzian lineshape. Brendel and Boreman proposed a model that uses a convolution of a gaussian and a damped harmonic oscillator to describe the dielectric function of silicon oxide and silicon nitride thin films [64].
This form of the dielectric function however does not fulfill Kramers Kronig relationships (KKR) at zero frequency, and thus violates causality. Some authors proposed different formulations that do fulfill causality [65], [66], [67], and have been successfully applied to materials with multiple phonon resonances like SiO2 (See [68] and references therein) or to metals in the interband absorption region [67]. The dielectric function $\epsilon(\omega)$ is described as a sum of oscillators based on gaussian functions that fulfills causality. We decided to apply this form of dielectric function in the case of InGaAs:

$$\epsilon(\omega) = \epsilon_\infty + \sum_1^N [G_{rn}(\omega) + iG_{in}(\omega)], \tag{2.7}$$

where $G_{rn}(\omega)$ and $G_{in}(\omega)$ are defined as :

$$G_{rn}(\omega) = \frac{2A_n}{\sqrt{\pi}} \left[D\left(2\sqrt{\ln 2}\frac{\omega + \omega_n}{\sigma_n}\right) - D\left(2\sqrt{\ln 2}\frac{\omega - \omega_n}{\sigma_n}\right)\right] \tag{2.8}$$

$$G_{in}(\omega) = A_n \exp\left[-4\ln 2\left(\frac{\omega - \omega_n}{\sigma_n}\right)^2\right] - A_n \exp\left[-4\ln 2\left(\frac{\omega + \omega_n}{\sigma_n}\right)^2\right] \tag{2.9}$$

In equation 2.8 and 2.9, A_n is the amplitude, ω_n the TO resonant frequency and σ_n the width of the n^{th} resonance. $D(x)$ is the Dawson function, usually available in standard programming languages (Matlab, Python,...) and defined by :

$$D(x) = \exp(-x^2) \int_0^x \exp(t^2) dt. \tag{2.10}$$

Experimental part

We used FTIR reflectivity and polarized Raman measurements to determine parameters of the InGaAs dielectric function. For this study, we prepared a thin film of 320nm InGaAs transferred on a detuned Salisbury screen structure made of 1μm Ge spacer and 200nm gold mirror. The Salisbury screen scheme was used to enhance the absorption in the thin InGaAs layer. Without the spacer from the Salisbury screen, the response of the InGaAs layer is weak.

The Salisbury screen was one of the first concepts used to create a radar absorbent material. It consists of a coating structure on a metallic surface, with the aim of rendering this highly reflective surface anti-reflective and creating good absorber at a given wavelength. The coating structure on the metallic surface consists of a quarter-wavelength thick lossless dielectric spacer $\lambda_0/(4n)$ (λ_0 is the wavelength in vacuum and n is the refractive index of the spacer) and a thin layer of absorber on top.

A light beam reflected on a highly reflective metallic surface creates a standing wave pattern resulting from interference of the incident and the reflected field, with nodes and anti-nodes. The spacer layer of large optical index squeeze this standing wave pattern in to a smaller thickness. Considering a TM wave reflection, by writing Maxwell equations at the interface, we can find that the tangential electric field E_x standing wave posseses a node at the metallic surface and an anti-node at $\lambda_0/(4n)$. Therefore, an absorber position at $\lambda_0/(4n)$ benefits from the anti-node and absorbs better the incident waves. On the other hand, normal electric field E_z standing wave posseses an anti-node at the metallic surface and a node at $\lambda_0/(4n)$. Therefore, the absorption of E_z component is limited at $\lambda_0/(4n)$.

This is what we observed by computation of our structure, in which we would like to have both E_x and E_z absorption non negligible respectively by TO phonons and the Berreman mode of the InGaAs layer. Therefore, we chose to detune the Salisbury screen structure at $\lambda_0/(8n)$ in order to observe both TO resonance and the Berreman mode. The structure of the obtained sample is represented in Figure 2.7a. A control sample is realized with similar structure to the main sample but without the InGaAs layer, as illustrated in Figure 2.7b.

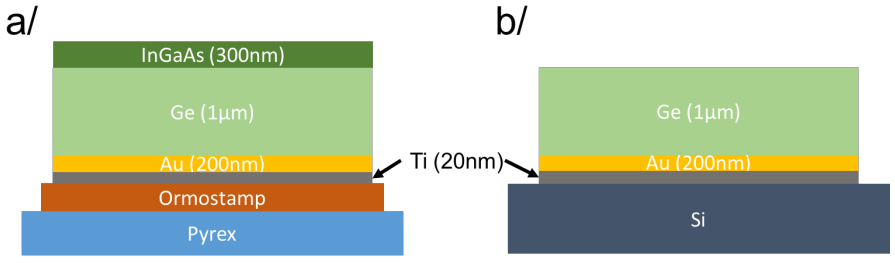

Figure 2.7 – Sample structure: a) InGaAs sample, b) Control sample

The reflectivity measurements are realized in far IR range. To obtain low noise measurements, we use a slow mirror scan rate (2.5kHz) and integrate over 1500 scans. We measure the reflectivity for TM and TE polarization. This way we can obtain angular and polarization resolved reflectivity measurements of our InGaAs and control samples.

We present the results for the InGaAs sample in Figure 2.8 and Figure 2.9. Results for the control sample are presented in Figure 2.10.

In Figure 2.8, we can see two type of dips in the reflectivity curves, located inside two frequency ranges. The broad reflectivity dips in the 400-600 cm^{-1} range are caused by Fabry-Perot resonances. Similar features appears in our control sample as depicted in Figure 2.10. In the 200-300 cm^{-1}, sharp peaks appear both in TM and TE. They are caused by optical phonons. We provided a detailed plot of the reflectivity in this frequency range in Figure 2.9.

In this figure, the reflectivity curves show multiple dips, both in TE and TM polarization. As there is no transmission through the sample due to the Au back-mirror, the reflectivity dips directly corresponds to absorption in the structure. Germanium having a quasi constant refractive index, with very low imaginary part in this frequency region [69], these absorption dips come from the thin InGaAs layer on top of the structure. We confirm this with measurements on the control sample, where no similar absorption dips are observed as illustrated in Figure 2.11.

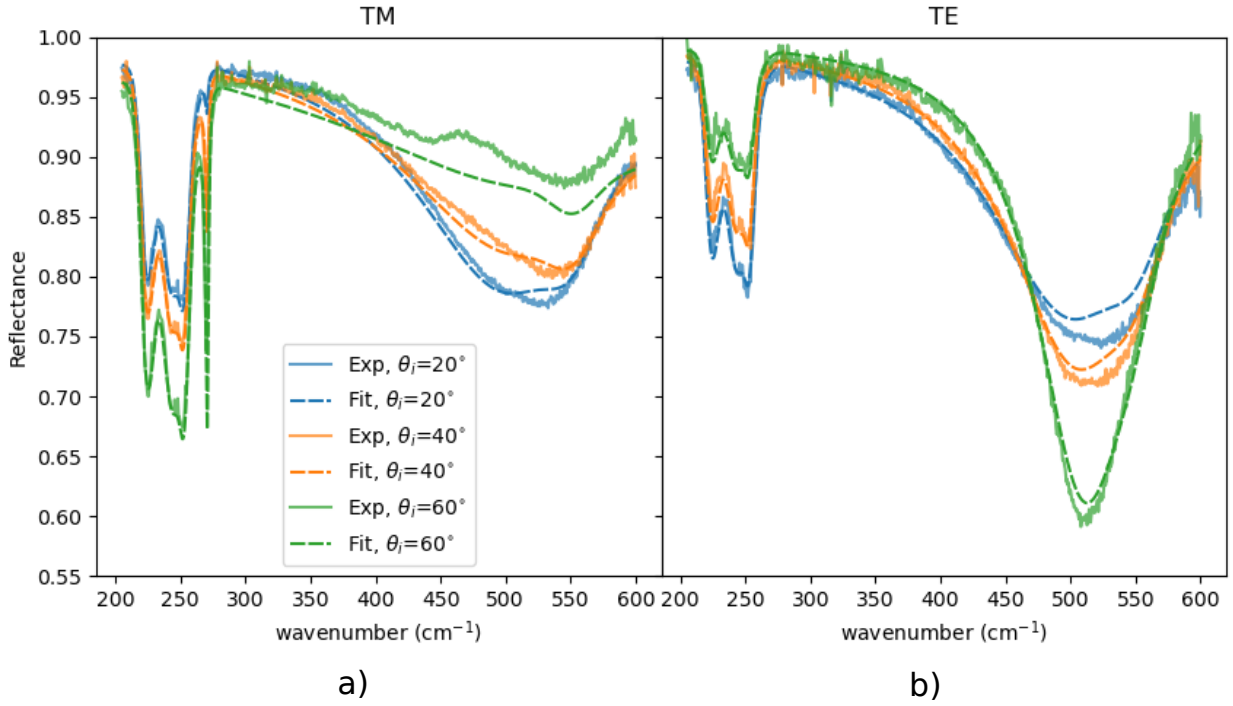

Figure 2.8 – Reflectivity of the InGaAs/Ge/Au sample. a) TM polarization, b) TE polarization.

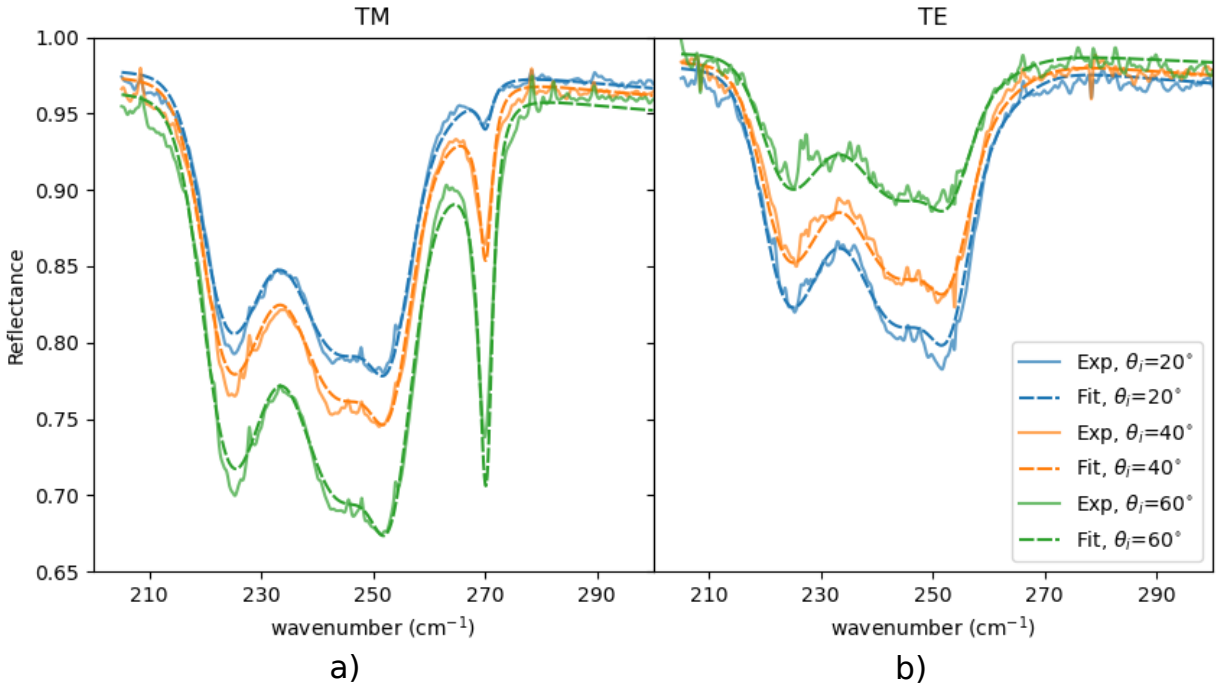

Figure 2.9 – Reflectivity of the main sample InGaAs/Ge/Au, zoom on optical phonon frequency range sample. a) TM polarization, b) TE polarization

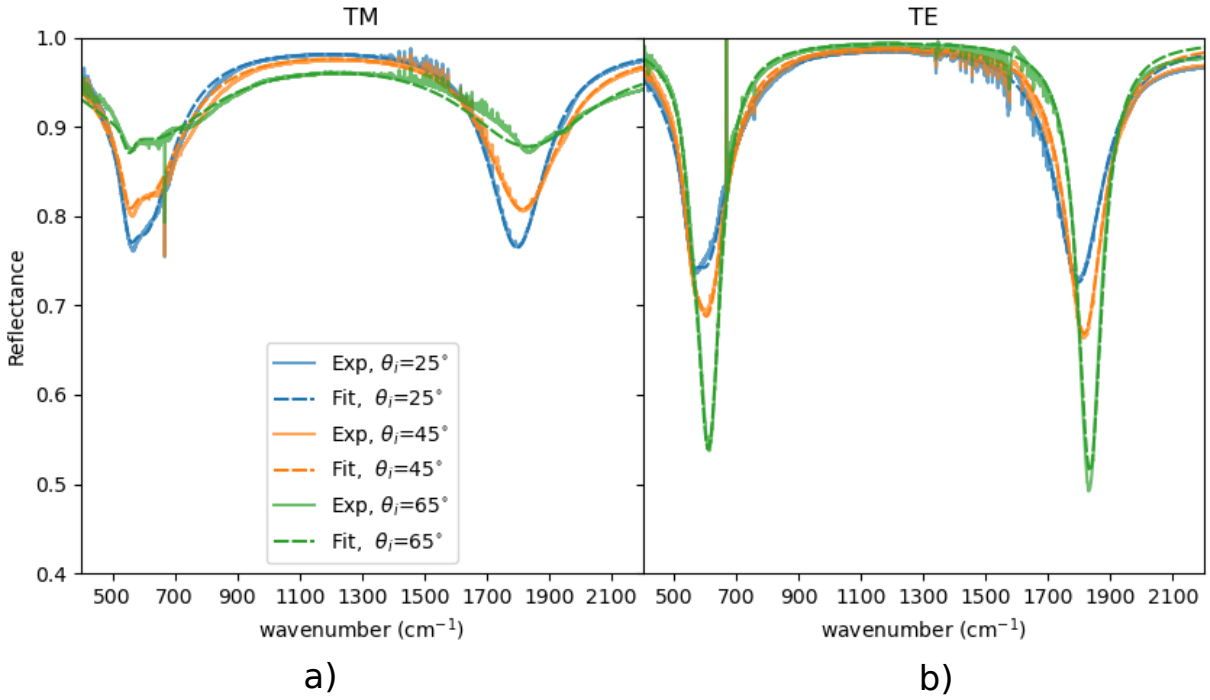

Figure 2.10 – Reflectivity of the Ge/Au control sample. a) TM polarization, b) TE polarization.

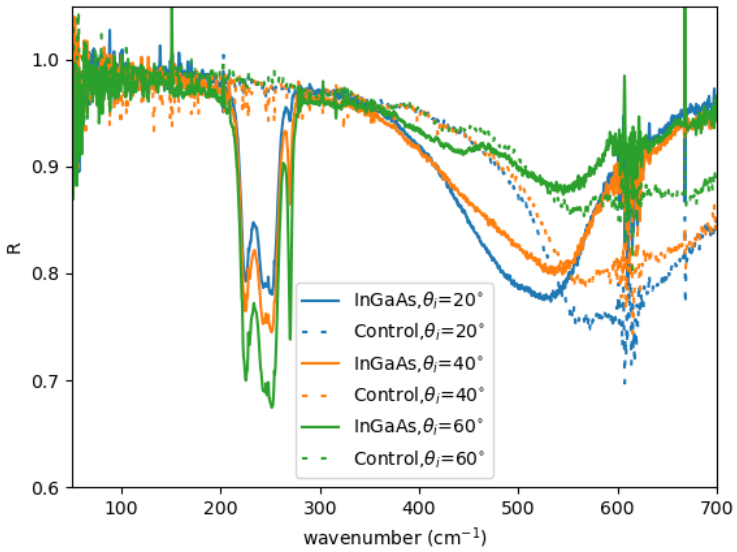

Figure 2.11 – Reflectivity of the main sample InGaAs/Ge/Au compared to the control sample Ge/Au, in TM polarization.

In TE polarization, absorption is the highest for small incidence angles, and is composed of three bands around 225 cm^{-1}, 244 cm^{-1} and 252 cm^{-1}. In TM polarization, the absorption is higher for larger incident angles. The same absorption bands as in TE are present. The behavior of these three absorption bands, appearing both in TE and TM polarization, points to an increase of the imaginary part of the dielectric function of InGaAs, corresponding to the TO phonon frequencies. In TM polarization only, an additional absorption peak at 270 cm^{-1} appears, whose depth increases with larger incident angles. This behavior is typical of the Berreman effect: InGaAs shows an ENZ behavior at this frequency (corresponding to the GaAs-like LO phonon, where $\epsilon' = 0$).

Data fitting

We first start by adjusting parameter for germanium and gold, using the experimental reflectivity of our control sample. Notice that the control sample presents a small resonance at around 550 cm^{-1} that can not be explained by Fabry-Perot resonances. We decided to add a Gaussian oscillator to the dielectric function of germanium [4].

Germanium				Gold
ϵ_∞	A_{ge}	$\omega_{ge}(TO)$ (cm^{-1})	σ_{ge} (cm^{-1})	γ (cm^{-1})
16.79	0.087	552.06	39.08	611.4

Table 2.1 – Parameters used to describe Germanium and Gold deduced from fits to the Control sample reflectivity.

4. This resonance does not influence much the fitting of InGaAs phonons later on, but simply help to better describe the control sample

The value of ϵ_∞ for germanium is between the bulk and thin-film value obtained from recent measurements by the authors of reference [69]. We obtain losses 1.6 times higher than reference [70] for gold, in agreement with measurements on other samples made with the same e-gun metal evaporator.

Then we keep the germanium and gold parameters fixed at the values of Table 2.1 and fit the InGaAs sample reflectivity with 3 oscillators to describe the optical phonons and ϵ_∞ as free parameters. Theoretical results describe very well the experimentally observed absorption dips, as well as their angular dependance for both polarization. We can extract the dielectric function of InGaAs. The TO phonon frequencies are directly accessible, while LO frequencies can be deduced from local maxima of $1/|\epsilon|$, as described in reference [71]. Fitting parameters are summarized in Table 2.2.

Raman measurements are taken in a backscattering at normal incidence, under $Z(XX)\bar{Z}$ and $Z(XY)\bar{Z}$ polarization configuration, where (X, Y, Z) = ([1$\bar{1}$0], [110], [001]). We present in Figure 2.12 the results of Raman measurements.

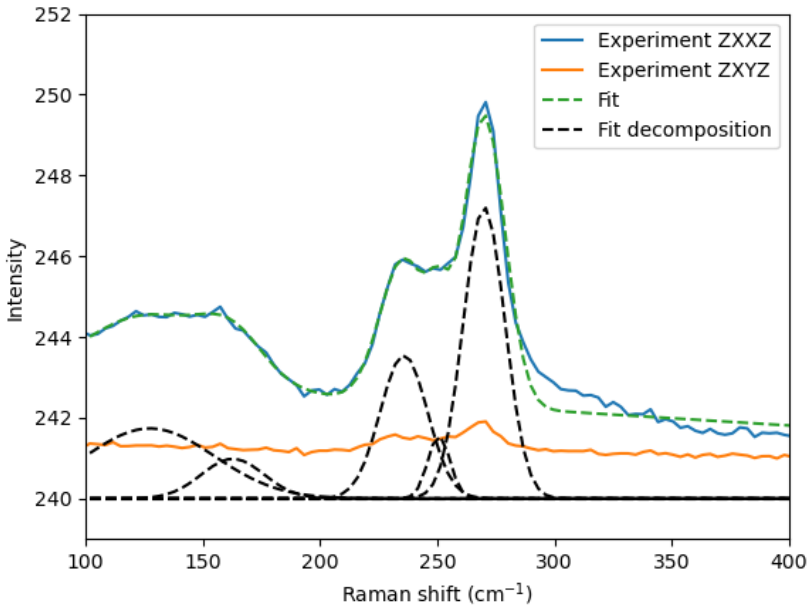

Figure 2.12 – Raman scattering in $Z(XX)\bar{Z}$ and $Z(XY)\bar{Z}$ configuration, with fits and Lorentzian decomposition.

Fitting of the Raman spectra with 3 Gaussian lineshapes yields LO-like phonons at frequencies of 233.7, 249.1 and 270.1 cm^{-1}. The lowest frequency mode is attributed to the InAs-like LO phonon, and the highest frequency mode is assigned to the GaAs-like LO phonon. The mode at 249.1 cm^{-1} is attributed to a disorder mode.

n	A_n	$\omega_n(TO)$	σ_n	$\omega_n(LO)^*$	$\omega_n(LO)$ Raman
1	17.94	225.30	12.11	233.42	233.7
2	20.46	245.27	23.18	247.97	249.1
3	9.65	254.14	7.13	270.32	270.1

Table 2.2 – Phonon frequencies extracted from FTIR reflectivity fits. * deduced from local maximums of $1/|\epsilon|$. The obtained value for ϵ_∞ is 10.96.

Parameters obtained from FTIR and Raman measurments are recapitulated in Table 2.2. LO phonon frequencies are in good agreement between two methods. It is also interesting to realize that we have three LO phonon modes active in Raman, but only one of them gives an absorption dip at 270.1 cm^{-1} in the FTIR reflectance spectra, corresponding to the Berreman mode. This is an experimental proof that the Berreman absorption in FTIR reflectance is not due to an LO phonon excitation but an ENZ normal field enhancement. Indeed, 270.1 cm^{-1} (equivalent to 37.1μm) is the only frequency where the dielectric function of InGaAs's phonon shows an ENZ behavior, as illustrated in Figure 2.13. From the dielectric function obtained, we have $\lambda_{ENZ} \sim 37.1\mu m$, $\epsilon''_{ENZ} \sim 0.88 < 1$, K_{ENZ} ~1.29.

Our study on optical phonon dielectric function of InGaAs is subject to a scientific paper, currently in the process of submission for publication. The phonon's contribution to the dielectric function will be taken into account in other dielectric function models later on in this work. ENZ effect due to InGaAs's optical phonon are in the far IR range. Now we will consider two other contributions, free electrons and ISB transition, which offer more freedom to engineer the ENZ wavelength in a large range of values.

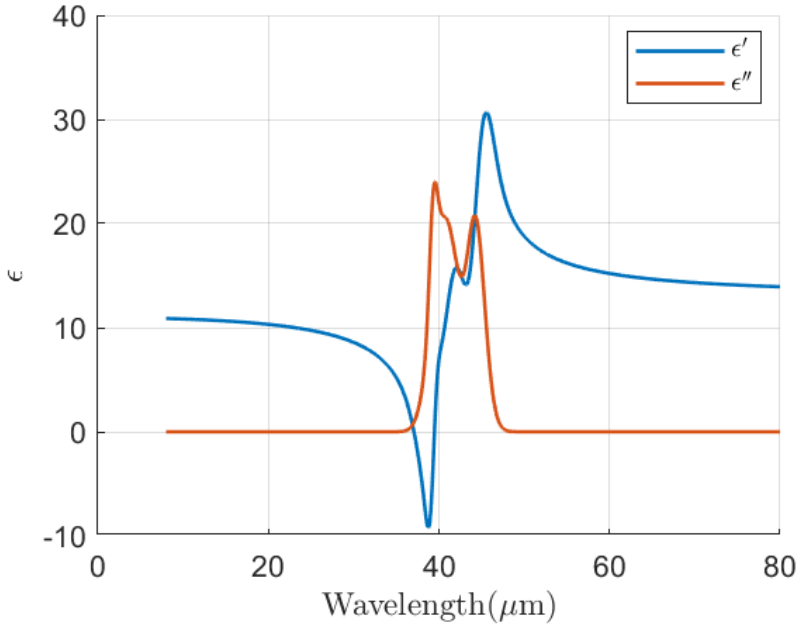

Figure 2.13 – Dielectric function of InGaAs's phonon

2.2.2 Free charges contribution

In InGaAs, we can achieve ENZ regime in a large range of frequencies by adjusting the doping concentration, as described in chapter 1.
However, we need to take into account some complexities in the Drude model in order to describe more accurately the dielectric function. Indeed, the damping factor and the effective mass of free electron depend on doping concentration. In addition, the contribution of interband transition (also called gap contribution) and optical phonon are frequency dependent and can be taken into account (they were considered as a constant represented by the ϵ_∞ term in section 1.2.1).

2.2.2.1 Literatures' values

Concerning the effective mass of electrons $m_0^\star$ in n-doped InGaAs, we gathered values from literature [72], [73], [74], and interpolated them by a 3rd degree polynomial fit of $m_{eff} = m_0^*/m_0$ (m_{eff} is the corrective factor of the effective mass) as a function of doping N in semilog scale (Figure 2.14a). We notice the effective mass increases by a factor of two when the doping concentration goes from $1{\times}10^{17} cm^{-3}$ to $1{\times}10^{19} cm^{-3}$. This increasing m_{eff} reduces the contribution of free charges to the dielectric function.

The values of the damping factor of free electrons in highly doped InGaAs are quite rare in the literature, and usually not in the specific range of frequency studied. Here, I use the damping factor values coming from two sources: Quinchard's thesis [75] and Metzger's work [73], depicted in Figure 2.14b and fitted with a linear relation between Γ and log(N). In Quinchard's thesis, Γ was obtained by fitting the reflectance of InGaAs Fabry-Perot resonators of different heights in mid IR range (work realized at III-V lab). In Metzger's paper, from Hall effect measurements, the authors gave the electron concentration N and the electron mobility $\mu = e\tau/(m_{eff} m_0)$ where $\tau = 1/\Gamma$ is the relaxation time. Metzger also fitted the plasma frequency ω_p from FTIR reflectance measurement, from which he deduced m_{eff}. By using these value, I computed the damping factor Γ [5]. Damping factor Γ coming from electron mobility concerns electronic transport loss while those obtained by FTIR reflectance fitting correspond to optical loss (which matches better to my study in optical regime). Losses in two regimes can have different origin and so these two kinds of damping factors are not necessarily identical. Despite this difference, the two sets of values match quite well as illustrated in Figure 2.14b. In the following part of the dissertation, the damping factor value of n-doped InGaAs in the Drude model will be interpolated from these two data sets.

5. As found in several other papers in the literature (e.g. [70]), Metzger used the convention $1/\tau = \Gamma$ as an angular frequency (unit rad/s) and not a time frequency (unit 1/s). There is a 2π factor difference which can be confusing if we respect the usual convention. To convert to electron-volts, we used $\hbar/(\tau e)$ and not $h/(\tau e)$ with data from Metzger's work.

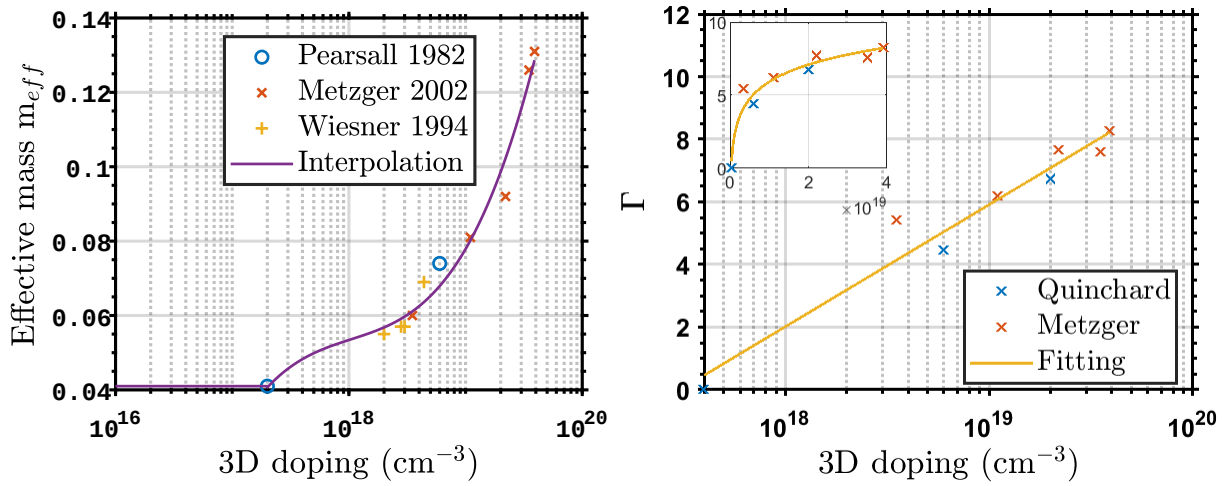

(a) (b)

Figure 2.14 – Evolution of a) the effective mass and b) the damping factor of free electron in InGaAs as a function of doping

From Quinchard's reference [75], the interband contribution of InGaAs is modeled by a Drude-Lorentz function with ω_p=510meV, Γ=73meV, ω_0=841meV (ω_0 also depends on doping).

With the damping factor, effective mass of electrons, contributions of interband and phonon, we can compute the dielectric function and deduce λ_{ENZ}, ϵ''_{ENZ} and $K_{ENZ}=\left|\frac{1}{\epsilon_{InGaAs}}\right|^2$ as shown in Figure 2.15 b, c, d.

Blue curves correspond to the Drude free charges (FC) contribution only, with constant m_{eff}=0.041.

Red curves correspond to the Drude free charges (FC) contribution with m_{eff} interpolated like in figure 2.14a. Compared to the constant m_{eff} case, λ_{ENZ} is red-shifted by about 3μm, ϵ''_{ENZ} increases for larger dopings, and consequently K_{ENZ} is reduced.

Yellow and purple curves take into account interband and phonon contribution, either with Menesces's model [65] (yellow curve, expertimental parameters from this work, section 2.2.1) or with a simple lorentzian (purple curve, Quinchard's work [75]) for the phonon term.

In Figure 2.15c, as the doping increases, ϵ''_{ENZ} shows a maximum at a doping of about $3\times10^{18}cm^{-3}$, then reaches a plateau for the first three models. This behavior can be explained by analyzing the analytical formula of ϵ''_{ENZ}:

$$\epsilon''(\omega_{ENZ}) = \epsilon_\infty \frac{\Gamma}{\sqrt{\omega_p^2 - \Gamma^2}} \sim \epsilon_\infty \frac{\Gamma}{\sqrt{\omega_p^2}} = \epsilon_\infty \frac{\Gamma}{\sqrt{\frac{Ne^2}{m_{eff} m_0 \epsilon_0 \epsilon_\infty}}} \propto \Gamma \sqrt{\frac{m_{eff}}{N}} \tag{2.11}$$

$\Gamma\sqrt{\frac{m_{eff}}{N}}$ is computed as a function of doping concentration N in Figure 2.15a. This quantity also displays a maximum at around $3\times10^{18}cm^{-3}$ then decreases as the doping N increases. This non-trivial behavior is mathematically explained by the fact that the product $\Gamma\sqrt{m_{eff}}$ increases with a slower rate at larger doping N. K_{ENZ} is simly the square of inverse of ϵ''_{ENZ}, therefore it displays also this behavior with a minimum at $3\times10^{18}cm^{-3}$, then reaches a plateau.

The additional phonon contribution explains the difference between the yellow and purple curves from the red one at lower doping concentrations (<$1\times10^{18}cm^{-3}$) in term of λ_{ENZ} and K_{ENZ}. At larger doping, three curves behave similarly because the ENZ crossover happens in the range of wavelength where free charges contribution dominates.

With a doping concentration of about $1\times10^{19}cm^{-3}$, the ENZ regime is reached at around 10μm, with $\epsilon''_{ENZ} \sim 0.5$, $K_{ENZ} \sim 4$.

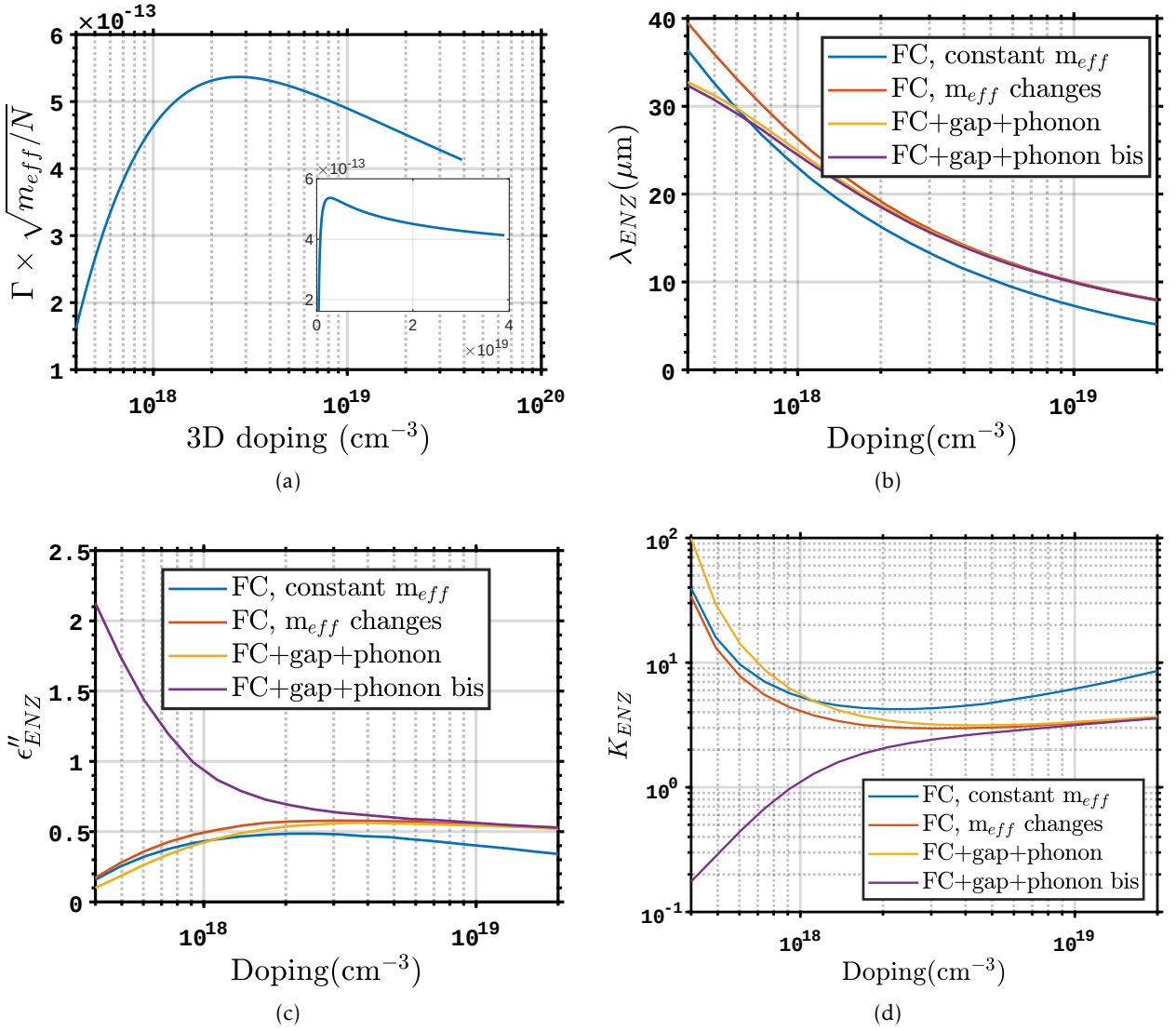

Figure 2.15 – Different quantities are plotted as a function of doping. a)$\Gamma\sqrt{m_{eff}/N}$, which is proportional to the imaginary part of ϵ at ENZ frequency $\epsilon''(\omega_{ENZ})$. This quantity increases with doping, then decreases slowly, due to evolution of m_{eff} and Γ. The inset depicts the same curve in linear scale. b) λ_{ENZ}, c) ϵ''_{ENZ}, d) $K_{ENZ}=\left|\frac{1}{\epsilon_{InGaAs}}\right|^2$ in n-doped InGaAs, as a function of doping, with different models.

2.2.2.2 Experimental values

Following the literature study, we want to fabricate an ENZ device with λ_{ENZ} around 9μm. Severals samples were prepared from the original epitaxy named TGB4545. Each sample will be marked with numbers to keep track of different processes. The samples consist of a 25nm slab of InGaAs heavily doped at $1.5\times10^{19}cm^{-3}$ nominally, sandwiched by two InP barriers layers of 10 and 50nm thicknesses as depicted in Figure 2.19.

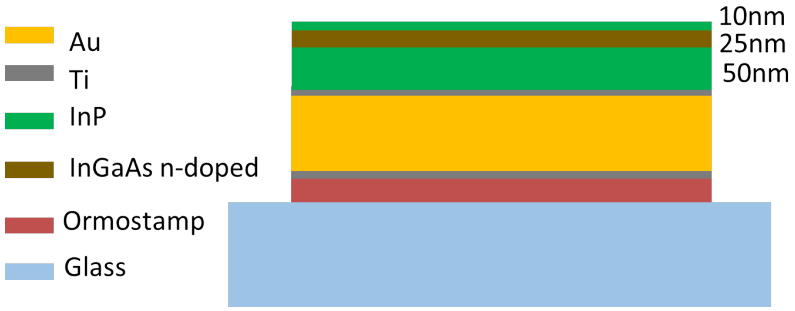

Figure 2.16 – Sample's structure from TGB4545 wafer: InP 10nm - n-doped InGaAs 25nm - InP 50nm, transfered on gold substrate.

Experimentally, I want to determine the free electrons concentration, the ENZ resonance wavelength λ_{ENZ} and the damping factor Γ of the sample. To do this, I performed Van der Pauw Hall effect, Raman scattering and FTIR reflectance measurements. Figure2.17 shows the result of a Van der Pauw measurement to determine the electron density of the doped InGaAs layer. I(V) characteristics are linear for each value of the magnetic field, and the Hall resistance, defined as R=V_H/I, also increases linearly with the magnetic field. The fitting of R(B) by the relation R=B/(n_Sq) gives the electron density in the sample. In this case, we obtain $N_{3D} \sim 1.064\times10^{19}cm^{-3}$.

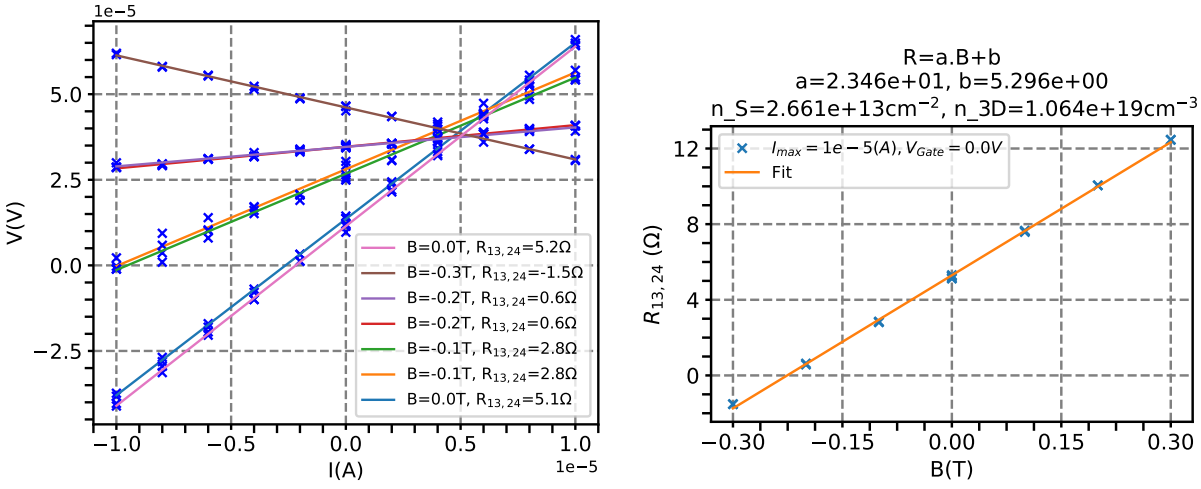

(a) (b)

Figure 2.17 – Van der Pauw - Hall effect measurement. a) I(V) characteristics at different magnetic field; b) Hall resistance and electron density fitting

Figure2.18 shows Raman scattering measurement of TGB4545-2-3. A broad peak at about 1117cm^{-1} is assigned to the L_+ mode of the plasmon-phonon coupling in the n-doped InGaAs layer. At high level of doping (nominal value above $1\times10^{19}cm^{-3}$), the L_+ branch of the plasmon-phonon coupling has essentially a plasmon characteristic and much less a phonon characteristic. This explains the broad linewidth of the L_+ peak compared to pure optical phonons mode due to a smaller damping factor for optical phonons. We deduce an electron density of about $1.325\times10^{19}cm^{-3}$ in the InGaAs layer. Other sharper peaks at around 650cm^{-1} are assigned to higher harmonic of InP phonons (ω_{LO} ~344cm^{-1}, ω_{TO} ~303cm^{-1} [28]).

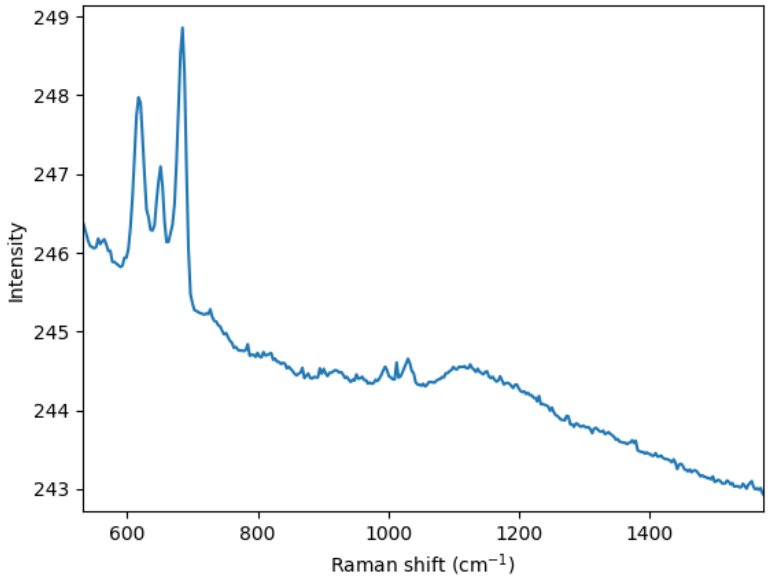

Figure 2.18 – Raman measurement of plasmon-phonon coupling in n-doped InGaAs. A broad peak at about 1117cm^{-1} is assigned to the L_+ mode. The corresponding electron density is about $1.325\times10^{19}cm^{-3}$. Other sharper peaks at around 650cm^{-1} are assigned to higher harmonic of InP phonons (ω_{LO} ~344cm^{-1}, ω_{TO} ~303cm^{-1} [28]).

Figure 2.19 shows an FTIR measurement of TGB4545-2-1's Berreman mode at various incidence angle θ_i in TM polarization. A dip at about 1070cm^{-1} whose amplitude increases at larger incidence angles is assigned to the Berreman mode in the n-doped InGaAs layer and corresponds to the plasma frequency. The experimental and fitted spectra are repscectively presented in dotted lines and solid lines. For the data fitting, we made a hypothesis that there exists a depletion zone at each InP-InGaAs interface of thickness $d_{depletion}$ given by:

$$d_{depletion} = \sqrt{\frac{2\epsilon_0\epsilon_\infty V_{CBO}}{eN}} \tag{2.12}$$

where V_{CBO} is the conduction band offset (V_{CBO} ~200meV for InP-InGaAs interface), N is the 3D electron concentration and e is the elementary charge. With this hypothesis, the data fitting gives an electron density of about $1.24\times10^{19}cm^{-3}$ in the layer and a damping factor $\Gamma \sim 71.9$cm^{-1}. The electron density is slightly lower than the value from Raman measurement and higher that the Van der Pauwn measurement. We can interpret this difference by additional free electrons

population excited optically with Raman laser. The FTIR's plasma frequency value will be used in later computation to avoid the small error induced by Raman laser.

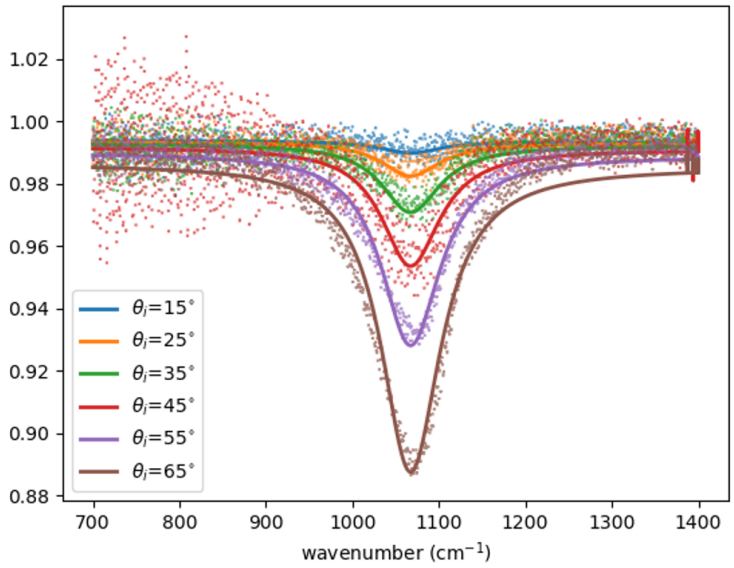

Figure 2.19 – FTIR reflectance measurement of TGB4545-2-1, transfered on gold substrate. A dip at about 1070cm^{-1} which becomes deeper at larger incident angle is assigned to the Berreman mode in InGaAs layer. We can deduce a doping of about $1.24\times10^{19}cm^{-3}$ in the layer and a damping factor $\Gamma \sim 71.9\text{cm}^{-1}$.

From these three measurements, we obtained $\omega_p \sim 1070cm^{-1}$ (132.7meV), $\Gamma \sim 71.9\text{cm}^{-1}$ (8.9meV) for the TGB4545 structure. The damping factor Γ is about 1.5 time larger than values reported by Quinchard and Metzger in Figure 2.14b (about 6meV at doping concentration $1\times10^{19}cm^{-3}$). One explaination for this difference is that samples in Quinchard and Metzger's papers are thick InGaAs layers (about several μm), whereas our sample is a 25nm thin InGaAs layer surrounded by InP. In our FTIR measurement, we probed the Berreman mode in thin InGaAs layer, which is sensitive to the normal electric field E_z and hence to the interfaces. Optical loss due to interface's scattering is more considerable in a thin layer (tens nm) than in a bulky layer (several μm). We also deduced the electron concentration of about $1.24\times10^{19}cm^{-3}$, however this value is directly correlated to other assumed parameters like the electron effective mass m^* and the background dielectric constant ϵ_∞ which change with the electron density. Using directly ω_p eliminates at least the incertitude on the value of m^*. With these considerations, I can now compute the dielectric function of the n-doped InGaAs layer from TGB substrate, as depicted in Figure 2.20. Interband and phonon contribution are also taken into account. We have $\lambda_{ENZ} = 9.33\mu$m, $\epsilon''(\lambda_{ENZ}) = 0.89$, $K_{ENZ} = 1.26$, $K_{ENZ,\,InP} \sim 111.1$.

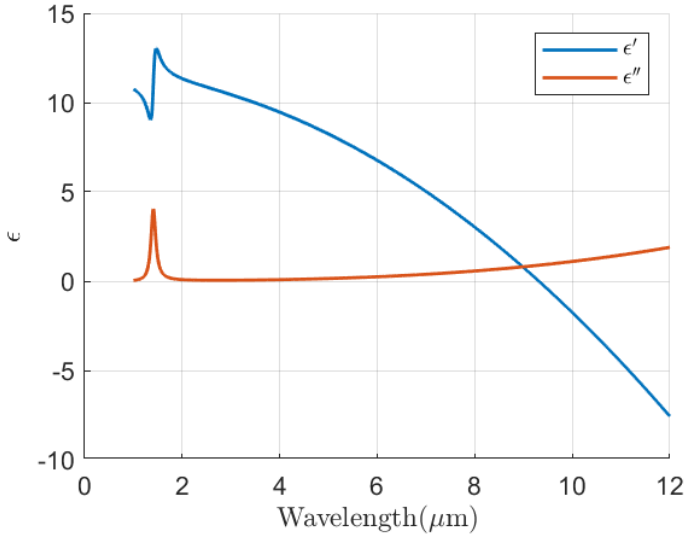

Figure 2.20 – Dielectric function of InGaAs n-doped N = $1.24\times10^{19}cm^{-3}$, ω_p = $1070cm^{-1}$, Γ= $71.9cm^{-1}$, with gap and phonon contributions.

2.2.3 ISB transition contribution

2.2.3.1 Drude-Lorentz model

Using Drude-Lorentz model with ω_{ISB}=0.132meV, L_{eff}=10nm, Γ_{ISB} and doping N changing, the ISB dielectric function is computed. λ_{ENZ}, ϵ''_{ENZ} and $K_{ENZ}=\left|\frac{1}{\epsilon_{InGaAs}}\right|^2$ are deduced from this computation (Figure 2.21).

For lower doping or larger damping factor, the zero crossover of ϵ' does not happen, as the Drude Lorentz perturbation is not enough to compensate the high frequency part of the dielectric function (ϵ_∞).

I consider 'ENZ' wavelength where $|\epsilon|$ is minimized. This new definition explains a different behavior of the blue curve in figure 2.21b from other, where for doping $5\times10^{17}cm^{-3}$, ϵ''_{ENZ} decreases with increasing damping factor. In fact the ϵ'_{ENZ} stays large and increasing, so K_{ENZ} decreases with increasing damping factor, just like other dopings's case.

Figure 2.21b and c show that to reach ENZ regime as defined previously where ϵ''_{ENZ} <1 or K_{ENZ} >1, we need a doping concentration larger than about $1\times10^{19}cm^{-3}$ and a damping factor smaller than about 7meV. The two parameters' effect can compensate each other. It is also noticeable that the same order of magnitude of doping concentration and damping factor are required in case of free charges Drude's model.

Up to now, we have considered a barrier like air with ϵ=1, to ease the comparison between different model. In the specific case of InGaAs quantum well with InAlAs barrier, ϵ_{InAlAs}=10.24 is in fact quite large, leading to a non negligeable field enhancement, as discussed in chapter 1. Here I compute the dielectric enhancement $K_{ENZ\,InAlAs} = (10.24/\epsilon_{InGaAs\,ISB})^2$ as illustrated in Figure 2.21d. We observe an enhancement factor larger than unity for all the couples doping-damping factor in the considered ranges.

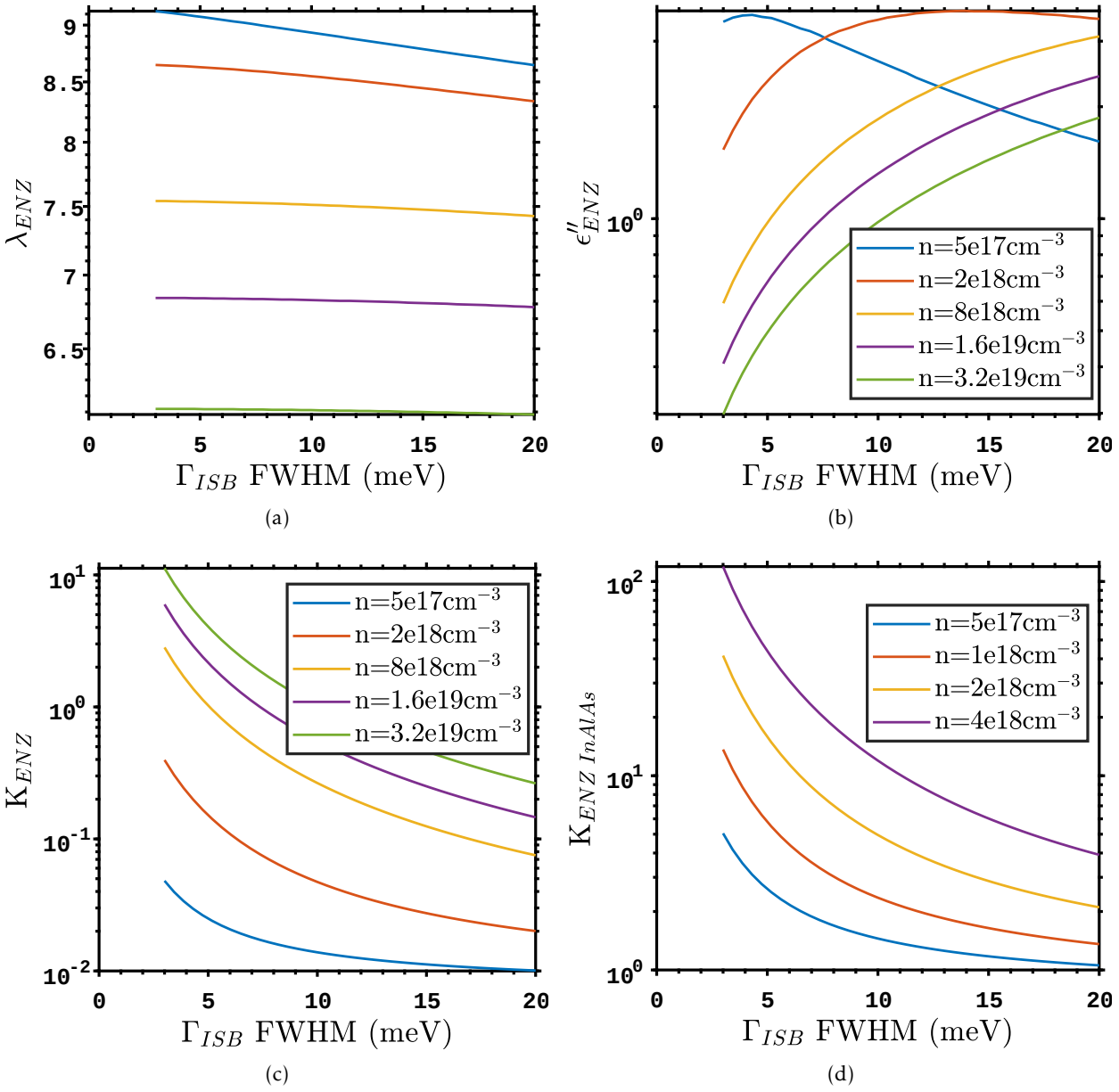

Figure 2.21 – (a)λ_{ENZ}, (b)ϵ''_{ENZ}, (c)K_{ENZ},(d)$K_{ENZ\ InAlAs}$ computed with different dopings and damping factors using DL model. a), b) and c) share the same legend for curves.

2.2.3.2 Experimental characterization

Hall effect Van der Pauw and Raman plasmon-phonon coupling measurements can be used to determine the electron concentration in the quantum well. However we had some difficulties to obtain conclusive data.

Indeed, I have 2 samples with InAlAs/InGaAs/InAlAs quantum well, n-doped nominally at 5×10^{11}cm^{-2} and 1×10^{12}cm^{-2}. Raman measurement of this sample is limited by the top layers made of InGaAs/InAlAs of about 150nm thickness which absorb the 532nm probe laser light (the skin depth of InGaAs is about 50nm at this wavelength). A careful time-controlled etching step is

needed to eliminate top layers without damaging the QW layer (we couldn't do it due to lack of time).

On the other hand, Hall effect measurement at room temperature are limited since the QW is transferred on a gold substrate, with low resistivity barriers at high temperature. Therefore, the Van der Pauw cross is short-circuited by the gold substrate and the Van der Pauw measurement is no longer applicable. This problem could be solved by adding an insulator layer between the gold substrate and the QW (e.g. SiO2).

These samples were measured in transmission multipass measurement, a method to determine the ISB transition absorption [23], [76]. However, our samples only have one QW and the absorption signal by this single QW is quite low. We observed a small sign of the ISB transition but it is not convincing, so I don't present the result here.

Further characterizations that confirm the position of the ISB transition will be presented in chapter 4, where we embed the single QW in a resonant structure, enhancing the QW absorption.

2.3 Chapter conclusion

In this chapter, I introduced Van der Pauw - Hall effect measurement, Raman and FTIR spectroscopies experimental setups used in this work. These techniques were applied to characterize different parameters of InGaAs dielectric function - our material of interest.

The optical phonons of InGaAs were studied in details using a detuned Salisbury screen, angle resolved polarized FTIR reflectance and Raman spectroscopy. The dielectric function is modeled by a sum of three gaussian lineshapes corresponding to three phonon modes, using a functional form that fulfills causality at all frequency. The phonon contribution leads to an ENZ behavior at about 37.1μm. This contribution is important in far IR range around 40μm but its influence extends further to the mid IR range. We give a full set of parameters to calculate the dielectric function, filling a gap in the literature. The result of this study is the subject of a scientific paper under submission.

Concerning the Drude contribution, the electron concentration N, the damping factor Γ and the electron effective mass are three main parameters to pilot the dielectric function in Drude-like n-doped InGaAs layer. I combined literature's values of the damping factor and the effective mass for further use in computation. The electron concentration and the damping factor were determined experimentally for the TGB4545 structure and will be used in the third chapter to realize an electro-optical modulator (EOM).

ISB transition's contribution to the dielectric function of an InGaAs/InAlAs single quantum well was studied theoretically using the Drude-Lorentz model. Similar to the Drude contribution, this ISB contribution is strongly dependent on the electron concentration and the damping factor. When taking into account the barrier's large dielectric function, the dielectric enhancement by ISB transition is non negligible. Experimental optical and electrical characterizations of bare single quantum well structure were attempted. They did not give proper results due to some complications of the samples and its low optical absorption. In chapter 4, it will be shown that by embedding the single QW in an optical cavity, we succeeded to clearly observe the ISB transition frequency and estimate its damping factor. These are interesting information for our further QCD studies presented in chapter 4.

3

ENZ Electro-optical modulator

This chapter is devoted to study the use of the ENZ mode in an electro-optical modulator. First, I will briefly present the state of the art of IR optical modulator. Then, I will show the working principle of our modulator based on the tuning of the ENZ mode between the strong coupling and the weak coupling regime with a cavity mode. After that, I will show the full study of two ENZ-EOM structures - first the HEMT-like and then the MOSFET-like structure - from device's conception and fabrication to characterizations and improvement. Finally I will further discuss about what can be learned from this ENZ-EOM study.

During this chapter, I will present the result of characterizations of various samples. To limit the confusion of readers, I remind the structure of these samples in Appendix A.

3.1 Electro-optical modulator, state of the art and working principle

3.1.1 State of the art of IR optical modulator

An optical modulator is a device that allows modulating light beam properties - amplitude, phase or polarization - either in free space or in guided configuration. Optical modulation has many applications [77]: well-known optical communication, but also other domains such as optical interconnect link, environmental monitoring, biological and chemical sensing, medical and military applications.

Modulators are often characterized by severals figures of merit. The main FOM are the modulation speed (modulation bandwidth) and the modulation depth (extinction ratio).

The modulation speed is usually defined as the frequency at which the modulation is reduced to half of its maximum modulation. While high modulation speed is highly appreciated in communication and interconnect applications, low to moderate modulation speed can be sufficent to other applications like sensing.

Typically, in fiber-optics communication, stand-alone optical modulator can be used to encode information at high rate, larger than 10 GHz, without destabilizing the light source (the LED or laser diode light source can be modulated directly by switching the current supply at moderate frequency up to several GHz, but this approach is limited by the rise and fall time of the source [2]).

The modulation depth is the ratio between the maximum and minimum intensities of modu-

lation, usually given in decibel $10\log(I_{max}/I_{min})$. Alternatively, we can also use the modulation contrast $(I_{max}\text{-}I_{min})/(I_{max}+I_{min})$ to characterize the intensity variation. Large modulation depth/modulation contrast is of course better and needed so that the modulation signal is still distinguishable from noise.

There are different ways to modulate light. If we dispose of a tiltable mirror, mechanically we can deflect light at the switching frequency of the mirror's motion. This is the principle of some Micro-Electro-Mechanical Systems (MEMS) optical switches/modulators [78], [79]. This approach offers high modulation contrast, adapted to different wavelengths, but is limited to low modulation speed, typically kHz to below MHz.

Another approach consists in modulating the dielectric function - ϵ' and ϵ'' - of the optical modulator's reactive material in order to modulate the output beam. The dielectric function can be controlled by electric voltage (electro-optical modulator), but also by optical excitation (all-optical modulator), acoustic excitation(acousto-optic modulator) or by temperature (thermo-optic modulator [80]). Thermo-optic modulation is also limited in speed like the mechanical approach. Acousto-optic modulator is faster in modulation speed but still limited below GHz range. All-optical modulator can be very fast (e.g. modulator using femto-second laser pulse as excitation), but they require a secondary complex and expensive source. Electro-optical modulator is the most popular approach, because of its ability to deliver high modulation speed and its simplicity in implementation.

A lot of research effort is focused on electro-optical modulator at telecom wavelength range (around 1.55μm) and on-chip configuration, driven by the demands in high speed communication and interconnect. Some usual kind of electro-optical modulators are electro-absorption modulator and electro-optic modulator [81]. Electro-absorption modulator uses Quantum-Confined Stark Effect or Franz–Keldysh effect in semiconductors, where an applied electric field changes the interband transition energy and shifts the absorption edge. The modulation concerns mostly the imaginary part of the dielectric function ϵ''. Electro-optic modulator often refers to a modulator with the real part of the refractive index n' or the real part of the dielectric function ϵ' changing under voltage. This includes Pockels effect, Kerr effect and carrier density effect in general. A refractive index change can be used to vary the phase difference between two optical beams and to induce constructive or destructive interference, typically using a Mach-Zenhder interferometer (MZI) scheme. A π-phase difference between two beams is required to realize destructive interference. Another way to use refractive index change in optical modulation is to include a resonant structure in the device, for instance a ring resonator modulator or photonic crystal cavity. A variation of the refractive index changes the resonant condition, allowing to switch between the on- and off-resonance states.

In most cases, these modulators use a waveguide structure. The light beam propagates along the length of the waveguide and interacts with the active layer over this whole propagation length. This is useful to accumulate either the electrically induced absorption in electroabsorption modulator or a π-phase change in Mach-Zenhder interferometer.

In reference [81] published in 2015, the authors presented a review on ultrafast and low energy-per-bit consumption in wavelength-size EOM. Authors show the trend in EOM researches to use nanophotonic structures in order to confine light at sub-wavelength scale. The Figure 3.1 from this review illustrates the improvement in performance of nanophotonic EOM structures (SPP, hybrid plasmonics) compared to conventional structures in term of modulation speed and energy-per-bit comsumption. The predicted or demonstrated modulation speeds of these nanophotonic EOM can vary from GHz up to THz range, with several orders of magnitude gain in

terms of energy consumption. This confirms the interest of light confinement and size reduction of the EOM devices.

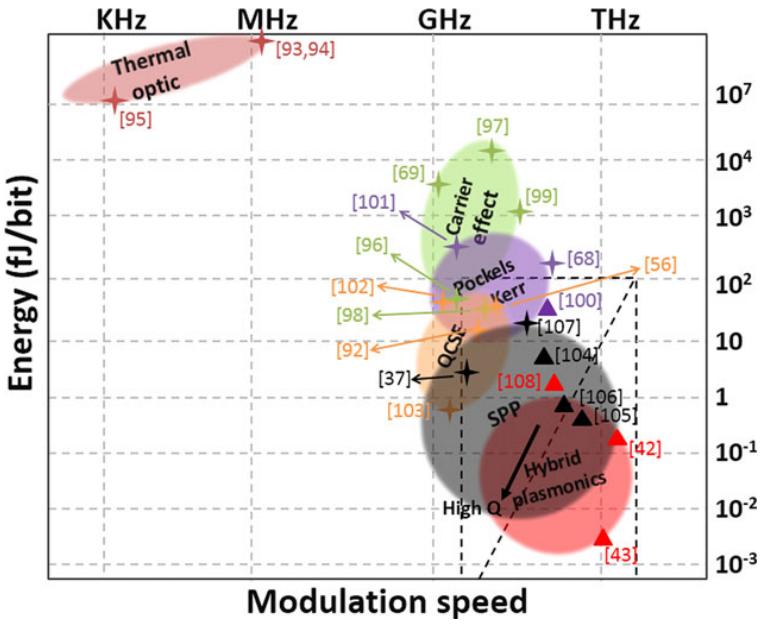

Figure 3.1 – Schematic drawing of energy-per-bit as a function of modulation speed of different EOM, adapted from reference [81]

Following the nanophotonic trend in EOM, the use of ENZ effect in EOM is actively studied in recent years, both theorically and experimentally [11, 12, 16, 17, 82] to cite some of them. The authors used waveguide structure with a thin ENZ layer, where most of the light is confined in the ENZ layer when the ENZ wavelength λ_{ENZ} matches the guided light wavelength. This induces a strong absorption peak at λ_{ENZ}. The optical modulation is based on charge carrier density modulation that modifies λ_{ENZ}. Experimentally, in 2018, Liu *et al.* [17] realized an ENZ-EOM with ITO on Si waveguide of 20μm length, achiving 3dB modulation depth, 2pJ/bit consumption and a modulation speed of 117kHz. Wood *et al.* [11] demonstrated an ENZ-EOM with In_2O_3 on Si waveguide of 4μm length, delivering 6.5dB modulation depth at a modulation speed of 2.5GHz. The structure of this device is illustrated in Figure 3.2. In 2020, Zhou *et al.* [12] realized an 8μm long plasmonic waveguide with ITO, achiving 3.2dB modulation depth, 100fJ/bit at 3.5GHz modulation speed.

In these cases, the ENZ layer is heavily doped, generally more than $1\times10^{20}cm^{-3}$. The charge carrier modulation is realized via MOS-like capacitor (Metal-Oxide-Semiconductor) either in accumulation or depletion regime ($7\times10^{20}cm^{-3}$ in Wood's paper and $6.5\times10^{20}cm^{-3}$ in Zhou's paper, both at accumulation regime). The use of ENZ materials in these devices helps to confine light, reduce the device foot print and offer a large optical bandwidth. In term of modulation speed, experimentally ENZ-EOM are still limited at several GHz. According to Zhou *et al.* [12], this is mainly due to lack of high-speed device design and fabrication quality. They also pointed out that the modulation speed is often limited by large capacitance of MOS capacitor. It can be improved with high mobility material like CdO, with estimated modulation speed over 40 GHz.

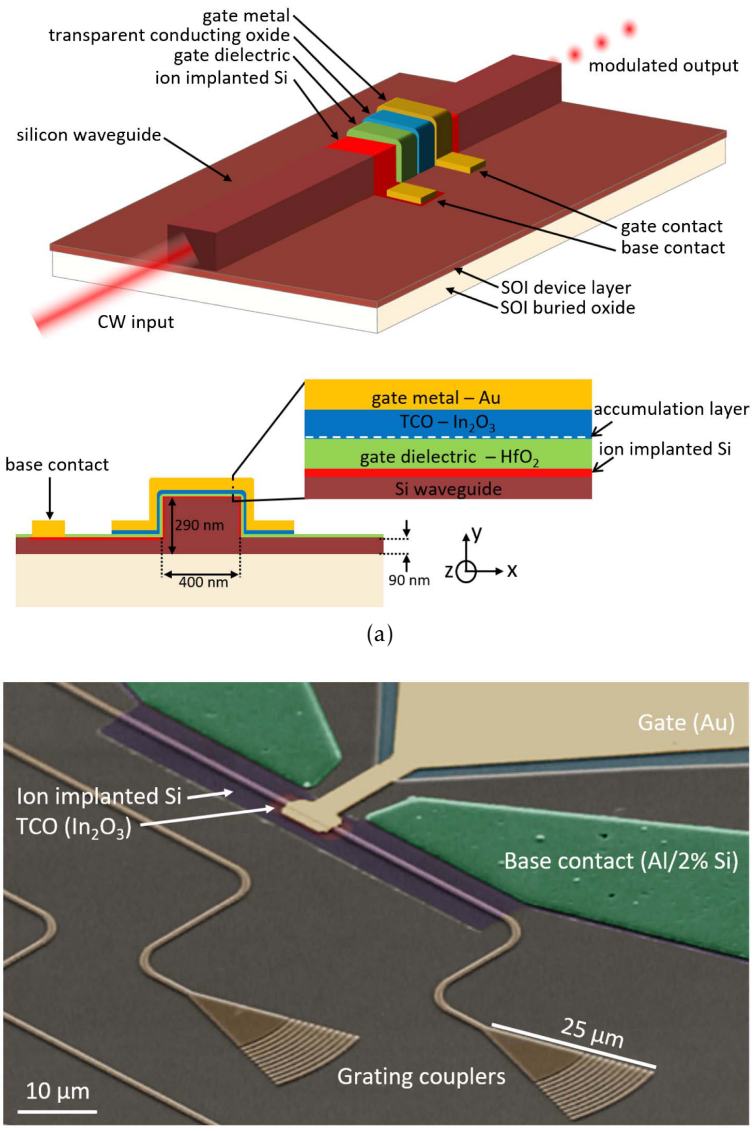

Figure 3.2 – Adapted from reference [11]: a) schematic of an ENZ-EOM with In_2O_3 as ENZ layer on Si waveguide. b) SEM image of the experimental device.

These nummerous demonstrations, with or without ENZ effect, concern mostly the telecom wavelength range 1.55μm. In the mid-IR and far-IR ranges, experimental realizations of EOM are much less popular.

Some demonstrations can be cited as references [3, 36, 39, 83]. These EOM do not use the waveguide transmission configuration but opted for a free space reflectance configuration. This configuration can actually be very convenient for free space applications such as Free Space Optical Communication, in which the complexity of coupling to a waveguide is removed.

These EOM also explored other mechanisms and materials sytems for modulation. Dabidian *et al.* [83] used graphene coupled to Fano resonance metasurface at a wavelength of around 7um. Graphene's charge density is modulated to shift the resonance. Vassant *et al.* [36] demonstrated an

EOM with phonon-resonances based ENZ combined with ISB transition in GaAs n-doped quantum well at 34μm. The ISB transition contribution is modulated to turn on/off the ENZ mode. In both examples, the modulation speed was not reported. Park [39] and Pirotta [3] use a system with two resonances in coupling. One of the two resonances is tunable, so we can switch between strong coupling and weak coupling regimes where resonance peaks are shifted.

Let's have a closer look at the last two examples which both use the transition between strong coupling and weak coupling regimes. In Park's 2015 paper, the authors realized an ENZ-EOM made of ITO as ENZ layer, embedded in a MIM optical cavity. The EOM structure is illustrated in Figure 3.3a. This ENZ-EOM functions at around 4μm wavelength, with a modulation of the reflectance of about 15% (modulation depth 1.25dB) at a rate of about 125kHz. In Pirotta's 2021 paper, a fast EOM at around 10μm is demonstrated using ISB transition coupled to a MIM mode in a system made of multiple-quantum wells embedded in a MIM cavity. The modulation is based on the depletion of electrons in quantum wells, in order to remove the ISB transition contribution. The computed band structure of the device is illustrated in Figure 3.4a. The reflectance change is illustrated in figure 3.4b, equivalent to a modulation depth of about 1.14dB. The modulation speed is reported to be 1.5GHz and is limited by lack of faster detector for characterization. We notice that in both Park and Pirrota's devices, electron depletion is not complete and it is difficult to reach the weak coupling regime where only the MIM mode exists.

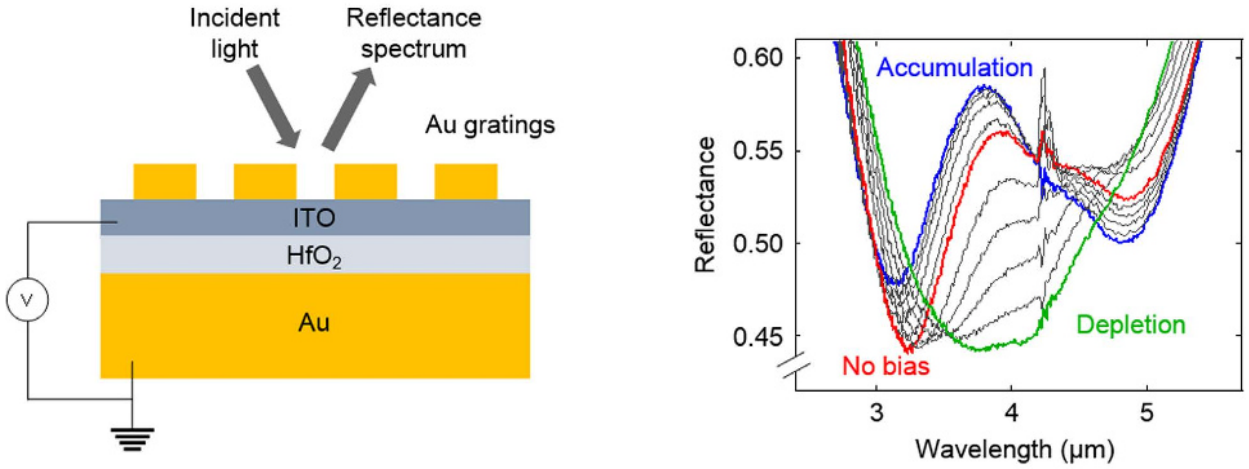

(a) (b)

Figure 3.3 – Adapted from reference [39]. a) Schematic of a free space ENZ-EOM with ITO as ENZ layer, embedded in a MIM cavity. b) Reflectance spectra of the device under voltage bias.

As pointed out in the paper of Pirotta [3], mid-IR optical modulator is largely under-developed. To date, a standalone, efficient and optically broadband modulator is not available in the mid-IR optoelectronic toolbox. A number of high potential applications like Free Space Optical Communication at LWIR range, gas spectroscopy, coherent detection,... motivate the developement of EOM at LWIR range.

This work was devoted to the development of a free space ENZ-EOM based on the mechanism of transition between strong coupling and weak coupling regimes at around 10μm wavelength. The two resonances in coupling includes an ENZ mode constituted by a III-V semiconductor Drude slab and a MIM cavity mode. The III-V semiconductor material system - InGaAs in this case - is different from ITO usually used in ENZ-EOM like the one in Park's paper. InGaAs is known

for low electron effective mass and high electron mobility. ENZ wavelength at 10μm instead of 1.55μm or 4μm also means that a smaller charge carrier concentration is needed. As compared to Pirotta's device, our ENZ-EOM use the ENZ mode in a 25nm-thick Drude slab of InGaAs instead of the ISB transition in multiple quantum wells spread over about 200nm of thickness. We expected that a thinner layer of active layer would be potentially easier to modulate in charge carrier concentration.

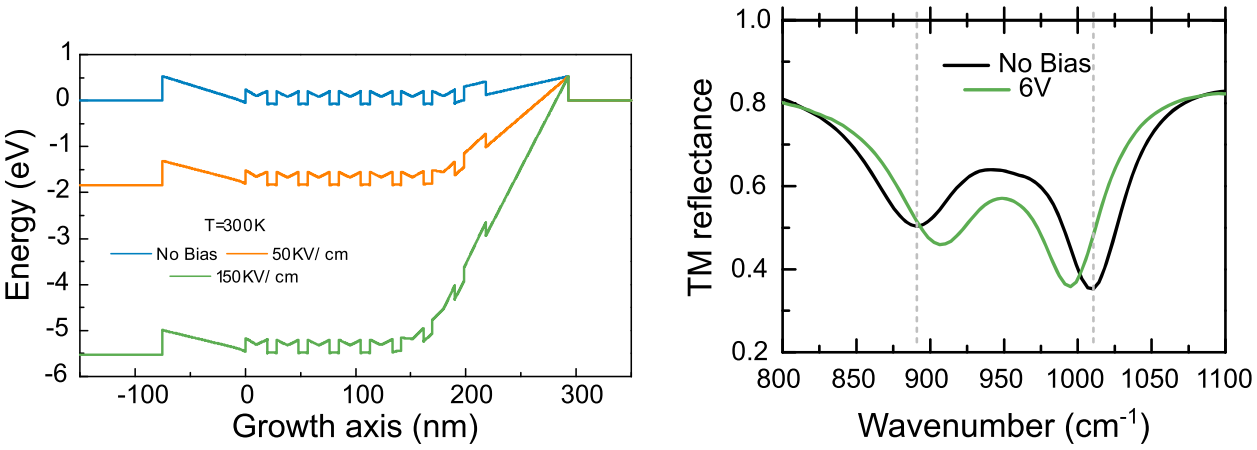

(a) (b)

Figure 3.4 – Adapted from reference [3]. a) Band structure of the modulator at different bias regimes. b) Reflectance spectra change between two regimes.

3.1.2 MIM resonator

We would like to couple and confine infrared light coming from free space into a highly sub-wavelength semiconductor active layer. In our devices, light confinement allows to increase the ovelap between light and the active layer, thus their interaction. To reach this goal, we used Metal-Insulator-Metal (MIM) resonator with one metallic part structured into a grating. [1]

The theory of MIM resonator can be found in several references [26, 75, 76, 84–86]. MIM resonator belongs to the plasmonic structure family, well-known for its light confinement capability. To get insight into the light coupling and confinement mechanism in our MIM resonator, we first consider a waveguide made of a semiconductor slab of thickness L sandwiched between two planar metallic mirrors. This planar waveguide supports TM and TE propagative modes - solutions of the Helmoltz equations. The TM and TE waves propagate along the x direction and are invariant along the y direction as depicted in Figure 3.5a. To simplify, we suppose that the metallic mirrors are perfect electric conductor (infinite conductivity at any frequency). This hypothesis implies that the tangential electric component is zero at the two metal-semiconductor interfaces (E_x=E_y=0 at z=0 and z=L). The confinement by two metallic mirrors imposes standing wave solutions in z direction for E_y(z) in TE mode and H_y(z) in TM mode.

In TE configuration, E_y(z=0, z=L)=0 implies that $E_y(z)=E_0\sin(\frac{m_z\pi}{L}z)$, where m_z=1,2,3... is the order of the mode.

1. MIM is also referred to as MDM or MSM (Metal-Dielectric/Semiconductor-Metal) in other works.

In TM configuration, E_x(z=0, z=L)=0 implies that $H_y(z)=H_0\cos(\frac{m_z\pi}{L}z)$, where m_z=0,1,2,3... [2].

Only TM wave generates a zero-order TM_0 with constant field profile along z direction, as illustrated in Figure 3.5a. Non zero-order modes TE_1, TE_2, TE_3, ... and TM_1, TM_2, TM_3, ... possess nodes in their field profile [3].

The dispersion relation of these modes is written as follows:

$$k_x = \sqrt{\epsilon\frac{\omega^2}{c^2} - \left(\frac{m_z\pi}{L}\right)^2} \tag{3.1}$$

$$= \sqrt{\epsilon\left(\frac{2\pi}{\lambda_0}\right)^2 - \left(\frac{m_z\pi}{L}\right)^2} \tag{3.2}$$

$$k_y = 0 \tag{3.3}$$

$$k_z = \frac{m_z\pi}{L}. \tag{3.4}$$

Non zero-order modes TE_1, TE_2, ... and TM_1, TM_2, ... have a cut-off frequency below which k_x becomes imaginary: $\omega \geq \omega_{cut-off} = m_z\frac{c\pi}{\sqrt{\epsilon}L}$. From equation 3.2, for each λ_0, there is also a lower bound of the cavity thickness $L \geq L_{cut-off} = m_z\frac{\lambda_0}{2\sqrt{\epsilon}}$. Non zero-order modes cannot confine light below this length $L_{cut-off}$. For a wavelength of $\lambda_0 = 10\mu$m and ϵ=11.6 in case of InGaAs, $L_{cut-off} \sim 1.5\mu$m with $m_z = 1$.

The TM_0 mode is the only mode that has neither cut-off frequency nor lower bound limit for light confinement length. Thus, we will use the TM_0 mode for highly sub-wavelength confinement.

---

2. We can deduce this from the relation $E_x = \frac{1}{i\omega\epsilon_x}\frac{\partial H_y}{\partial z}$

3. They are comparable to Fabry-Perot cavity modes. In the case of Fabry-Perot cavity, at least one of the two mirrors is not totally opaque. Light is injected into the cavity through the top and accumulates a multiple of 2π phase change after one round in the cavity. We usually consider normal or close to normal incidence.

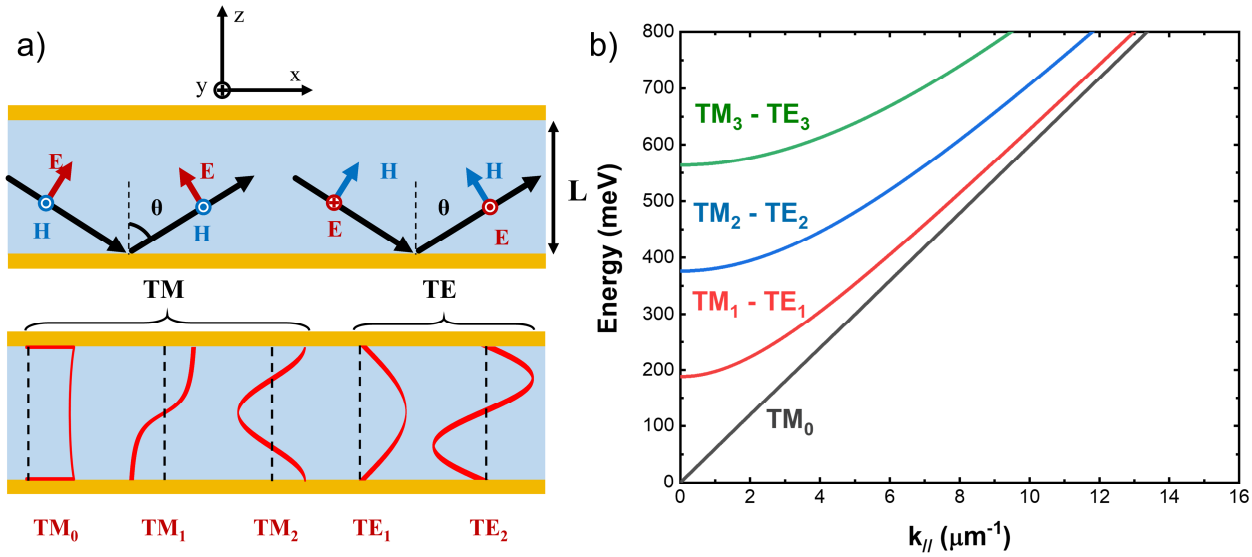

Figure 3.5 – Adapted from reference [76]. a) TE and TM modes in a planar waveguide. b) Dispersion relations of TE and TM modes

In this planar waveguide, light is injected from its edge and not directly from the top since the two mirrors are opaque. This coupling is usually difficult and not effective because of the small thickness L. Rather than using planar waveguide, we can structure one of the two mirrors into antennas in order to couple free-space light into the cavity. Here, we chose to use a metallic grating structure, made of strips of width S and repeated periodically with a period P along the x direction, as illustrated in Figure 3.6a. The strip's width S is designed to be a multiple of half the wavelength of the guided mode of interest. Each strip acts like a half-wave dipole antenna. We suppose that the period P is large enough so that these strip antennas are independent. Under a TM-polarized incident electromagnetic field, charges in the strip oscillate in resonance in a standing wave pattern, as illusated in Figure 3.6b. The induced oscillating dipole allows to couple efficiently free-space incident wave into the MIM cavity. Inside the cavity, the field profile along the vertical z direction is similar to planar waveguide modes, allowing confinement of light. In addition, in the horizontal x direction, a standing wave pattern is formed under metallic strips. The confinement along x direction is explained by Todorov *et al.* [87], [84] as a difference of effective indices between the metal-insulator-metal (M-I-M) region and metal-insulator-air(M-I-A) region. The authors stated that the effective index of a TM-guided mode inside a M-I-M region is close to the index of the insulator ($n_{eff_{M-I-M}} \sim 3.4$ for InGaAs), whereas in a M-I-A region, the effective index is close to the index of air ($n_{eff_{M-I-A}} \sim 1$) if the insulator thickness L is much smaller than the wavelength.

The resonance wavelength (in vacuum) is given by:

$$\lambda_{0\,m_x} = \frac{2n_{eff_{M-I-M}}S}{m_x}, \tag{3.5}$$

where m_x=1,2,3... is the order of the mode along x direction and $n_{eff_{M-I-M}}$ is the effective index of the MIM mode. The notation $TM_{m_z m_x}$ is now used to denote the MIM mode confined in both z and x directions. It's worth noticing that due to symmetry at normal incidence, even m_x order mode (eg. TM_{02}, TM_{04}, ...) do not induce net dipole, and thus can not be excited. They can only be

excited at oblique incidence where the symmetry is broken. Odd order modes (eg. TM_{01}, TM_{03}, ...) always induce dipole and therefore can be excited at both normal and oblique incidences. According to references [85], [75], [86], $n_{eff_{M-I-M}}$ given by:

$$n_{eff_{M-I-M}} = n_I \sqrt{1 + \frac{i\lambda_0}{\pi L \sqrt{\epsilon_M}}}, \tag{3.6}$$

where n_I and ϵ_M are respectively the index of bulk insulator and the dielectric function of the metal.

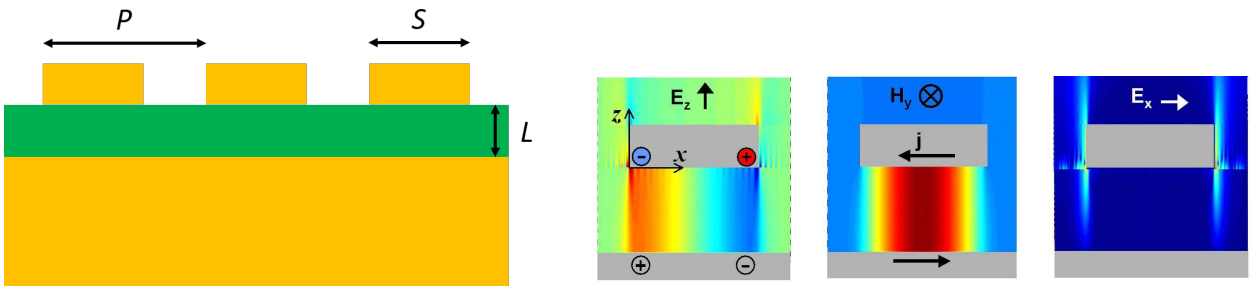

(a) (b)

Figure 3.6 – a) Geometry of a MIM grating cavity. b) Field distribution of a TM_{01} mode, adapted from reference [84].

According to equation 3.5, the resonance wavelength depends mainly on the strip's width S and the mode's effective index $n_{eff_{M-I-M}}$. The resonance is independent of the incidence angle, and thus the dispersion relation of these modes $TM_{0\,m_x}$ is flat as a function of k_x. This non-dispersive regime of the MIM cavity mode is very practical for device's usage.

However, this non-dispersive regime is only valid when each strip acts as an independent antenna. This is no longer the case when the cavity thickness L is increased or the distance between two adjacent strips P-S is reduced. Indeed, the electromagnetic field is not strictly confined under the strip but leaks into the M-I-A region. This leakage is usually referred to as the fringing field in patch antenna and is illustrated in Figure 3.7. When the fringing field of two adjacent strips start to superimpose, the modes confined under each strip couple with each other. These modes then form delocalized bands and become dispersive.

According to Quinchard [75], the extension of the fringing field is approximately equal to the cavity's thickness L. The criteria for the non-dispersive regime is that the adjacent fringing fields do not superimpose, or:

$$P > S + 2L \tag{3.7}$$

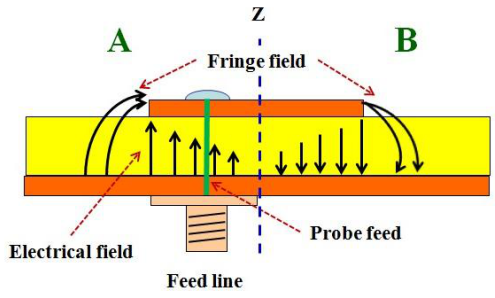

(a)

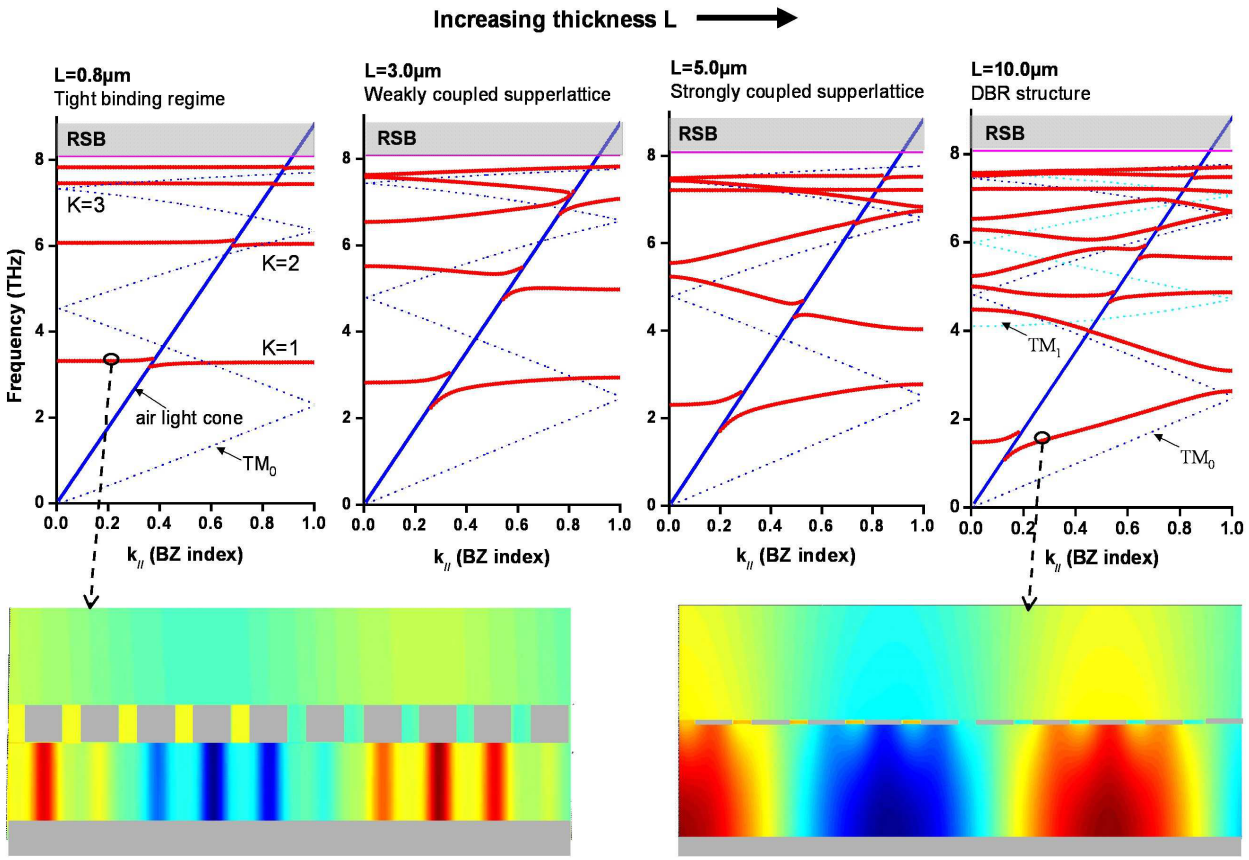

(b)

Figure 3.7 – a) Fringing field in patch antenna in microwaves [88]; b) Angular dispersion relations of MIM grating, where the period and strip's width are kept constant P=11.5μm, S=5.5μm, and the cavity's thickness is increased from left to right (L=0.8, 3, 5, 10μm) [84]. Red curves are the computed dispersion relations, blue lines depict the limit of the light cone. K corresponds to m_x order in our case. As the cavity's thickness increases, the dispersion lines are no longer flat but become dispersive.

The transition from the non-dispersive regime to dispersive regime with the cavity thickness L changing is illustrated in Figure 3.7b, adapted from reference [84]. The period and strip's width are kept constant P=11.5μm, S=5.5μm. For thin cavity L=0.8μm, $S+2L = 7.1\mu m < P$, the red curves

showing the dispersion relation of TM_{01}, TM_{02}, TM_{03} are flat. At L=3μm, S+2L = 11.5μm = P, the modes start to delocalize, the dispersion relations become curved. As the cavity's thickness increases to 5μm and 10μm, the modes become strongly coupled.

3.1.3 Field effect for electron density modulation

Electron density in an n-doped semiconductor layer can be modified by several approaches. The population of electron in conduction band can be increased by optical pumping, creating additional electron-hole pairs. This method is often used in all-optical modulators, the density modulation depends on the optical pump's power. The device can also be designed to be a capacitor. The n-doped semiconductor layer is in contact with one metallic plate and is separated from the second metallic plate by an insulator layer. The charge and discharge regimes of the capacitors modify the electron density in the semiconductor layer [4]. This approach is used in Park's paper [39], illustrated in Figure 3.3a. Field effect transistors are also popular structures allowing to modulate electron density in thin doped semiconductor layer. Here, we will concentrate on two transistor structures: HEMT and MOSFET.

HEMT or High Electron Mobility Transistor (also called MODFET or Modulation-doped Field Effect Transistor) was invented in 1979 by T. Mimura [89]. HEMT employs semiconductor heterojunctions: a small gap material (e.g. GaAs), a barrier material (e.g. AlGaAs) delta doped, a metal gate deposited on the barrier material creating a Schottky contact. The band structure is illustrated in Figure 3.8. A 2D electron gas (2DEG) is formed at the interface of the two semiconductors. This 2DEG density can be controlled by a voltage applied between the gate and the substrate thanks to field effect. The Schottky contact imposes a Schottky barrier between the metal and the barrier material. Ideally, the Schottky barrier blocks the charge current from circulating in the device, the band structure is bended as a function of the gate voltage, modifying the free charge distribution. The doping is typically 0.7×10^{12}cm^{-2} [89], 3×10^{12}cm^{-2} [90], 4×10^{12}cm^{-2} [91], [92], 1×10^{13}cm^{-2} [93].

MOSFET or Metal–Oxide–Semiconductor Field-Effect Transistor is another popular transistor structure in which the electron density is modulated by field effect. In this case, a thin layer of large band gap oxide is inserted between the metal gate and the semiconductor. The oxide plays the insulator role here, preventing current from circulating in the device. Similarly to HEMT, by applying a bias voltage between the gate and the substrate, the electron density can be modified.

4. The depletion length is limited by the Debye length, also called the Thomas-Fermi screening length in doped semiconductor case, $L_D = \sqrt{\frac{\epsilon_0 \epsilon k_B T}{e^2 N}}$, where N is the free electron concentration. For T=300K, ϵ = 11.6, we have L_D=12.9nm with N=1×10^{17}cm^{-3} and L_D=1.3nm with N=1×10^{19}cm^{-3}.

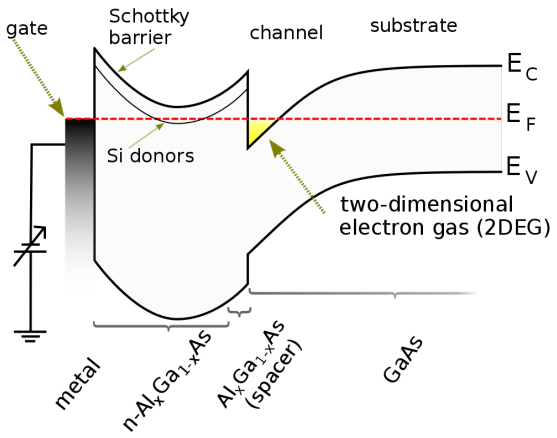

Figure 3.8 – HEMT band structure. The device is made of a hetero junction of GaAs and AlGaAs barrier, modulation doped, with a Schottky contact on top. The 2DEG density at the interface of GaAs and AlGaAs is controlled with the gate voltage [5]

.

3.1.4 Working principle of ENZ-EOM

We designed our ENZ-EOM as a Drude ENZ slab embedded in a MIM cavity. The principle and the structure are illustrated in Figure 3.9. The MIM resonance ω_{MIM} is controlled via strip's metal width S and the ENZ resonance ω_{ENZ} is controlled via the electron concentration of the ENZ slab: $\omega_{ENZ} \propto \sqrt{N}$. Both are polaritonic modes. Seperately, they are designed to have the same resonance frequency: $\omega_{ENZ} = \omega_{MIM} = \omega_0$. When being put together, they interact due to the overlap of the two modes in the cavity. The system is analogous to two coupled mechanical springs system. The coupling between the two modes results in two new hybrid modes at shifted resonant frequencies, as illustrated by the blue curve in Figure 3.9b. This coupling between the MIM mode and the ENZ mode is qualified as a strong coupling regime if the Rabi splitting (the splitting between the two hybrid modes) is larger than the sum of the ENZ and MIM resonance damping factors. The strong coupling regime is also accompanied by a low absorption at the initial resonant frequency ω_0, located in between the two hybrid mode frequencies.

The ENZ mode is expected to be electrically tunable by applying a voltage to modulate the electron concentration N. As will be detailed in section 3.2.2, by applying a voltage, we expect to first reduce the thickness of the ENZ layer while having the 3D electron concentration N almost constant, then to reduce both the thickness of the ENZ layer and electron concentration N. With a decreasing thickness of the ENZ layer, the overlap between the ENZ mode and the MIM mode is reduced, and so does the Rabi splitting, making the two hybrid modes approach each other and eventually merge. This is the transition from a strong coupling regime to a weak coupling regime. On the other hand, a reduction of the 3D electron concentration N induces a shift of the ENZ frequency ω_{ENZ} towards smaller values. This shift of ω_{ENZ} corresponds to a detuning of the two resonances, where one hybrid mode follows the reduction of ω_{ENZ} and the other hybrid mode moves towards the initial MIM frequency. When the EZN layer is totally depleted, there is only the MIM mode left in the system, characterzied by a strong absorption at ω_0. We pass from a highly reflective state at ω_0 to a highly absorptive state (respectively illustrated by the blue curve and red curve in Figure 3.9b).

In terms of electrical configuration, the design is inspired from the HEMT structure in the

first place and then from the MOSFET structure. In HEMT-like structure, the InGaAs ENZ slab is surrounded by InP barriers, as illustrated in Figure 3.9a. Metals like Ti, Au forms Schottky contact on InP. The two Schottky contacts on two interfaces are expected to block the current when a bias voltage is applied to the structure, allowing electron density modulation. In MOSFET-like structure, an insulator layer made of SiO_2 is added to further reduce the current in the system under bias. Optically, the MOSFET-like structure is more complex than the two mode coupling described above. It brings into play a third mode - an ENZ mode due to optical phonon of SiO_2. This mechanism will be detailed in the MOSFET-like ENZ-EOM section.

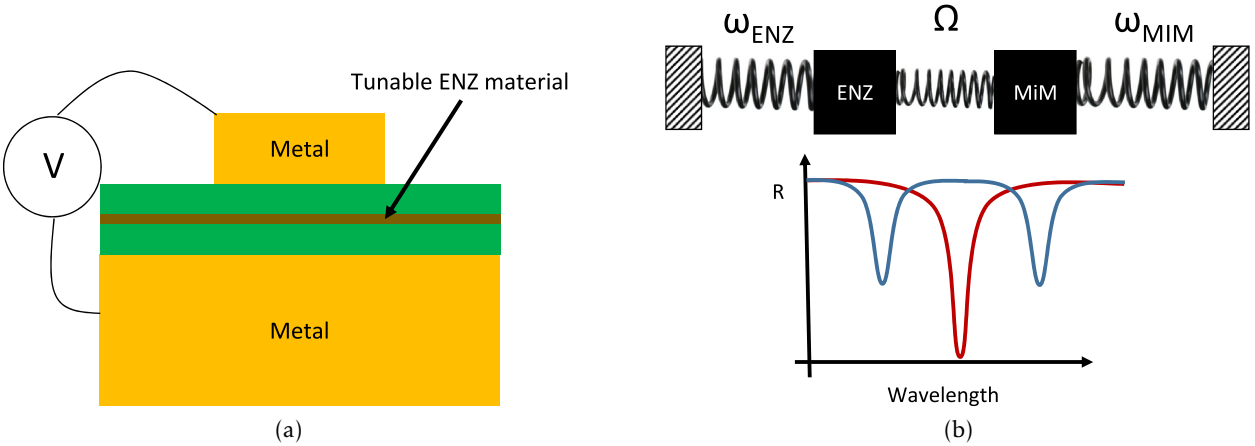

Figure 3.9 – Schematic of ENZ-EOM working principle: a) Our ENZ-EOM structure consist of a tunable ENZ layer embedded in a MIM cavity. The ENZ property can be controlled electrically via the application of a voltage. b) Two coupled resonators and analogy to two coupled mechanical springs system. Two resonantors in this case are: the ENZ mode and the MIM cavity mode in resonant ($\omega_{ENZ} = \omega_{MIM} = \omega_0$), creating two hybrid modes (blue dips). The reflectance is large at ω_0 in the strong coupling regime. An applied voltage modulates the electron density profile in the ENZ layer and detune away the ENZ resonance ω_{ENZ}. The MIM resonance is restored at ω_0 (red curve) and the structure become highly absorptive at ω_0.

3.2 Design of optical cavity's geometry of HEMT-like ENZ-EOM to optimize modulation amplitude

In this section, I will present the electromagnetic computation and electronic band structure computation of the HEMT-like ENZ-EOM. By changing geometrical parameters of the cavity, we optimized the structure in order to improve the modulation amplitude.

3.2.1 Electromagnetic optimization

The electromagnetic behavior of the ENZ-EOM is studied with a code called Reticolo. I will briefly introduce the code's principle, then present the results of the electromagnetic optimization.

3.2.1.1 Introduction to Reticolo code

To compute the EM response of our device, we use Reticolo, an Rigorous Coupled-Wave Analysis code (RCWA, also known as Fourier modal method or FMM) developed since 2005 by Jean Paul Hugonin and Philippe Lalanne from IOGS [94]. This code was applied in a number of experimental and theoretical studies: wideband absorber [95], high efficiency solar cell [96], thermal emitter [97] to name some of them.

RCWA is a Fourier resolution method in k-space. In Reticolo, the dielectric function in a periodic medium, defined by their period, filling factor, thickness, can be expanded by Fourier transform in a plane waves basis composed of spatial modes. The Helmholtz equation of each mode is solved like in a homogeneous medium to determine the wavevector of the mode. The periodic medium is fully described by its modes. For a multilayer of periodic media, the scattering matrix is used to compute modes' propagation through each layer and to match modes' amplitude at interfaces. The resulted EM field is obtained by summing over responses of these spatial modes. In the case of RCWA, the accuracy of the computation result depends mainly on the number of spatial modes k_x taken into account in the computation. The tricky part of RCWA computation is the Fourier decomposition of the dielectric function of structured media. High dielectric contrast interfaces can be troublesome if not handled carefully (non converged even with a large number of spatial modes).

In our case, we used a metalic grating having discontinuity in dielectric profile between metalic strips and air in horizontal direction. To ensure a better convergence, we used Granet transformation [98] - a coordinate transformation. The idea of this transformation is to provide variable spatial sampling density, with an increased density of sampling points around discontinuities. Thanks to this method, the convergence is reached with fewer spatial mode terms. A similar space sampling is applied to compute the electromagnetic field. Without such sampling method, we can obtain negative absorption in certain layers due to computation inaccuracy.
A reflectance convergence test is performed prior to main modulation computation, to estimate the number of spatial modes M needed for the computation. The scattering matrix size is M^2, so computation time increases proportionaly to M^2. From the convergence test's result, as illustrated in Figure 3.10, we typically use M=50 in following computations.

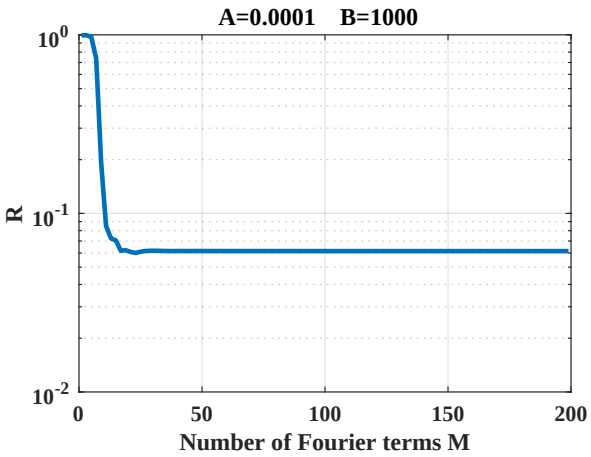

Figure 3.10 – Convergence test of reflectance of a metallic grating structure as a function of the number of Fourrier terms.

3.2.1.2 Geometrical optimization

I used Reticolo to compute the reflectance of our ENZ-EOM structure, illustrated in Figure 3.11. The MIM cavity consists of an Au top grating, a flat semiconductor heterostrcuture and an Au back mirror (semi-infinite). Thin Ti adhesion layers between Au and semimiconductor are also taken into account in Reticolo computation. The top grating is periodic with a period P, metallic strip's width S, fixed thickness 200nm. The heterostructure is made of 10nm InP top barrier, 25nm InGaAs quantum well n-doped and InP bottom barrier of varying thickness L_{bot}. The heterostructure's thickness is L_{Total}. The gold back mirror is considered semi-infinite. Ti adhesion layers are 2nm-thick. Parameters to define the dielectric functions of these materials are listed in Table 3.1 [6].

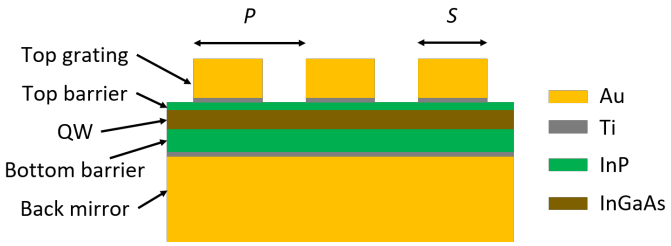

Figure 3.11 – Scheme of the EOM structure used in computation.

We would like to realize the optical amplitude modulation at 9μm. The n-doped InGaAs layer reaches ENZ regime at 9μm with an electron concentration estimated at N=1.3×10$^{19}cm^{-3}$. Therefore, for the strong coupling regime of the ENZ-EOM, I performed reflectance computation with the initial electron concentration N_1=1.3×10$^{19}cm^{-3}$, as illustrated in Figure 3.12a. To characterize the weak coupling regime of the ENZ-EOM, I computed the reflectance of the structure at two depletion levels: N_2=5×10$^{18}cm^{-3}$ (more than half of the initial concentration, which requires a more reasonable voltage for electron depletion according to band structure simulation presented in the next section) and N_2=0 (total depletion), as illustrated in Figures 3.12b and 3.12c. The optimizing function to maximize here is the absolute value of the modulation amplitude - that is the difference of reflectances between two regimes R_{N_1}-R_{N_2}, where R_{N_1} and R_{N_2} are respectively the reflectance in strong coupling and weak coupling regimes. This modulation amplitude R_{N_1}-R_{N_2} is depicted in figures 3.12d and 3.12e, corresponding respectively to partial and complete depletion levels, obtained by subtraction of corresponding reflectance maps.

These reflectance and modulation amplitude maps are computed at 9μm, normal incidence, with a period P=4μm. On the horizontal axis, the total semiconductor thickness L_{total} changes from 0.045 to 0.445μm. On the vertical axis, the metallic strip's width S changes from 0.2 to 3.80μm. The reflectance is encoded in pseudo-color from 0 (blue) to 1 (red). The reflectance maps of the weak coupling regime in Figures 3.12b and 3.12c show two highly absorptive line features at about S=1μm and 3.5μm, whereas the reflectance map of the strong coupling regime 3.12a shows high reflectance at these places. The absorptive line features in the weak coupling regime correspond to the absorption of the MIM mode TM_{01} ($S \sim 1\mu$m) and TM_{03} ($S \sim 3.5\mu$m). These absorptive line features are directly translated into the modulation amplitude maps 3.12d and 3.12e by narrow red lines, indicating large modulation amplitude (R_{N_1}-R_{N_2} >0.8). In the complete depletion case N_2=0cm^{-3}, the absolute value of the modulation amplitude is maximized (reaching

6. At the begining of the project, we used Ordal's values for Au and Ti dielectric functions. Later on, we used Olmon's value for Au Rakic's value for Ti, which offer a better match to experimental results.

about 0.90-0.93) at S~1.04-1.08μm and L_{total} ~0.085-0.110μm.

Further computations with different values of period P show little dependance of the modulation amplitude features on P. Therefore, for further computation, we chose S=1.04μm, L_{total}=0.085μm, P=4μm. I computed the reflectance spectra for different electron concentrations with these geometrical parameters, as illustrated in Figure 3.13. This Figure is consistent with the optical modulation by the transition from a strong coupling regime (orange curve with two absorption dips at about 7.4μm and 12.4μm and high reflectance at 9μm) to a weak coupling regime: yellow and purple curves where the ENZ mode is detuned away by electron depletion, giving a low reflectance around 9μm.

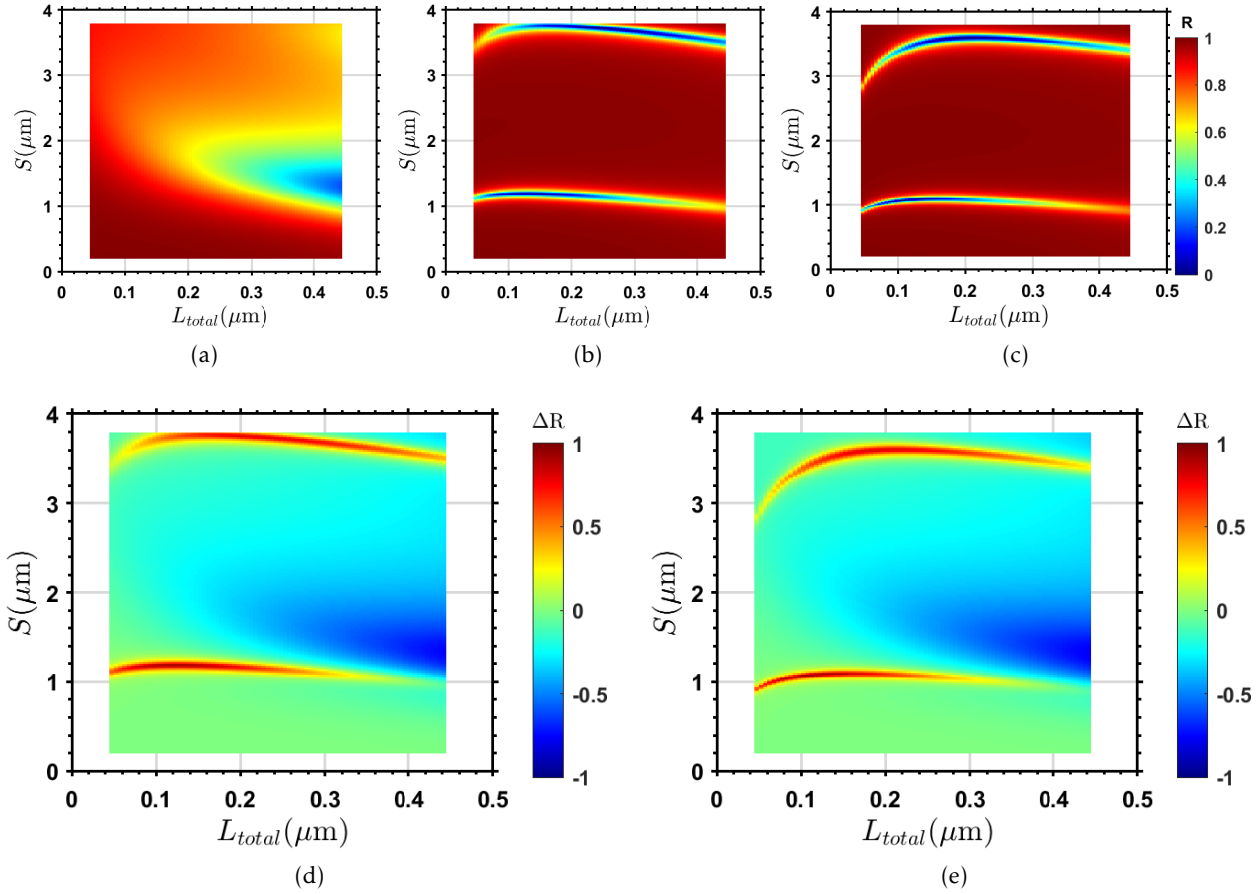

Figure 3.12 – a,b,c) Computed reflectance map R of ENZ-EOM structure at different electron concentrations, normal incidence: a) N=1.3×10$^{19}cm^{-3}$, b) N=5×10$^{18}cm^{-3}$, c) N=0cm^{-3}. They share the same colorbar. d,e) Modulation amplitude maps between the strong coupling regime N=1.3×10$^{19}cm^{-3}$ and two depletion regimes: N=5×10$^{18}cm^{-3}$ in d) and N=0cm^{-3} in e). Computation inputs: λ =9μm, TM polarization, incidence θ=0°, P=4μm Ordal's Au/Ti dielectric function [99].

For simplicity, the absorption peaks of the HEMT-like structure will be referred to as peaks ***(a)***, ***(b)*** for wavelengths around 7.4μm, 12.4μm and N=1.3×10$^{19}cm^{-3}$, and ***(c)*** for wavelength around 9μm and N=0. The EM field maps are also computed the the optimized structure (S=1.04μm, L_{total}=0.085μm, P=4μm) at three wavelengths 7.4μm, 12.4μm and 9μm in order to visualize the

mode profiles in the strong coupling regimes (peaks ***(a)*** and ***(b)***) compared to the MIM-only configuration (peak ***(c)***). Figure 3.14 reports these field distributions in TM polarization at normal incidence: the first two columns correspond to $|H_y|$ and $|E_z|$ components of the field [7]. The third column depicts $|E_z|^2$ averaged over the whole length of a period P. The three rows corresponds to the three modes ***(a)***, ***(b)*** and ***(c)***. The magnetic conponent $|H_y|$ shows similar vertical profiles with one node, typical to the TM_{01} MIM mode. For $|E_z|$ component, the three mode behave differently.

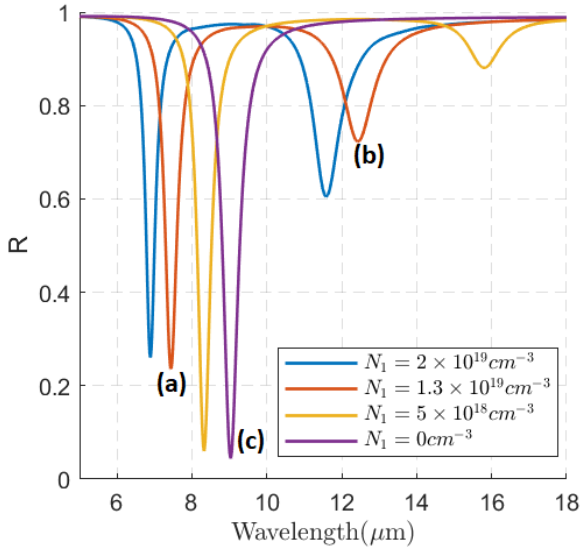

Figure 3.13 – A plot of computed device's spectral response at different electron concentrations N. In the ENZ-EOM mechanism, we expected a transition from a strong coupling regime with N=$1.3\times10^{19} cm^{-3}$ (double peaks ***(a)*** 7.40μm and *(b)12.40μm*) to a complete depletion N=0 with only the MIM mode left at 9μm or peak (c). Inputs: S=1.04μm, TM polarization, incidence θ=0°, P=4μm, Ordal's Au/Ti dielectric function [99].

Peak ***(a)*** at 7.40μm has $|E_z|$ confined in the QW layer, with locally an enhancement up to about 25 times the norm of the incident electric field. This enhancement is due to both the MIM cavity and the dielectric contrast in the QW, accounting respectivly for an enhancement factor of about 10 and 2.5 (the final enhancement factor is the product of both). In terms of averaged $|E_z|^2$, in the QW, the field is enhanced by a factor of about 70, compared to a factor of 10 in the barrier layers. The dielectric contraste enhancement is $K_{dielectric}$ ~7 [8] (not far from 2.5^2, consistent with a local enhancement of about 2.5 of $|E_z|$ in the QW layer compared to $|E_z|$ in the InP bariers).

Peak ***(b)*** at 12.40μm has a different behavior in $|E_z|$. The field is similar to a MIM's field profile, with an enhancement factor of about 10. The field $|E_z|$ is not further enhanced in the QW but rather be reduced by a small factor. Among the three modes, peak ***(b)*** has the smallest field enhancement compared to the incidence field.

Peak ***(c)*** at 9.0μm on the other hand has a local enhancement in the thin InP top barrier layer, not observed in the two other modes' profile.

7. $|E_x|$ can also be computed, but in MIM cavity, the E_x component is weak and negligeable compared to E_z under the grating structure.

8. We should not confound $K_{dielectric}$ with K_{ENZ} here since the ENZ effect is designed to happen at 9μm with doping N=$1.3\times10^{19} cm^{-3}$.

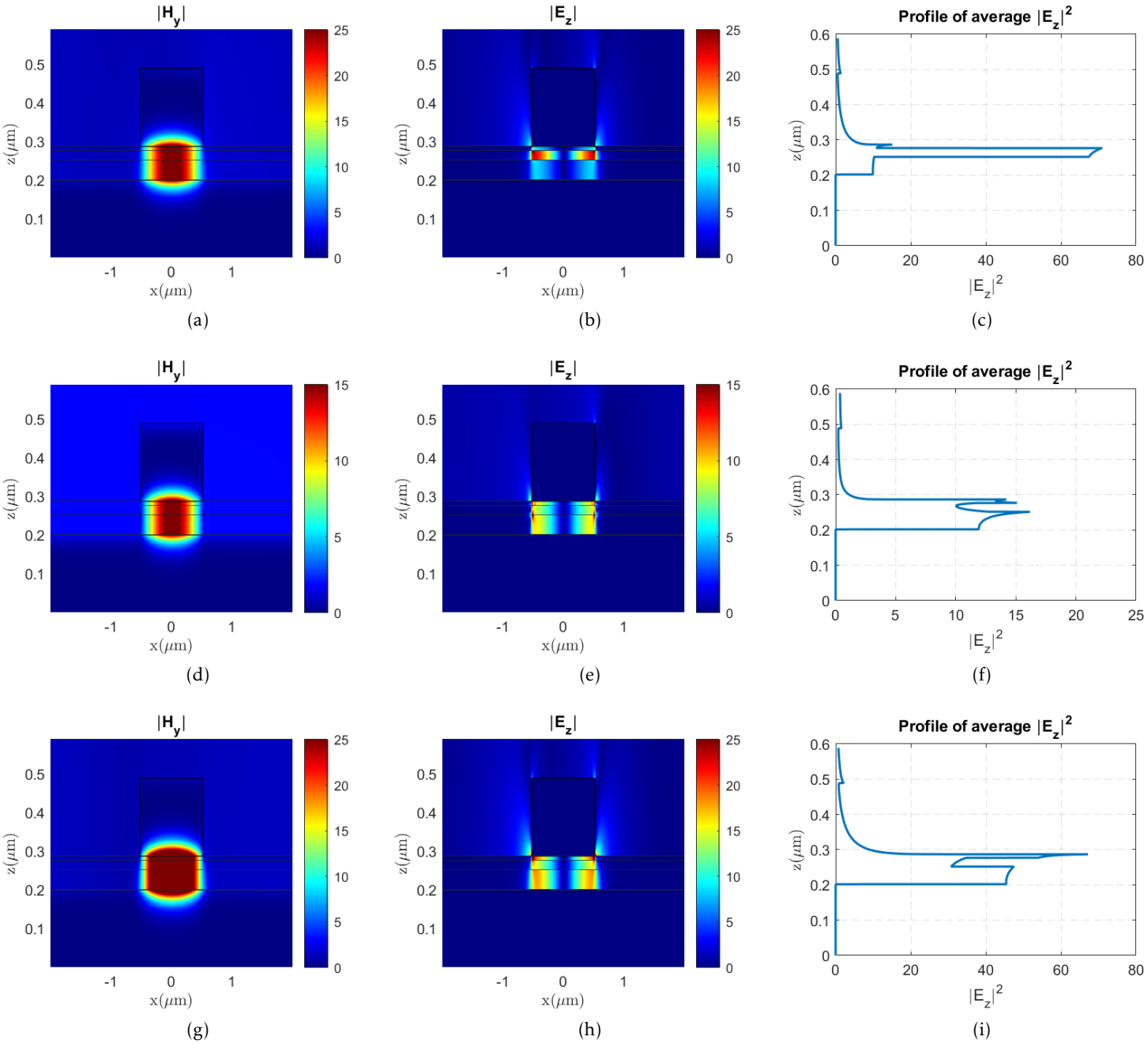

Figure 3.14 – Field distribution of the strong coupling regime and weak coupling regime. a), b), c) are computed for the peak ***(a)*** and d), e), f) for the peak ***(b)*** of the strong coupling regime. g), h), i) are computed for the peak ***(c)***. Inputs: S=1.04μm, TM polarization, incidence θ=0°, P=4μm, Ordal's Au/Ti dielectric function [99].

Material	ϵ model	Parameters	Parameters' source
Au	Drude FC	$\omega_P = 72800cm^{-1}$, $\Gamma = 215cm^{-1}$	Ordal [99]
Ti	Drude FC	$\omega_P = 20300cm^{-1}$, $\Gamma = 382cm^{-1}$	Ordal [99]
InGaAs	Drude FC Phonon Interband	$\epsilon_\infty = 11.22$ N=$1.3\times10^{19}cm^{-3}$, $\omega_P = 1108cm^{-1}$, $\Gamma = 72cm^{-1}$ N=$5\times10^{18}cm^{-3}$, $\omega_P = 783cm^{-1}$, $\Gamma = 38cm^{-1}$	Section 2.2.2 this work
InP	Drude-Lorentz phonon	ϵ_∞=9.61, ω_{LO}=$345.0cm^{-1}$, ω_{TO}=$303.7cm^{-1}$, Γ_{ph}=$3.5cm^{-1}$	Palik [28]

Table 3.1 – Dielectric functions' parameters of different materials used in ENZ-EOM Reticolo computation.

3.2.2 Electronic band structure computation

The electronic band structure of the multilayer stack was computed using 1D Poisson, a code developed by G. Snider [100]. This code solves the self-consistent Poisson-Schrödinger equation in 1D multilayer planar structure by a recursive loop. Indeed, the Poisson equation connects the potential energy to the charge distribution. This charge distribution's potential energy intervenes in the Schrödinger equation, whose solutions are the electronic wave functions. The norm of the electronic wave function is proportionnal to the electron density distribution. If the charge distribution resulting from the wave function does not match the initial charge distribution, the new distribution will be reinjected in the Poisson equation in the next step of the recursive loop. We set a convergence limit as a criteria for ending the recursive loop. When the difference between the initial charge distribution and the solution is smaller than this limit, we obtain a satisfactory approximation of the self-consistent solution to the problem [9].

We computed the electron density in the multilayer stack illustrated in Figure 3.11, made of an HEMT-like structure with 10nm InP/ 25nm InGaAs n-doped/ 50nm InP, sandwiched between Ti/Au plates. In this 1D problem, the stack is supposed to be infinite in x and y direction and thus we ignore edges' contribution. The doping concentration is set at $1.3\times10^{19}cm^{-3}$, homogeneously distributed in the QW layer. A Schottky contact with a Schottky barrier of 0.4eV is set at two metal-InP interfaces.

The solution to the Poisson-Schrödinger of the structure at zero bias is illustrated in Figures 3.15a and 3.15b. Figure 3.15a depicts the band diagram (conduction band edge E_c in blue, valence band edge E_v in orange), the Fermi level (black dashed line E_f) and the z-component of the wave functions (plotted at their eigen energy value). Five wave functions from $|\Psi_0\rangle$ to $|\Psi_4\rangle$ have their eigen energies below the Fermi level. They are electron populated states. Figure 3.15b depicts the normalized electron density distribution (green curve). The electrons seem to be distributed quite homogenously in the QW. This homogeneous distribution of the electrons justify the consideration of a homogeneous dielectric function in EM modelling of the QW, a hypothesis that we already accepted and used without discussion in the previous EM computation section.

9. The 1D-Poisson code does not treat the drift-diffusion current equation. The structure need to be in thermodynamic equilibrium.

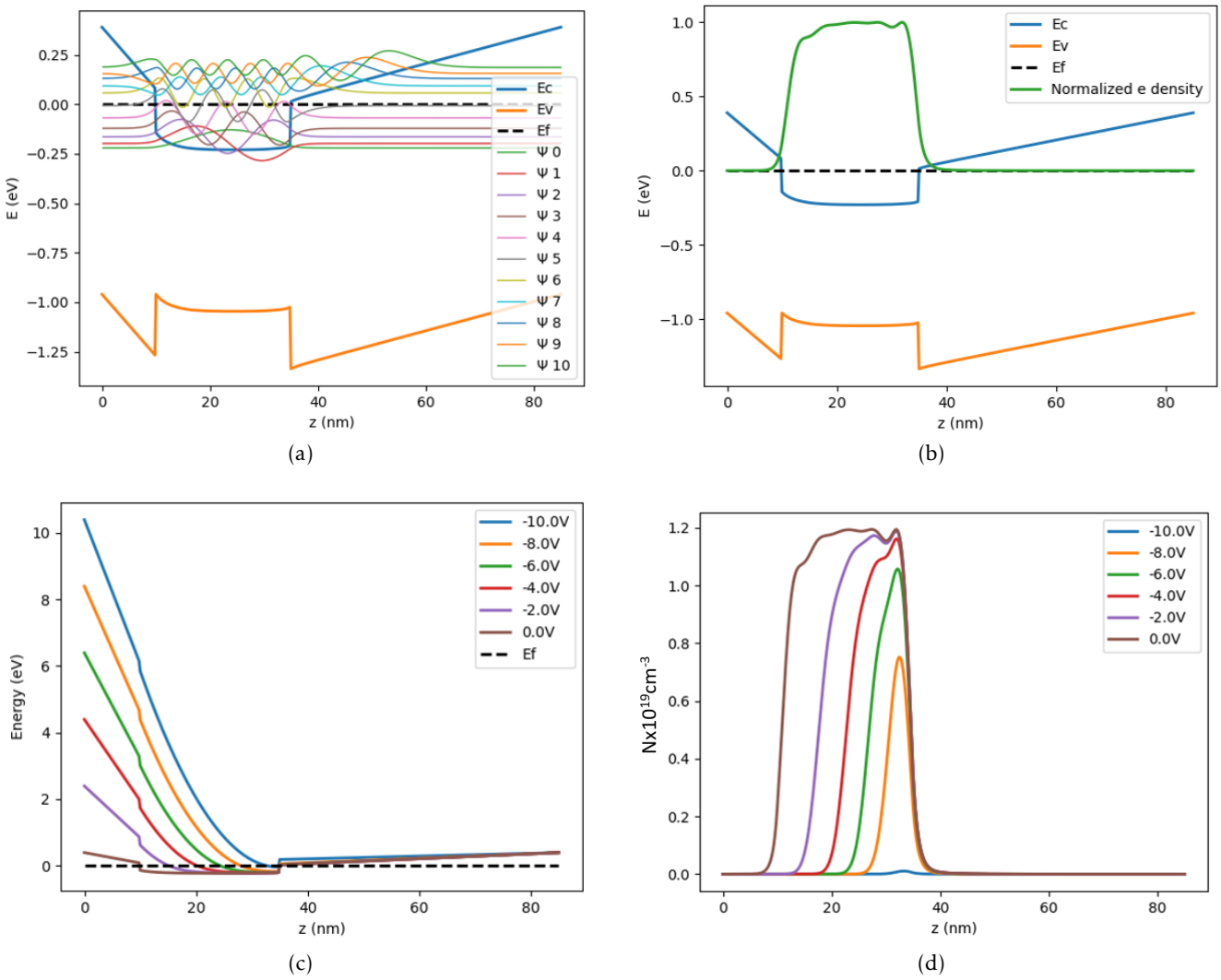

Figure 3.15 – Band diagram and electrons density of modulator structure without and with bias, as computed with 1D Poisson. a) Band diagram at zero bias. Blue and orange thick solid lines are respectively the conduction and valence band edges. A Schottky barrier of 0.4V is imposed as boundary condition. Black dashed line indicate the Fermi level in the structures. Thin solid lines Ψ_0 to Ψ_{10} correspond to the z-component of the wave functions. Ψ_0 to Ψ_4 are bound states below the Fermi level.
b) Electron density profile (green curve) in the structure at zero bias.
c) Conduction band edge at various bias values from 0V to -10V.
d) Corresponding electron density profile at various bias values from 0V to -10V. The width along the z direction of the electron gas is reduced by half at -4V bias while the maximum of the electron density stays close to $1.2{\times}10^{19} cm^{-3}$. At -6V, the width of the electron gas continues to decrease and the maximum of the the electron density also starts to decrease (in correspondence, $\omega_{ENZ} \propto \sqrt{N}$ starts to decrease). This tendency continues at more negative biases: at -8V bias, the maximum of the electron density is reduced to about $0.8{\times}10^{19} cm^{-3}$; at -10V bias, the QW can be considered as totally depleted.

Figure 3.15c illustrates the conduction band edge bending under negative bias voltage up to -10V. Figure 3.15d illustates the corresponding electron density profile under bias. Compared to the 0V bias (brown curve), a -2V bias (violet curve) induces about 1/4 of the QW width to be depleted. A -4V bias (red curve) leads to about half of the QW being depleted, and a -10V bias (blue curve) depletes completely the QW. At -6V, the width of the electron gas continues to decrease and the maximum of the the electron density also starts to decrease (in correspondence, $\omega_{ENZ} \propto \sqrt{N}$ starts to decrease). This tendency continues at more negative biases: at -8V bias, the maximum of the electron density is reduced to about $0.8\times10^{19} cm^{-3}$; at -10V bias, the QW can be considered as totally depleted. Computation with other values of thickness of the barrier indicates that the bias voltage needed for electron depletion increases when the top barrier InP gets thicker. For this reason, we chose to fix this thickness at 10nm.

The computation of the electron density under bias indicates that the electron density can be modulated by applying sufficiently strong negative bias. Together with the electromagnetic computation results, these simulations indicate that it is possible the realize electro-optical modulation with our ENZ-EOM structure. From these results, we proceeded to the experimental fabrication of the ENZ-EOM device with the following parameters: heterostructure InP top barrier 10nm, QW InGaAs n-doped at $1.3\times10^{19} cm^{-3}$ 25nm, InP bottom barrier 50nm, top grating with S=1.04μm, P=4μm.

3.3 Sample fabrication

In this section, I will describe the fabrication process of an HEMT-like ENZ-EOM device. The side view and top view of our HEMT-like ENZ-EOM structure are depicted in Figure 3.16a and 3.16b. The main active structure consists of an Au/Ti grating, the semiconductor heterostructure InP/InGaAs/InP, a Ti/Au back mirror.

Optically, the Au/Ti grating plays the role of an antenna and electrically, it plays the role of top gate electrode for bias application. The grating is made of strips with a period P=4μm and various strip's width S, on a total area of 150x150μm^2. The size of this optically active region is chosen so that it is large enough for the optical characterization and small enough to statistically avoid having defect of the semiconductor layer inside the device.

In Figure 3.16b, above and below the grating, two pads (referred to as gate pads) of 75x150μm^2 are directly connected to the grating for applying bias voltage. On the left and the right of the grating, we added two Ti/Au pads 75x150μm^2 non connected to the grating, but in contact with the QW InGaAs layer. These two pads are referred to as QW contact pads, playing the role of electron reservoirs for electron evacuation during the electron depletion step.

On one sample, we have many devices arranged into rows and columns, with strip's width S varying from 0.8 to 1.7μm by step of 100nm nominally. Each device is named individually by its row and column, e.g. 'AB' for a device in row A and column B. The semiconductor surrounding each device is removed in a mesa etching step to isolate electrically different devices.

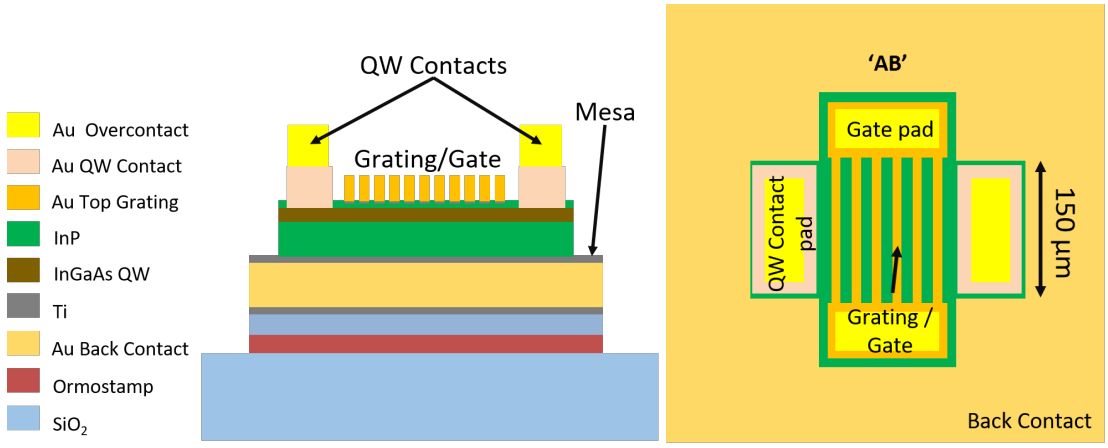

Figure 3.16 – Final structure of EOM: a) side view, b) top view. Optically, the active structure is located under the grating zone, with an area of 150x150μm^2. Electrically, the device consists of three electrical terminals: the top gate, the QW contact and the back contact.

The active semiconductor heterostructure is grown by epitaxy on InP substrate. The fabrication process consists of first realizing the back mirror, then transferring the active multilayer on a new substrate and finally performing several lithography steps to realize the devices' final structure. The main goal of the substrate transferring step here is to expose the non-metallized surface of the active multilayer (by flipping the active multilayer up-side-down and removing the substrate) in order to realize the top grating on this surface. This is an important step since it will affect other steps' choice of process and the mechanical strength of the final device.

Several techniques are usually used for the substrate transfer process at C2N: polymeric bonding (Ormostamp, BCB), gold-gold thermocompression bonding, anodic bonding.
In this work, we chose the Ormostamp polymeric bonding, developed by Andrea Cattoni of C2N. In this process, UV light is used to polymerize the Ormostamp in order to glue the active multilayer on a glass substrate without heating. Room temperature process and simplicity are the main advantages of this technique compared to other bondings. For comparison, at C2N, BCB bonding process requires about 30 minutes of heating at 300°C, under a pressure of 500N/cm^2 [86]. Anodic bonding process requires 1 hour of heating at 210°C (suggested by Christophe Dupuis, C2N). Gold-gold bonding process requires 20 minutes of heating at 320°C, under a pressure of 400N/cm^2 (suggested by Nathalie Isac, C2N). A lower temperature process was reported in Quinchard's thesis and some other references for gold-gold bonding at 200°C during about 20 minutes [75], [101]. On the other hand, gold-gold bonding is generally known for better thermal conductivity and mechanical strength compared to polymeric bonding. The risk of gold diffusion into III-V semiconductor at high temperature [75], [102] motivated our choice of the Ormostamp bonding at room temperature.

The fabrication process is further detailed in what follows (illustrated in Figures 3.17 and 3.18):

Epitaxy growth: The active multilayer was grown by MOVPE on InP substrate at III-V Lab. The growth order of the active layers is flipped so that the back surface in the final device of the active multilayer appears on top of the epitaxy.

Back mirror deposition: Deoxidation (HCl 37%/H2O 1v/9v, 1min), followed up right after

by metallization by thermal evaporation: 2nm Ti/ 400nm Au/ 20nm Ti. Ti is always deposited at a slow rate of 0.1nm/s to form a continuous layer and plays the role of adhesion layer. Au is usually deposited at 0.5-1nm/s at low pressure of about $1\times10^{-7} mbar$ in order to limit impurities and maintain optical loss of Au as low as possible. 200nm of SiO_2 (sputtering at 0.11nm/s) is added to reinforce mechanically the multilayer stack.

Substrate transfer: Low temperature Ormostamp bonding. The process is reported in Appendix B.1.

Initial substrate removal:

- Optional edge protection with wax.
- 500μm-thick InP substrate removal by wet etching in HCl 37% (etch rate about 8μm/minute). InP walls removal by cutter.
- Stop-etch layers removal: 200nm InGaAs, 20nm InP, 10nm InGaAs, using $H_3PO_4/H_2O_2/H_2O$ 9v/3v/120v (etch rate about 100nm/min) for InGaAs and HCl 37% for InP.

After these etching steps, we obtain a multilayer stacking of active layers on gold back mirror, bonded to glass substrate by Ormostamp polymer.

Lithography: The sample is patterned into EOM devices by 4 steps of UV lithography, illustrated in Figure 3.18. UV lithography was chosen instead of e-beam lithography because it is less time consuming, requires lower baking temperature and is more adapted to scale up torward industrial applications.

- **L1 Top Grating:** this is the most challenging lithography step due to small strip patterns of around 1μm to be realized on substrate transferred sample. Careful removal of all the residues of InP walls and Ormostamp. UV lithography using AZ5214E resist in negative mode, 125°C baking, with careful edge-bead removal (in AZ5214E's positive mode) in order to obtain high resolution patterns. Metalization: Ti/Au 2/200nm. Lift-off in acetone. See Appendix B.2 for more details.
- **L2 QW Contact:** Deoxidation before resist spin-coating to avoid large underetch, followed by UV lithography with AZ5214E resist in negative mode, 125°C baking. 10nm-thick top barrier InP etching by 'flash' etch in HCl 37%. Metalization: Ti/Au 5/200nm. Lift-off in acetone. See Appendix B.2 for more details.
- **L3 Overcontact:** The overcontact is needed to thicken the grating pads and the QW contact pads, so that we can put probe tips on these pads without damaging them. UV lithography with AZ5214E resist in negative mode, 125°C baking. Metalization: Au 400nm. Lift-off in acetone.
- **L4 Mesa etching:** Deoxidation before resist spin-coating to avoid large underetch, followed by UV lithography with AZ5214E resist in positive mode, 125°C baking. 1 min plasma O_2 treatment to remove resist residues for homogeneous mesa etching. Mesa etching: 4s in HCl 37%, rinsing and drying; 30s in $H_3PO_4/H_2O_2/H_2O$ 9v/3v/120v, ringsing and drying; 5s in HCl 37%, rinsing and drying.

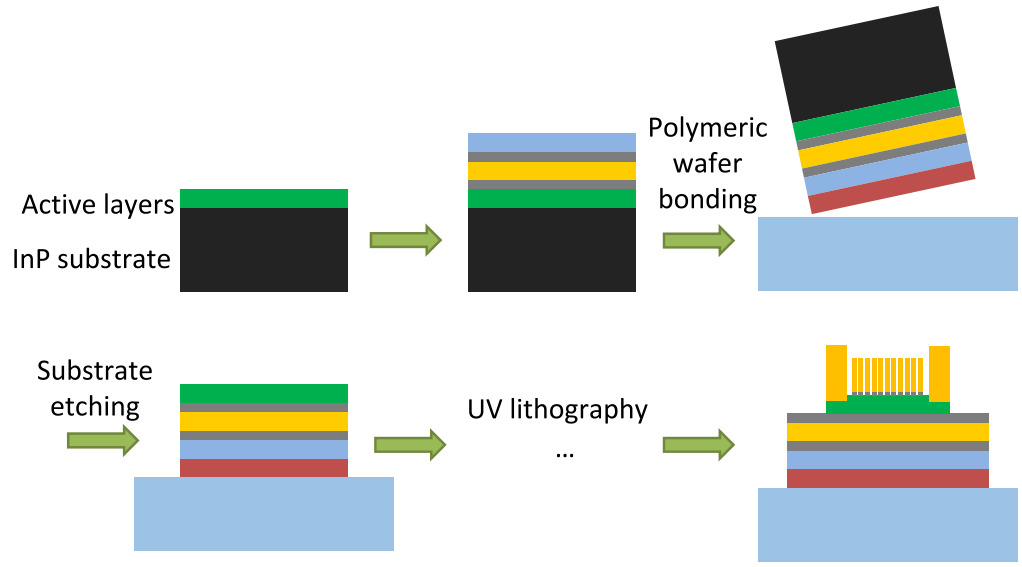

Figure 3.17 – Steps of the fabrication process.

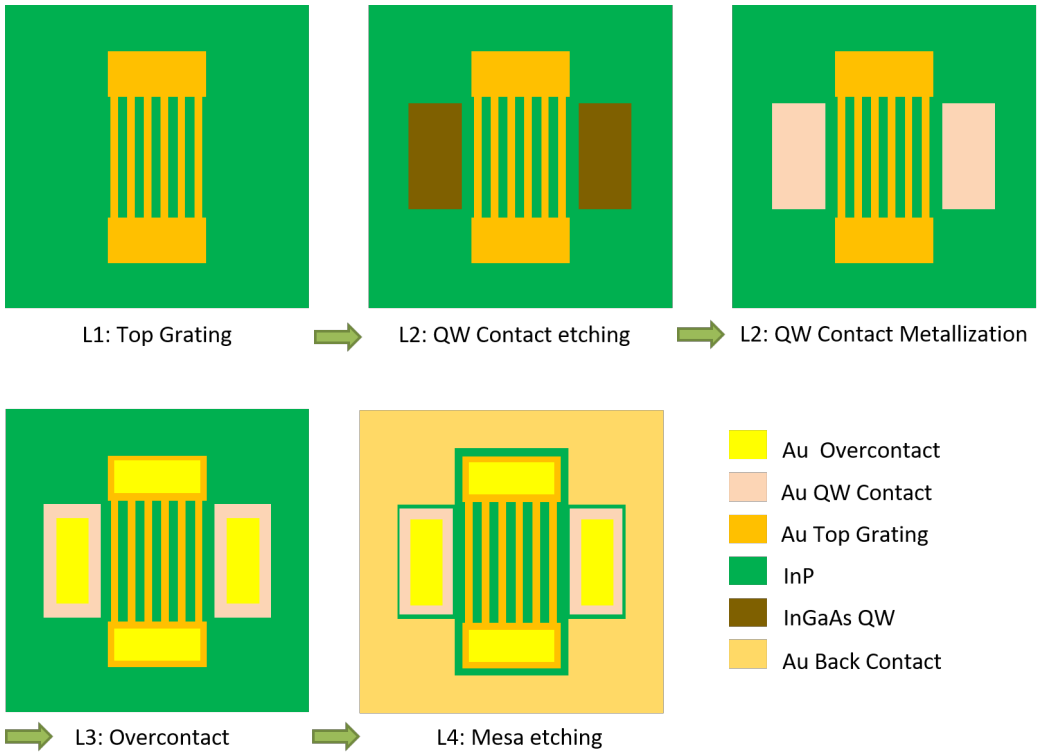

Figure 3.18 – Lithography steps:
L1 Top Grating: metallization Ti/Au 2/200nm.
L2 QW Contact: InP top barrier etching to expose InGaAs QW, metallization Ti/Au 5/200nm.
L3 Overcontact: metallization Au 400nm for thicknening of electrical pads.
L4 Mesa etching: etching down to back contact Au/Ti for devices isolation.

Figure 3.19 depicts optical and SEM images of EOM devices after fabrication process.

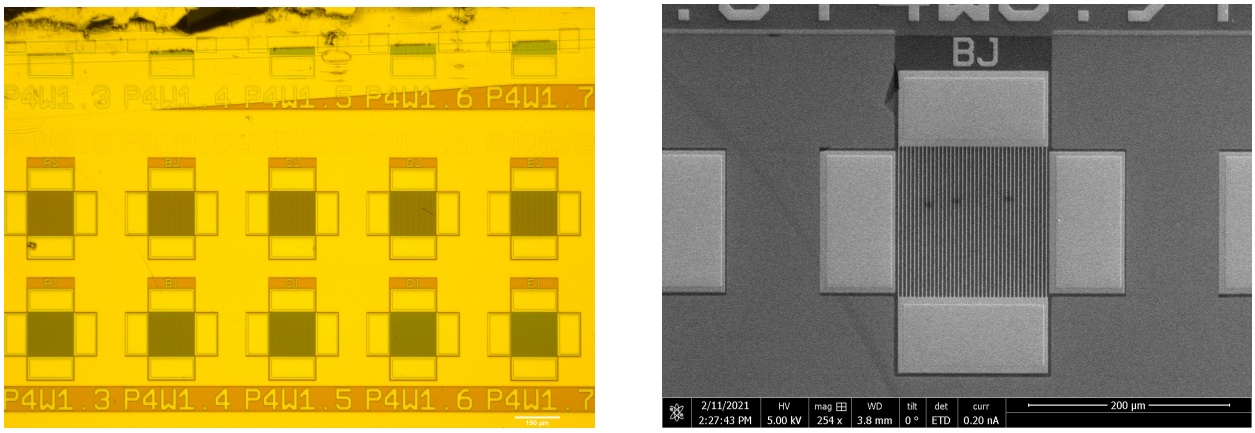

(a) (b)

Figure 3.19 – a) Optical and b) SEM images of the devices in TGB4545-6-1. a) depicts the whole array of EOM with different antenna width S, nominally varying from 0.8 to 1.7μm, incremented by 0.1μm each. b) shows the complete structure of an EOM.

3.4 Characterization results

After fabrication, ENZ-EOM devices are characterized optically by FTIR measurement to verify the positions of resonances and electrically by *I(V)* characteristics measurement to control the Schottky contact requirement. Once the devices satisfy optical and electrical requirements, I realized the optical amplitude modulation characterization by performing FTIR measurement with bias voltage.

3.4.1 HEMT-like structure

3.4.1.1 Grating's reflectance measurement by FTIR

I measured the reflectance of various HEMT-like ENZ-EOM devices without voltage bias, using a μFTIR setup as discussed in section 2.1.3. The probed zone is about 100x100μm^2 in the center of the total 150x150μm^2 surface area of each grating structure. Figure 3.20a depicts the experimental reflectance spectrum (blue solid line) of a device with experimental strip width S_{exp}=1.270μm (measured with SEM image). The spectrum is plotted together with a simulated curve realized with Reticolo (orange dashed line), using the same parameters set for dielectric functions as in the design step and with S=1.270μm. Around 9μm zone, we observe two dips (at about 8μm and 12μm on the experimental curve), corresponding to the strong coupling of the MIM mode and the ENZ mode as predicted by modelling. However, the simulated peaks are narrower in terms of linewidth and having larger amplitude. The experimental peaks splitting is smaller than simulation's estimate of about 1.5μm in wavelength.

At smaller wavelength, we also observe other absorption peaks, with two noticeable peaks at about 5.2μm and 3.3μm. These peaks appear in simulation and are shifted when S changes but not when the incidence angle changes. They correspond to the TM_{02} and TM_{03} MIM modes and can be verified with the relation 3.5: $\lambda_{0\,m_x} = \frac{2n_{eff_{M-I-M}}S}{m_x}$, where $n_{eff_{M-I-M}} \sim 3.9$. The mode TM_{02}

is forbidden at normal incidence but here is excited (with weak amplitude) due to non normal incidence in μFTIR measurement (incidences 12-24°). In the simulated orange line, we also observe a sharp peak around the TM_{02} mode. This peak is shifted when the incidence angle change, as illustrated in Figure 3.20b with dashed yellow and orange lines respectivly computed at incidence 18° and 20°. It corresponds to a diffraction mode of the grating, appearing as a sharp feature in simulation with a single incidence angle. Experimentally, this diffraction mode appears larger in linewidth and weaker in amplitude (thus difficult to distinguish) due to the integration of all incidence angles in the range of 12-24°.

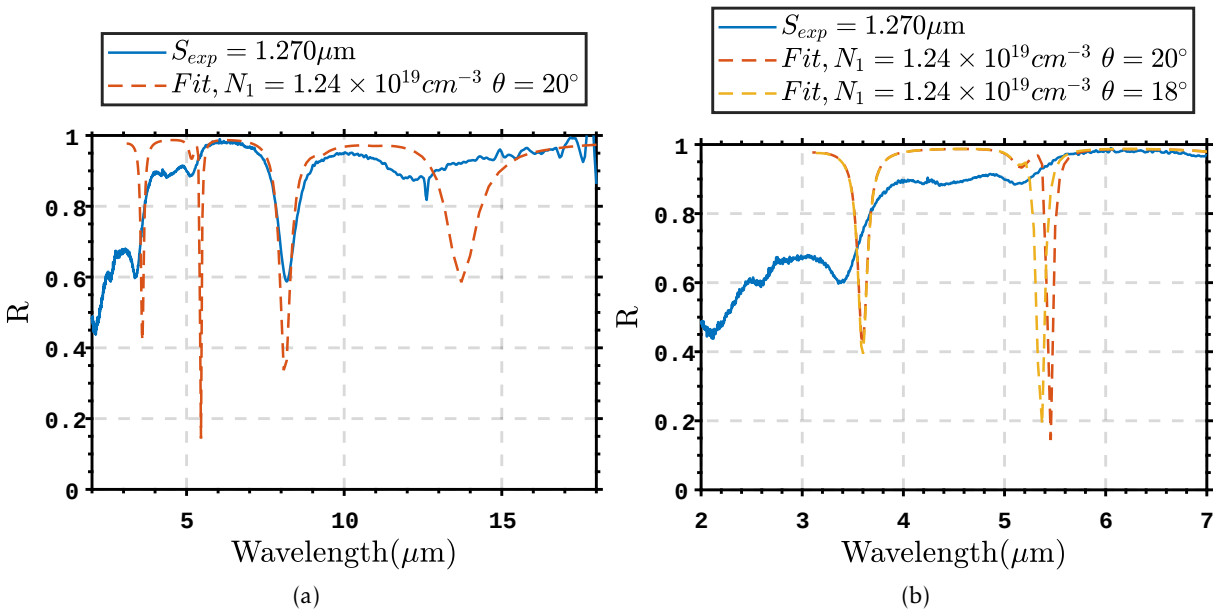

Figure 3.20 – μFTIR reflectance measurement at zero bias. a) Experimental reflectance of a device with S_{exp} = 1.270μm (blue solid line) and simulated curve by Reticolo (orange dashed line) with S_{exp} = 1.270μm and Au/Ti's dielectric function of Ordal. Two coupled modes of the MIM and ENZ coupling are observed around 8μm and 12μm. b) Zoom at the small wavelength range of the figure a) and a simulated curve at an incidence angle of 18° is added (yellow dashed line). We observe two MIM modes TM_{02} and TM_{03} around 5.2μm and 3.3μm respectively. A sharp angular-dependent feature is observed in simulation but does not appear clearly experimentally (due to a large range of incidence angles). This feature corresponds to a diffraction mode of the grating.

Figure 3.21 depicts the reflectance of devices with different strip width S on the same sample TGB4545-6-1. From the blue curve to the gray curve, the nominal strip's width S increases from 0.8 to 1.5μm by step of 0.1μm. The baseline of each of these reflectance curves are shifted by 0.1 each time to ensure visibility and to observe the peak shifts. With the variation of the metallic strip's width around 1μm, the MIM resonance alone varies around 9μm (not shown, from simulation and experimentally verified with test samples). In the presence of an ENZ mode at 9μm, the two mode couple together. Anti-crossing is observed in Figure 3.21, illustrated by two dashed-dotted black lines to guide the eyes. Rabi splitting in this case is larger than the sum of damping factors of two constituent resonances. This is a signature of the strong coupling regime.

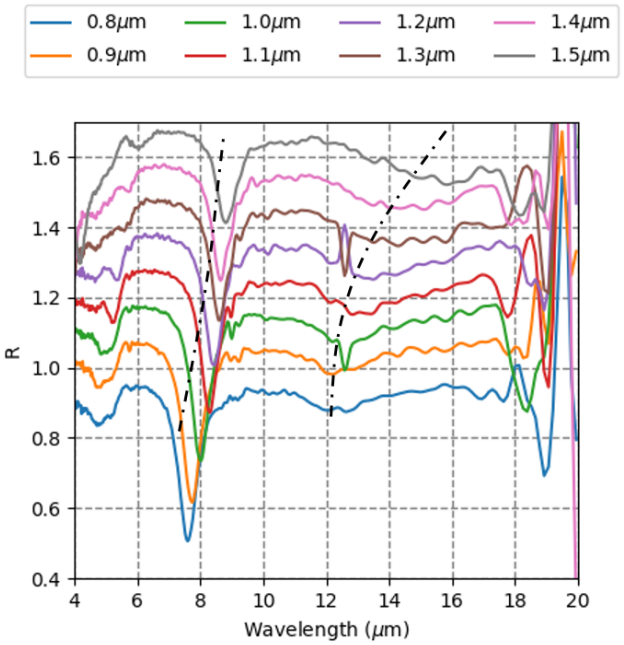

Figure 3.21 – μFTIR reflectance measurement at zero bias. Reflectance of devices with various strip width S (nominal values), increasing from 0.8 to 1.5μm by step of 0.1μm, on sample TGB4545-6-1. R values are offset for clarity. Anti-crossing of MIM mode and ENZ mode is observed. Two dashed-dotted black lines are added, connecting the peak positions, to guide the eyes.

3.4.1.2 Electrical characterization of contacts

As illustrated in Figure 3.16a, electrically, our HEMT-like ENZ-EOM device consists of three terminals: gate (Ti/Au grating deposited on InP top barrier), QW contact (Ti/Au pad deposited on InGaAs QW), back contact (Ti/Au deposited under InP bottom barrier). We expect a Schottky contact behavior for Ti/Au deposited on InP and ohmic contact behavior for Ti/Au deposited on doped InGaAs. I realized the current-voltage *I(V)* characterizations to control the Schottky contacts. The measurements are performed using 4-wires setup on a probe station at C2N.

Figure 3.22a depicts two *I(V)* characteristics of the device DJ on sample TGB4545-6-1. The blue dotted curve is measured between back contact level (+) and the QW contact level (-). At positive bias, the current *I* increases exponentially, reaching about 4mA at +0.1V bias. This is also observable by a linear branch at positive voltage in Figure 3.22b - having the same curves plotted in semi-log scale on the current axis. On the negative bias side, the blue curve shows a much slower increase of the current norm with negative bias, reaching 4mA at about -1.75V. This behavior is in agreement with a Schottky contact having a leaky tail at negative bias. The blue curve also shows a measurement artifact with a constant plateau at bias smaller than -1.75V, due to the compliance limit imposed to the measurement.

The orange dotted curve is measured between gate level (+) and the QW contact level (-). In contrast with the blue curve, the orange curve is linear in Figure 3.22a. This indicates an ohmic behavior, with a resistance R$\sim$ 31Ω, instead of a Schottky diode behavior. The gate level and the InGaAs QW are short-circuited. The ohmic behavior between gate and QW contact levels is found in all samples with HEMT-like structure described in section 3.2.

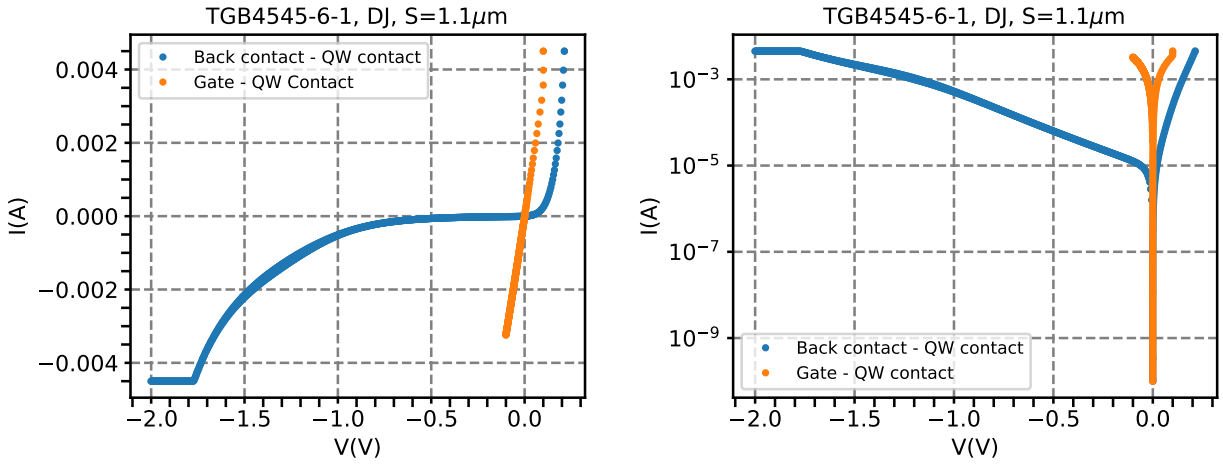

(a) (b)

Figure 3.22 – *I(V)* characteristic of HEMT-like EOM. *I(V)* Back contact - QW contact (blue line) shows a Schottky diode behavior whereas *I(V)* Gate - QW Contact (orange line) shows an Ohmic behavior. a) Linear scale plot, b) Semilog scale plot of the same data.

Figure 3.23 depicts the *I(V)* characteristic between QW contact and back contact levels of an HEMT-like structure. By fitting the forward bias branch with the *J(V)* diode model from references [103,104] [10], I found a Schottky barrier Φ_B of about 0.4eV (by averaging over many devices' fitting result) and a factor of non-ideality n∼1.5. This value of Schottky barrier is a bit smaller than the value reported in reference [103] of about 0.5V. The value of Φ_B=0.4V was reinjected in the initial *1D Poisson* computation to compute the electron density distibution in our structure.

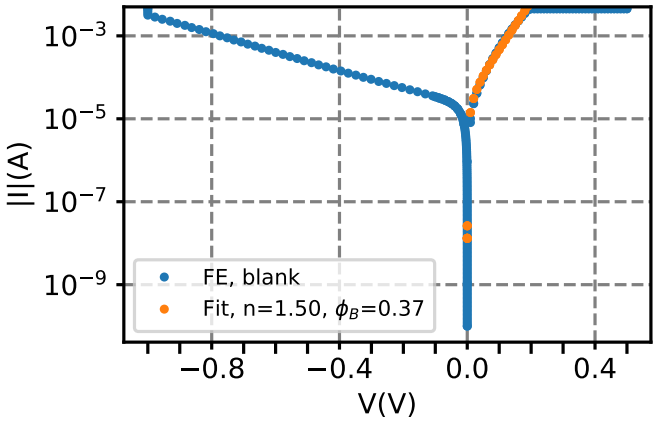

Figure 3.23 – Diode model fitting of TGB4545-5-1 FE

10. $J = A^{\star\star}T^2 exp(e\frac{-e\Phi_B}{nk_BT})\left[exp\left(\frac{eV}{nk_BT}\right)-1\right]$, where Φ_B is the Schottky barrier's energy, $A^{\star\star}$ is the Richardson constant, n is a non-ideality factor, e, V, T, k_B are usual quantities respectively standing for elementary charge, the applied voltage, the temperature and the Boltzmann's constant.

3.4.1.3 Hall effect characterization

I realized Van der Pauw - Hall effect measurement of a Van der Pauw cross with Ti/Au gate on top. The semiconductor heterostructure under the gate pad is InP/InGaAs/InP while the four Van der Pauw contacts are deposited on the InGaAs QW. We observed a non-linear characteristic of R_{13-24} as a function of the magnetic field amplitude B, different from the curve presented in Figure 2.17 of chapter 2. This is another indication that the InP top barrier does not correctly isolate the metallic gate from the QW electron gas.

3.4.1.4 Verification of InP top barrier thickness by AFM measurement and SEM imaging

I(V) resistance measurement and Hall effect measurement indicate that the InP top barrier is not working properly as expected. One possible explanation is that the InP top barrier is thinner than expected, due to overetch during the removal of the 10nm-thick InGaAs etch-stop layer just above the InP top barrier. I want to make sure that the 10nm-thick InP top barrier is not etched away during the process.

For this goal, I prepared a substrate-transferred sample named TGB4545-5-2 with multiple steps obtained from consecutive lithography-etching following the same etching time as with the main ENZ-EOM devices. Figure 3.24a depicts optical image of the sample TGB4545-5-2 with multiple steps. Within this range of thickness around 100nm of semiconductor on gold substrate, the sample color is highly dependent on the thickness. A change of several nm in thickness is perceptible by color change due to thin film interference. The right side of the Figure 3.24a depicts steps between InP etch stop (dark green) - InGaAs etch stop (orange) - InP top barrier (orange-yellow) - InGaAs QW (yellow) - InP bottom barrier (light green). On the left side of the sample, I etched the sample 5s more in InGaAs etchant while protecting the right side with photoresist, in order to observe overetch consequence on InP. On InP zones, we observe almost no change in color, indicating that the InP is hardly etched during 5s in InGaAs etchant. The total etching time of the 10nm-thick InGaAs etch-stop layer is 10s, so the effect of overetching on InP top barrier is likely negligeable.

This is confirmed with AFM measurement of the step formed in the InP top barrier - InGaAs QW, as shown in Figure 3.24b. From the AFM scanning map, the experimental thickness of the InP top barrier is estimated to about 8.9-9.5nm. AFM measurements of other steps confirm the thickness of different layers staying close to the nominal values: InP etch-stop 19.9nm, InGaAs etch-stop 9.4-10.3nm, InGaAs QW 25.8 - 26.4nm, InP bottom barrier 39.0-39.2nm [11]. AFM measurement between InP zones on the right side and on the left side (with a further 5s etching in InGaAs etchant) does not show a thickness difference larger than the sample roughness of about 1nm. The etch rate of InP in $H_3PO_4/H_2O_2/H_2O$ 9v/3v/120v is therefore smaller than 12nm/minute. Compared to the etch rate 100nm/minute of InGaAs in the same solution, the etching selectivity ratio InGaAs/InP is larger than 8.3.

11. The last layer InP bottom barrier is the only one showing a significant difference of about 10nm compared to the nominal thickness (50nm). This can be an actifact since we measures a step between InP-gold which do not have the same mechanical hardness.

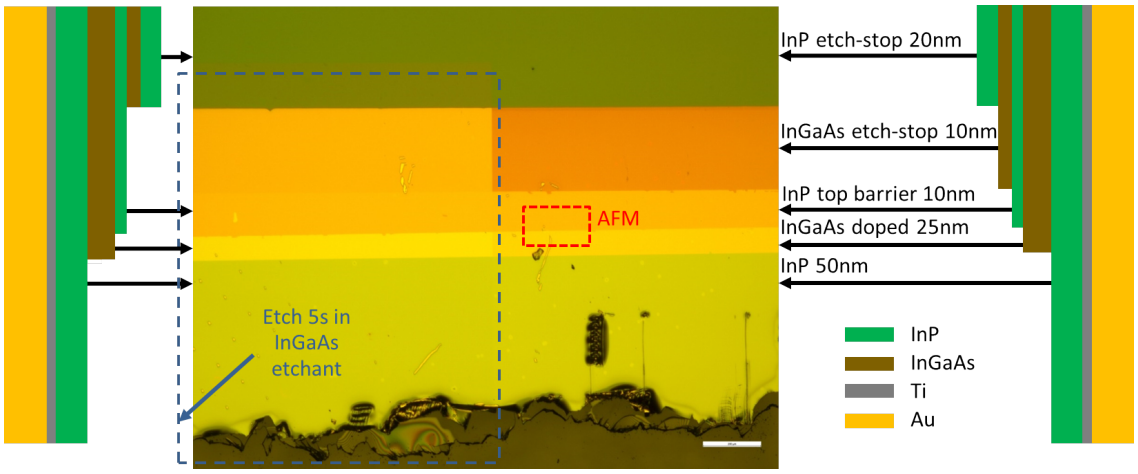

(a)

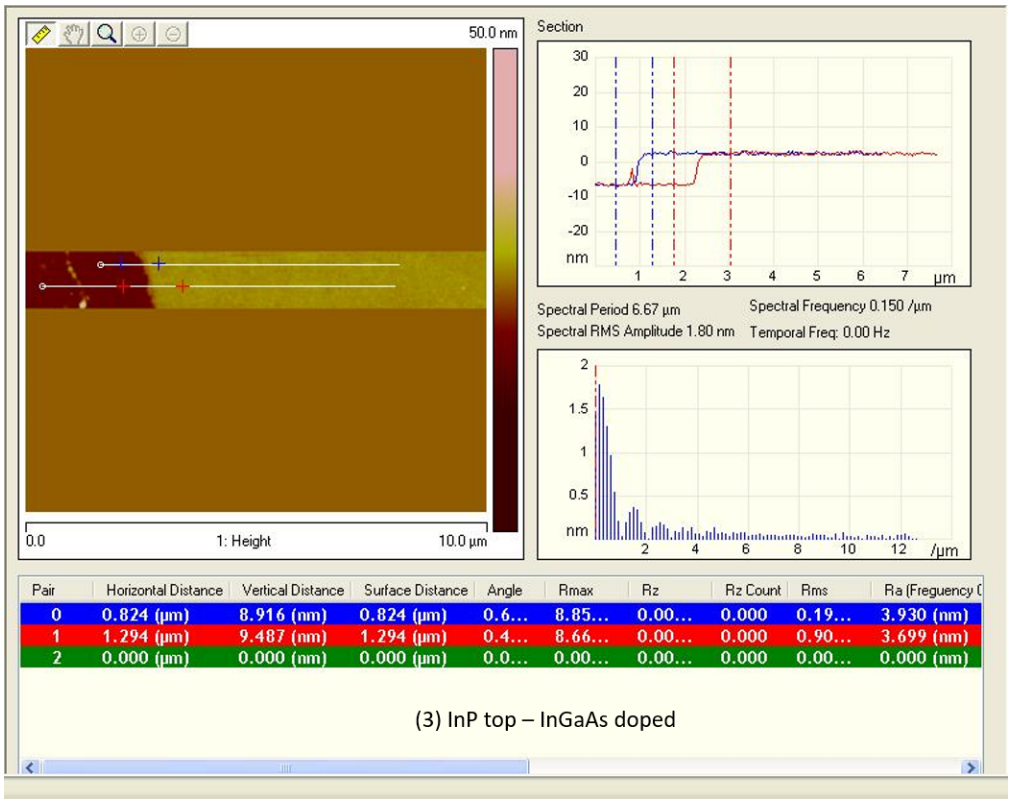

(b)

Figure 3.24 – a) Optical image of a multi-steps sample for AFM thickness measurements. The etching of steps are illustrated with the two schmematics on the right and the left of the image. Each step has a different color due to thin film interference and having small change in thickness of the steps. The zone for the AFM scan in b) is illustrated in red dashed rectangle, marking the InP top barrier - InGaAs QW step. b) AFM measurement of InP top barrier - InGaAs QW step, indicating a thickness of 8.9-9.5μm of the InP top barrier layer.

In parallel, I realized a second estimation of the InP top barrier thickness by SEM imaging. Bare TGB4545 substrate is cleaved right before the SEM observation. The edge of this freshly cleaved

piece of substrate is imaged by tilting the sample holder appropriately. Figure 3.25 depicts SEM images of two regions on the edge of the TGB4545 substrate. The contrast between InP (lighter zones) and InGaAs (darker zones) is enough to distinguish them. The high stability and good signal level of the SEM (*Magellan* at C2N) allowed us to image very thin layers. In bare substrate (prior to substrate transferring step), InP bottom barrier appears on top, following by the InGaAs QW, then InP top barrier,... We found consistent values of thickness of different layers compared to the AFM measurements [12]. The InP top barrier thickness is estimated to be 8.5-9.6nm.

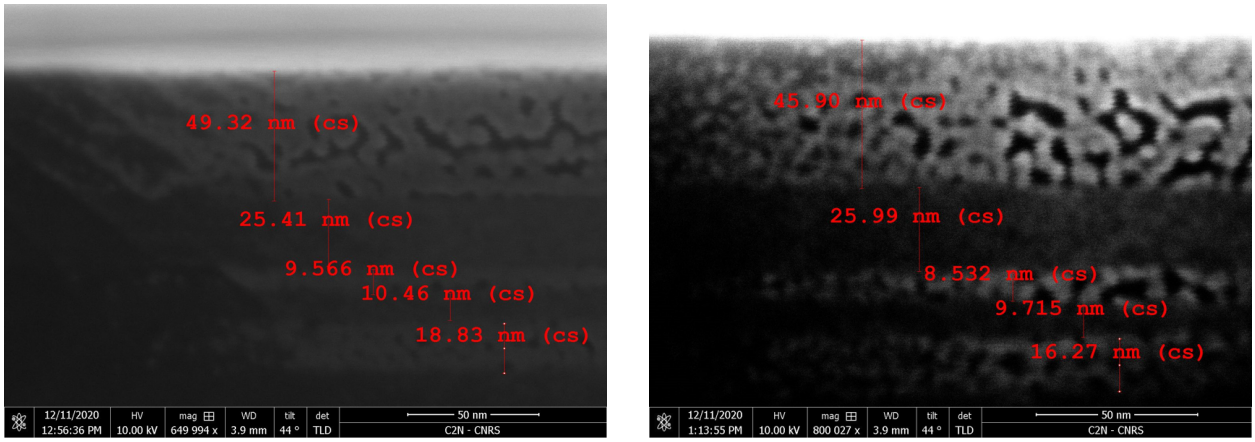

(a) (b)

Figure 3.25 – SEM images of TGB4545's egde. Different layers of the active structure are distinguishable and their thicknesses are measured.

From the AFM and SEM characterizations, we confirm that the InP top barrier is still present and is about 9nm thick. However, the lack of a good insulation barrier between the top gate and the InGaAs QW shown in electrical characterizations is detrimental to the electron depletion in HEMT-like ENZ-EOM. The 10nm InP top barrier seems not to be thick enough to effectively block the current. Therefore, we decided to realize a MOSFET-like ENZ-EOM structure, by inserting an SiO_2 insulator layer between the top metallic grating and the InP top barrier. The following section is dedicated to study MOSFET-like ENZ-EOM structure.

3.4.2 MOSFET-like structure

To realize the MOSFET-like ENZ-EOM structure, we first need to choose the insulator material. Popular choices for insulators are SiO_2, Al_2O_3, HfO_2. However they all have optical phonons in the mid IR range, which can strongly pertrubate the optical response of the ENZ-EOM as compared to the HEMT-like structure. Alternative insulators like YF_3, Y_2O_3 are found in the literature [105, 106]. They do not have optical phonon around 9μm and are relatively transparent in this range. However, they are not readily available at C2N and their physico-chemical properties as well as their use in III-V devices fabrication process are poorly known.

SiO_2 is the most studied and is readily available in C2N lab for thin layer deposition by either sputtering or Atomic Layer Deposition (ALD). Our EM computation of the ENZ-EOM in the

12. InP bottom barrier thickness is about 45.9-49.3nm, larger than the AFM measurement and closer to nominal thickness.

MOSFET-like configuration presented here below indicates that the presence of a very thin layer of SiO_2 will not significantly spoil the optical modulation mechanism of our ENZ-EOM. Therefore, we decided to use SiO_2 as the insulator.

3.4.2.1 Electromagnetic modeling of MOSFET-like ENZ-EOM

First, we want to compute the optical response of the MOSFET-like ENZ-EOM, where a thin layer of SiO_2 is added under the metallic gate, keeping all other thicknesses the same as in the HEMT-like structure. The dielectric function of amorphous SiO_2 comes from reference [68], in which multiple gaussian lineshape oscillators are used to describe ϵ_{SiO_2}.

Figure 3.26 illustrates the reflectance maps and modulation amplitude maps of the MOSFET-like ENZ-EOM. The reflectances are computed at 9μm and normal incidence. The vertical axis depicts the metallic width whereas the horizontal axis depicts the thickness of the SiO_2 layer, varying from 0 to 10nm. This Figure is similar to previous reflectance maps in Figure 3.12 (HEMT-like structure) but here I keep the semiconductor thickness L_{total} equal to the nominal thickness of the TGB4545 substrate. The full electron population state N=1.3×$10^{19} cm^{-3}$ is highly reflective, independently of L_{SiO_2}, as illustrated in Figure 3.26a. In the cases of partial and total depletion states (Figures 3.26b and 3.26c), we observe two reflectance dips for the strip's width S around 1 and 3.5μm, similarly to the HEMT-like structure. However, as the SiO_2 thickness increases from 0 to 10nm, the reflectance dips are no longer as deep as without SiO_2. For L_{SiO_2}=5nm and S around 1μm, the reflectance dips are about 0.5. The modulation amplitude in this case is about 0.5 for both partial and total depletion, instead of about 0.9 in HEMT-like structure, as illustrated in Figures 3.26d and 3.26e.

We decided to choose the thickness of SiO_2 layer L_{SiO_2}=5nm, as a compromise between being thin enough for a reasonable theoretical modulation amplitude and being thick enough for electrical insulation (as will be shown in preliminary test). Figure 3.28 depicts the spectral response of the MOSFET-like ENZ-EOM. We observe at least three absorption peaks instead of two as it was the case of a strong coupling scheme between the MIM cavity mode and the ENZ mode in InGaAs layer. Indeed, the thin SiO_2 layer also has the dielectric function reaching ENZ regime due to optical phonon at around 8μm. Therefore, in the MOSFET-like ENZ-EOM structrure, we are dealing with three coupled modes.

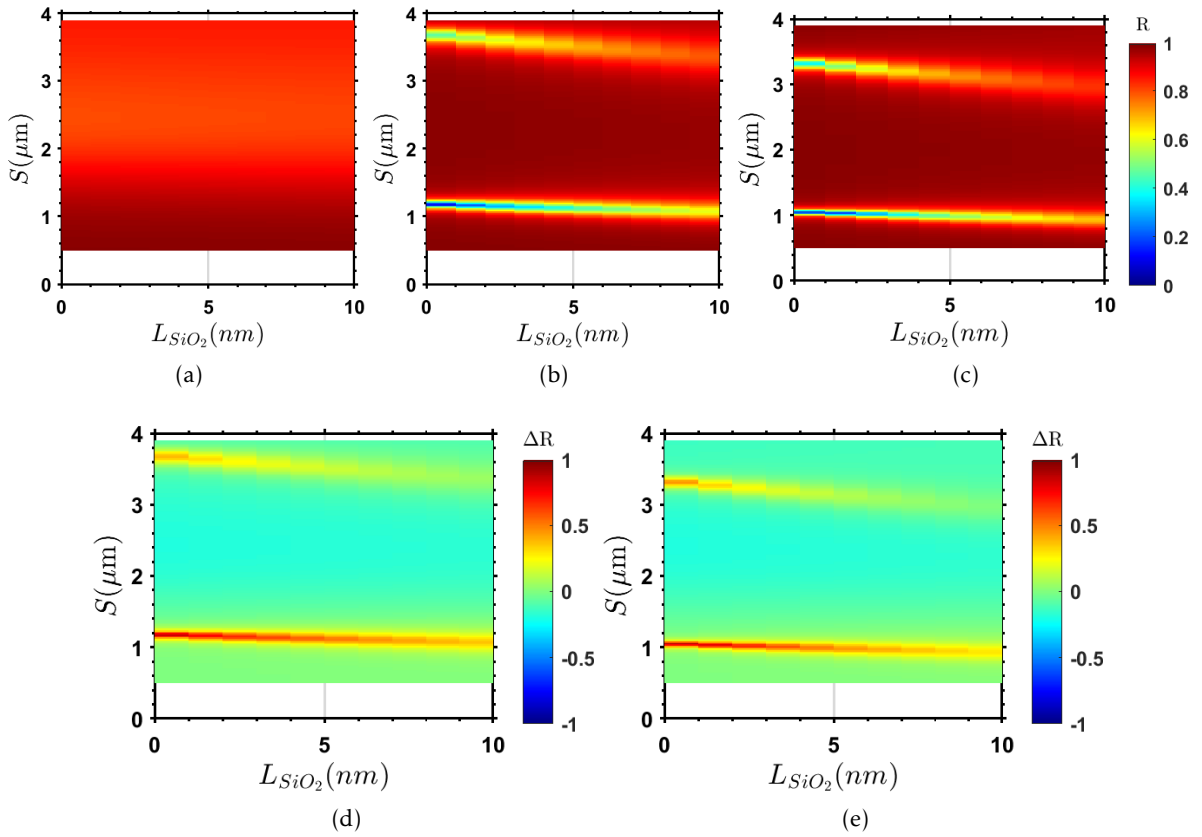

Figure 3.26 – a, b, c) Reflectance map of MOSFET-like ENZ-EOM structure at different electron concentrations, normal incidence: a) N=1.3×10$^{19}cm^{-3}$, b) N=5×10$^{18}cm^{-3}$, c) N=0cm^{-3}. a, b, c) share the same color scale. d, e) Modulation amplitude maps between the strong coupling regime N=1.3×10$^{19}cm^{-3}$ and two depletion regimes N=5×10$^{18}cm^{-3}$ in d) and N=0cm^{-3} in e).

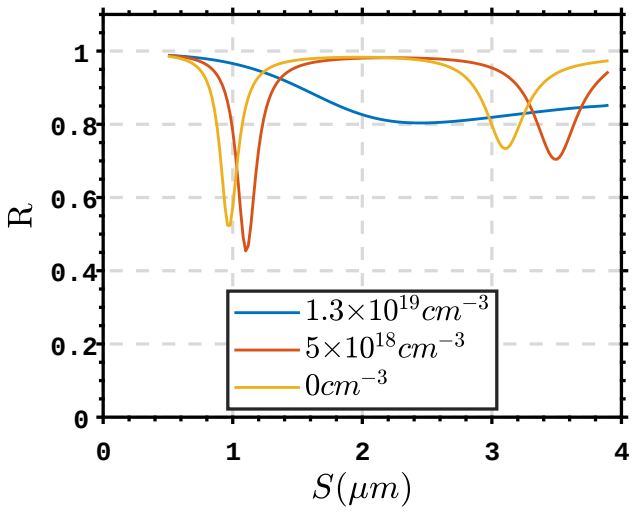

Figure 3.27 – Reflectance of ENZ-EOM MOSFET-like with 5nm of SiO_2, as a function of metallic strip's width, computed at 9μm.

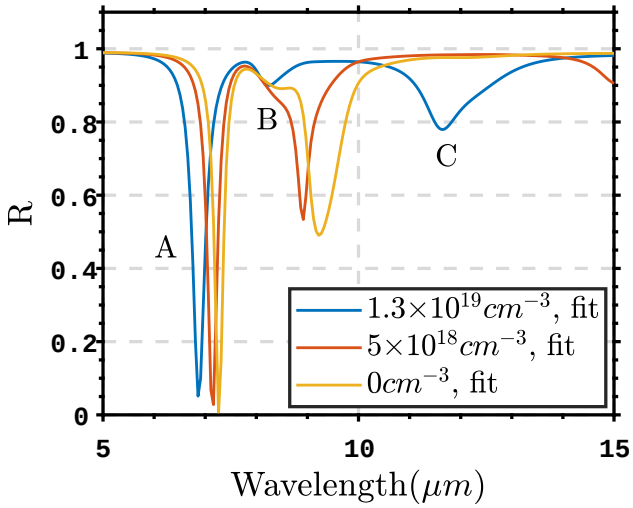

Figure 3.28 – Reflectance spectra of MOSFET-like ENZ-EOM at different electron concentrations, S=1.04μm.

The field distribution of $|E_z|$ is computed at three absorption peaks of the optimized structure. These three mode profiles are depicteded in Figure 3.29. The mode A at 7.50μm in a) is mostly located in SiO_2 layer with an enhacement of $|E_z|$ up to about 70 locally. The mode B at 8.76μm is mostly located in the two ENZ layers: SiO_2 and InGaAs QW. The mode C at 11.5μm spreads between the two ENZ layers and a vertical MIM mode profile in the cavity.

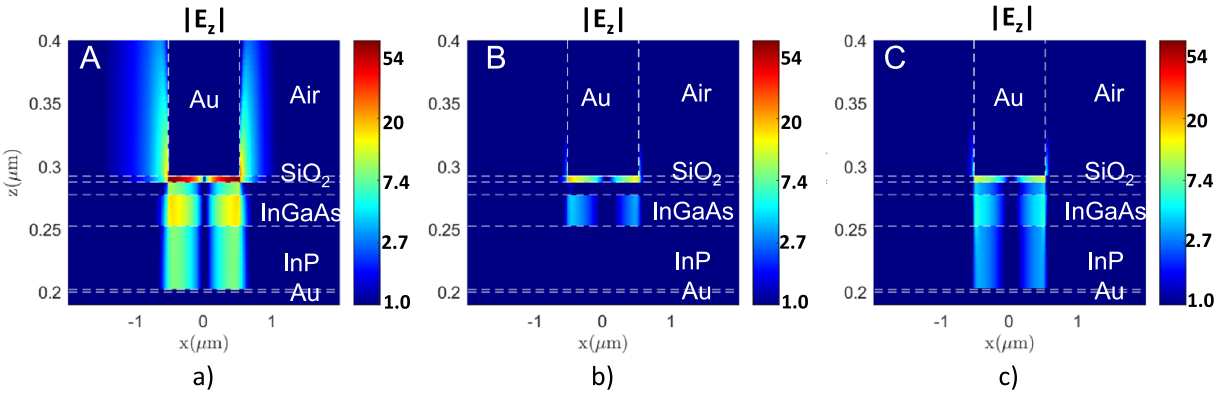

Figure 3.29 – $|E_z|$ distribution in the MOSFET-like structure at N=1.3×10$^{19}cm^{-3}$, S=1.04μm, computed at various wavelengths corresponding to absorption modes: a) 7.50μm (A), b) 8.76μm (B), c) 11.5μm (C). The colorscales are represented in logscale. The mode at 7.50μm in a) is mostly located in SiO_2 layer with an enhacement of $|E_z|$ up to about 70 locally. The mode at 8.76μm is mostly located in the two ENZ layers: SiO_2 and InGaAs QW. The mode at 11.5μm spreads between the two ENZ layers and a MIM mode profile in the cavity.

3.4.2.2 Preliminary tests of SiO_2 electrical and optical properties

The next step was to verify if a thin layer of 5nm of SiO2 is enough as electrical insulator when strong bias voltage is applied on our structure. For this purpose, I realized the sample H7739-3-1-1 with similar structure to the MOSFET-like ENZ-EOM, but the semiconductor heterostructure

is replaced with only one layer of 100nm of InGaAs n-doped at about N$\sim 1\times10^{19}cm^{-3}$. 5nm of SiO_2 (sputtering) is deposited during the grating deposition step, prior to Ti/Au metallization. A control sample (H7739-3-2) was realized together with H7739-3-1-1, having similar structure without the SiO_2 layer.

Figure 3.30 illustrates the *I(V)* characteristics between the top gate level and either the back contact level (blue dotted curve) or the QW contact level (orange dot). The *I(V)* characteristics are realized in cyclic diode-mode, in which we start at 0V, measure V(I) for positive bias, *I(V)* for negative bias and finish by returning to 0V. Compared to Figure 3.22b, the current *I* here is at least 4 order of magnitude smaller under comparable voltage bias *V*. The interface between InGaAs n-doped and Ti/Au back contact behaves like an ohmic contact, thus electrical insulation in this case is mainly due to the SiO_2 layer. At about -2V for the blue curve and -1.2V for the orange one, we observe an irreversible electrical breakdown of the structure, where the induced current *I* increases quickly and reaches the compliance limit. When the negative bias is reduced towards 0V, *I(V)* does not follow the previous path (irreversibility).

This preliminary electrical characterization indicates that 5nm of sputtered SiO_2 alone already blocks significantly the current. However, the bias voltage is limited by the breakdown of the material. Sputtered SiO_2 is known for being 'porous', less dense than other types of SiO_2 prepared by Atomic Layer Deposition (ALD) or thermal SiO_2. On the other hand, sputtering has the advantage of being a low temperature process (without heating) compared to ALD where the sample is heated during the growth. ALD deposition of SiO_2 is available at C2N. The lowest growth temperature is 150° (1 hour for 5nm), compatible with the sample fabrication process. Therefore, ALD SiO_2 is chosen for the next step of MOSFET-like ENZ-EOM fabrication.

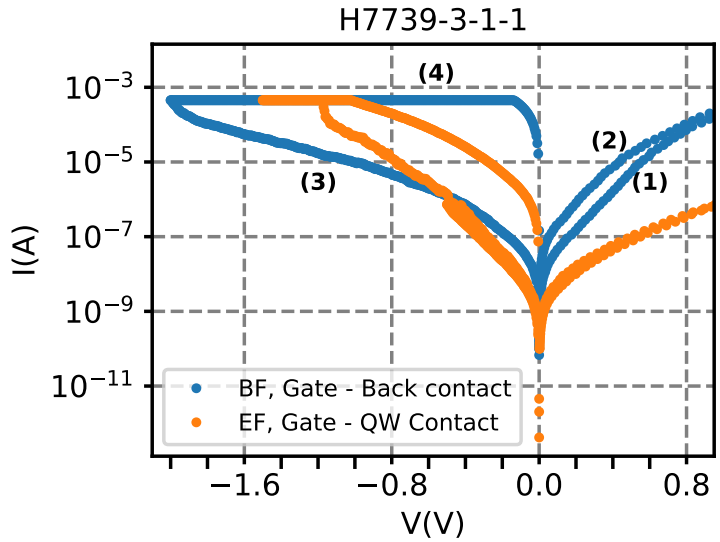

Figure 3.30 – *I(V)* characteristics of H7739-3-1-1 with 5nm of SiO_2 sputtering as insulator. Foward *V(I)* scan starts at I=10^{-10}A. The order of the scan is indicated by numbers (1), (2), (3), (4) for the blue curve.

The sample H7739-3-1-1 (with 5nm of sputtered SiO_2) and the control sampe (without SiO_2) are also characterized in μFTIR, as reported in Figures 3.31b and 3.31a. On the control sample, I measured the reflectances of a set of tens devices with nominal strip's width *S* increasing from

0.8 to 1.7μm by step of 0.1μm. Only the MIM mode resonance is observed as illustrated in Figure 3.31a. The MIM mode resonance moves towards larger wavelengths with increasing S (though, the experimental value of strip width S does not follow exactly the nominal value, due to limitation of the lithography process for small patterns). In Figure 3.21, we observe clearly a system of two absorption peaks around 8μm in Figure 3.31b, corresponding to the strong coupling between the MIM cavity mode and the ENZ mode in SiO_2 layer. This ENZ mode of SiO_2 lies at about 8μm experimentally, observable when the MIM is far from the ENZ mode.

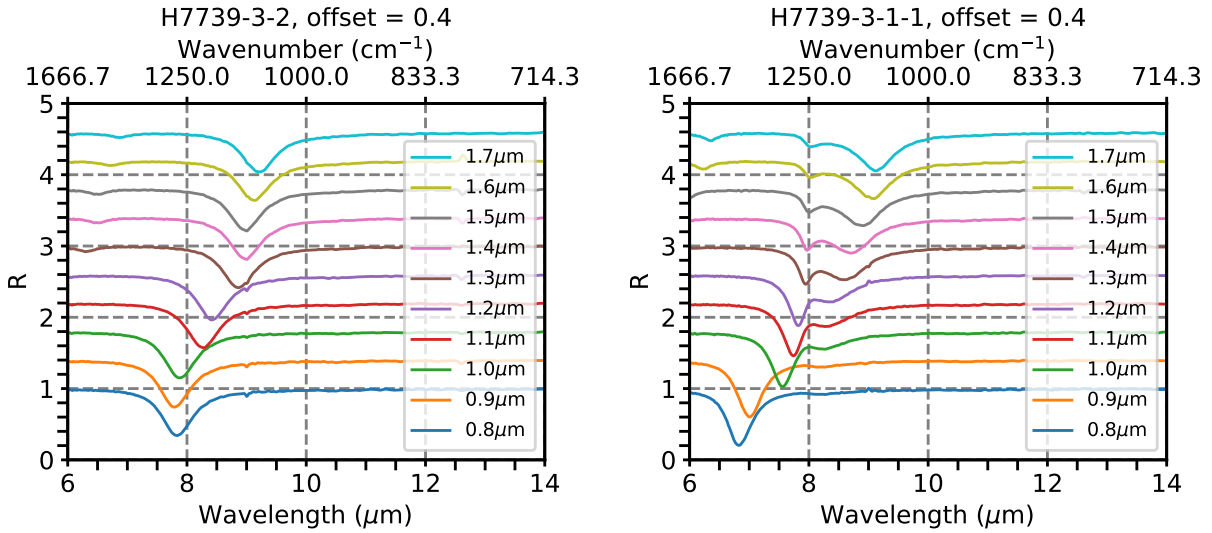

(a) (b)

Figure 3.31 – Reflectance spectra of devices with various nominal value of S on a control sample (without SiO_2) in a) and H7739-3-1-1 sample (with 5nm sputtered SiO_2) in b). a) MIM mode absorption is observed in the range 7.5-9μm, with resonance wavelength moving toward larger frequency when S_{exp} increases. Experimental value of S does not increase linearly like nominal values due to fabrication limitation. b) Reflectance spectra of devices with various nominal value of S on H7739-3-1-1 sample, strong coupling of MIM cavity mode and SiO_2 phonon ENZ mode is observed around 8μm.

Figure 3.32a reports the fitting of reflectance spectra of H7739-3-1-1, in order to determine resonance frequencies and linewidths of two coupled mode. A simple sum of two lorentzians does not describe well the absorption of the two coupled modes. We used a model with a product of Lorentzian lineshapes, analogous to multiple-phonon dielectric function model, referred to in equation 2.6. From least square fitting, we obtained values of the parameter set: 'ω_{L1}', 'ω_{T1}', 'ω_{L2}', 'ω_{T2}' for resonance frequencies and 'Γ_{L1}', 'Γ_{T1}', 'Γ_{L2}', 'Γ_{T2}' for the corresponding linewidths (though they do not correspond to physical LO and TO phonon frequencies). Experimental spectra are presented in solid lines and fitted spectra are presented in dashed lines of the same color.

Figure 3.32b reports the frequencies of the two coupled modes as a function of the strip width S. Anti-crossing is observed and the Rabi splitting is about 70cm^{-1}, reached at S=1.2μm.

We also notice in Figure 3.32a that the linewidth of the modes descreases when they approche the EZN frequency of SiO_2 (1240cm^{-1}). Figure 3.32c reports the quality factor Q=$\frac{\omega_{resonance}}{\Gamma}$ ($\frac{\omega_{Li}}{\Gamma_{Li}}$

and $\frac{\omega_{Ti}}{\Gamma_{Ti}}$ in this case, where i=1,2). Due to the reduction of Γ, Q increases from about 10 far from ω_{ENZ} to about 30 close to ω_{ENZ}.

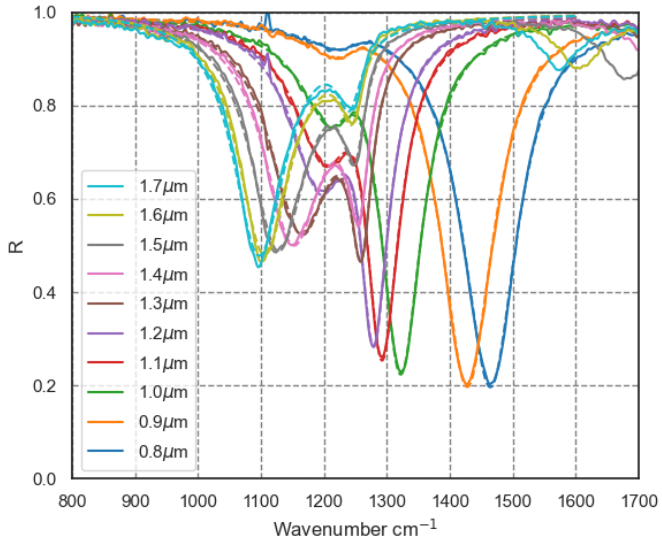

(a)

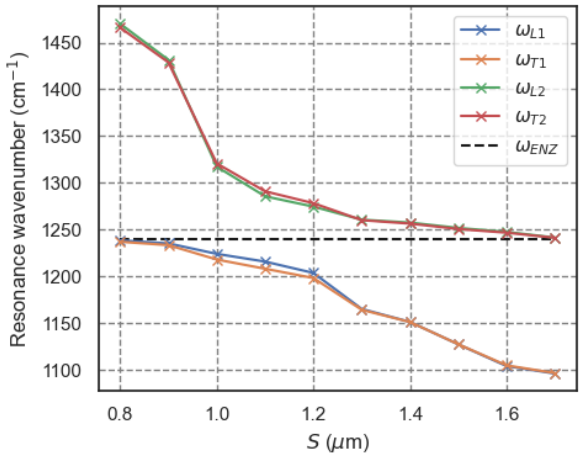

(b)

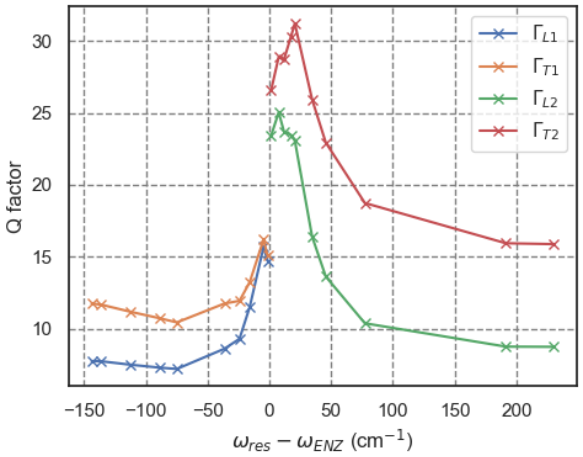

(c)

Figure 3.32 – a) Data fitting of reflectance spectra with various S of H7739-3-1-1. Experimental spectra are in solid lines, fitted spectra are in dashed lines of the same color. The model of product of lorentzian lineshapes is used, analogous to multiple-phonon model, referred to in equation 2.6. Nevertheless, in this case, the model is simply used to extract peak positions of two coupled modes and damping factors (namely 'ω_{L1}', 'ω_{T1}', 'ω_{L2}', 'ω_{T2}' and 'Γ_{L1}', 'Γ_{T1}', 'Γ_{L2}', 'Γ_{T2}' although they do not correspond to physical LO and TO phonon frequencies). b) Peaks' position in wavenumber. Anti-crossing is observed. The Rabi splitting is about 70cm^{-1} reached at S=1.2μm. c) The quality factor Q increases when the mode approaches the SiO_2's phonon frequency.

3.4.2.3 Optical and electrical characterizations of MOSFET-like ENZ-EOM

I prepared a MOSFET-like ENZ-EOM structure, named TGB4545-6-2. For insulation, I deposited 5nm of SiO_2 by ALD at 150°C on flat sample prior to top grating lithography step. For the QW contact level, before Ti/Au deposition, SiO_2 on contact pads is etched away by Reactive Ion Etching with SF_6 gas. Other fabrication steps are similar to HEMT-like ENZ-EOM fabrication. After fabrication, I characterized the sample by μFTIR for optical resonances verification, *I(V)* measurement for insulation properties and Hall effect under gate voltage for electron depletion control.

Figure 3.33b depicts reflectance spectra of three devices with various strip widths S. For all three devices, we observe a system of three absortion peaks (a strong absorption peak at around 7μm, two weaker peaks at around 8 and 12μm). The existence of these three absorption peaks are in agreement with simulation, as illustrated in Figure 3.33b, computed with S=1.176μm, incidence θ=18° and using Ordal's dielctric function for Au/Ti. Futher parameter fitting for better matching the experimental and simulated data will be detailed in Discussion part.

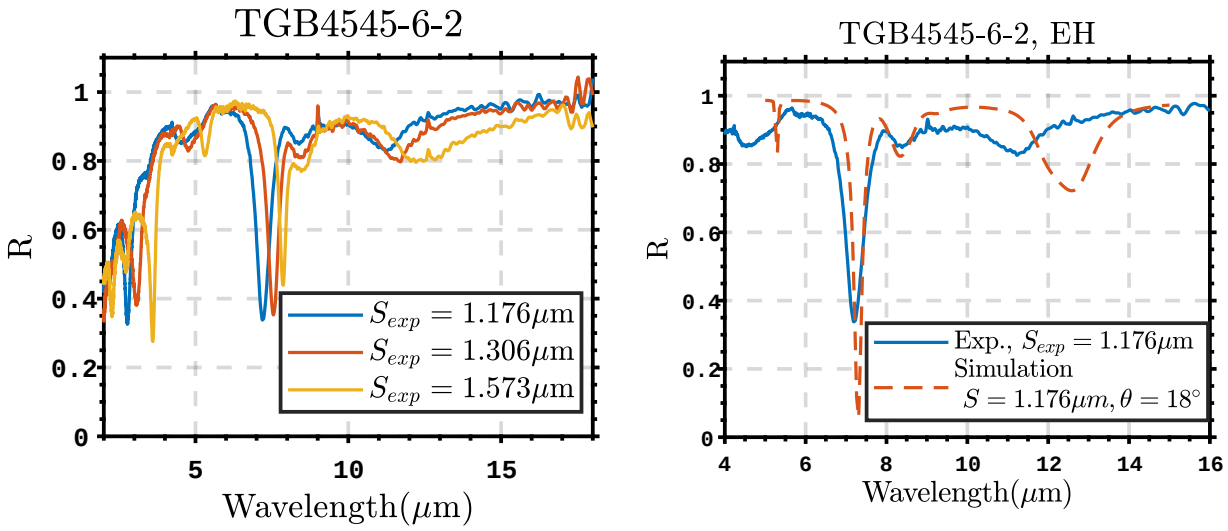

(a) (b)

Figure 3.33 – a)μFTIR measurement with floating bias. A strong absorption at around 7μm two weaker peaks at around 8 and 12μm correspond to the coupling between MIM mode, InGaAs free charges ENZ mode and SiO_2 phonon ENZ mode. b) Experimental and simulated reflectance spectra with S_{exp} = 1.176μm, Au Ordal.

Figure 3.34 shows two *I(V)* characteristics measured between the top gate and the back contact levels, on the same device *'FD'*. The measurements also follow the cyclic diode mode. The norm of the current is smaller than 10^{-7}A for bias voltage in range (-5V, 5V). At 5V, we reach the compliance voltage imposed to the measurement, so these vertical points in *I(V)* characteristics should be ignored. In both positive and negative bias, we observe hysteresis. For positive bias, the measured voltage V increases from 0V to 5V when I increases from 10^{-10}A to about 10^{-7}A (1), then decreases and reach about 1.5V when I returns to 10^{-10}A (2). For negative bias, when the voltage V decreases from 0 to -5V then returns to 0V, the norm of the current increases from 10^{-9}A to

about 10^{-7}A (3), then dips to less than 10^{-12}A before coming back to 10^{-10}A [13]. Hysteresis effect is noticeable in presence of SiO_2 layer in MOSFET-like structures (as illustrated in Figures 3.34 and 3.30) whereas it is almost not observable in HEMT-like structure (illustrated previously in Figure 3.22b). Nevertheless, in TGB4545-6-2 sample with 5nm of SiO_2 as insulator, the devices can withstand up to ±5V before breakdown (the breakdown is not shown here).

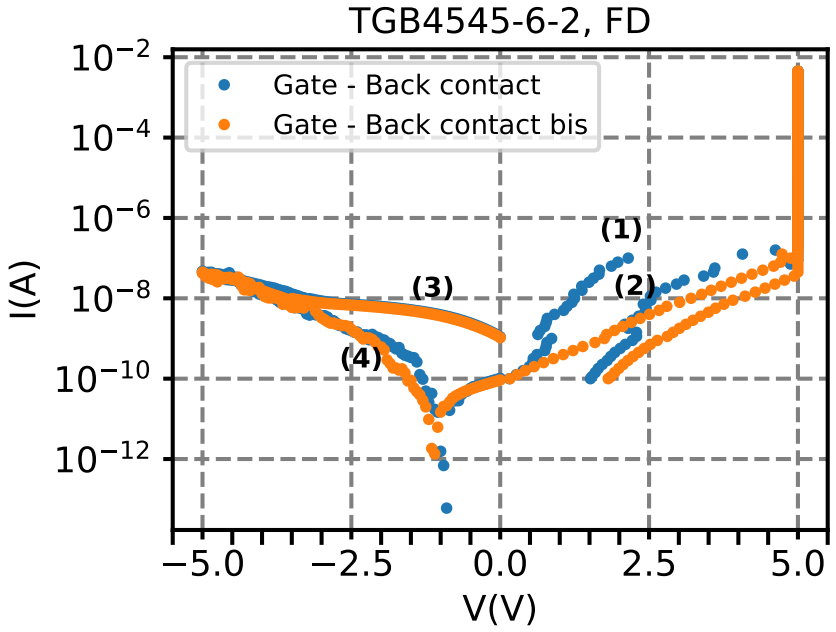

Figure 3.34 – *I(V)* characteristic of MOSFET-like EOM TGB4545-6-2: *I(V)* Gate-Back Contact show an insulator behavior, with hysteresis. Foward *V(I)* scan starts at I=10^{-10}A. The order of the scan is indicated by numbers (1), (2), (3), (4) for the blue curve.

On the same TGB4545-6-2 sample, we also have Van der Pauw crosses with Ti/Au gate pad above SiO_2 insulator. Figures 3.35a, 3.35b and 3.35c show the transverse resistance $R_{13,24}$ as a function of the magnetic field B, respectively at 0V, -2.5V and -4V bias voltage between the gate and the back contact levels. The $R_{13,24}(B)$ are highly linear. From these characteristics, I extracted the 2D and 3D electron density in the InGaAs QW layer, using the fomula 2.2. At 0V bias, we obtained N_{3D} ~$1.06\times10^{19}cm^{-3}$, in the same order of magnitude as the expected value. However, at -2.5V bias, the electron density is only reduced by about $5\times10^{17}cm^{-3}$ to reach $1.01\times10^{19}cm^{-3}$. This electron depletion represents only about 5% of the total electron density. At -4V bias, the electron density is reduced to $0.99\times10^{19}cm^{-3}$, representing a reduction by about 7% of the total electron density.

13. The minimum of the current I happens at a non-zero voltage V, indicating the the presence of a photocurrent in the device, though its origine is unclear.

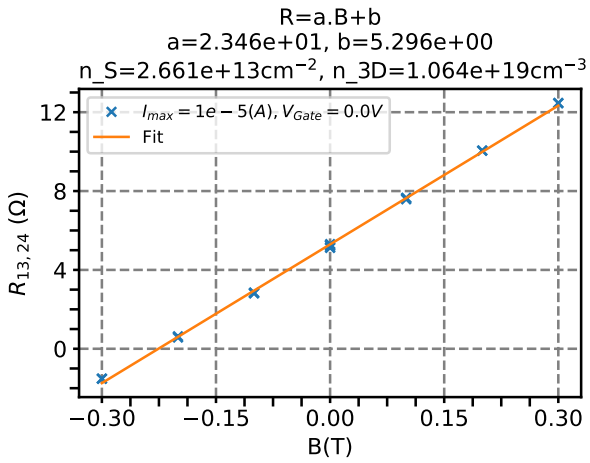

(a)

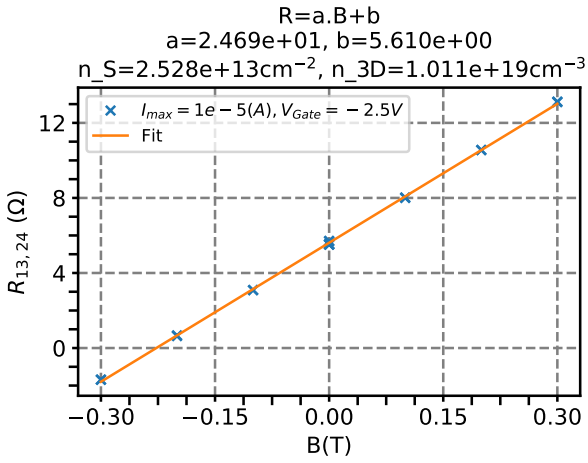

(b)

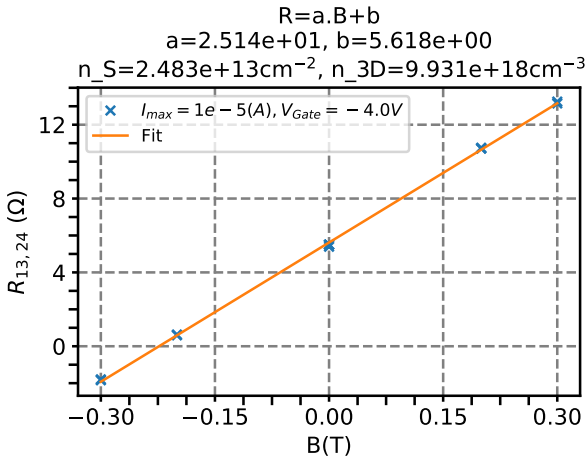

(c)

Figure 3.35 – Hall effect Van der Pauw measurements under bias Grid-Back contact a) Zero bias, b) -2.5V bias, c) -4V bias. The 3D electron density at 0V bias is about $1.06{\times}10^{19} cm^{-3}$. At -4V, the electron concentration is reduced to $0.99{\times}10^{19} cm^{-3}$, representing a reduction by about 7% of the total electron density.

3.4.2.4 Electro-optical characterization of MOSFET-like ENZ-EOM

After optical and electrical characterizations, finally I studied the electro-optical response of the MOSFET-like ENZ-EOM. The measurement took place at ONERA lab. The reflectance of the sample TGB4545-6-2 is measured with μFTIR (Hyperion 2000) while applying a DC voltage bias between the top gate (+) and the back contact (-). The bias is applied via a metallic tip and a common back contact pad. The DC bias voltage is switched from 0 to ±3-4V and back to 0V [14]. The typical acquisition time is about 1 minute per spectrum and each measurement is repeated at least twice (or more, not all of them are reported here) at the same bias to get an idea of time

14. A few values of the current I as a function of the bias V are recorded: $I(V{=}{+}4V){\sim}90nA$, $I(V{=}{+}2V){\sim}1nA$, $I(V{=}{+}1V){\sim}0.08nA$. They are of the same order of magnitude to the $I(V)$ characteristic presented in Figure 3.34.

variation of the measurement. Main measurements were realized on 4 devices of TGB4545-6-2: *'CH'*(S_{exp}=1.167μm), *'EH'*(S_{exp}=1.176μm), *'EE'* (S_{exp}=1.486μm), *'IG'*($S_{nominal}$=1.5μm).

Figure 3.36a and 3.36b depict the measured reflectance spectra at various bias voltage on two devices *'EE'* and *'CH'*. For visibility, the specctra are shifted by +0.05 each time in the chronological order of acquisition, starting from t_0 (bottom) to t_{end} (top). Globally, on both devices, we do not observe large shift and amplitude modulation as expected theoretically when the bias changes from 0V to about ±4V. The absence of large optical modulation is indeed consistent with a small modulation of electron density in the structure with bias, as announced by the Hall effect measurement under bias, illustrated in Figure 3.35.

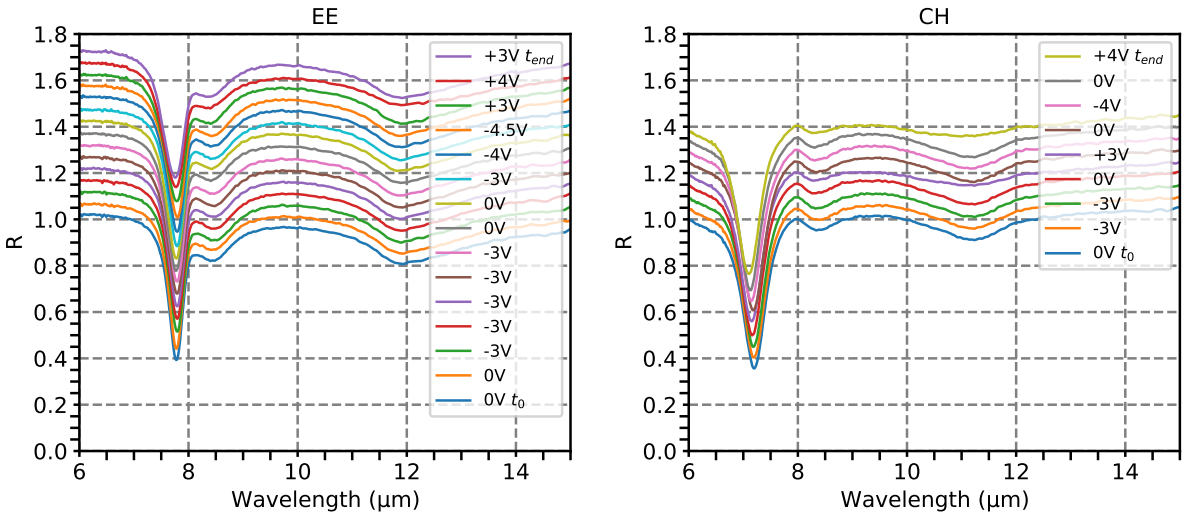

(a) (b)

Figure 3.36 – μFTIR measurement under bias. a) and b) correspond to devices *'EE'* (S_{exp}=1.486μm) and *'CH'* (S_{exp}=1.167μm). Large optical modulation is not observed experimentally. The specctra are shifted by +0.05 each time in the chronological order of data acquisition, starting from t_0 (bottom) to t_{end} (top).

Nevertheless, a small but reproducible variation of reflectance is observed in different devices. This shift is the most visible for the absorption peak around 7.5μm (referred to as peak *A*), illustrated in Figure 3.37a for device *'EE'*. The first two spectra at the bottom were acquired at 0V, then five next spectra were acquired at -3V: the peak *A* is shifted from about 7.770μm to 7.793μm (∼ 23nm shift). The peak position does not evolve in time under the same bias. When the bias is switched back to 0V, the peak returns to the initial wavelength. The measurements realized on four devices indicate that the reverse bias regime (negative bias) is relatively reversible. A negative bias induces a red-shift of the peak *A* toward larger wavelengths.

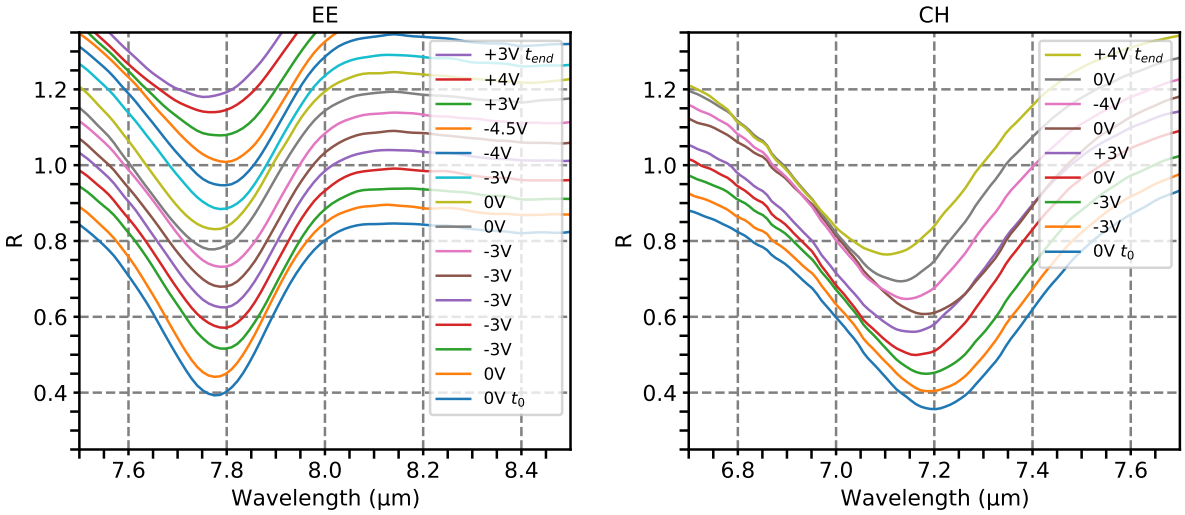

(a) (b)

Figure 3.37 – μFTIR measurement under bias. Devices: 'EE' S_{exp}=1.486μm, CH S_{exp}=1.176μm. The specctra are shifted by +0.05 each time in the chronological order of data acquisition, starting from t_0 (bottom) to t_{end} (top). A small but reproducible optical modulation is observed in the reverse bias regime (both *'EE'* and *'CH'*). The irreversible behavior is observed in *'CH'* in the forward bias regime.

On the other hand, a positive bias (forward bias regime) induces a blue-shift of the peak *A* toward smaller wavelengths, but this regime seems to be irreversible in the measurement time scale. Indeed, after applying a positive bias, when the bias is reduced to 0V and then to negative value, the peak *A* shows a red-shift and then a blue-shift rather than two consecutive red-shifts if the measurement was totally reversible. This behavior is observed in spectra of the devices *'CH'* and *'IG'*, illustrated in Figure 3.36b (passage from +3V to 0V then to -4V on *'CH'*) and Figure 3.39a (passage from +4V to 0V then to -4V on *'IG'*).

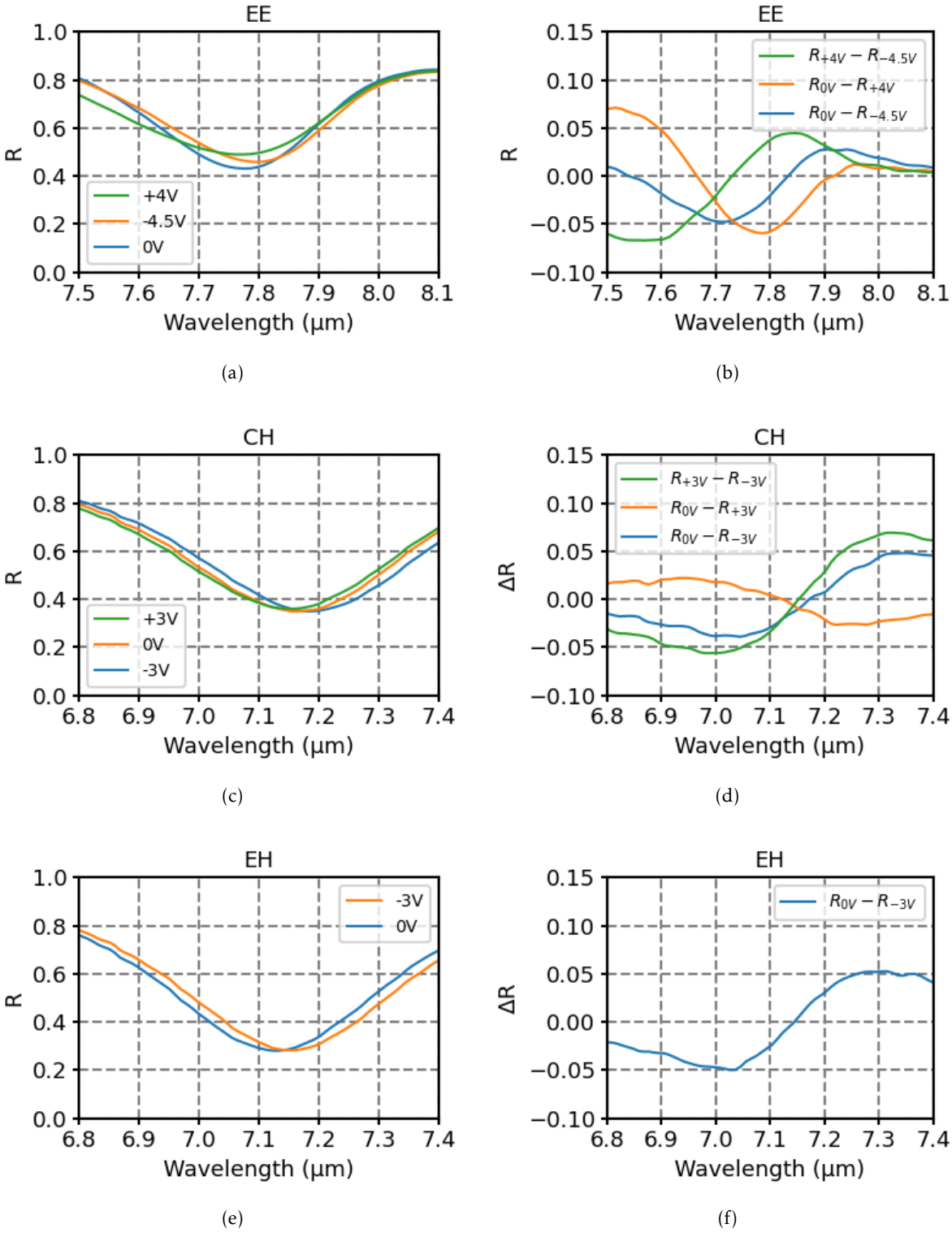

Figure 3.38 – a) μFTIR measurement under bias. Reflectance spectra at various biases are reported on the left and the corresponding modulation amplitude is reported on the right. The legends are presented from bottom to top in chronological order of the acquisitions. The amplitude of modulation is about 0.05 (or 0.5dB of modulation depth). In reversible regime, negative bias induce a red-shift and positive bias induces a blue-shift of the absorption peak. A shift of typically 20nm is observed for a bias -3V compared to 0V bias case.

Conversely, the passage from an initial reverse bias regime to 0V and then to positive bias shows two consecutive blue-shifts as illustrated in Figure 3.38c for the device *'CH'*. Therefore, we need to pay attention to the chronological order of the measurements in order to understand the behavior of the devices. Figures 3.38 and 3.39 gather some spectra of the four devices, plotted without offset for comparison and consideration of the optical amplitude modulation. The legends are presented from bottom to top in chronological order of the acquisitions. Figure 3.38 shows the devices *'EE'*, *'CH'*, *'EH'* with reversible behavior and Figure 3.39 shows the device *'IG'* with irreversible behavior. Figures 3.38a), c) ,e) and 3.39 a) (on the left hand side) display the spectra of the peak *A* at various biases. On the right hand side, Figures 3.38b), d) ,f) and 3.39 b) depict the amplitude of the optical modulation. They are obtained by making the subtraction between spectra in the corresponding Figure on the left. The maximum of the amplitude modulation is about 0.05 (for *'EE'*, *'CH'*, *'EH'*) and up to 0.1 for *'IG'*, equivalent to about 0.5-1.2dB of modulation depth.

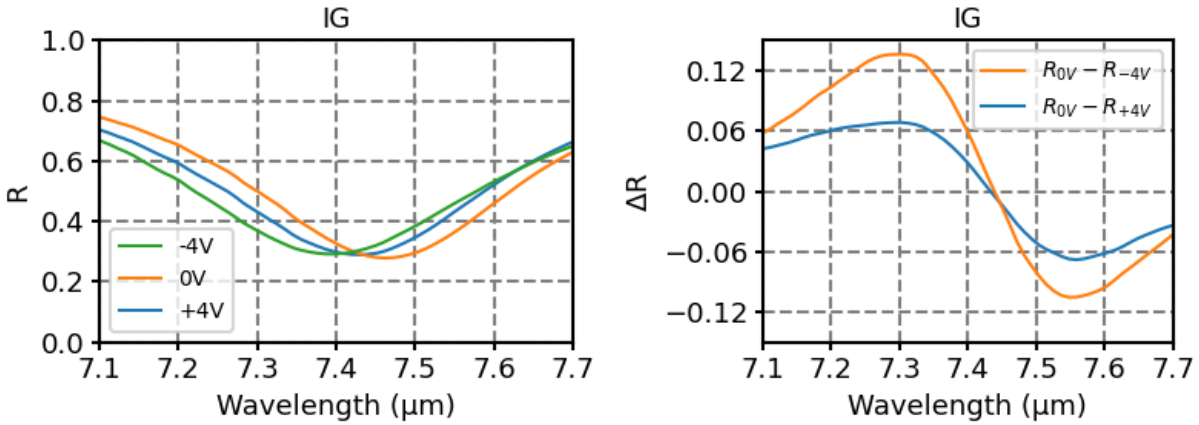

(a) (b)

Figure 3.39 – a) μFTIR measurement under bias. Devices: *'IG'* $S_{nominal}$=1.5μm. The amplitude of modulation is about 0.10 (or 1.2dB of modulation depth). The device shows an irreversible behavior after positive bias.

Experimentally, the two absoption peaks at around 8.5μm and 12μm (referred to as peaks *B* and *C* respectively) show a very small change for reverse bias (about 0.01 for peak *B*) and a more significant amplitude modulation at forward bias (about 0.04 for peak *C*), as illustrated in Figure 3.40.

Figure 3.41 depicts the experimental amplitude modulation of the device *'CH'* (blue curves) and the simulated ampltidue modulation (orange curves) realized with Reticolo for comparison. The simulations correspond to small variation of the total electron density N as predicted by Hall effect measurement (in this case -5%N and +3%N, where N=1.24×$10^{19}cm^{-3}$ is the electron density at zero bias). Figure 3.41a corresponds to a negative bias of -3V experimentally and a reduction of 5%N of the electron density in the QW in simulation. Figure 3.41b corresponds to a positive bias of +3V experimentally and an increase of 3%N of the electron density in the QW in simulation. In both cases, we observe a relatively good agreement between the experimental result and the simulation around the peak *A*, whereas experimentally the peak *B* is weaker and the peak *C* is non observable.

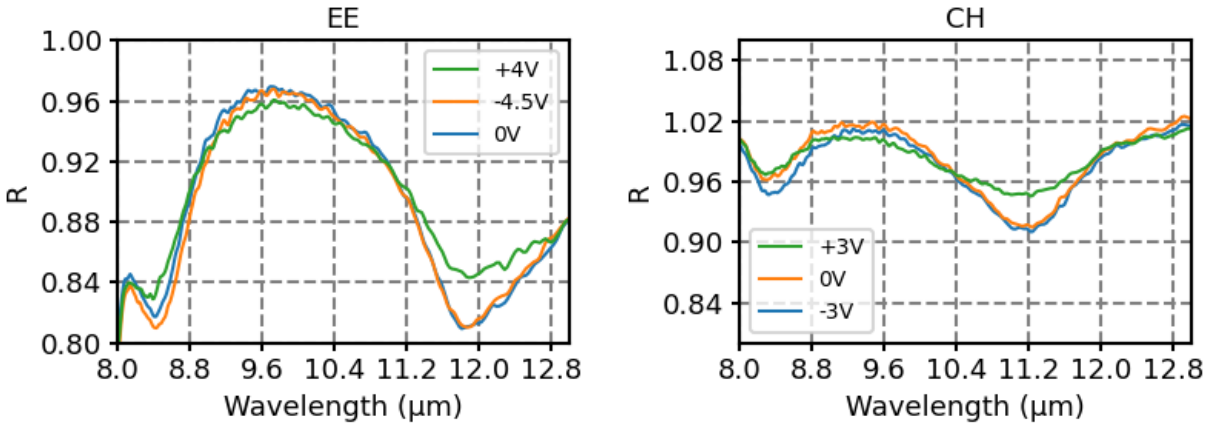

(a) (b)

Figure 3.40 – μFTIR measurement under bias. Two absorption peaks at 8.5μm (B) and 12μm (C)

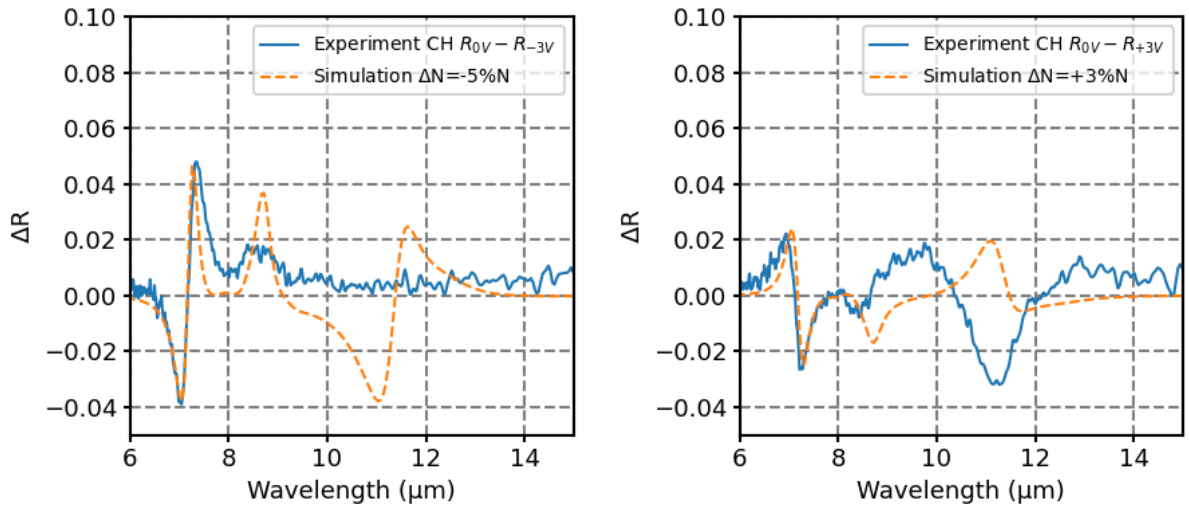

(a) (b)

Figure 3.41 – Comparison between the experimental modulation amplitude of the device *'CH'* (S_{exp}=1.167μm) and the simulation. a) A negative bias of -3V in experiment and a reduction of 5%N of the electron density in the QW in simulation. b) A positive bias of +3V in experiment and an increase of 3%N of the electron density in the QW in simulation. Good agreement betwwen experiment and simulation is observerved around the peak A but not around the peaks B and C.

3.4.2.5 Electrical breakdown

During sample's characterization, we faced an important problem: the degradation and electrical breakdown of the ENZ-EOM device at high bias voltage. Figure 3.42 depicts optical images of the device named *'IG'* before and after strong bias application (-4V). We observe the formation of bubble-like defects on top gate pads. This degradation is observed on other devices as well when

the bias passed a threshold of about -4V, and usually followed up by electrical breakdown of the device.

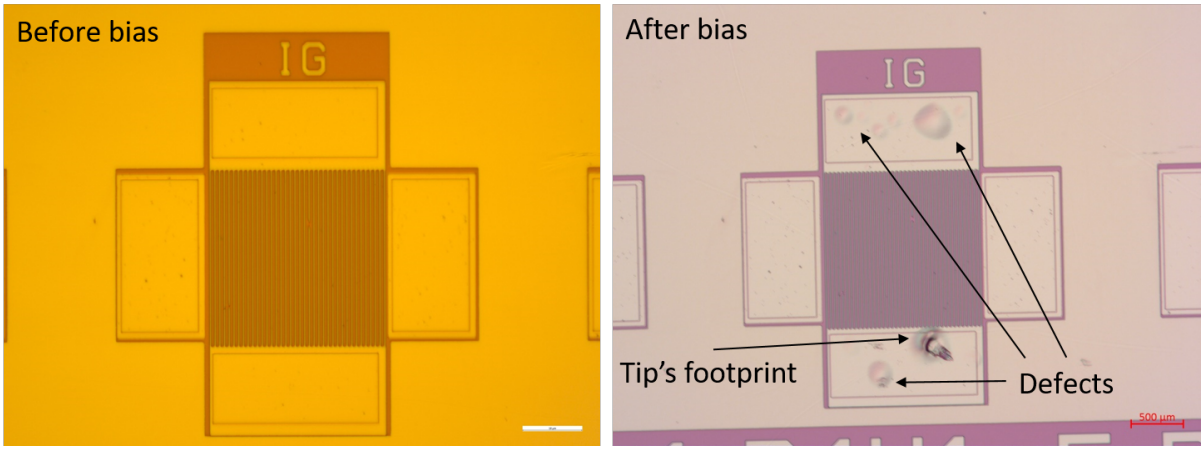

Figure 3.42 – The device before and after high bias voltage (-4V) application. Some bubble-like defects appear on the top gate pads.

3.5 Discussions

3.5.1 Fabrication and measurement difficulties

During the realization of ENZ-EOM structures, we have been confronted to other technical challenges. The substrate transferring process increases the roughness of the sample, which renders the optical UV lithography process difficult concerning patterns smaller than 1μm (here mostly the top grating). Eventhough this difficulty can be overcome by careful elimination of edge beads and residues, the process is not always reproducible on the whole sample. It usually happens that only a part of the sample, where the mask-sample contact during lithography is the best, delivers EOM devices with expected dimensions.
The electrical characterizations with probe station were also challenging, with the risk of piercing the sample during tip contacting. Non-etched semiconductor under gate pads increases the leakage current circulating in the device. These points can be improved by increasing further the gate pads's metal thickness and adding an insulator layer under the metal of the gate pads.

3.5.2 Data fitting and further discussions

Reflectance measurements of ENZ-EOM in both HEMT-like and MOSFET-like structures indicates the strong coupling regime between the MIM cavity mode and the ENZ mode(s) as expected in EM computation. However, the experimental absorption peaks are not exactly at the same positions as predicted by initial computation. This is mainly explained by the high sensitivity of the MIM resonance position to the grating strip width and the dielectric functions of the materials. Hereafter, I will present an analysis to better fit the computation to the experimental data.

3.5.2.1 SEM image analysis

MIM resonance is highly sensitive to the antenna strip width S. Depending on the type of lithography (UV or e-beam) and the degree of optimization of the fabrication process, the strip width S can be different from the nominal value of the lithography mask and vary among different strips of the same grating. In order to fit the reflectance data correctly, the strip width S is measured experimentally by doing statistics on SEM images of many strips in a gratig. Figure 3.43a depicts an SEM image of two Au strips of one device. Each strip image has two bright bands on the edges of typically 40-50nm large. These bands correspond to the trapezoidal sides of the metalic strip, as illustrated in Figure 3.43b, which scatter electrons more strongly in SEM images, giving a bright contrast.

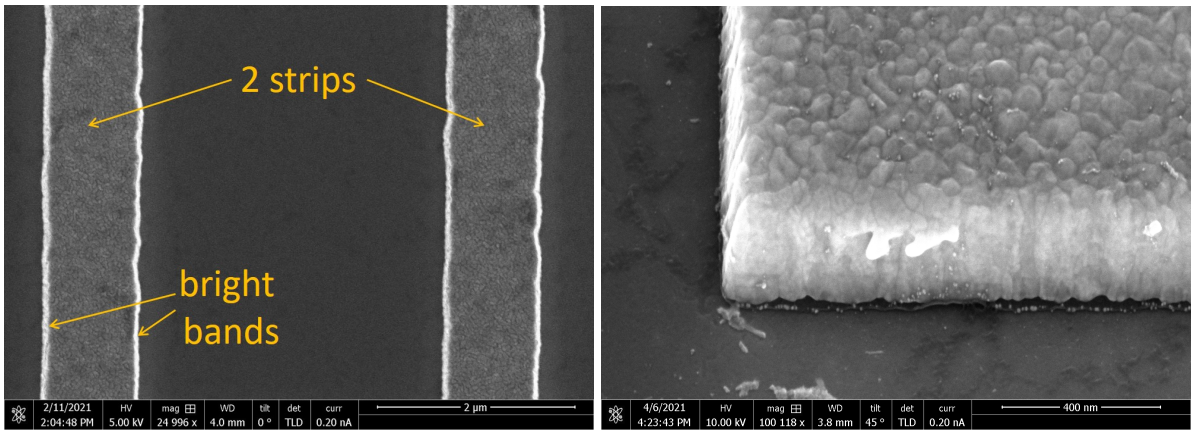

(a) (b)

Figure 3.43 – SEM images of grating strips. a) shows a zoomed SEM image of the grating, which is used to determine the experimental width of the antenna strip. b) shows a tilted image, illustrating the trapezoidal profile of the gold strip

We use an edge detection algorithm written in Python to determine the edges of each strip, then compute the width in pixel and convert it to the real length. The scale calibration is based on either the scale bar given by SEM calibration system or the period of the grating pattern. There exists a small difference between the two calibrations, the one based on the period of the grating pattern results in strips smaller by about 10-30nm compared to the SEM calibration. The SEM image is treated with an edge detection algorithm based on gradient computation, as illustrated in Figures 3.44a and b. The width determined by our algorithm corresponds to the width of the Au strip's lower base in contact with the semiconductor surface, whose edges usually have the largest contrast value in the image. A histogram of all the value of S for one strip is depicted in Figure 3.44c. The process is repeated on different strips, typically 2 on the left side, 2 in the middle and 2 on the right side of a grating for a better statistics of the mean value and the standard deviation of S.

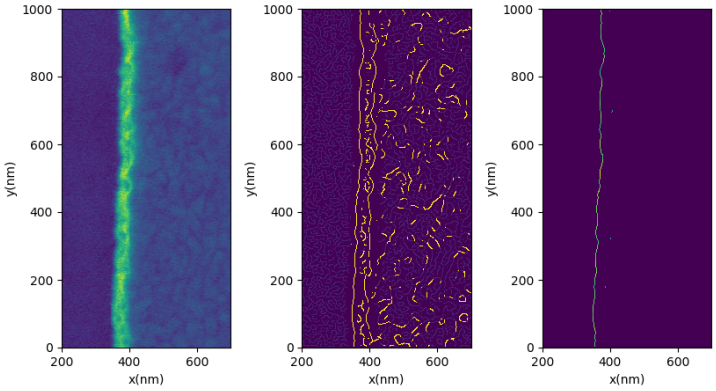

(a)

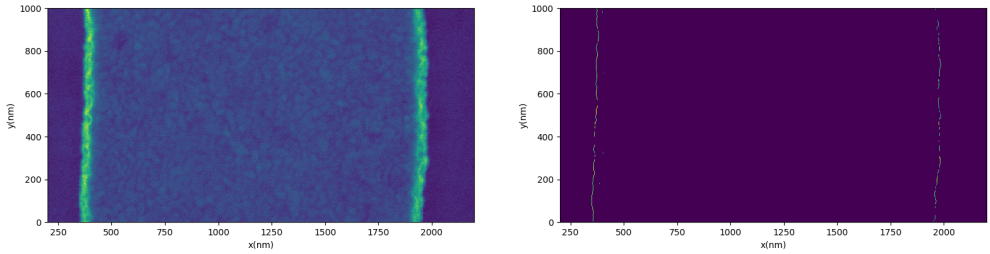

(b)

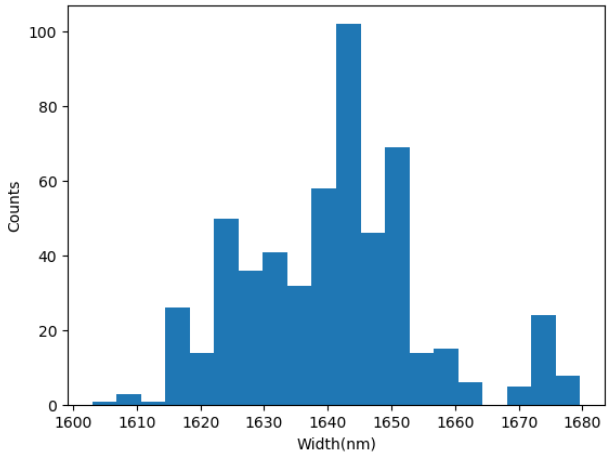

(c)

Figure 3.44 – Images processing to determine the strips width. a) Edge detection in an initial image (left) by gradient computation (middle) and threshold filter (right). After filtering with a threshold, we obtain the line corresponding to the largest gradient of pixels' intensity. In this case, the largest gradient in intensity in the image usually corresponds to the edge between the lower base of the Au strip and the semiconductor.
b) From the initial image of a strip (left), the algorithm returns two lines corresponding to two edges of the strip's lower base. The strip width S of each pixel row of the image is obtained with a peaks detection algorithm.
c) Histogram of all strip width S values in the initial image. Here, S has a mean value of 1641nm and a standard deviation of 14nm. The process is repeated on different strips, typically 2 on the left side, 2 in the middle and 2 on the right side of a grating for a better statistics of the mean value and the standard deviation of S.

3.5.2.2 Reflectance data adjusting

Reticolo's computation time is relatively long (several minute per spectrum), automatic fitting using least square method with many fitting parameters is quite complex. Here, for reflectance spectra simulation, I simply adjusted manually several parameters of the input set and verified if the results matched with the experimental data of many devices. The dielectrics functions of semiconductors from our database are considered fixed. The damping factors of metals' dielectrics functions are adjusted to match the experimental linewidth of absorption peaks. The strip width S of of all the devices are obtained from SEM images. To give a degree of freedom to the MIM resonance wavelength during the data adjusting process, I chose to modify the all the experimental strip widths S of different devices by the same offset.

Initial computation with Ordal's dielectric function [99] for Au and Ti delivered narrower and more intense absorption peaks than the experimental data. We tested various wavelength-dependent dielectric functions for Au reported in the literature, among which Olmon and Rakic's papers [70, 107] are usually cited, with almost similar parameters. We decided to adopt Olmon's parameters for Au (ω_P = 8.5eV, Γ = 0.047eV) and increase the damping factor by a factor 1.5 (Γ = 0.071eV) to better fit the experimental data. For 2nm-thin Ti adhesion layers, it is quite difficult to model properly because of unmastered chemistry (oxidation of Ti during and after deposition, making the layer different from bulk metallic Ti) and potentially inhomogeneous surface coverage. A proper electromagnetic modelling of a thin Ti adhesion layer, especially its optical loss, requires dedicated studies that we have started recently. Here, for simplicity we consider the 2-nm thick Ti layer as homogeneous and we use Ti's dielectric function from Rakic's paper.

With this set of dielectric function, the computed absorption peak linewidths and amplitudes match better the experimental data in both HEMT-like and MOSFET-like structures. In correspondence, all the values of S_{exp} are subtracted by an offset of 80nm. This adjustment gives good agreement for the MIM mode position on many devices and different samples (both ENZ-EOM of this chapter and ENZ-QCD that will be presented in chapter 4).

We also observed that the experimental peaks splitting in strong coupling regime is not as large as predicted in our initial simulation. This splitting is mainly controlled by the plasma frequency of the ENZ film and the overlap between the MIM mode and ENZ mode. One possible explanation for this difference is that the conduction band offset between InGaAs and InP induces a depletion zone at their interface.

$$d_{depletion} = \sqrt{\frac{2\epsilon_0\epsilon_\infty V_{CBO}}{eN}} \tag{3.8}$$

where $d_{depletion}$ is the thickness of the depletion zone, V_{CBO} is the conduction band offset, N is the 3D electron concentration and e is the elementary charge. With V_{CBO} ~200meV for InP-InGaAs interface and N~$1.24\times10^{19} cm^{-3}$, we obtain $t_{depletion}$ ~ 5nm. This depletion reduces the overlap integral. Actually, by reducing the width of the InGaAs QW from 25nm to 15nm (and replacing by 10nm of intrinsic InGaAs), the computed peaks splitting match better the experimental data.

The experimental reflectance spectra and simulated spectra with all parameter adjustments above are presented in Figures 3.45 for HEMT like structure and 3.46 for MOSFET like structure. We observe quite good agreement for all presented devices in terms of peaks position and linewidth. However, we cannot recover exactly the experimental ampltitude of reflectance with our simulation with this parameter set.

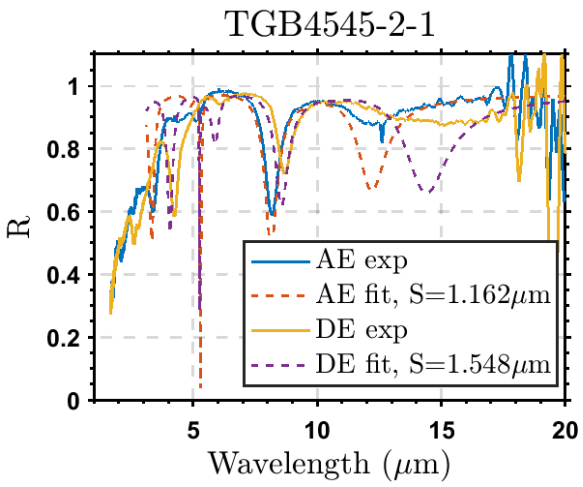

Figure 3.45 – μFTIR measurement at 0V bias of HEMT-like structure on TGB4545-2-1 sample compared to Reticolo simulation.

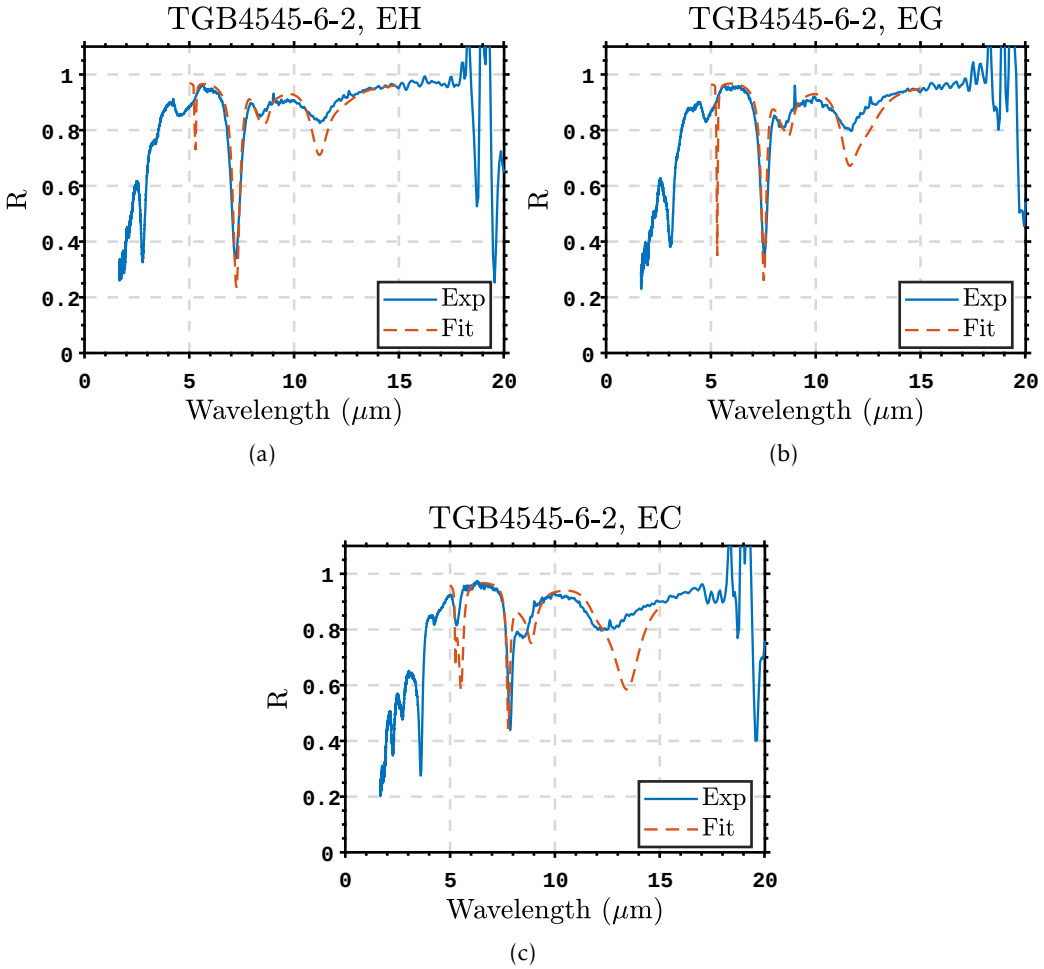

Figure 3.46 – μFTIR measurement at 0V bias of MOSFET-like structure on TGB4545-6-2 sample compared to Reticolo simulation.

3.5.3 Q factor and optical modulation in MOSFET-like structure

Figure 3.47a reports the reflectance spectra of devices of various nominal strip width S on TGB4545-5-2, a similar sample to TGB4545-6-2 with 15nm of sputtered SiO_2. Similarly to the case of H7739-3-1-1 with SiO_2 embedded in a MIM cavity, we observe a reduction of the linewidth of the mode A around 1300cm^{-1} (7.5μm) zone when this mode approches the EZN wavenumber of SiO_2 (1240 cm^{-1}). The mode A is fitted with a single lorentzian in order to determine the peak's frequency and linewidth. These values are used to compute the quality factor Q, presented by black triangles in the Figure 3.47a. The value of Q increases by a factor of 3, from 11 to 32, when the mode approches the ENZ wavenumber of SiO_2.

Indeed, this mode has the E_z field very localized in the SiO_2 layer, as reminded in Figure 3.47b. The optical loss due to SiO_2 phonon is smaller than metal of the MIM cavity, which explains the reduction of the absorption linewidth and the increasing of Q factor when the mode approches the ENZ wavenumber of SiO_2. Furthermore, a higher Q factor also induces a larger variation of reflectance amplitude for the same shift of resonance frequency, making the amplitude modulation easier. We think that this larger Q improves the optical modulation of this mode A in sample TGB4545-6-2 presented in section 3.4.2.4.

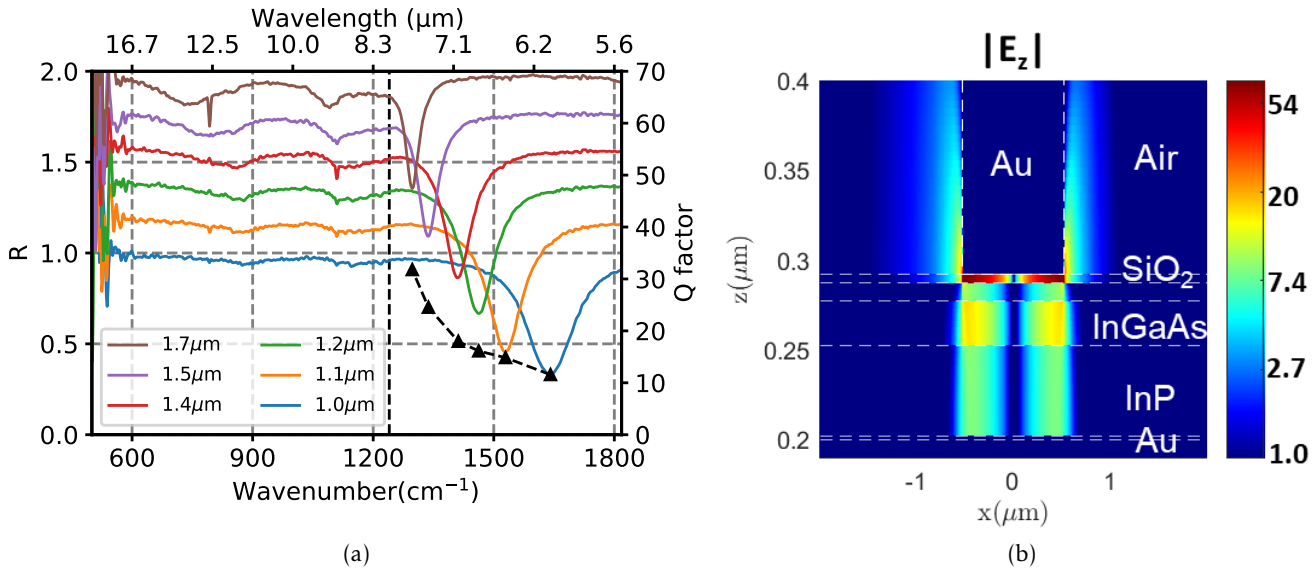

(a) (b)

Figure 3.47 – a) Reflectance spectra of devices with various nominal S of TGB4545-5-2, similar to TGB4545-6-2 but having 15nm of sputtered SiO_2. The spectra are shifted by an offset of +0.2 each time. The peak A around 1330cm^{-1} (7.5μm) zone becomes narrower when approching the ENZ frequency of SiO_2 1240cm^{-1}. The peak A is fitted with a single lorentzian to estimate the peak's frequency and linewidth in order to compute its quality factor Q (represented by black triangles). Q increases by a factor of 3, reaching a value of 32 when the peak is near the ENZ frequency of SiO_2 1240cm^{-1}.
b) Reminder of the field distribution of the mode A: the E_z field is strongly confined in the SiO_2 layer.

It is also interesting to point out that in this case we modulated the frequency of the mode A, which is essentially a phononic mode of SiO_2. The phonon frequency is usually intrinsic to a material. In III-V semiconductor, this frequency can be modified slightly with additional free electrons from dopants directly implanted in the semiconductor layer (plasmon-phonon coupling). Here, the frequency of the phononic mode A can be modulated by field effect via modulation of electron density in another layer of

the cavity (InGaAs QW), spatially separated from the SiO_2 layer. This is a new mechanism of modulation using a three-mode coupling regime (ENZ SiO_2, ENZ InGaAs, MIM). Though this shift is quite small, a high Q factor of the 'phononic' mode *A* thanks to lower optical phonon loss in the SiO_2 layer translates the frequency shift into a non negligible amplitude modulation. This is an interesting mechanism with potential for further studies.

3.5.4 Explanation for the non-tunability of ENZ-EOM

In both cases of HEMT-like and MOSFET-like ENZ-EOM, we observed experimentally in reflectance spectra the strong coupling regime between the MIM cavity mode and the ENZ mode(s). However, electro-optical characterizations in prevous section indicate that the optical modulation with bias voltage does not happen as expected. Hall effect measurement of Van der Pauw crosses with gate pad under bias voltage pointed out that only about 7% of the total electron density in the InGaAs QW is depleted for a bias of -4V. At -4V bias, we started to observe degradation of the top gate pads with the appearance of bubble-like defects. A bias voltage larger than -5V leads to breakdown.

It is clear that we were not able to modulate the electron density as strongly as expected in preliminary computation for HEMT-like ENZ-EOM structure. In the HEMT-like structure, band structure modeling by *1D Poisson* is only capable of modelling heterostructure at thermodynamic equilibrium. Drift-diffusion equation is not taken into account. When the current in the device is not negligible, the model applied in the computation does not hold anymore. And we see from experimental measurements for the HEMT that the current increases and gets large for V around -0.5V. Futhermore, we are considering heavy doping concentrations. At these doping values, the computation of the band diagram can be inaccurate due to non-parabolicity of subbands and exchange interaction not taken into account.

For the MOSFET-like ENZ-EOM, the presence of SiO_2 layer reduces considerably the current in the device. However, it also introduces interface states with charges that can screen the voltage applied to the heterostructure. Similar reduction of gate voltage effect in presence of interface states is reported for example in reference [108]. The phenomena of charges appearance in the SiO_2 layer is complex and I have limited understanding of the problem. The application of a MOSFET-like structure with SiO_2 as insulator for the goal of electron depletion is not as straight forward as expected.

Controlling the electron density by gate field effect is indeed non trivial and is a common problem for modulators working based on strong coupling - weak coupling transition [3, 39]. Further studies are needed to better understand and hopefully overcome this difficulty.

3.6 Chapter conclusion

In this chapter, I presented our design for an ENZ-EOM structures. The optical modulation is based on detuning an ENZ mode which is initially in strong coupling with a cavity mode, where the detuning consists in electron depletion with a voltage bias. I studied theoretically two kinds of structures, HEMT-like and MOSFET-like ENZ-EOM. Electromagnetic computation shows a strong confinement of light in the ENZ layer and a significant amplitude modulation (up to 90% in HEMT-like structure).

Experimetnally, I fabricated the HEMT-like ENZ-EOM made of InP/InGaAs/InP heavily doped embedded in a MIM cavity and the MOSFET-like ENZ-EOM made of the same materials with an additional SiO_2 insulator layer. We observed a strong coupling regime in both structures, between ENZ mode and MIM cavity mode in HEMT-like structure, and with a third mode - ENZ optical phonon of SiO_2 insulator - in MOSFET-like structure. However, a significant electron depletion appears to be challenging in both

structures, attributed mainly to unmastered interface conditions and too high doping level. We have also been confronted with other limitation of the initial design, among which the absence of Schottky barrier for top gate and the electrical breakdown limit just to cite some. Nevertheless, an optical modulation of about 5-10% (equivalent to a modulation depth of 0.5-1.2dB) is observed in the MOSFET-like structure at around 7.5μm, linked to the presence of thin SiO_2 layer. Also, we observe an increasing Q factor up to 3 times when this mode approches the ENZ frequency of SiO_2. These observations possibly pave the way to study a new modulation mechanism which involves three coupled modes.

4 ENZ Quantum Cascade Detector

This chapter is devoted to the study of the application of the ENZ effect and nanophotonic structure MIM cavity to single-period Quantum Cascade Detector (QCD). First, I will introduce the state of the art of the QCD and the motivation for a single-period structure. Then I will present the electromagnetic conception of the device structure. I will show the device fabrication process, followed by different characterizations: temperature dependance reflectance, I(V) characteristics, photocurrent and spectral response measurements. Finally, I will discuss about different analyses and interpretations of the experimental results.

4.1 State of the art and device physics

4.1.1 Infrared detectors

Infrared detectors are used in a very large range of applications: IR spectroscopie, thermal imaging, communication,... Gaz and organic compounds have spectral 'fingerprints' in the mid-IR range, their identification and quantification by IR spectroscopy are useful for product quality control during production, air quality control. Thermal imaging was initially motivated by military use but nowadays finds civil applications like controlling thermal insulation of buildings, thermal monitoring of data centers or photovoltaic power station,... The huge applications of IR fiber communications and potential applications of Free Space Optical Communication in LWIR range are already discussed in chapter 3. These applications also require fast and efficient IR detectors.

The history of IR detectors is well covered in the review of Rogalski A. [109]. In short, there exists many technologies for IR detectors, they can be classified into thermal detectors and photon detectors according to Rogalski. Thermal detectors (bolometer, thermopile, pyroelectric) are based on the conversion of temperature variation (due to IR radiation absorption) to an electric signal. Typically, they exploit thermoresistance, Seebeck effect, ... Thermal detectors are usually low cost, operate at ambient temperature and respond to a large range of wavelength. However, thermal effects are usually accompanied by a long relaxation time, typically microsecond to milisecond. Speed is thus the main limitation of thermal detectors.

In the photon detectors category, we can cite some popular examples such as intrinsic IR detector (Mercury Cadmium Telluride detector - MCT or HgCdTe, with small tunable bandgap, controlled by composition), quantum well photodetector (Quantum Well Infrared Detector - QWIP, Quantum Cascade

Detector - QCD, Quantum-Dot Infrared Photodetector - QDIP,...). MCT is probably the most popular nowaday, offering a large detectivity and a large spectral range. However, material instabilities due to weak Hg-Te bond, non-uniformity in Focal Plane Array devices and the need of liquid nitrogen cooling for operation are some main drawbacks of MCT [110].

4.1.2 Intersubband detectors

We will focus now on quantum wells devices and more specifically on the family of intersubband detectors: QWIP and QCD.

4.1.2.1 QWIP

QWIP was first demonstrated by Levine B. F. *et al.* in 1987 [111]. The detection principle is illustrated in Figure 4.1. A QWIP consists of multiple active quantum wells as absorbant material. Popular material choices are GaAs/AlGaAs or InGaAs/InAlAs. Typically, each quantum well has an occupied ground bound state and an unoccupied excited state near the barrier's conduction band edge. The excited state can be below, above or at the same level of the conduction band edge, we call these configurations respectively bound-to-bound, bound-to-continuum and bound-to-quasi-continuum transition. Resonant photon absorption between the two states promotes an electron from the ground state to the excited state. The electron is then extracted thanks to an electric field applied on the structure. QWIP operates like a photoconductor whose resistance is reduced under illumination and where an external bias is necessary to generate a photocurrent. The total acquired current includes also a dark current due to thermal excitation and electron tunnelling through barrier layer between quantum wells. The dark current can become dominant over the photocurrent and be the limiting factor of QWIP, especially when operating temperature increases. Another challenge for QWIP device is the difficulty to correctly model the electron continuum state.

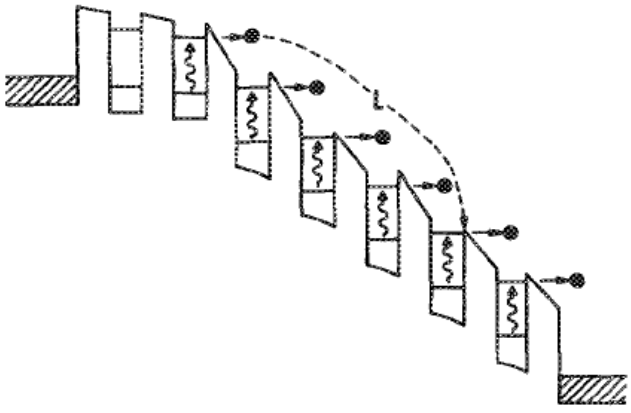

Figure 4.1 – QWIP's band structure under bias, adapted from reference [111] - the first demonstrated QWIP. The device is a photoconductive detector, made of a repetition of identical GaAs/AlGaAs n-doped quantum wells. Using bound-to-bound configuration, under illumination, an electron is promoted to the excited state by photon absorption, then tunnels out of the QW into the continuum, creating a photocurrent.

4.1.2.2 QCD's state of the art and device physics

QCD was proposed in the early 2000s by Hofstetter et al. [112] in 2002 and Gendron et al. [113] in 2004, inheriting developements of QWIP and another technology, the Quantum Cascade Laser (QCL). Figure 4.2a depicts the band structure of one period of a QCD on the left and a TEM image of the whole QCD structure on the right. A QCD period consists of an active quantum well with two bound states and an electron extractor cascade stage (which plays the role of an electron injector stage for the adjacent period). The ground state of the active quantum well is occupied. Electrons in the ground state can absorb a photon and be promoted to the excited state. The excited electron can either relax back to the ground state of the active QW or be scattered by an LO phonon into the extractor cascade. We denote as p_e the probability of a photoexcited electron in the excited state of the active QW to be extracted through scattering into the extractor cascade. As discussed by Delga in his review [4], in the latter case, the photon absorption and the electron scattering to the adjacent active QW create a local pertubation of the stationnary state. This pertubation propagates to the other periods and to the external circuit, leading to the generation of photocurrent in the circuit, without the need for other photon absorption events. This is the eulerian point of view of the electronic transport in QCD.

Compared to MCT, QWIP and QCD have lower detectivity and a narrower optical bandwidth due to their resonant characteristic. Nevertheless, a narrow optical bandwidth can become an advantage at long wavelength above 10 μm. Indeed, at these wavelengths, all objects in the environment are IR sources, a narrow optical bandwidth response offers a better contrast than large bandwidth one. ISB devices such as QWIP and QCD also have short carrier lifetime (typically a few ps) due to LO phonon scattering, which limits the photocurrent response but also means that these devices can work at very high frequency (the theoretical limit is in the 100GHz range, QCD with 23GHz operation was experimentally demonstrated, acccording to [4]).

As opposed to QWIP which operates in photoconductive mode and can not work at zero bias, QCD operates in photovoltaic mode and can work at zero bias. The key difference between these two detectors is the asymetric band structure of QCD. The extractor stage has a cascade of potential energies at zero bias, allowing the excited electrons going downward the cascade and preventing them from going upward, creating a photocurrent at zero bias. The near zero bias functioning of QCD allows reducing significantly the dark current (which is zero when the bias is rigorously zero), as compared to QWIP.

One period of QCD is quite similar to a Schottky diode in terms of electric transport. The ground state of the active QW plays the role of 'the metal' while the excited state and the extractor cascade act like 'the semiconductor' in analogy to the Schottky diode. This is illustrated in Figure 4.2b.

Some important quantities for QCD are:

- The absorption efficiency η_{abs} is the probability that an incident photon is absorbed by an ISB transition of the active QW (also referred to as the useful absorption $A_{z\,QW}$ in the rest of this chapter).
- The Internal Quantum Efficiency (IQE), denoted as η_{int}, is the conversion rate of a photoexcited electron into an electron flowing in the external circuit.
- The External Quantum Efficiency (EQE), denoted as η_{ext}, is the efficiency of the conversion of an incident photon into an electron flowing in the external circuit: $\eta_{ext} = \eta_{abs}.\eta_{int}$.
- The ISB photocurrent $I_{phot\,ISB}$ (in A) is the photocurrent corresponding to the ISB absorption events. I reserve this term $I_{phot\,ISB}$ to denote the ISB photocurrent due to the target IR source without other background contributions. $I_{phot\,ISB} = \eta_{ext}.\Phi_{photon}.e$, where Φ_{photon} is the photon flux integrated over the detector surface (in photons/s) and e is the elementary charge.

- The dark current I_{dark} and background current $I_{background}$ (in A). I_{dark} is the current produced without illumination, I_{dark}=0 at zero bias. $I_{background}$ takes into account the photocurrent created by the background beside the target IR source: $I_{background} = I_{dark}+I_{phot\,background}$. The photocurrent created by the target IR source is the difference between the total current and the background current: $I_{phot\,ISB} = I_{total}$-$I_{background}$.
- The responsivity $\mathcal{R}$(in A/W) is ratio between the photocurrent (in A) and the total incident optical power (in W) arriving on the detector surface. $\mathcal{R} = \eta_{ext}\frac{e}{h\nu}$ where $h\nu$ is the energy of the detected photon.

Other quantities like Noise Equivalent Power, detectivity,... are usually mentioned in discussions about detectors but require longue description and are beyond the scope of this chapter. Readers interested in the subject can find well developed discussions about these quantities in Delga's review [4].

Also in this review, author pointed out that QCD generally have low EQE value. Figure 4.2c depicts the reported EQE value of QCD from various publications. This figure is adapted from Quinchard's thesis [75] (published in 2021), reproducing a figure from Delga's review (published in 2020) updated with recent data from LPENS and III-V Lab groups. All reported EQE values are around 1% or below, with one exception: the QCD of TUW group (Schwarz et al. [114]), reaching an EQE of about 40%. The particularity of the latter QCD is the use of a single-period QCD structure (embedded in a ridge waveguide). This is the only publication on single-period QCD found in the literature to my knowledge. Published QCD structures have at least several periods, and usually around 10-30 periods.

Delga pointed out in his review that from the QCD eulerian electronic transport point of view, the Internal Quantum Efficiency is reduced with the number of period N_p as $\eta_{int} = p_e/N_p$. QCD (and QWIP) are known for having low optical absorption. Without special optical structure, the optical absorption per QW is less than several percent, which motivates the use of many period in order to increase the total absorption efficiency η_{abs} ($\eta_{abs} \propto N_p$ in the case of small absorption per QW). Nevertheless, η_{abs} can be improved with nanophotonics structures (plasmonic hole array [115], patch antenna [75], ...). The EQE can be greatly increased by realizing a single-period QCD imbedded in a nanophotonic structure allowing to enhance the absorption of the single quantum well in the structure.

This is exactly what we want to study in the framework of applying the ENZ effect to optoelectronic devices. Indeed, the ENZ effect coupled to a MIM cavity allows enhancing the normal component E_z of light and confining the light electric field in highly sub-wavelength layer, which can improve the absorption of light in this layer. The ISB transition is only active to the normal component E_z of light, matching well with the ENZ and MIM configuration. The MIM grating allows free space light to couple into the structure, which is an advantage compared to the ridge waveguide configuration in Schwarz's paper [114] where light is injected from the edge of the sample.

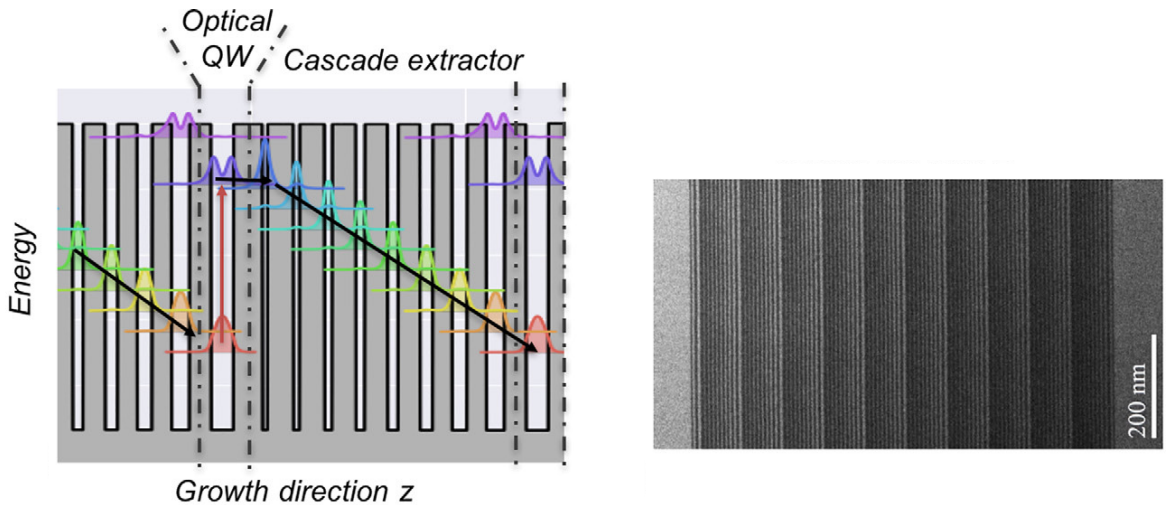

(a)

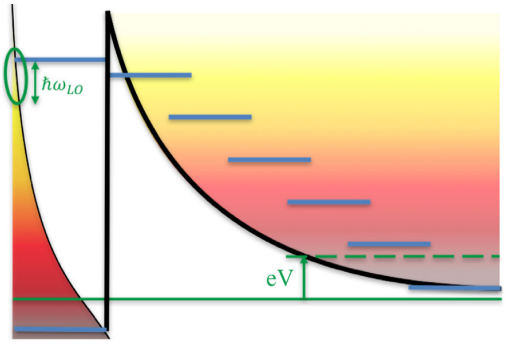

(b)

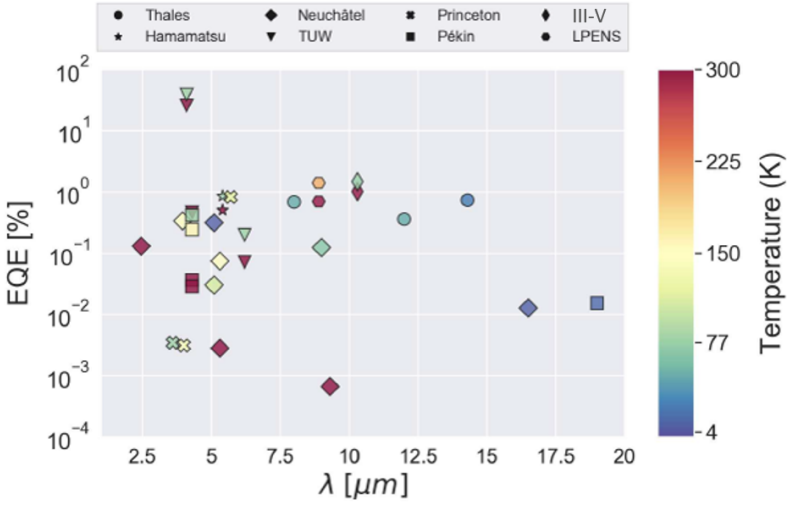

(c)

Figure 4.2 – a) Left: Band structure of one QCD period, with the active optical quantum well and the cascade extractor stage. Right: TEM image of 10 periods of a QCD structure. b) Analogy of QCD band structure to a Schottky diode model. a) and b) are adapted from [4]. c) EQE of QCD, adapted from [75] and [4].

Figure 4.3 depicts the band structure of a single-period QCD in waveguide geometry in reference [114]. In his paper, Schwarz et al. gave some insights about the challenging electronic design of a single-period QCD compared to conventional multiple-period structures [114]. In conventional structure with a large number of periods, we can assume periodic boundary condition for band calculation and ignore the effect of the edges contact layers during the band structure design. The contact layers induce band bending, which can lead to subbands misalignment and influence strongly the energy levels of the first and the last periods. Therefore, the boundary conditions must be treated with special care in single-period QCD design, making this design difficult and worth the present study.

I will now present our work to realize a single-period ENZ-QCD.

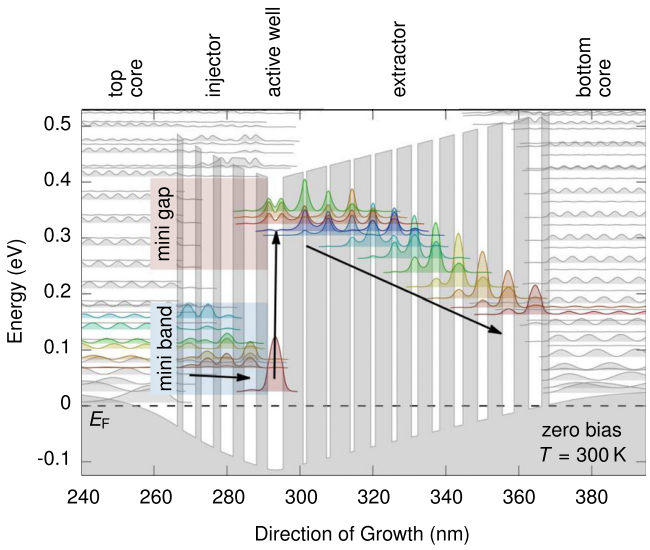

Figure 4.3 – Band structure of a single-period QCD in reference [114]. The structure consists of an injector, an active well and an extractor, the whole sandwiched between contact layers. The band edge is bent as compared to a flat band edge in multiple periods QCD as depicted in Figure 4.2a. The injector is designed to have a mini gap at the energy level of the active well's excited state, in order to prevent scattering of photoexcited electron from the active well back to the injector.

4.2 Electromagnetic and transport optimization of QCD structure

The general structure of our ENZ-QCD consists of a single-period QCD semiconductor stack imbedded in a 1D grating MIM cavity, as depicted in Figure 4.4. The design of this QCD structure includes an electromagnetic optimization and a transport optimization. To begin with, I realized the electromagnetic optimization of the QCD-ENZ structure with a given QCD period structure made of InGaAs/InAlAs. From this optimization, we got an idea of some target parameters: the ISB energy ω_{ISB}, the QW doping level and the total thickness of the QCD stack. Then, the electrical transport optimization with these provided parameters was realized by Lagrée Mathurin - PhD student of III-V lab and collaborator in the mEtaNiZo project. The transport optimization consists in engineering small thicknesses of QW of the QCD stack. These modifications of thickness are mostly 'invisible' optically. Even if these small modifications have almost no influence on the optical properties of the total structure, I verified the electromagnetic response of the final structures.

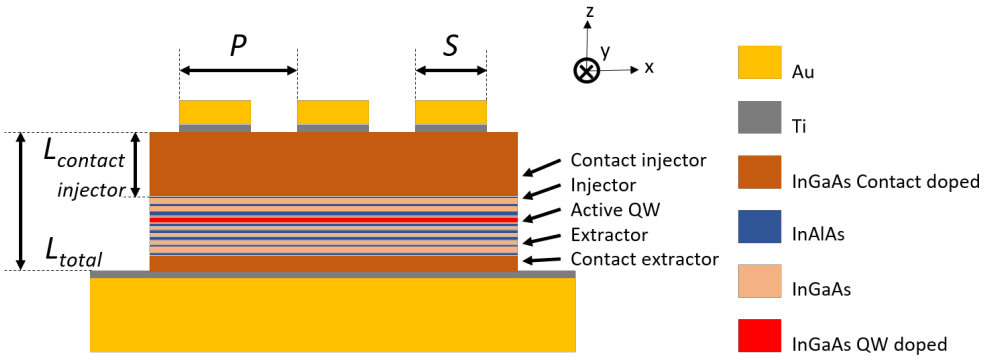

Figure 4.4 – Schemtatic of QCD device

4.2.1 Electromagnetic optimization

I used Reticolo code (introduced in section 3.2.1.1) to compute the absorption A_z in the QW (due to E_z component) and the reflectance R. The goal is to determine the parameters' value that maximize the useful absorption A_z in the active quantum well ($A_{z\,QW}$), which is the absorption efficiency of QCD η_{abs}. The parameters to be studied are:

- The ISB energy ω_{ISB},
- The thickness of the contact injector layer $L_{contact\ injector}$ (used to adjust the total MIM cavity thickness L_{total}),
- The QW doping level N_{QW},
- The grating parameters S and P.

4.2.1.1 Dielectric function of the active QW and ENZ contribution

Since we want to maximize the useful absorption $A_{z\,QW}$, it is essential to have a correct description of the QW's dielectric function. In contrast with ENZ-EOM electromagnetic computation performed with a homogeneous isotropic 25nm-thick QW layer, here we treat the 10nm-thick QW layer as a homgeneous anisotropic layer. The dielectric function of the QW is described by a Drude model for the in-plane components $\epsilon_{QW\,x}$, $\epsilon_{QW\,y}$ and an ISB transition dielectric function for the perpendicular component $\epsilon_{QW\,z}$.

I used the ISB dielectric function generated by METIS code (Modelling of the Electronic Transport of Intersubband Structures), developped by III-V lab. This code takes into account more complex characteristics, such as the electronic wave function extension in the effective length of the QW: L_{eff} and the non-parabolitcity of subbands at large doping.

Figure 4.5 depicts the dielectric function in the z direction of the QW $\epsilon_{QW\,z}$ obtained with METIS, at different electron concentrations N and damping factors Γ_{ISB}. Figures 4.5a, 4.5c, 4.5e on the left correspond to Γ_{ISB}=12meV, and Figures 4.5b, 4.5d, 4.5f on the right correspond to Γ_{ISB}=6meV (as will be discussed later in the discussion, Γ_{ISB}=12meV and 6meV are respectively the value of the ISB damping factor at room temperature and at 78K). These curves are computed with the same QW's thickness L_{QW}=10.1nm, corresponding to an initial ISB transition energy $\omega_{0\,ISB}$=131.8meV without doping. Due to non-parabolicity of the subbands, we observe a redshift of the resonance with increasing electron con-

centration N in Figures 4.5a, 4.5c and Figures 4.5b, 4.5d [1]. For instance, let's consider N=1×$10^{18}cm^{-3}$ represented with yellow curves. The ISB transition energy is reduced from $\omega_{0\,ISB}$=131.8meV (black dashed vertical line) to ω_{ISB}=127.0meV with Γ_{ISB}=12meV and ω_{ISB}= 128.9meV with Γ_{ISB}=6meV (orange dashed vertical line) as illustrated in the plot of $\epsilon''_{QW\,z}$ in Figures 4.5c and 4.5d. It is interesting to notice the lineshape of ϵ'' in data generated by METIS. Due to non parabolicity consideration, the lineshape is different from a Lorentzian, especially at larger N. The linewidth of ϵ'' increases with N and is no longer equal to Γ_{ISB}, which is very different from the Drude-Lorentz model for ISB transition presented in chapter 1.

A second effect, the depolarization shift, moves the QW's ISB absorption peak in the opposite direction toward larger energy. As already discussed in section 1.76 about Berreman's absorption in a flat thin film, the A_z absorption of a QW is proportional to $\omega\mathrm{Im}\left(\frac{-1}{\epsilon}\right)$, as given in the following equation:

$$A_{zQW} = \frac{\omega}{c}\frac{sin\theta^2}{cos\theta} Im\left(\frac{-1}{\epsilon_{QW\,z}}\right)|\epsilon_{InAlAs}|L_{QW} = \frac{\omega}{c}\frac{sin\theta^2}{cos\theta}\frac{\epsilon''_{QW\,z}}{|\epsilon_{QW\,z}|^2}|\epsilon_{InAlAs}|L_{QW}, \tag{4.1}$$

where θ is the angle of incidence. The origin of the depolarization shift is the lowering of the real part of the dielectric function $\epsilon'_{QW\,z}$ due to the ISB transition's contribution. This lowering leads to an enhancement of E_z in the quantum well, leading to a maximum absorption located at the maximum of $\omega\mathrm{Im}(\frac{-1}{\epsilon})$. We have $A_z \propto \omega\mathrm{Im}\left(\frac{-1}{\epsilon}\right) = \omega\frac{\epsilon''}{|\epsilon|^2}$, meaning that A_z is proportional to a product of the initial aborption lineshape ϵ'' and the ENZ enhancement factor $\frac{1}{|\epsilon|^2}$. $\omega\mathrm{Im}\left(\frac{-1}{\epsilon}\right)$ is plotted in Figures 4.5e and 4.5f. $\omega\mathrm{Im}\left(\frac{-1}{\epsilon}\right)$ has a lorentzian lineshape and a FWHM equal to Γ_{ISB}. The absorption peak is shifted to $\tilde{\omega}_{ISB} = \sqrt{\omega_{ISB}^2 + \omega_P^2}$, where ω_P [2] is the plasma frequency. Typically, for N=1×$10^{18}cm^{-3}$ (yellow curves), the absorption peak is shifted to $\tilde{\omega}_{ISB}$=136.2meV for Γ_{ISB}=12meV and $\tilde{\omega}_{ISB}$=137.9meV for Γ_{ISB}=6meV (illustrated by yellow dashed-dotted vertical line). These blueshifts correspond to a plasma frequency of about ω_P ∼49meV and a depolarization shift of about 9meV. [3] The quantity $\omega\mathrm{Im}\left(\frac{-1}{\epsilon}\right)$ is increased by a factor of about 3-6 between the value computed at ω_{ISB} (where $\omega\mathrm{Im}\left(\frac{-1}{\epsilon}\right) \sim 5$) and the one computed at $\tilde{\omega}_{ISB}$ (where $\omega\mathrm{Im}\left(\frac{-1}{\epsilon}\right) \sim 15-30$), meaning that to maximize $A_{z\,QW}$, we should optimize the structure at $\tilde{\omega}_{ISB}$ and not at ω_{ISB} [4].

1. Indeed, when $k_{//}$ increases, the vertical transition's energy is reduced, so in average the intersubband transition shifts towards smaller energy.

2. $\omega_P = \sqrt{\frac{Ne^2 f_{osc}}{m_0^* \epsilon_0 \epsilon_\infty}}$, where f_{osc} is the ISB transition oscillator's strength.

3. It's interesting to notice that eventhough ω_P does not depend on Γ_{ISB}, the absorption peak $\tilde{\omega}_{ISB}$ does. Indeed, the redshift by non-parabolicity of the subbands depends on Γ_{ISB}, and transmits this dependence to ω_{ISB}, then $\tilde{\omega}_{ISB}$.

4. The factor 3-6 is mainly attributed to a large $\frac{1}{|\epsilon|^2}$ at $\tilde{\omega}_{ISB}$ (small $|\epsilon|$) and a small $\frac{1}{|\epsilon|^2}$ at ω_{ISB} (large $|\epsilon|$ due to resonance).

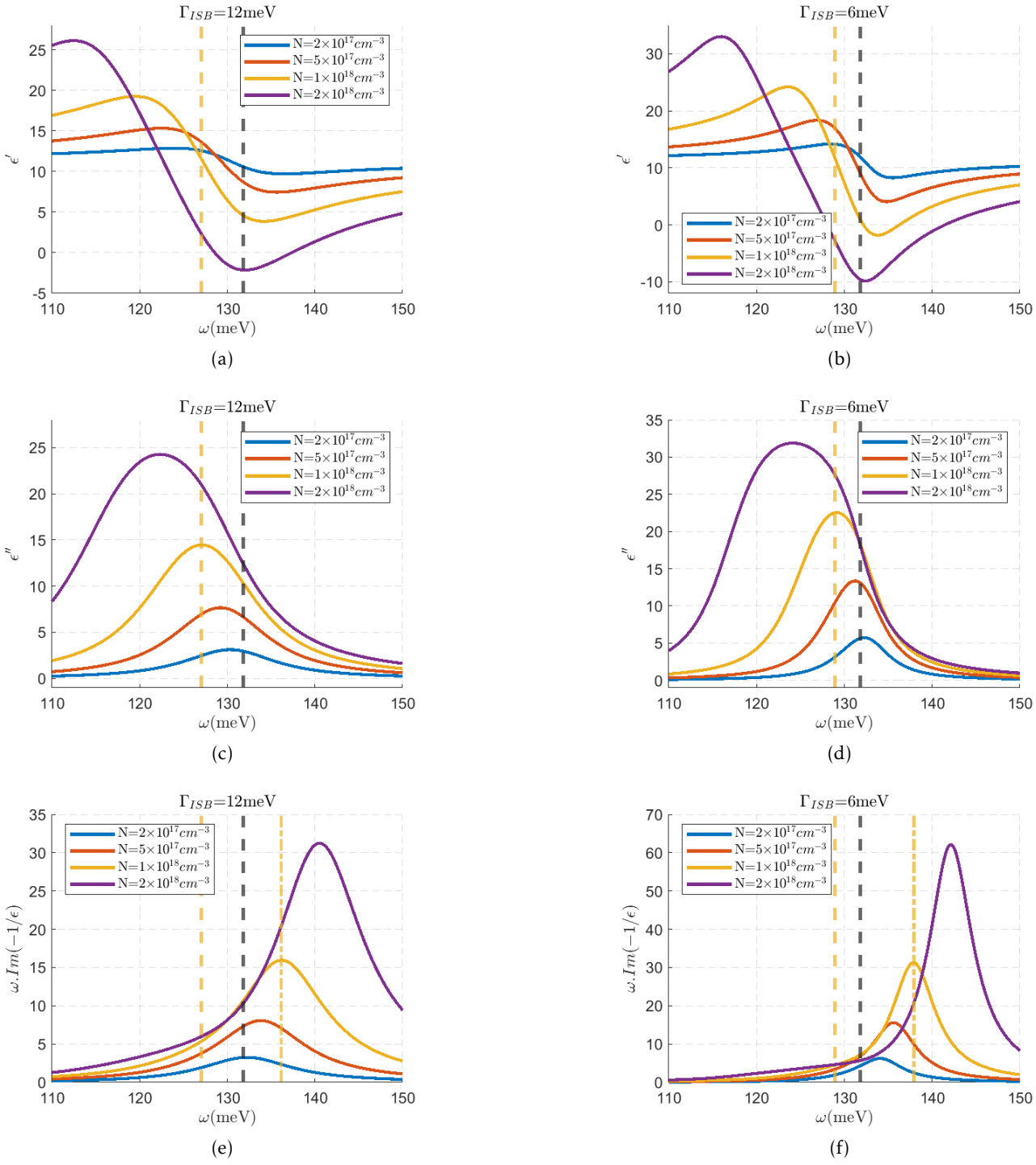

Figure 4.5 – a), c), e) Evolution of ISB dielectric function $\epsilon'_{QW\,z}$, $\epsilon''_{QW\,z}$ and the absorption lineshape $\omega\mathrm{Im}\left(\frac{-1}{\epsilon}\right)$ as a function of electron concentration N, generated by METIS. Γ_{ISB}=12meV, L_{QW}=10.1nm. $\epsilon'_{QW\,z}$ and $\epsilon''_{QW\,z}$ are redshifted to ω_{ISB} (yellow dashed vertical line for N=1×10$^{18}cm^{-3}$) compared to $\omega_{0\,ISB}$=131.8meV (black dashed vertical line) due to non-parabolicity of subbands. The absorption lineshape $\omega\mathrm{Im}\left(\frac{-1}{\epsilon}\right)$ peaks at $\tilde{\omega}_{ISB}$(yellow dashed vertical line for N=1×10$^{18}cm^{-3}$) due to depolarization shift. b), d), f) Similar plots with Γ_{ISB}=6meV.

In general, to get a large ENZ enhancement factor $\frac{1}{|\epsilon|^2}$ and thus maximize the useful absorption $A_{z\,QW}$, we want a large doping N and a small Γ_{ISB}. On the other hand, when the doping N increases, the dark current and noise in QCD also increase exponentially, as stated in the formula:

$$J_{dark} = N_{QW}^{excited\ state}\Gamma^{LO} = \frac{\rho_{2D}}{\beta} exp\left[\beta\left(E_F - \hbar\omega_{ISB}\right)\right]\Gamma^{LO} = \frac{\rho_{2D}}{\beta} exp\left[\beta\left(\frac{N}{\rho_{2D}} - \hbar\omega_{ISB}\right)\right]\Gamma^{LO} \tag{4.2}$$

where:

- J_{dark} is the electron dark current density ($cm^{-2}.s^{-1}$),
- $N_{QW}^{excited\ state}$ is the 2D electron density populating the excited state of the QW (cm^{-2}),
- E_F is the Fermi energy (eV),
- N is the 2D electron density of the QW (cm^{-2}),
- ρ_{2D} is the density of state of the QW ($eV^{-1}.cm^{-2}$),
- $\beta = 1/(k_B T)$ is the inverse of the thermal energy (eV^{-1}),
- $\hbar\omega_{ISB}$ is the ISB transition energy (eV).
- Γ^{LO} is the electron scattering rate between the QW and the extractor stage due to LO phonon (s^{-1}).

This formula is derived from a similar formula for dark current in QWIP device in reference [24]. Indeed, when N increases, the Fermi level of the QCD structrure gets closer to the excited state of the active QW, increasing the population of the QW's excited state, thus increasing the dark current and noise exponentially. We chose a compromise between optimizing $A_{z\,QW}$ and having a reasonable level of noise. We opted for two structures, one doped at $5{\times}10^{17} cm^{-3}$ and the other at $1{\times}10^{18} cm^{-3}$ for experimental realization of ENZ-QCD.

The evolution of $K_{ENZ\ InAlAs}$ as a function of N and Γ_{ISB} is illustrated in Figure 4.6. For N=$1{\times}10^{18} cm^{-3}$ and Γ_{ISB}=12meV, the minimum of $\epsilon'_{QW\,z}$ is about 4 and the minimum of $|\epsilon_{QW\,z}|$ is about 6. We do not reach the ENZ regime in this case, nevertheless we already benefit from a dielectric enhancement $K_{Dielectric\ InAlAs} \sim 2.7$. For N=$1{\times}10^{18} cm^{-3}$ and a Γ_{ISB}=6meV, $\epsilon'_{QW\,z}$ crosses zero and $\epsilon''_{QW\,z} \sim 4$ at 9.2μm, leading to $K_{ENZ\ InAlAs} \sim 6.5$.

Finally, it's important to point out that the depolarization shift is related to the continuity equation of the electric displacement D_z. As a consequence, we should not include the depolarization shift to the ISB dielectric function used in electromagnetic computations based on Maxwells equations like Reticolo, as it is already taken into account in the computation, thanks to a proper description of the structure and its boundary conditions. Other computation methods like the Coupled Mode Theory (CMT, will be described in the discussion 4.5.1.2) do not treat electromagnetic continuity equations and thus require including the depolarization shift in the description of the ISB transition.

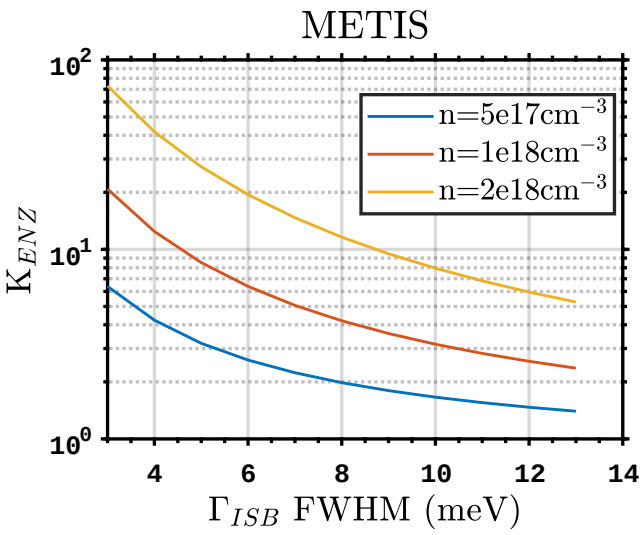

Figure 4.6 – $K_{ENZ\ InAlAs}$ computed with different dopings and damping factors using METIS data. For N=1×10$^{18}cm^{-3}$, $K_{Dielectric\ InAlAs} \sim 2.7$ for Γ_{ISB}=12meV and $K_{ENZ\ InAlAs} \sim 6.5$ for Γ_{ISB}=6meV.

4.2.1.2 Reticolo electromagnetic computation

The target wavelength for detection is 9μm (137.8meV). After fixing the doping N_{QW} at 5×10$^{17}cm^{-3}$ and 1×10$^{18}cm^{-3}$, I chose the ISB transition energy $\omega_{0\,ISB}$ respectively to be 135.3meV (L_{QW}=9.9nm) and 131.8meV (L_{QW}=10.1nm), so that the plasma-shifted frequency $\tilde{\omega}_{ISB} \sim$ 137.8meV (9μm). Values for L_{QW} are given from III-V lab's database. For these electromagnetic optimization, I used Γ_{ISB}=12meV. The QCD structure is reminded in Figure 4.8a.

I mapped the useful quantum well absorption $A_{z\,QW}$ and the reflectance R as a function of doping and geometrical parameters: S, P and $L_{contact\ injector}$, at normal incidence and with TM polarization. As in the ENZ-EOM case, the resonance frequency depends little on P. P is chosen to be 6μm, larger than the one of the ENZ-EOM (P=4μm) in order to facilitate the grating fabrication by lithography. Figures 4.7a ad 4.7b depicts the mapping of $A_{z\,QW}$ for the two doping levels, with P=6μm and Ordal's value for Au and Ti dielectric functions [99]. We observe two strong absorption lines at $S \sim 3.42\mu$m (MIM mode TM_{03}) and $S \sim 1.00\mu$m (MIM mode TM_{01}) on both maps. The TM_{03} mode has a larger absorption line in S than TM_{01} (meaning a larger fabrication tolerance for S value). We chose the TM_{03} ($S \sim 3.42\mu$m) mode over TM_{01} ($S \sim 1.00\mu$m) also to ease the fabrication by lithography. The TM_{03} mode has a maximum of $A_{z\,QW}$ reaching 58% and 72% of the incidence power, with cavity thicknesses L_{total} of 347nm and 407nm respectively for N_{QW}=5×10$^{7}cm^{-3}$ and 1×10$^{18}cm^{-3}$. These values are kept as optimal geometrical parameters for QCD structure.

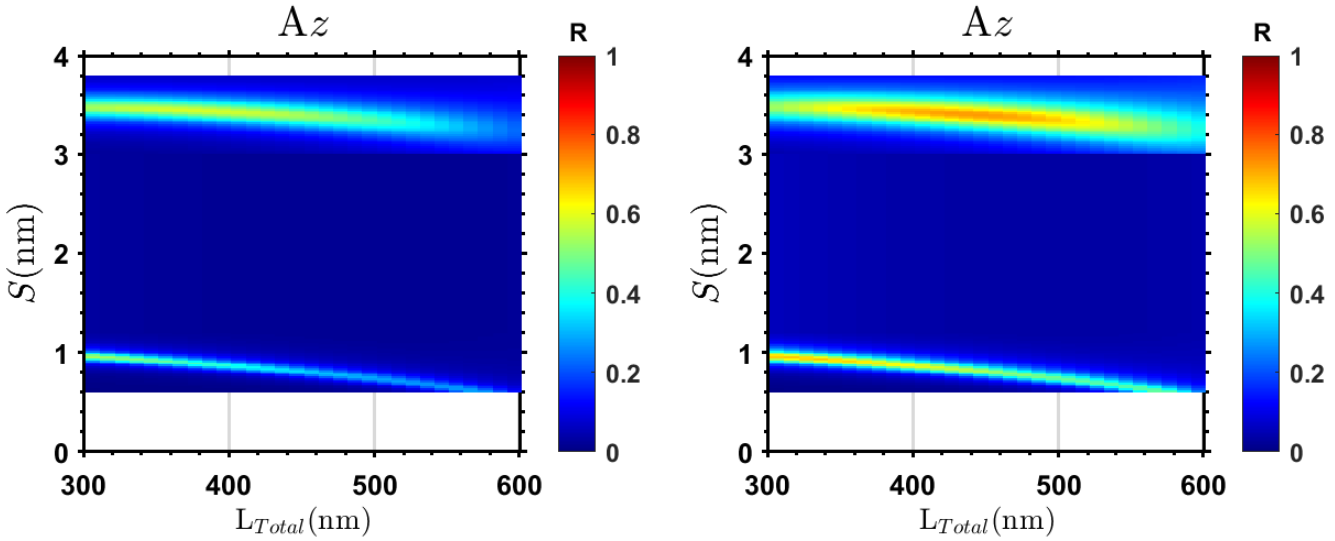

(a) (b)

Figure 4.7 – Computation with Reticolo: Optimization of $A_{z\,QW}$ as a function of strip's width S and total semiconductor thickness L_{total}. The period P is fixed at 6μm. The doping concentration of the QW is $5{\times}10^{17} cm^{-3}$ in a) and $1{\times}10^{18} cm^{-3}$ in b).

Figures 4.8b,c,d depict the field distribution of $|H_y|$, $|E_x|$, $|E_z|$ at normal incidence, TM polarization in the optimized QCD structure with N_{QW}=$1{\times}10^{18} cm^{-3}$. We observe the typical vertical profile with three antinodes in H_y map, characteristic of a TM_{03} mode. The E_x component is quite small in the semiconductor layer compared to E_z (Figure4.8c). As expected, the E_z field is enhanced in the QW layer, as illustrated in Figures 4.8d (for $|E_z|$) and 4.8e (for $|E_z|^2$). Locally, $|E_z|^2$ can be enhanced up to 80 times the norm of the incidence electric field (normalized to 1), thanks to a combination of the dielectric enhancement and the MIM cavity enhancement. The MIM cavity accounts for an enhancement factor of about 28 and the dielectric contrast enhancement (ENZ enhancement) multiplies the field with another factor of about 2.9 (in agreement with the $K_{Dielectric\ InAlAs} \sim 2.7$ for N=$1{\times}10^{18} cm^{-3}$, Γ_{ISB}=12meV computed in Figure 4.6). Figure 4.8f depicts the $|E_z|^2$ field averaged on the whole width of one period P. On average, the MIM cavity accounts for an enhancement factor of about 7.0 of $|E_z|^2$ and the dielectric contrast enhancement for an enhancement factor of about 2.9 to reach a final enhancement of about 20 time the incidence $|E_z|^2$ in the QW layer.

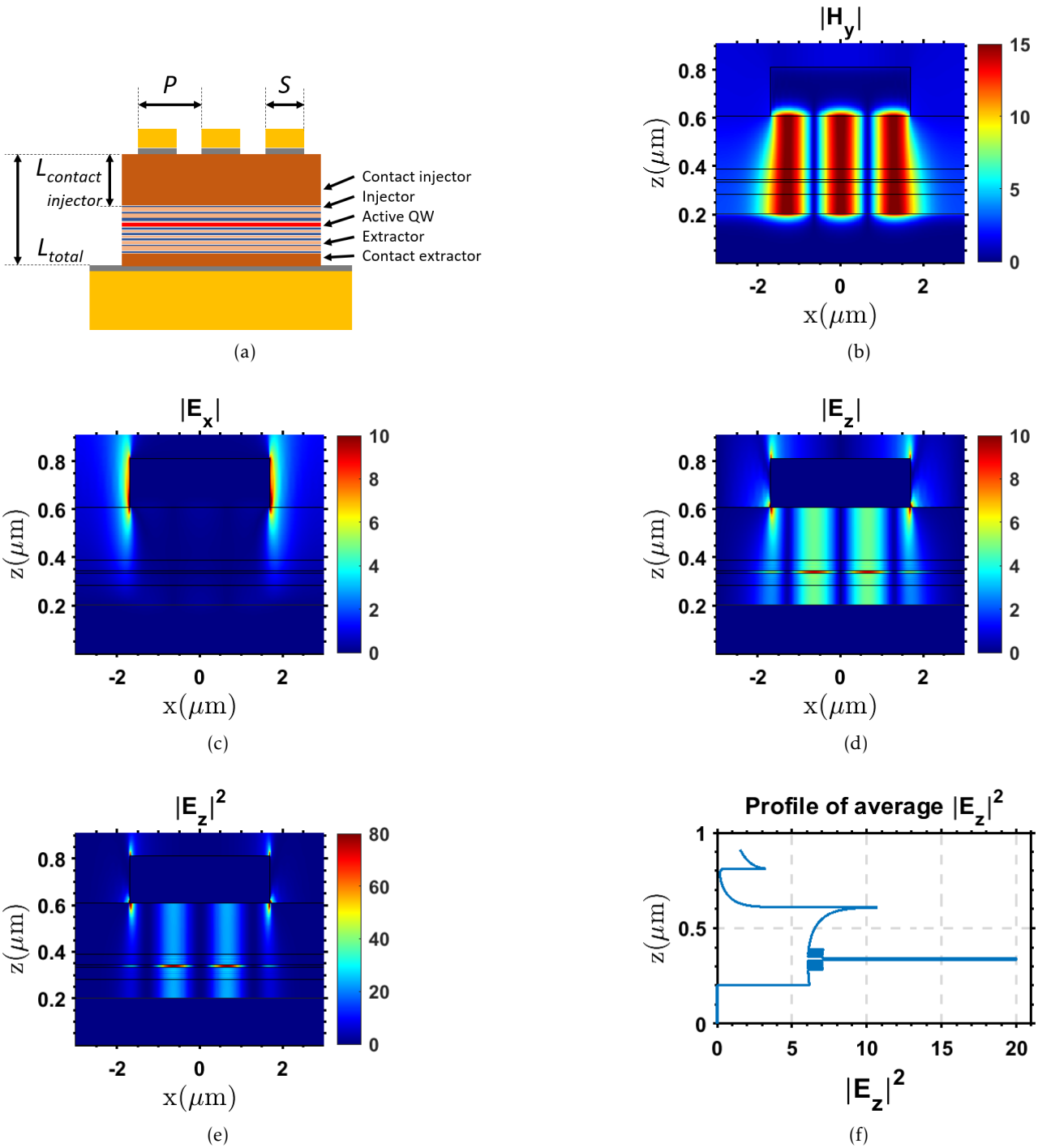

Figure 4.8 – a) Schematic of QCD device b,c,d) Field distribution of $|H_y|$, $|E_x|$, $|E_z|$, computed with Reticolo at $\lambda = 9\mu$m, normal incidence, TM polarization, $N_{QW}=1\times10^{18}cm^{-3}$, P=6μm, S=3.42μm, L_{Total}=407nm. The corresponding useful absorption is $A_{z\,QW}$=72%. The field distributions show a typical vertical profile with three antinodes in H_y map, characteristic of a TM_{03} mode. The $|E_z|$ field in enhanced in the QW layer, up to a factor of about 9 locally. $|E_x|$ component is quite small in the semiconductor layer compared to $|E_z|$. e) $|E_z|^2$ distribution. f) $|E_z|^2$ profile in the z direction, averaged over the whole period P. $|E_z|^2$ is enhanced up to 80 times of the incidence field locally and and up to 20 times when averaged over the whole period. The value of $|E_z|^2$ in the QW is multiplied by a factor of about 2.85 compared to the field in the InAlAs barrier, due to the dielectric contrast enhancement.

Figures 4.9a and 4.9b depict the angular dispersion maps of the useful absorption $A_{z\,QW}$ and the reflectance R in the optimized QCD structure doped at N=1×10$^{18}cm^{-3}$ in TM polarization. The horizontal axis depict k_x, the in-plane wave vector, defined as $k_x = k_{x\,max}sin(\theta) = \frac{\omega}{c}sin(\theta)$ where θ is the angle of incidence, varying from 0 to 90°. We observe the non-dispersive characteristic of the MIM mode (because $P > S + 2L_{total}$) in both $A_{z\,QW}$ and R maps: the mode is almost horizontal as k_x increase from 0 to $k_{x\,max}$. Interestingly, we also observe an anti-diagonal line on both maps, cutting the MIM mode dispersion at $k_{x\,cutoff}$ about half of $k_{x\,max}$ in air. For $k_x > k_{x\,cutoff}$ (corresponding to a cuttoff angle of 30°), $A_{z\,QW}$ decreases while R increases. Indeed, this anti-diagonal line corresponds to the first diffraction mode of the 6um period grating. The useful absorption of the designed QCD is almost constant for incidence angles smaller than 30° and is reduced for incidence angle larger than 30° by about a factor of 2 (from 72% to about 35%). This directional filtering effect can be an interesting feature for an infrared detector, offering a reduction of the background signal coming from the surrounding and not the source of interest which is usually oriented at normal incidence of the detector.

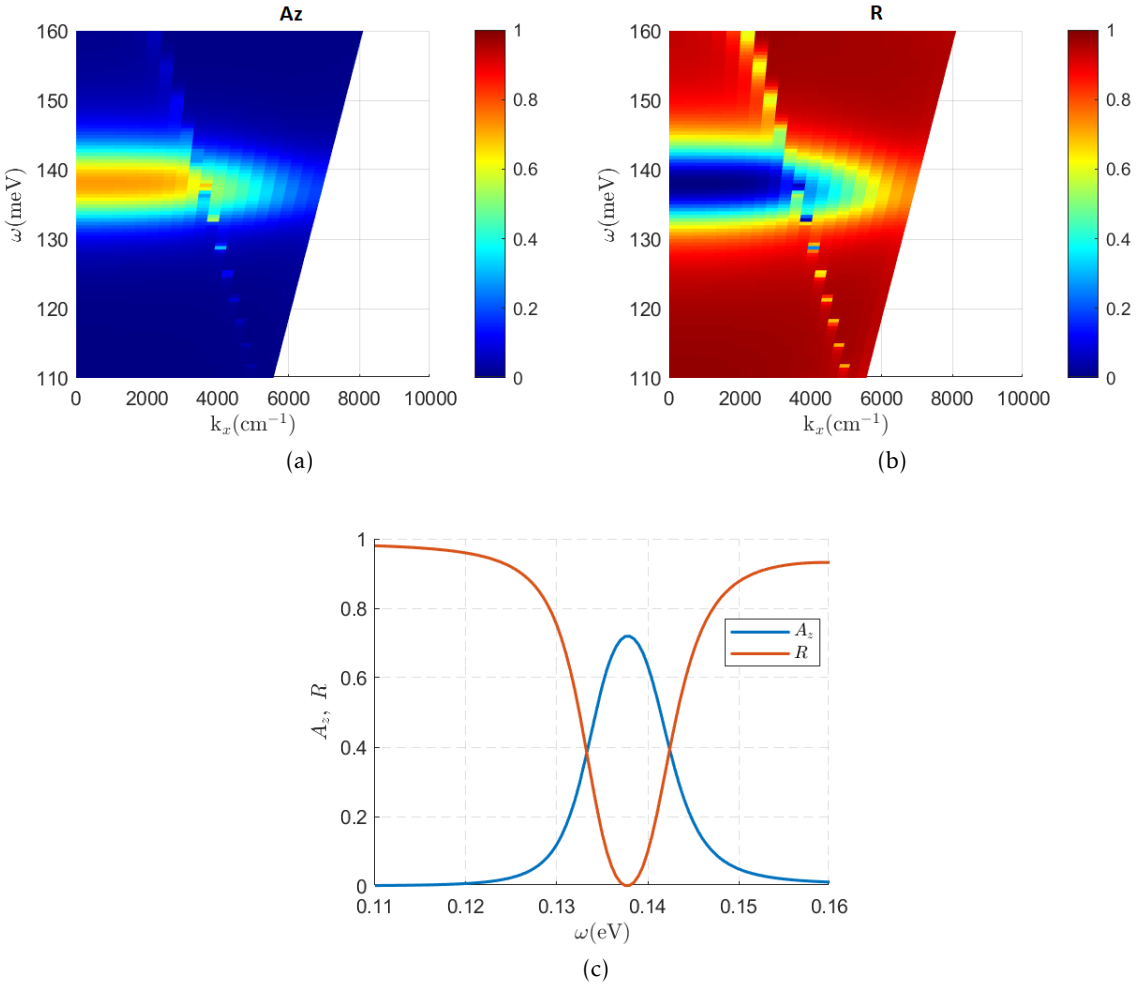

Figure 4.9 – Computation with Reticolo: a,b) Useful absorption A_z and reflectance R of QCD. c) Absorption A_z and reflectance R spectra at normal incidence. Ordal dielectric functions for Au, Ti.

Figure 4.9c depicts the $A_{z\,QW}$ and R spectra at normal incidence of the same structure. The absorption $A_{z\,QW}$ reaches 72% of the incidence power at 137.7meV and has a linewidth of about 12meV

(FWHM). The reflectance R on the other hand goes down to zero at 137.7meV.

4.2.2 Transport optimization

The transport optimization was realized by Mathurin Lagrée (III-V lab), using METIS. Usual QCD structures designed with METIS have multiple periods and use periodical boundary conditions. For this single-period QCD structure, he took into account the presence of semiconductor contacts layers, doped at $1\times10^{17}cm^{-3}$. The optimized structures are depicted in Figure 4.10a (QCD40, doping $N_{QW}=5\times10^{17}cm^{-3}$) and Figure 4.10b (QCD41, doping $N_{QW}=1\times10^{18}cm^{-3}$) [5]. The electron extraction probabilities P_e are estimated to be 48% and 47% respectively for QCD40 and QCD41.

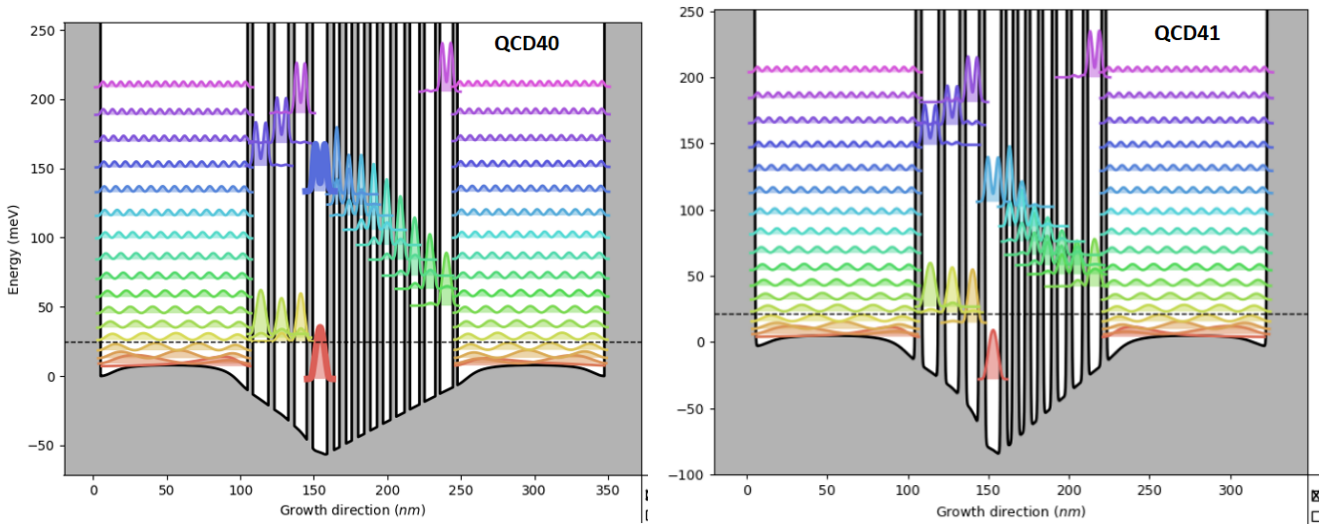

(a) (b)

Figure 4.10 – Band structure of the QCD device, computed by Mathurin Lagrée with METIS code, a) QCD40 and b) QCD41. $P_e \sim 48\%$ and 47% respectively for QCD40 and QCD41.

4.3 Device fabrication

We have two substrates: QCD40 ($N_{QW}=5\times10^{17}cm^{-3}$) and QCD41 ($N_{QW}=5\times10^{17}cm^{-3}$), grown by MBE on InP. The epitaxy structures are reported in Appendix B.3. In addition to the active QCD stack, we use 200nm InGaAs/ 200nm InAlAs as etch-stop layers. An SEM image of the stack QCD41 before substrate transfer is depicted in Figure 4.11. From bottom to top, we have 192nm InGaAs etch-stop, 206nm InAlAs etch-stop, 321nm of the QCD active layers, 170nm Au, followed up by Ti/SiO_2/Ti.

The fabrication process followed the same main steps as the ENZ-EOM fabrication: the active layer is transferred on gold substrate, followed up by different lithography steps to pattern the devices.

- Substrates dicing into square samples of 1x1cm^2.
- Deoxidation, metallization (Ti/Au/Ti 5/200/20 nm) and reinforcement with SiO_2 sputtering (200nm).
- Ormostamp wafer bonding on Pyrex glass substrate.

5. Real doping is a little bit higher to compensate charge transfer to the contact layers.

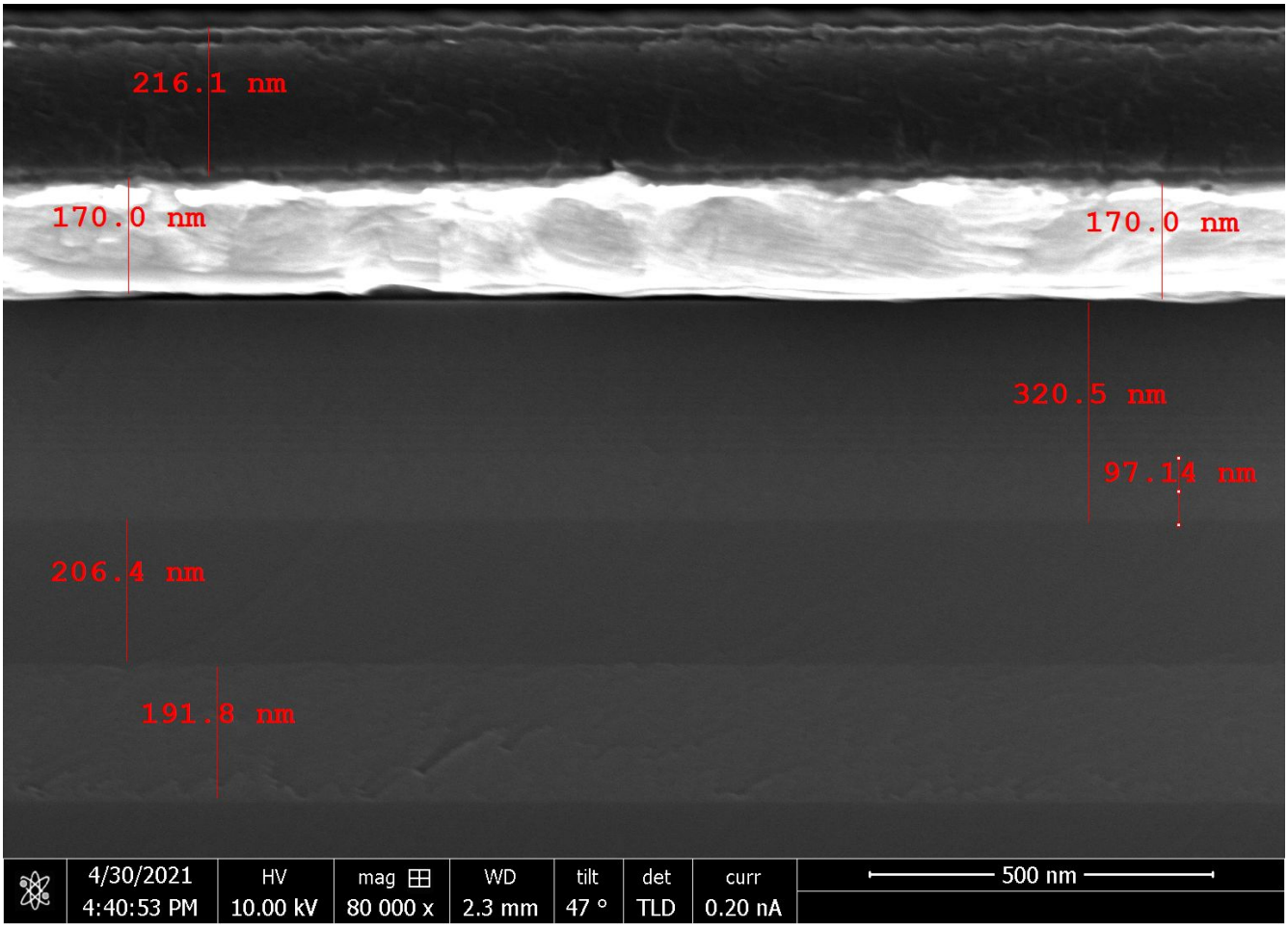

Figure 4.11 – SEM image of QCD41 substrate's cross section with Ti/Au/Ti/SiO_2/Ti on top. The one of QCD40 is given in Appendix B.3.

- Subtrate InP etching in HCl 37%.
- Etch-stop layers (200nm InGaAs, 200nm InAlAs 52% Al) removing with selective etchings citric acid solution:H_2O_2 1v:1v (for InGaAs) and HCl:H_2O 3v:1v (for InAlAs, etch rate non-linear in time).
- Lithographies

The lithography process is depicted in Figure 4.12a. There are four process levels: the top grating deposition (L1), the mesa etching (L2), the insulator bands deposition (L3) and the top contact pads deposition (L4). I realized three main samples: QCD40-2-1, QCD41-2-3 and QCD40-2-3. QCD40-2-1 (N_{QW}=5×10$^{17}cm^{-3}$) and QCD41-2-3 (N_{QW}=1×10$^{18}cm^{-3}$) are realized at the same time in most steps, they underwent low temperature process using UV lithography, below 125°C. QCD40-2-3 (N_{QW}=5×10$^{17}cm^{-3}$) is realized separately from the two others, underwent higher temperature process using e-beam lithography (about 12 minutes at 170°C in total).

- L1: The top grating is realized either by e-beam lithography (PMMA A7 negative resist, process 170°C) or UV lithography (AZ5214E negative mode, 125°C), followed up by deoxidation and deposition of Ti/Au 5/200nm. Two contact strips ('languettes') of 40x40μm^2 size are designed on the grating's extremities for electrical connection with the top contact pads in L4. This design reduces the surface of non-etched semiconductor out of the optically active grating zone, thus reduces the dark current in the device.
- L2: Deoxidation, UV lithography (AZ5214E, positive mode, 125°C). The semiconductor surrounding the grating is completely etched down to Au substrate, using H_3PO_4:H_2O_2:H_2O 9v:3v:120v.
- L3: UV lithgraphy (NLOF2070, thick negative resist, 105°C, detailed in B.3). SiO_2 sputtering is deposited to create large bands of insulator [6]. 200nm SiO_2 for QCD40-2-1 and QCD41-2-3, 350nm SiO_2 for QCD40-2-3. The insulator bands overlap the grating's contact strips, ensuring insulation between the top contact pad and the back contact.
- L4: UV lithgraphy (NLOF2070, thick negative resist, 105°C). Deoxidation and metallization Ti/Au 5/1000nm.

6. Ensuring the mechanichal adhesion of SiO_2 on Au, usually fragile for small contact surface patterns.

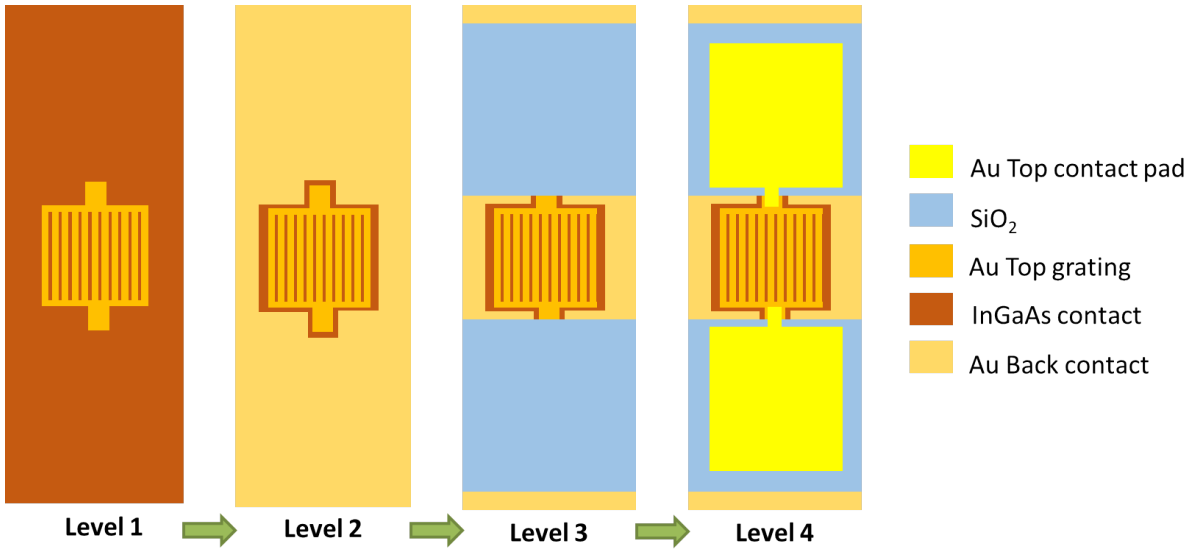

(a)

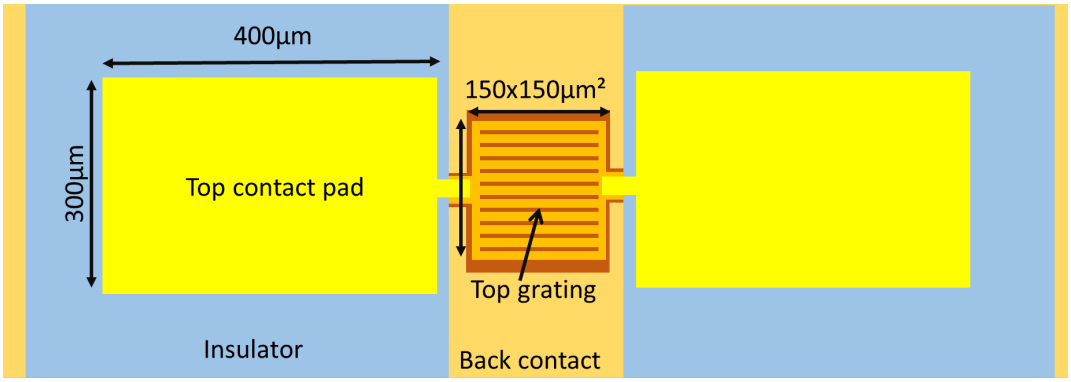

(b)

Figure 4.12 – a) Lithography process: Level 1 (L1) Top grating deposition, Level 2 (L2) Mesa etching, Level 3 (L3) Insulator band deposition, Level 4 (L4) Top contact pads deposition. b) Top view of the final device.

Like with ENZ-EOM samples, devices with various S from 3.00 to 3.80μm with a step of 100nm are made. In what follows, they are named individually after their row and column. For instance, row 'C' has 12 devices from *'CA'* to 'CL', their name, their nominal and experimental values of S are reported in Table 4.1. Depending on sample, the experimental value of S are typically 100-150nm larger than the nominal value. We also have *'CF'* fully covered with Au, served as reference mirror, and *'CL'* without grating for comparison.

Figure 4.11 depicts an SEM image of QCD devices after fabrication. Several black dots and lines correspond to SiO2 residus after L3 step. Oblique lines on the gratings are artifacts of SEM imaging due to a Moiré effect between the scanning electron beam and the grating. Figure 4.13b shows a contact strip. SiO_2 is known for usually creating curved tail residues after lift-off, which can prevent continuous metal connection on top. In our case, this effect seems not to be important and the contact is in good condition.

Name	CA	CB	CC	CD	CE	CG	CH	CI	CJ	CK
Nominal S (μm)	3.00	3.10	3.20	3.30	3.35	3.40	3.50	3.60	3.70	3.80
S_{exp}(μm) QCD40-2-3	3.113	3.201	3.322	3.434	3.484	3.545	3.660	3.767	3.866	3.974
S_{exp}(μm) QCD41-2-3	3.183	3.314	3.377	3.508	3.585	3.569	3.691	3.810	3.879	4.001

Table 4.1 – Table of S value of main devices on QCD40-2-3 and QCD41-2-3. *For QCD41-2-3, experimentally we have S_{exp}('CE')> S_{exp}('CG'), contrary to nominal values.

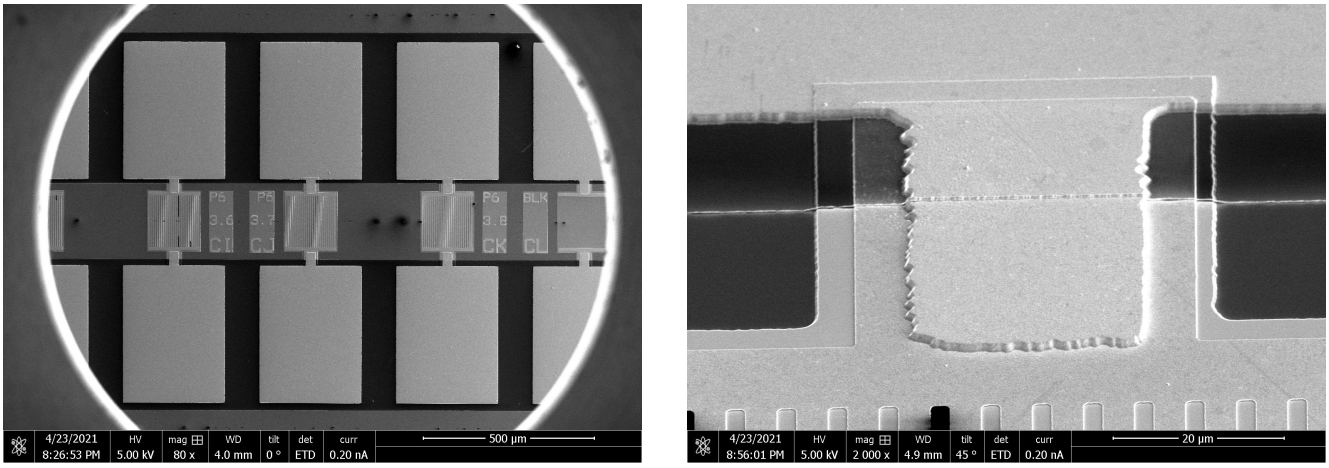

(a) (b)

Figure 4.13 – SEM images of QCD devices and contacts levels.

4.4 QCD characterizations

In this section, I will present optical, electrical, and opto-electrical characterizations of single-period ENZ-QCD samples. I realized reflectance measurements in a large range of temperature, I(V) characteristics, photocurrent and spectral response of these QCD. The experimental determination of the ISB transition (resonant frequency, FWHM) of a single QW is difficult. We will see in this section that the FTIR measurement of devices with different antenna strip width S provides rich information.

4.4.1 Optical characterization of resonance by μFTIR

The reflectance of QCD is measured with the μFTIR coupled with a Linkam module for temperature control, at ONERA lab. Figure 4.14 depicts the experimental setup. The sample in enclosed inside the Linkam's chamber, in contact with a holder where low temperature N_2 fluid circulates. The chamber's windows is made of BaF_2, transparent in visible and infrared ranges up to about 12μm, adapted to our wavelength range of interest. The chamber is purged with N_2 gas during several minutes in order to reduce the percentage of water vapor.[7] The lowest nominal set temperature of the Linkam module is 79K[8].

7. During the cooldown, we observed the formation of water condensation on the sample. Nevertheless, these condenstations did not prevent the reflectance measurement from giving clear MIM resonance signature, in good agreement with simulation results.

8. The real temperature of the sample may be higher than this set value.

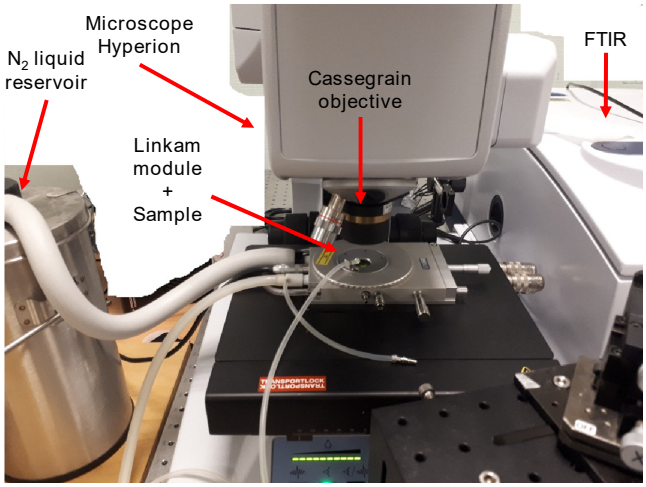

Figure 4.14 – μFTIR setup with Linkam module for low temperature reflectance measurement.

Figures 4.15a and 4.15b depict the reflectance spectra of QCD devices respectively on samples QCD40-2-3 and QCD-41-2-3, measured at room temperature. Figures 4.15c and 4.15d depict similar measurements realized at 79K. The reflectance spectra are acquired on different devices *'CA'* to *'CL'*. As detailed in the fabrication section, on these devices, S increases nominally from 3μm to 3.8μm, with the exception of 'CF' (fully covered with Au) and 'CL' (without grating). The lower x-axes depict the frequency ω in meV and the upper x-axes depict the corresponding wavelength in μm to ease the interpretation.

At room temperature, we observe essentially a regular evolution of the MIM resonant frequency as a function of the antenna strip width S. On sample QCD40-2-3 (lower doping), if we compare the reflectance dip amplitude of the devices array *'CA'* to *'CK'*, it reaches its lowest value (about 0.1) in *'CA'*, then increases till *'CG'* where it reaches about 0.2, before slightly decreasing from *'CH'* to finally increases again with *'CK'*. There is indeed a local maximum of the reflectance dip amplitude as a function of the strip width S at about 9.3μm for the *'CG'* deivce. The absorption linewidth also increases towards *'CG'* and *'CE'* (FWHM ~9.60 meV) as compared to *'CA'* and *'CK'* (FWHM ~8.25 and 7.80meV), as illustrated in Figure 4.16a. This is a sign of the ISB transition in these devices at room temperature. Indeed, we observe similar evolution of the reflectance dip amplitude and the absorption linewidth in simulation depicted in Figure 4.17b, in which the plasma shifted ISB transition is fixed at 9μm ($\tilde{\omega}_{ISB}$=137.7meV), and S varies from 3.05 to 3.75μm. The reflectance dip becomes shallower when S tends to 3.4μm and the MIM resonance tends to 9μm, where the ISB transition happens. The absorption linewidth also increases for S around 3.4μm. Figure 4.17c depicts the absorption $A_{z\,QW}$ in these structures. $A_{z\,QW}$ is largest for S=3.35μm and its absorption peaks at 9μm, corresponding to the same value S where reflectance dip amplitude reaches a local maximum as depicted in Figure 4.17b. For comparison, I also computed the reflectance of the same structures, in which the doping N_{QW} is reduced to zero, as depicted in Figure 4.17a. In the absence of doping, there is no ISB absorption, and the reflectance dip amplitudes are almost constant and reach zero for all S values.

On sample QCD41-2-3 (higher doping), similar behaviors are observed: a local maximum of the reflectance dip at about 9.5μm with the *'CG'* device and an broadenning of the reflectance dip toward *'CG'*. However, the tendency is not as regular as on sample QCD40-2-3. Indeed, devices *'CD'*, *'CG'* and *'CJ'* have some defects during fabrication process and correspondingly we observe irregularities in their spectra compared to other spectra of devices on the same row.

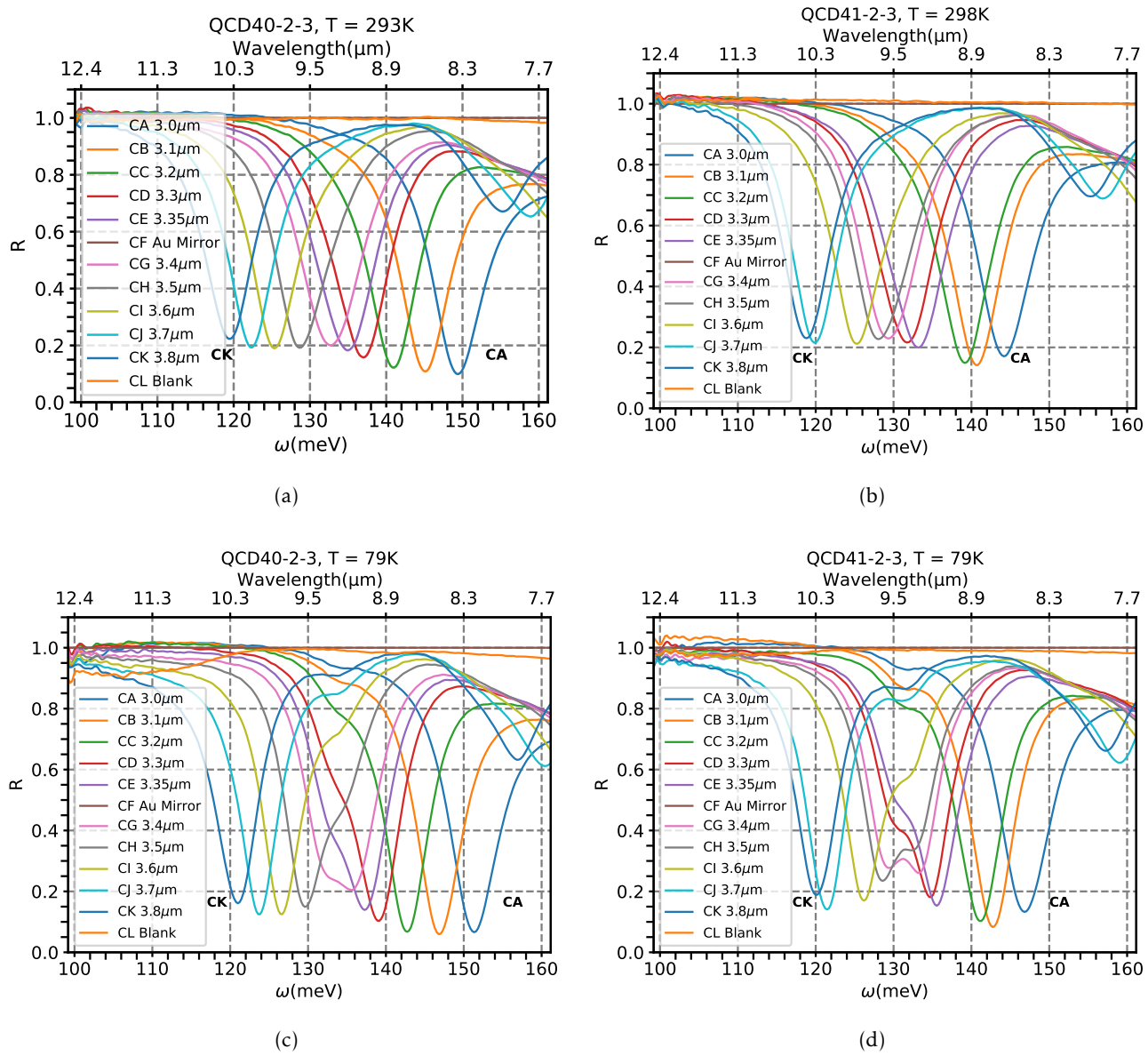

Figure 4.15 – a) and b) Reflectance spectra of devices with various strip width S on samples QCD40-2-3 and QCD41-2-3 at room temperature. The reflectance dip amplitude becomes shallower and the absorption linewidth increase towards *'CG'* device. This is a sign of the ISB transition in the QCD structure at room temperature.
c) and d) Similar to a) and b), but measured at 79K. The experimental plasma shifted ISB transition is observed at about 9.3μm (133.3meV) on sample QCD40-2-3 and 9.4μm (131.9meV) on sample QCD41-2-3.

At low temperature (79K), as illustrated in Figures 4.15c and 4.15d, we clearly observe the appearance of a second absorption dip in addition to the MIM resonance, as compared to room temperature measurement. This new resonance appears at about 9.3μm (133.3meV) on sample QCD40-2-3 and 9.4μm (131.9meV) on sample QCD41-2-3. We assign this resonance to the experimental plasmashifted ISB transition $\tilde{\omega}_{ISB}$. These experimental $\tilde{\omega}_{ISB}$ are a bit smaller than expected (137.7meV). On both

samples, the device *'CG'* corresponds to the closest MIM resonance with respect to the observed ISB resonance. However, we still observe two shallower dips instead of only one deeper reflectance dip. This is a signature of the strong coupling regime between MIM mode and ISB excitation: actually, these optical measurements indicate that the MIM mode is in closest resonance with the ISB transition around 9.3-9.5μm, on devices named *'CG'*. These devices *'CG'* and their adjacent neighbors are QCD that will potentially deliver largest photocurrent under illumination.

Figures 4.18a and 4.18b depict the reflectance spectra of the 'CG' device respectively on sample QCD40-2-3 and QCD41-2-3 at different temperatures, from room temperature down to 79K. We clearly observe the appearance of the ISB absorption peak and a transition from the weak coupling to the begining of the strong coupling regime between the ISB transition and the MIM mode.

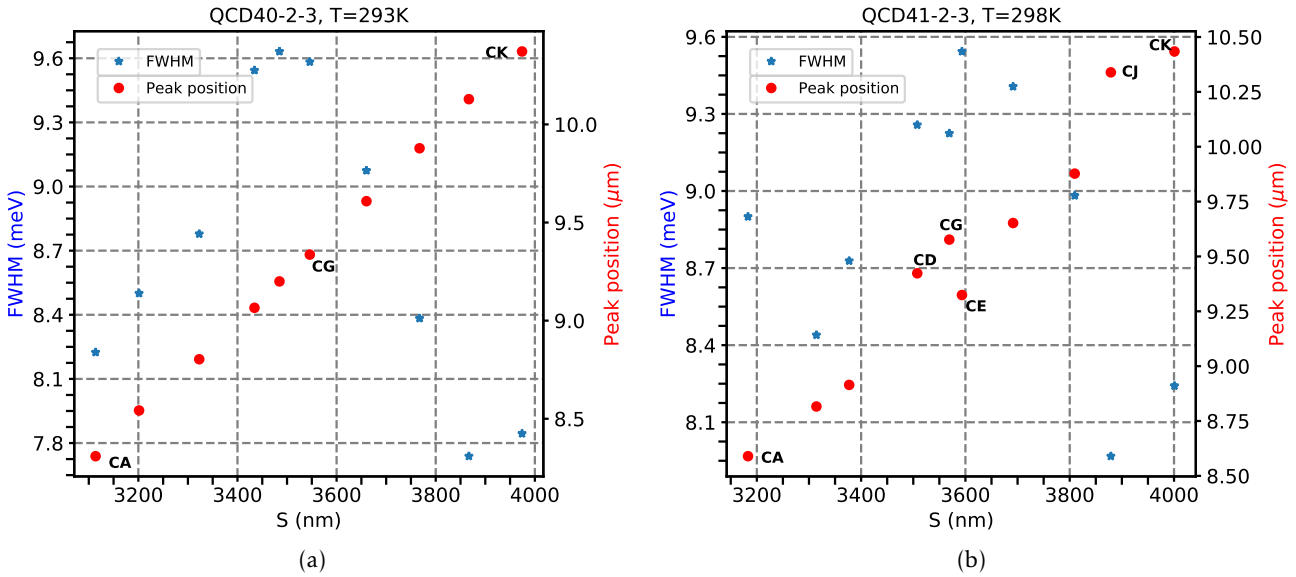

(a) (b)

Figure 4.16 – Evolution of the FWHM (blue star, left axis) and the resonance wavelength (red dot, right axis) as a function of the experimental antenna strip width S. a) QCD40-2-3: The peak position (in wavelength) increases almost linearly with the experimental strip width S. The linewidth increases towards *'CG'* and *'CE'*. b) QCD41-2-3: the peak position does not increase as regularly with S as in QCD40-2-3. Experimentally from SEM image, we have S_{exp}('CE')>S_{exp}('CG'). Three devices *'CD'*, *'CG'*, *'CJ'* have the wavelength of the peak position larger than the linear curve of other device. Indeed, these three devices have fabrication defects (observed in optical image) that potentially change their resonance.

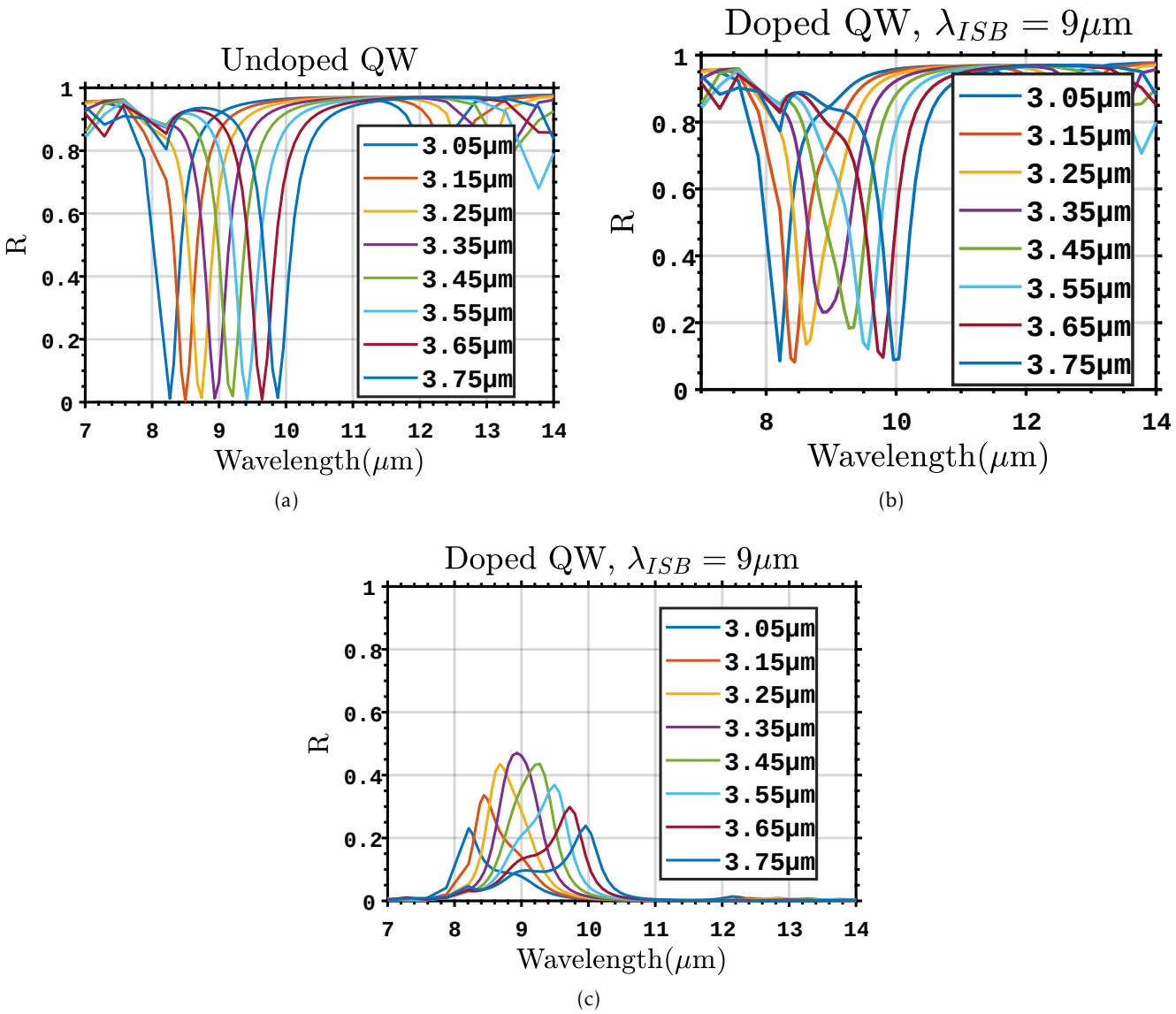

Figure 4.17 – Reticolo computations, carried out with Γ_{ISB} = 12meV, plasma shifted ISB transition at 9μm, Olmon Au dielectric function. a) Reflectance spectra of QCD structure with undoped QW: only MIM absorption is visible, the amplitude of the reflectance dip is almost constant and reaches zero. b) Reflectance spectra of similar QCD structure with QW doped at $1{\times}10^{18}$cm^{-3}. The reflectance dip becomes shallower when S tends to 3.4μm and the MIM resonance tends to 9μm, where the plasma shifted ISB transition happens. The absorption linewidth also increases for S around 3.4μm. c) Useful absorption Az of QW of the same QCD structure with QW doped at $1{\times}10^{18}$cm^{-3}. The absorption increases when S tends to 3.4μm.

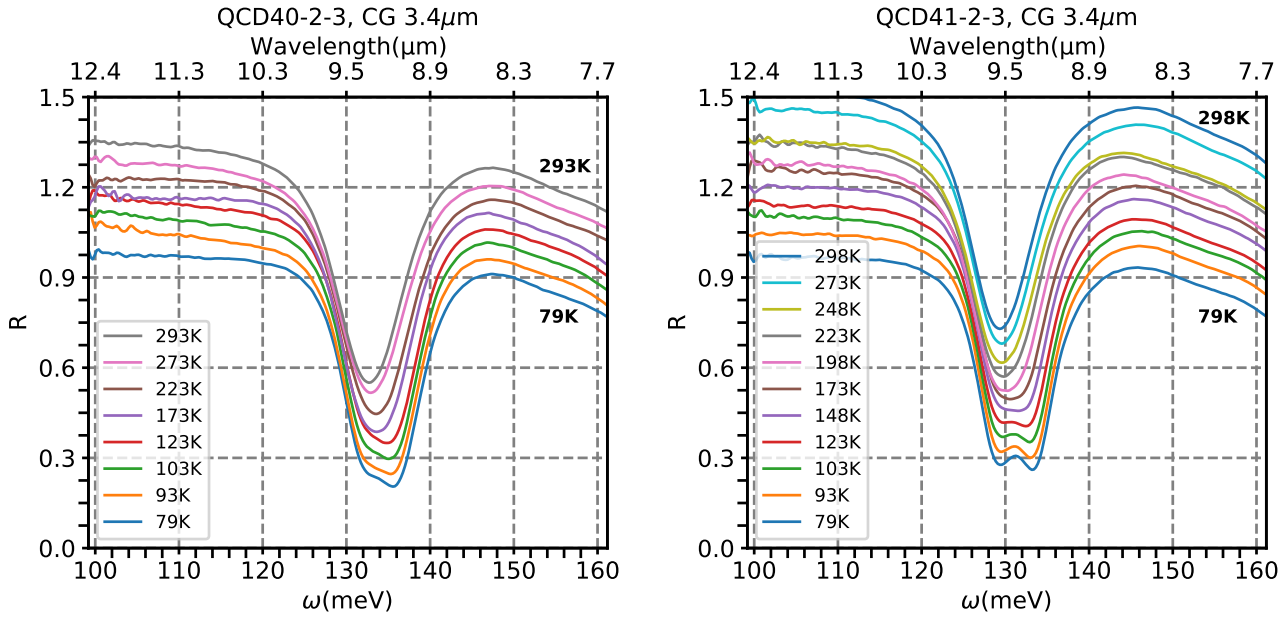

(a) (b)

Figure 4.18 – a) and b) Reflectance spectra at different temperatures of device 'CG', whose S=3.4μm nominally. Each sprectrum is offseted by 0.05 from the previous one. We observe the appearance of the ISB absorption peak when the temperature decreases from room temperature down to 79K.

4.4.2 Electrical and opto-electrical characterization of QCD

After the determination of devices offering the best resonance condition by optical measurements, I carried out electrical and opto-electrical characterizations at room temperature and cryogenic temperature. For cryogenic measurements, we chose to use a cryostat with probe station (Janis serie ST-100) with liquid nitrogen cooling. The experimental setup is depicted in Figures 4.19a and 4.19c. The sample is fixed vertically on a metallic cold finger which is in contact with liquid N_2. The cryostat is kept under primary vacuum to avoid water condensation. The sample can be accessed electrically via two probe arms [9] on the sides and optically via a ZnSe windows [10] in the front. After cooling down by liquid N_2, the temperature can be modified by a resistor element and a temperature controller (Lakeshore 335). The temperature probe is positioned close to the sample holder of the cold finger [11].

A first optical setup was designed to measure photocurrent and to estimate the EQE of the QCD devices. We used a blackbody (CI System SR-20) heated at 1200°C as IR source, coupled to a collimator (CI System ILET-4-2.0, 10.2cm and focal length 76.2cm). The collimator is followed by a lens made of ZnSe (5cm of diameter, 20cm of focal length) mounted on an xyz-translation stage, then a Germanium longpass filter with an edge at 8.11 microns and optionally an IR polarizer.

- The output flux of the blackbody is chosen with a set of pinholes of different sizes (0.5mm, 2mm, 4mm, 20mm of diameter), located at the focal point of the collimator.

9. The probe holders are also connected to the cold finger with metallic wires for cooling down as low as possible.
10. Optical transmission of about 80% around 10μm.
11. The probe is not directly on the sample so we can expect a small offset difference (of several Kelvin) between the set temperature and the sample's real temperature.

- The collimator is represented in the schematic 4.19c as a big lens for simplicity, but it is indeed an off-axis parabolic mirror. After the collimator, the IR beam is collimated, homogeneous in intensity and has a diameter of about 10cm, equal to its aperture.
- A significant part (∼25%) of this collimated beam is focalized on the QCD devices thanks to the ZnSe lens. Without this lens, the excitation is not strong enough to yield a distinguishable photocurrent from noise and background current. Thanks to the xyz-translation stage, the position of the lens is finely adjustable in all three directions of space. Thus, by displacing the lens, we scan the focal point of the lens throughout the devices' matrix, searching for the wanted one. The initial collimated beam is twice as large as the lens, thus, while staying in the collimated beam, the irradiance at the lens' focal point should be constant.
- The Germanium longpass filter 8110nm eliminates the blackbody emission with wavelength smaller than 8110nm. Without this filter, we recorded parasitic photocurrent due to the blackbody emission's visible - near IR excitation with energy above InGaAs's bandgap on the semiconductor zones non-covered by metal [12]. The spectrum of the parasitic current is given in Appendix C.
- The IR polarizer allows realizing polarization-dependent photocurrent measurement. Due to the grating structure, our QCD ISB transtion response is only active for TM polarization (**E** field perpendicular to metallic strips) and not to TE polarization (**E** field parallel to metallic strips). Thus, the IR polarizer provides a good way to distinguish the ISB transition photocurrent from parasitic photocurrent (independent of light polarization).
- We used a CCD camera (Thorlabs) equipped with visible light source and a mirror positioned at approximately 45° in front of the cryostat windows to visualize the sample inside the cryostat. In this observation configuration, we can position and bring probes into contact electrically with individual QCD devices. The mirror is easily removable, allowing to switch between this observation configuration and the main measurement configuration.
- For dark current estimation, we put an aluminium screen (high reflectivity, low emissivity) right in front of the cryostat's windows.
- To distinguish the contribution to the photocurrent due to the blackbody source from the lab's background [13], we switched between illumination and background conditions by uncovering and covering the collimator's outlet with the aluminium screen. This aluminium screen stays at room temperature and thus also emits IR radiation around 10μm. Nevertheless, its emission is much smaller compared to the blackbody source due to lower temperature and small emissivity.
- The electric signal is acquired with a multimeter Keithley 6430, equipped with a preamplifier module (Keithley 6430 Remote PreAmp), designed for small current measurements (sub-femtoamp).

This first optical setup was used for I(V) characteristics measurement in dark condition at different temperatures and for photocurrent measurements under illumination by the blackbody source SR-20.

12. This parasitic photocurrent is quite large with respect to the ISB transition photocurrent, e.g. up to 400nA with a pinhole of 4mm and with the ZnSe lens.

13. The background scene also radiates thermally in the 10μm range at room temperature.

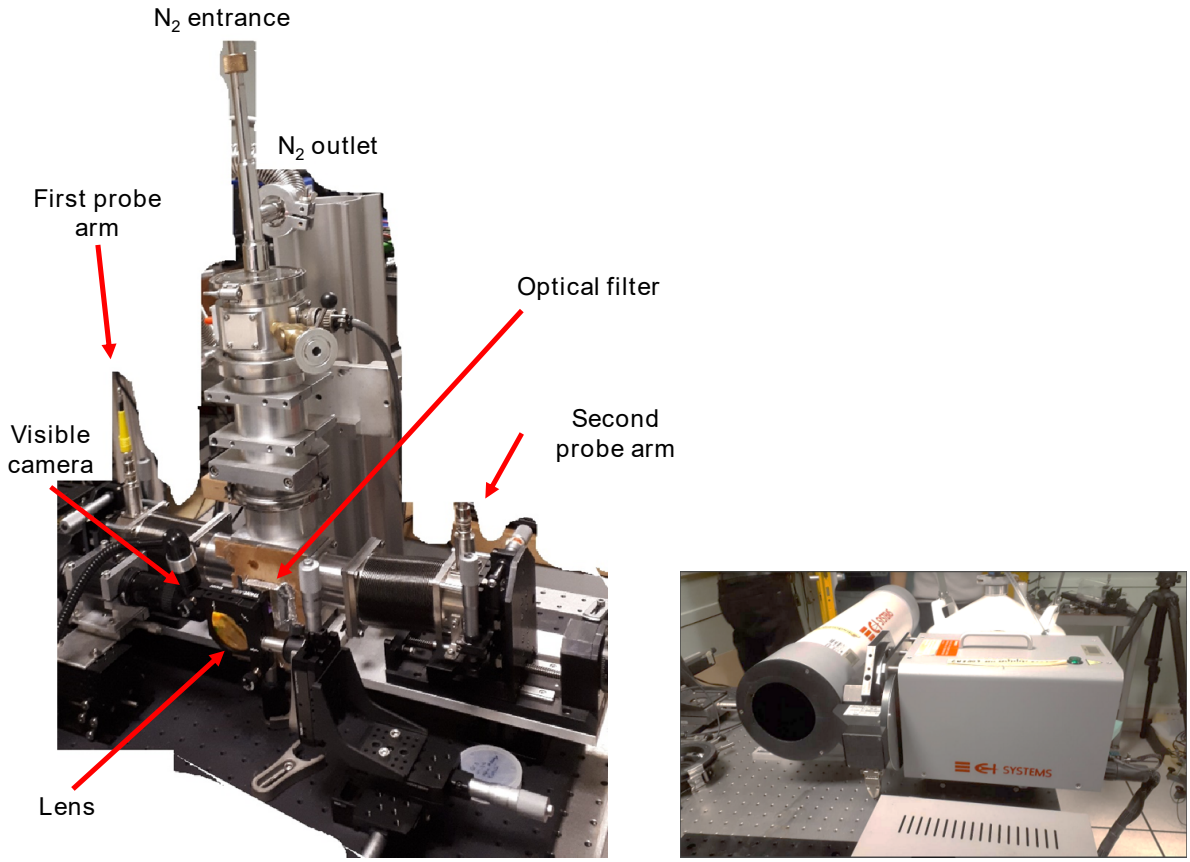

(a) (b)

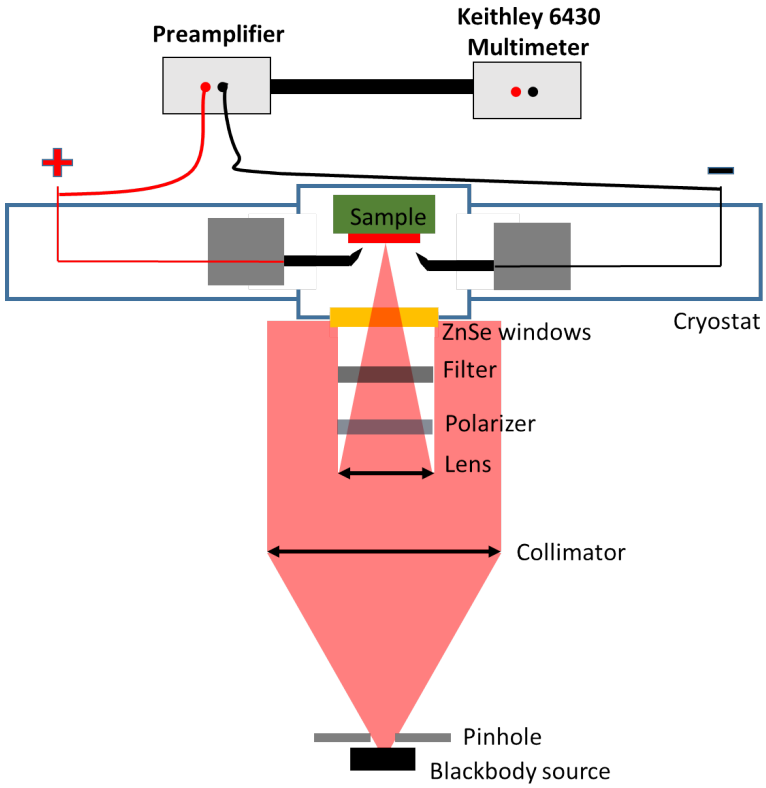

(c)

Figure 4.19 – Photocurrent measurement setup. a) Janis cryostat and optics. b) Blackbody source and collimator. c) A horizontal cut schematic of the setup.

4.4.2.1 Dark characteristics

In this section, we characterize how our single-period QCD behave electrically in dark condition as compared to the expected behavior of a multiple QW QCD: namely a Schottky diode-like behavior in I(V) characteristics and a strong dependence on temperature of the device resistance at 0V bias.

Figure 4.20a reports typical I(V) characteristics in dark condition at 78K of QCD devices covered with Au ('blind pixel') on three samples: QCD40-2-1, QCD41-2-3, QCD40-2-3. QCD40-2-1 and QCD41-2-3 display a leaky diode-like behavior: the current in forward bias (V>0) branch is larger than in the reverse bias (V<0) branch. QCD40-2-3 does not behave like a diode and is at least two orders of magnitude less resistive than the two previous samples.

Figure 4.20b reports the current density characteristics *j(V)* for square devices of various sizes, covered with Au on sample QCD40-2-3 at 78K in dark condition. While the forward bias branch of the different characteristics mostly superimpose, the reverse bias branch displays scattered behavior. Larger patterns (a=250 and 200μm) have smaller reverse bias current than forward bias and present a rectifying behavior. Smaller patterns (a=150, 100 and 50μm) present rectifying behavior in the opposite direction. This is a sign of non negligeable peripheral current with respect to volume current.

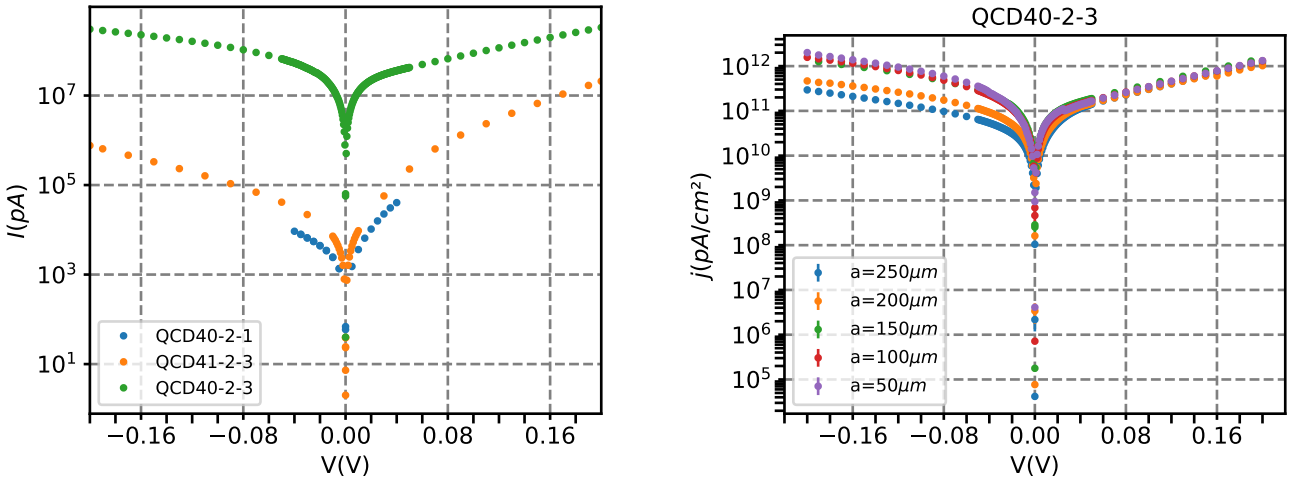

(a) (b)

Figure 4.20 – a) I(V) at 78K in dark of three devices on samples QCD40-2-1, QCD41-2-3, QCD40-2-3. We observe a rectifying behavior for QCD40-2-1, QCD41-2-3 in the expected direction, whereas QCD40-2-3 presents a rectifying behavior in the opposite direction.
b) Current density as a function of voltage V from squares devices of different sizes, decreasing from 250μm to 50μm, measured in dark condition. Devices with largers or smaller size present opposite rectifying behaviors.

I realized I(V) measurement in dark condition at various temperatures. Each time the temperature is modifed, the probes are retracted. We should wait at least 10 minutes after stabilisation of the measured temperature before bringing the probes into contact with sample to avoid a piercing of the sample by probes due to thermal expansion of materials.

Figure 4.21b depicts the evolution of dark I(V) characteristics at various temperatures (78K-200K) of the 'blind pixel' device *'CF'* of QCD41-2-3. As expected, the device is less resistive at higher tem-

perature, delivering larger current at the same voltage. Since in first approximation, the current has an exponential dependence on 1/T ($I_{dark} \propto exp(-E_a/k_BT)$), the current I is more sensitive to a change of T around 80K than around 200K. From these I(V) characteristics, we computed the differential resistance at 0V R_0=dV/dI(V=0). The product of R_0A is reported in Figure 4.21b for three samples QCD40-2-1, QCD41-2-3, QCD40-2-3, where A~$3.2\times10^{-4}cm^2$ is the total area of QCD's semiconductor mesa. The horizontal axis is the inverse of temperature 1000/T and the plot is in semilog in vertical axis.

For QCD40-2-1 (blue dot) and QCD41-2-3 (orange star), in semilog scale, the evolution of R_0A as a function of 1000/T is mostly linear, corresponding well to an exponential dependence $R_0A = dV/dI(V=0) \propto 1/exp(-E_a/k_BT) = exp(E_a/k_BT)$. We observe a slight change of slope between 1000/T>10 and 1000/T<10. This is attibuted to the existence of at least two activation energies. By fitting two seperate sets of data for 1000/T>10 and 1000/T<10, I extracted corresponding activation energy E_a, as depicted in Figures 4.22a and 4.22b. In Figure 4.20, I used the nominal set value of temperature T, from which we obtained E_{a1}=84meV for QCD40-2-3 and E_a=64meV for QCD41-2-3, with 1000/T>10 (T<100K). The activation energy E_{a1} corresponds to the difference between the Fermi level and the excited state of the QW. From the transport model, E_a is estimated to be about 109meV and 79 meV respectively for QCD40 and QCD41, about 15-25meV larger than the values found for T<100K. We can also compare R_0A(1000/T) characteristics of QCD40-2-1 and QCD41-2-3 to reported values of QCD from literature, depicted in Figure 4.24. Figure 4.23a, adapted from reference [116], reports R_0A(1000/T) measured and simulated for a QCD operating at 8μm, with 10 periods, each active QW being doped at $3.5\times10^{11}cm^{-2}$. We observe similar behavior and order of magnitude to R_0A in QCD40-2-1 and QCD41-2-3. Figure 4.23b, adapted from reference [114], reports R_0(1000/T) (red curve) of the single-period QCD of Schwarz's group, being doped at $8\times10^{17}cm^{-3}$ and operating at 4μm. The area of the device was not reported in this reference. The resistance R_0 of the device is about $10^{11}\Omega$ at 80K, 5 orders of magnitude larger than R_0(80K) of QCD40-2-1 and QCD41-2-3 (about $10^6\Omega$). This difference is due to the difference in operating wavelength and the device's area.

For QCD40-2-3, we measured R_0A at 78K and 300K. Compared to QCD40-2-1 and QCD41-2-3, at 78K, the resistance of device on QCD40-2-3 at 0V is at least two orders of magnitude smaller (9kΩ compared to 1-3MΩ). We attribute this difference to the fabrication process. QCD40-2-3 underwent e-beam lithography and the semiconductor active layer in contact with the Ti/Au back mirror underwent 12 minutes of baking at 170°C. QCD40-2-1 and QCD41-2-3 only underwent UV lithography process with baking temperature limited to 105-125°C and shorter total baking time. It is likely that Au diffused into the extractor contact layer of the QCD structure (and even further), reducing the resistance of the devices.

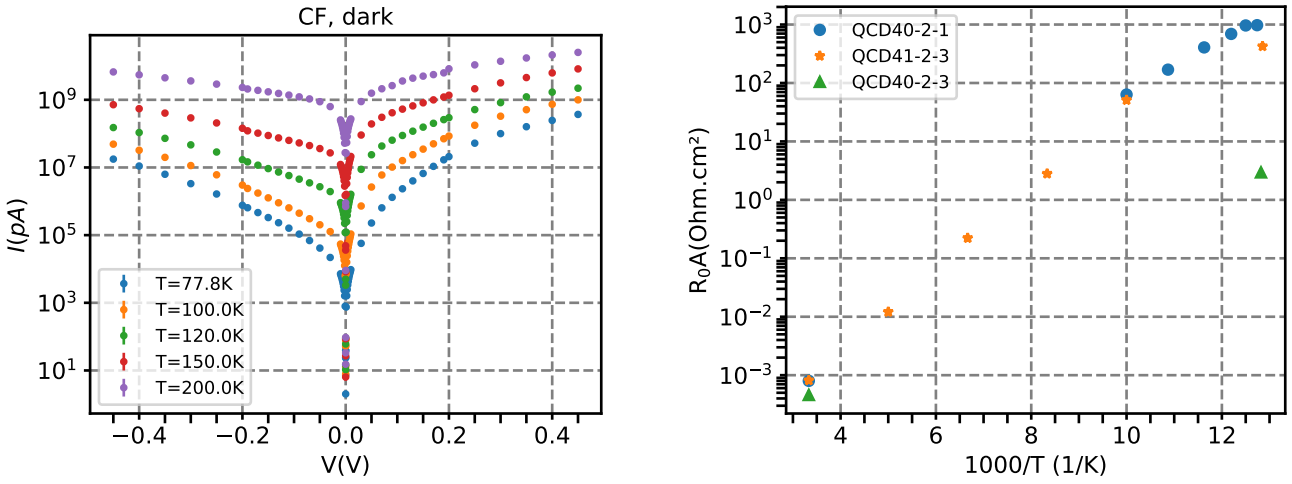

(a) (b)

Figure 4.21 – a) I(V) characteristics of a 'blind pixel' at various temperatures on sample QCD41-2-3. b) R_0A measured at various temperatures.

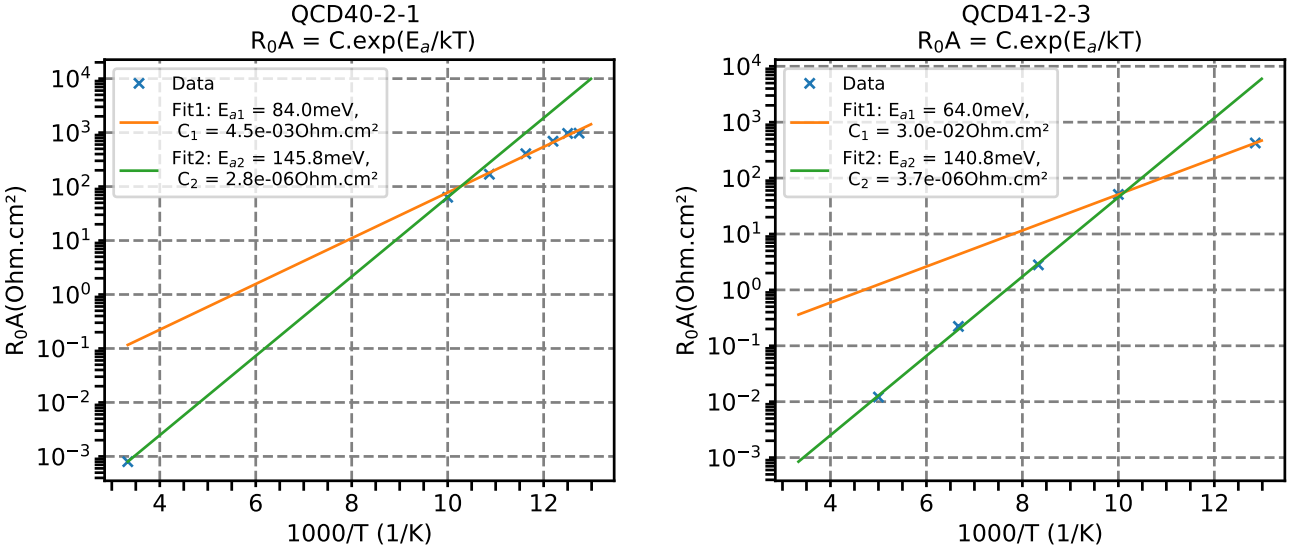

(a) (b)

Figure 4.22 – Fitting of R_0A with the relation $R_0A=C.\exp(E_a/kT)$ for two sets of data: $1000/T>10K^{-1}$ (T<100K, orange line) and $1000/T<10K^{-1}$ (T>100K, green line). a) QCD40-2-1: E_{a1} = 84.0meV; E_{a2} = 145.8meV. b) QCD41-2-3: E_{a1} = 64.0meV; E_{a2} = 140.8meV.

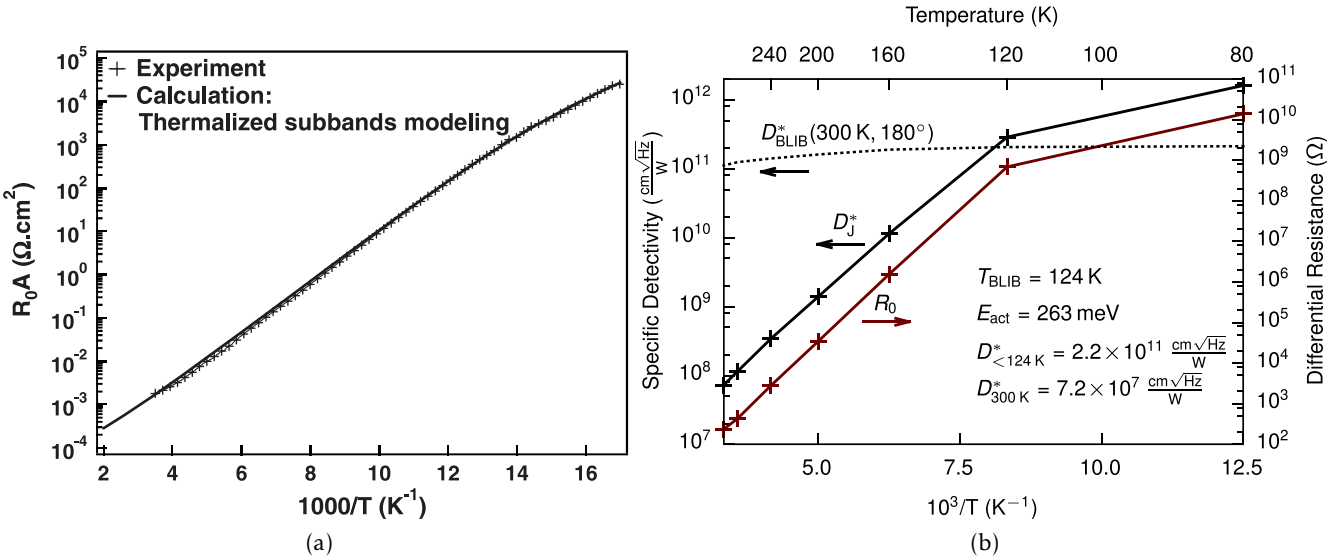

Figure 4.23 – a) Adapted from reference [116]: R_0A measurement and computation (with thermalized subbands model) for a QCD device operating at 8μm, having 10 periods with doping $3.5\times10^{11} cm^{-2}$ for each active QW. R_0A(1000/T) curve in a) behaves quite similarly and having R_0A of the same order of magnitude with samples QCD40-2-1, QCD41-2-3 (Figure 4.22b).
b) Adapted from reference [114]: We consider here specifically the red curve (right vertical axis) depicting the differential resistance R_0 as a function of temperature in a single-period QCD in rigde waveguide.

Figure 4.24 reports time evolution of the dark current of a device on the sample QCD40-2-1 at 0V bias (illustrated in Figure 4.24a) and at 20mV bias (illustrated in Figure 4.24b). The integration time is 1s per data point. At 0V bias, the mean value and the standard deviation of the current are respectively 31-36pA and 1.1pA. We observe a drift of the current of about 2-4pA over a measurement time of 500s. At 20mV bias, the mean value and the standard deviation of the current are respectively 4850pA and 64pA. There are periods of time when the current varies for about more than 150pA (for instance around t=200s).

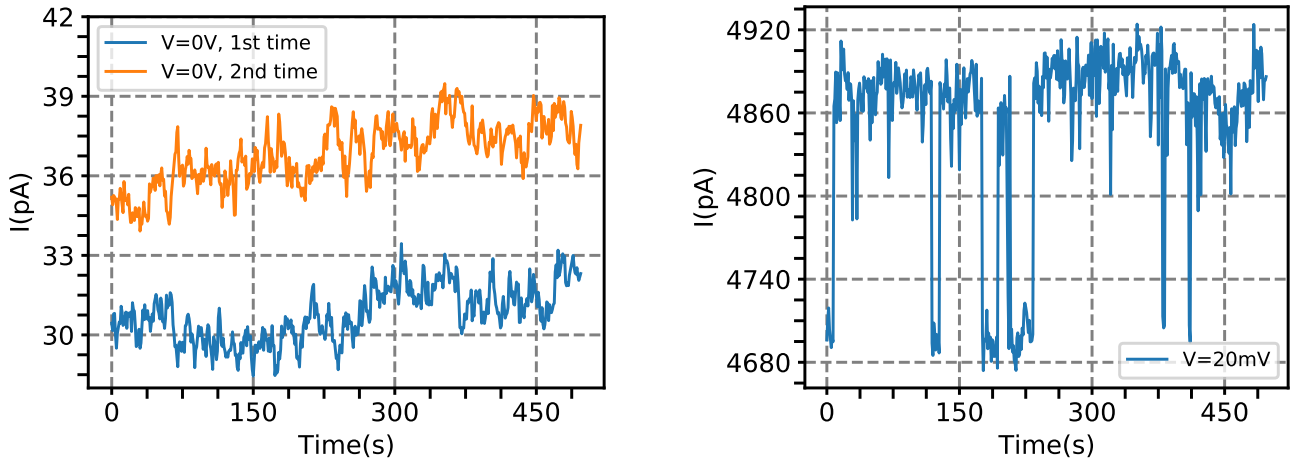

(a) (b)

Figure 4.24 – Evolution of dark current as a function of time of a device on QCD40-2-1, integration time 1s per data point: a) V=0V, mean value of I 31-36pA and standard deviation of I 1.1pA. b)V=20mV, mean value of I 4850pA and standard deviation of I 64pA.

4.4.2.2 Photocurrent measurement

In this section, I will present three kinds of photocurrent measurement. The first one consists in a long duration (typically 10 minutes) *I(V)* acquisiton without and with IR illumination. The two other ones consist in acquiring I current at fixed voltage while rotating the polarization or cutting the IR source's illumination with the aluminium screen typically every minute. QCD40-2-1 and QCD41-2-3 have a different behavior compared to QCD40-2-3 in terms of photocurrent, they will be presented seperately.

First set of samples: low photocurrent

The *I(V)* characteristic in dark and illumination conditions are usually reported in other works to illustrate the effect of illumination on the photocurrent. For comparison purpose, we report such measurement on sample QCD41-2-3 (device *'AG'*, [14]) in Figure 4.25, where the IR blackbody source is covered (orange curve) and uncovered (blue curve). In semilog scale, we can see that the change due to photocurrent is small compared to the background current. In addition, due to long acquistion time for one complete *I(V)*, the measured current can also be subject to a global drift. However, one should notice that the photocurrent is not equal to a simple difference between the illumination and background currents but drift needs to be taken into account, especially when the photocurrent is small.

14. *'AG'* supposed to deliver strong photocurrent due to good optical resonance

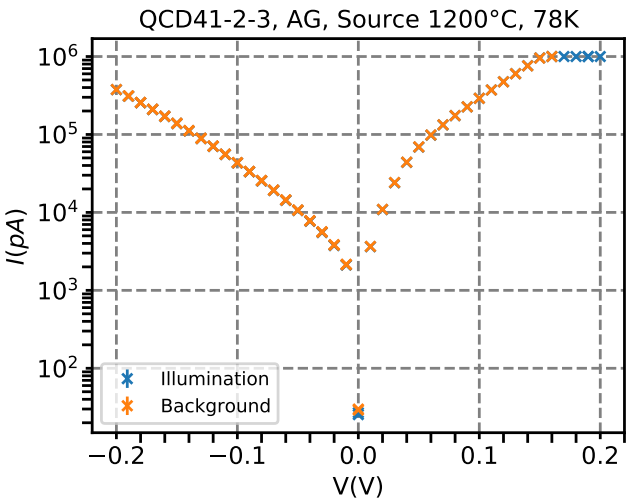

Figure 4.25 – I(V) measured with IR blackbody source uncovered (illumination, blue cross) and source covered (background current, orange cross).

A second way of photocurrent measurement consists in having a IR polarizer turned after short acquisition time (about 30s). The polarizer rotation is made by 10° or 20° incremental step in chronological order. By varying the polarization of the excitation, we obtained a clear variation of the total current due to the ISB photocurrent contribution. This measurement is illustrated in Figures 4.26a and 4.26b respectively for devices *'CG'* of QCD40-2-1 (with pinhole 20mm) and *'DE'* of QCD41-2-3 [15](with pinhole 20mm). The polarizer angle is defined such that 0° and 90° correspond respectively to TM and TE polarizations. The TM component of the electric field varies as $E_{total}Cos\theta$ and the corresponding irradiance varies as $E^2_{total}Cos^2\theta$. This TM component is the one converted into ISB photocurrent. We observe a clear variation in $Cos^2\theta$ of the measured current *I*. From data fitting, we obtained an ISB photocurrent amplitude of 4.7pA and 2.1pA respectively for*'CG'* of QCD40-2-1 (with pinhole 20mm) and *'DE'* of QCD41-2-3 [16]. The background current is about 25-50pA at zero bias voltage. Shorter acquisition time reduces the effect of drift in this method of measurement. The $Cos^2\theta$ modulation of the signal also allows to fit more easily the photocurrent amplitude out of noise and drift contributions.

With the Planck's law for blackbody emission and radiometry calculation (detailed in Appendix 42), a photocurrent of about 0.88μA would correspond to an EQE of 100%. From measured photocurrents, we thus extrapolate an EQE of these devices of about 5.3×10^{-4}% and 2.4×10^{-4}%. These EQE values are much lower than theoretical estimations.

15. Both having good optical resonance.
16. Similar behavior and order of magnitude of photocurrent are found for other equivalent devices on samples QCD40-2-1 and QCD41-2-3.

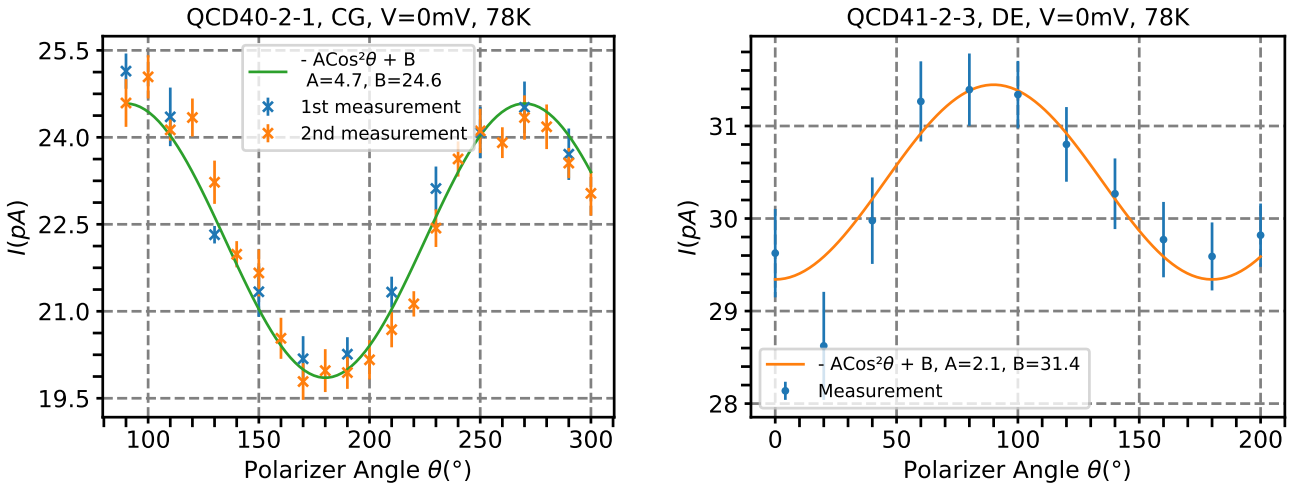

(a) (b)

Figure 4.26 – Photocurrent in a) QCD40-2-1, pinhole 20mm, and b) QCD41-2-3, pinhole 4mm.

Second set of samples: larger photocurrent

Similar photocurrent measurement using polarization dependence is carried out on sample QCD40-2-3, device *'CE'* and is depicted in Figure 4.27. Once again, we observe a clear variation in $\mathrm{Cos}^2\theta$ of the measured current I. But in this case, the fitted amplitude of variation is 482.7pA, two orders of magnitude larger than in previuous set of samples. The reason for this difference is not clear yet and will be discussed later. The background current at zero bias voltage is about 7nA, also two orders of magnitude larger than in previous set of sample, overall the ratio of the photocurrent to the background current is reduced in this second set.

A third way to measure the photocurrent consists in toggling between covering ('Light OFF' state) and uncovering ('Light ON' state) the collimator output during short period of time (~100s), as depicted in Figure 4.27. The integration time is 1s per data point. The polarizer is removed from the optical path in this measurement. The difference between the mean value of 'Light ON' and 'Light OFF' states gives an estimate of the ISB photocurrent. The plot also provides an idea of the noise and the drift tendency.

The measurement is realized respectively on three devices with different antenna strip width *'CG'*, *'CE'*, *'CD'*, while keeping similar experimental condition. Previous optical characterization in Figure 4.15c indicates that among these three devices, the device *'CG'* offers the best resonance between MIM mode and ISB transition, followed by *'CE'*, then *'CD'*. This is confirmed by the photocurrent values in the three devices, varying from 513.7pA for *'CG'* down to 269.6pA for *'CD'*. The value of photocurrent estimated in this measurement for *'CE'* device is 367.5pA, about 100pA less than the value reported in the turning polarization measurement, due to non equivalent experimental conditions [17]. The noise standard deviation calculated from the data is about 100pA in these three devices (for an integration time of 1s per data point), meaning that the SNR varies from 5.0 down to 2.5. The EQE of *'CG'* device is about 0.057%, the way to compute this value is similar to previous set of samples. The corresponding responsivity is $\mathcal{R}$=4.3mA/W, for $h\nu$=134meV. All these values are reported in Table 4.2.

17. The pinhole size is reduced from 20mm to 4mm. For a pinhole of 4mm, rotating polarization measurement on *'CE'* gives 400pA of photocurrent.

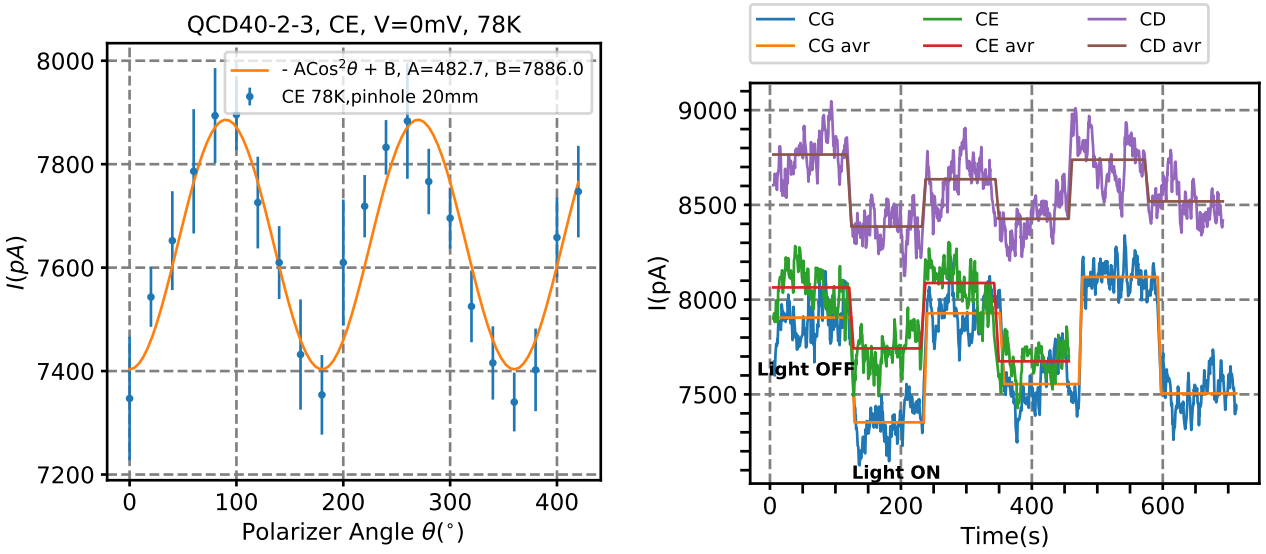

(a) (b)

Figure 4.27 – a) Photocurrent of *'CE'* device in QCD40-2-3 with turning polarization, pinhole size 20mm. The photocurrent fitted amplitude is 482.7pA. b) Photocurrent as a function of time, measured on different devices, with the light source uncovered ('Light OFF') and open ('Light ON'), pinhole size 4mm. The integration time is 1s per data point.

	CG	CE	CD
I_{ph}(pA)	513.7	367.5	269.6
Noise(pA)	102.9	99.6	107.4
SNR	5.0	3.7	2.5
EQE	0.057%	0.042%	0.031%

Table 4.2 – Values of photocurrents I_{ph}, noise standard deviation and SNR of different devices on sample QCD40-2-3

4.4.2.3 Spectral response measurement

I realized spectral response measurement with sample QCD40-2-3, having the largest photocurrent among the three samples. The configuration of this second optical setup, illustrated in Figure 4.28, is quite similar to the first one presented earlier, but the IR source is replaced by a globar source of an FTIR (Vertex 80v, Bruker) via an external path (KBr windows). The QCD current is converted to voltage by a transimpedance amplifier (TIA, Keithley 428 current amplifier). The voltage signal is fed back to the FTIR using an adapter for external input. The QCD plays the role of an external photodetector for the FTIR. The spectral response of the QCD can be obtained by acquiring the response to the same excitation of the QCD device (external detector) and an internal detector whose spectral response is already known, then inferring the spectral response of the QCD device. In our case, we used the internal detector DTGS for normalization. In this setup, there is no polarizer and a shorter focal length ZnSe lens (5cm of diameter, 10cm of focal length) is used for a stronger focalization of the excitation.

The TIA provides a current suppressing function, allowing the background current substraction

before amplification to avoid saturation of the amplifier. The TIA applied a bias voltage to the QCD and acquire a current to be amplified and converted. The bias is chosen to maintain the background current as close as possible to zero. For these measurements, a bias of -15mV is used. The TIA output is also sent to a voltmeter to keep track of the voltage evolution during the measurement. The amplifier gain is increased incrementally while keeping suppressing the background current and verifying with the voltmeter that there is no saturation. We obtain the photocurrent signal converted to voltage of about 0.5V in amplitude with an amplifier gain 10^9V/A, adapted to the FTIR external input (which requires a voltage signal level of about 1V). The current to be suppressed is about -40nA and slowly drifts during a long acquisition series of measurements, requiring to repeat the current suppression after each measurement to avoid signal saturation.

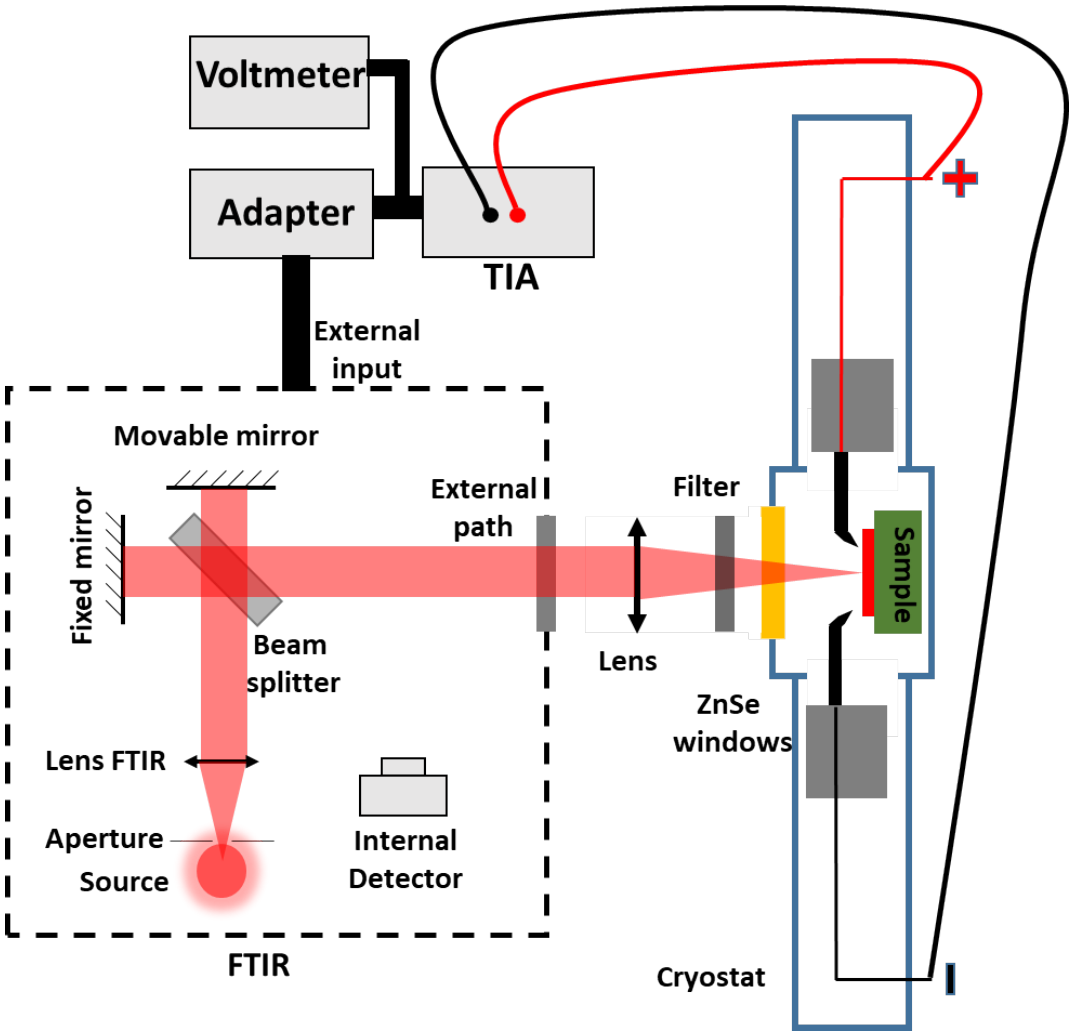

Figure 4.28 – Schematic of the experimental setup for spectral response measurement.

The spectral response measurement is realized with QCD devices named *'CI'*, *'CG'*, *'CE'* on sample QCD40-2-3. The FTIR acquisition is realized with the following parameters: 64 scans per measurement, scan speed 10kHz, resolution 2cm^{-1}, aperture size 6mm. To reduce noise in the spectrum, the measurement is repeated 10 times for 'CE', 7 times for 'CG' and 4 times for 'CI', then the interferogram is averaged for each sample between these measurements before being converted to spectral response.

The photocurrent spectral response of these devices are depicted in Figure 4.29 (solid lines), together with the corresponding experimental optical reflectances (dashed lines) introduced in section 4.4.1. The photocurrent spectral responses are normalized to their maximum.

As expected, the photocurrent spectral responses of all three devices present peaks with their maximum around the plasma shifted ISB transition energy $\tilde{\omega}_{ISB}$. *'CG'* (orange curves) has the narrowest photocurrent spectrum, with only one peak at 134.0meV, whereas the corresponding optical reflectance displays two dips at about 132.6 and 135.5meV. The photocurrent peak of *'CG'* has a FWHM of about 6meV and a symetrical lineshape. *'CE'* has a slightly larger FWHM, with a slightly asymetrical lineshape(larger right shoulder, toward higher energy). We still observe only one maximum in photoresponse at 134.4meV whereas the reflectance displays clearly two dips at about 133.2meV and 137.1meV. *'CI'* has the largest FWHM of 10.6meV among the three devices. The photocurrent peak of *'CI'* is broadened towards lower energy compared to *'CG'* and *'CE'*. It does not have a single lorentzian lineshape but is composed of two peaks. However, the noise in the spectrum (due to fewer total acquisitions to be averaged) makes it hard to clearly observe this double-peaks behavior. This behavior is in agreement with computation results as will be detailed in the Discussion section. The broadening of *'CE'* and *'CI'* photocurrent peaks compared to the one of 'CG' coincide with the shift of the corresponding MIM resonance around the ISB transition energy.

The experimental linewidth and lineshape of photocurrent in these devices are useful information used to accurately estimate the EQE of the devices.

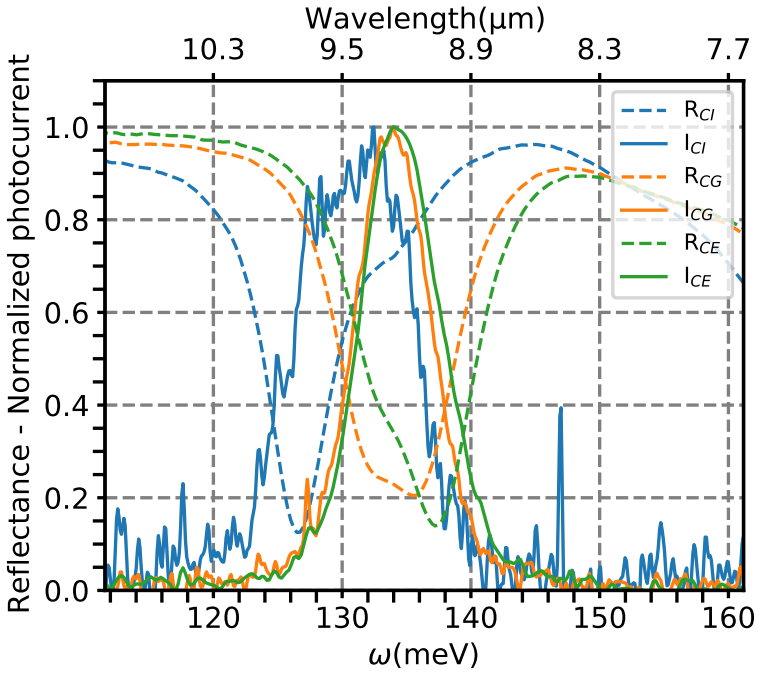

Figure 4.29 – Experimental normalized photocurrent spectra (I_{CI}, I_{CG}, I_{CE}) and corresponding experimental reflectance spectra (R_{CI}, R_{CG}, R_{CE}), on QCD40-2-3 sample. The photocurrent spectra peak at around the ISB transition. The linewidths and lineshapes of the photocurrent spectra vary correspondingly to the evolution of the MIM resonance with respect to the ISB transition. *'CG'* device has the narrowest linewdith of photocurrent, with FWHM of about 6meV and and peaks at 134.0meV (9.253μm).

4.5 Discussions

4.5.1 Data fitting of reflectance and photocurrent spectra

We benefit from a wide set of data with reflectance spectra of several QCD devices with several antenna strip width S and acquired at various temperatures, on samples QCD40-2-3, QCD41-2-3. Raw data displays an interesting transition between room temperature and cryogenic temperatures. From one absorption peak at room temperature, we observe the appearance of a second absorption peak and the peaks positions are shifted with temperature.

In addition, we benefit from photocurrent spectra and photocurrent amplitude measurements of several QCD devices on sample QCD40-2-3.

In this section I'll confront our experimental results with numerical calculation to gain further insights in the response of our QCD detectors. First I'll present computation realized with Reticolo, which has the advantage of giving rigorous computation from the given dielectric functions and the geometrical parameters. It also takes into account the dielectric fucntion dispersion and other optical effects (like diffraction or higher order resonance). However, Reticolo takes long computation time (typically 5 minutes per spectrum), making it too time-consuming to realize automatic data fitting of our complete experimental set with many parameters using method like standard least square fit. Instead of automatic data fitting, I chose to compute with values estimated 'manually' and observe the comparison with the experimental data.

A second method of data fitting is realized by Mathurin Lagrée (III-V lab) and myself, using a code written by Lagrée based on Coupled Mode Theory (CMT). This is a phenomenological method that is not based on Maxwells equations. It employs the theory of coupled resonators and empirical values of the studied resonances to describe the optical response of the whole system. This method is succesfully applied in several references [117–119]. It has the advantage of being very fast in terms of computation (typically less than a second per spectrum) and it is convenient for data fitting in our case. In addition, in reference [117], Lagrée et al. offered an analysis of both optical and photocurrent spectral response of QCD detector embedded in a patch antenna cavity, which is quite close to our case.

4.5.1.1 Data adjusting with Reticolo

The main parameters used for the adjustment are : the antenna strip width S, the semiconductor dielectric function, the initial ISB transition $\omega_{0\,ISB}$ and the damping factor Γ_{ISB}. Other parameters are fixed using our knowledge from previous chapters, including the dielectric functions of Au (Drude model, ω_P = 8.5eV, Γ=71meV, similar to Olmon's values with Γ being increased by a factor of 1.5 [70]) and Ti (Rakic's value [107]). The empirical adjustment of parameters procedure consists in:

- Keeping all dielectric functions as known. Adding an offset of -80nm to all the antenna strip widths S measured with SEM images. With this common offset, we matched the computation result with the room temperature reflectance.
- Adjusting a linear change to the semiconductor dielectric functions to account for temperature's effect. With this step, we matched roughly positions of resonance peaks at 78K.
- Adjusting $\omega_{0\,ISB}$ to better match the ISB absorption peak.
- Adjusting a linear change to the damping factor Γ_{ISB} to account for temperature's effect. With this step, we adjust the absorption linewidths and also slighltly the peaks' postion.

- Compute the useful absorption $A_{z\,QW}$ and compare their linewidth and lineshape with experimental data.

Concerning the temperature dependence of the spectra, we observe a blueshift of the MIM mode when the temperature decreases. This shift is observed in both MIM resonator without ISB transition (sample H7739-2-5, made of 85nm of intrinsic InGaAs embedded in MIM cavity TM_{01}) as illustrated in Figure 4.30a and with ISB transition far from the MIM mode (QCD40-2-3, device *'CA'* with resonance at 15meV higher than the ISB transition, as illustrated in Figure 4.30b). The experimental blueshift due to cooldown from room temperature to 79K is about 100nm (or 1.6meV) for device *'IB'* of H7739-2-5 (S=1.1μm (measured), TM_{01} mode) and is about 150nm (or 2.7meV) for device *'CA'* of QCD40-2-3. The MIM resonance wavelength can be estimated by the relation $\lambda_0 = 2n_{eff\,M-I-M}S$ as discussed in chapter 3. Thermal expansion alone which changes S cannot explain this frequency shift. We attribute the MIM mode frequency shift mainly to a change of the semiconductor dielectric functions, thus the effective index $n_{eff\,M-I-M}$ [18]. The dielectric functions of InGaAs and InAlAs are changed by: $\epsilon(293K) - \epsilon(79K)$=0.280 (equivalent to n(293K) - n(79K)~ 0.043, $\Delta n/\Delta T \sim 2.0\times10^{-4}K^{-1}$) to match the shift due to lower temperature. The coefficient $\Delta n/\Delta T \sim 2.0\times10^{-4}K^{-1}$ is in agreement with experimental values reported in reference [120] and references therein: $\Delta n/\Delta T \sim 2-3\times10^{-4}K^{-1}$ for InAs and GaAs.

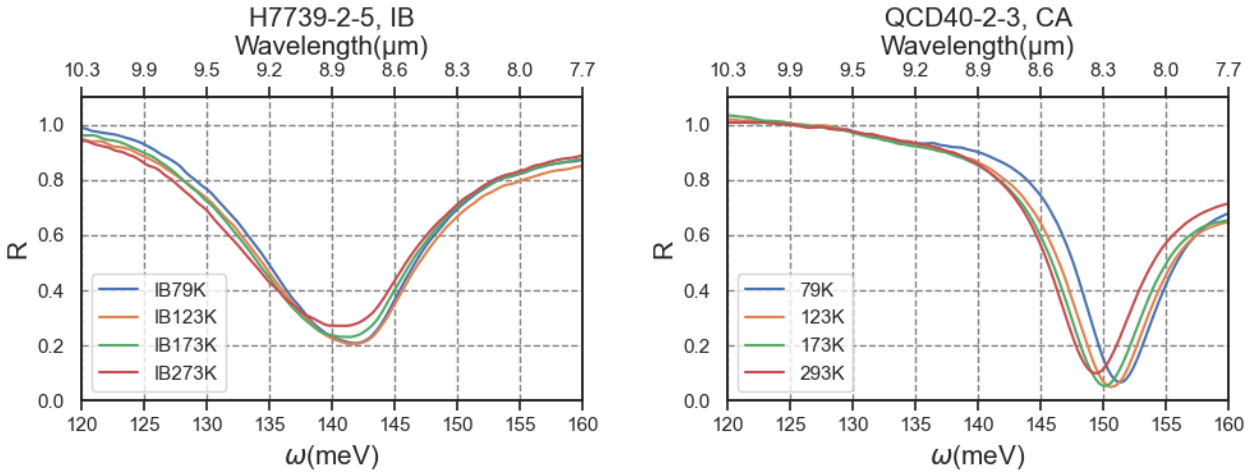

(a) (b)

Figure 4.30 – Temperature dependence of MIM mode frequency. a) H7735-2-5: 85nm-thick intrinsic InGaAs embedded in Ti/Au MIM resonator (S=1.1μm (measured), TM_{01} mode). Wavelength shift due to temperature change from 273K to 79K is a blueshift of about 100nm. b) QCD40-2-3: *'CA'* is a device with MIM mode (S=3.1μm (measured), TM_{03}) distanced from the ISB transition of about 15meV. The MIM mode wavelength displays a blueshift of about 150nm when the temperature reduces from 293K to 79K.

Figure 4.31a depicts the experimental reflectance spectra (solid lines) of devices *'CA'* and *'CI'* at 293K and simulated curves (dashed line). At 293K, Γ_{ISB}=12meV and $\omega_{0\,ISB}$=131.9meV (corresponding $\tilde{\omega}_{ISB}(\Gamma_{ISB}$=12meV) = 134.0meV), $\epsilon_{\infty\,InGaAs}$=11.22 and $\epsilon_{\infty\,InAlAs}$=10.24 were used for computation. Simulated curves reproduce quite well the MIM resonance in experimental data. The sharp peak ap-

18. Change of strip width S by thermal effect is estimated about 9nm for S=3.1μm using thermal expansion coefficient $\alpha_{Au} = 13.9\times10^{-6}K^{-1}$. This is not enough to explain the 150nm shift in *'CA'*, QCD40-2-3.

pearing at 155meV in simulated curves correspond to a diffraction mode and its frequency is angular dependent. While the simulation was performed at θ=18°, we could have integrated over the interval [12°-24°] (the μFTIR's angular aperture) to better take into account the angular dependence, but this procedure requires long computation time. This explains the difference between the simulated and measured reflectivity curve for this particular feature.

For reflectance data at 78K, Γ_{ISB} is reduced to 6.5meV in simulation to reproduce the absorption peak linewidths. $\omega_{0\,ISB}$ is kept at 131.9meV (however, the corresponding $\tilde{\omega}_{ISB}$ changes to 135.5meV). ϵ_∞ of InGaAs and InAlAs are reduced by 0.280 compared to the values used at 293K. Experimental and simulated reflectance spectra are reported in Figure 4.31b. We observe quite good matching both in peaks' position and amplitude for the MIM mode and ISB transition. We also have a similar behavior of the diffraction mode above 155meV as encountered in reflectance spectra at 293K.

The useful absorption $A_{z\,QW}$ spectra were computed with the same dataset and reported in Figure 4.31c (dashed lines), together with the experimental photocurrent spectra (solid lines). All photocurrent spectra are normalized to their own maximum. Computed $A_{z\,QW}$ spectra reproduce quite well the position of the peaks and general lineshapes. The linewidth of the $A_{z\,QW}$ spectra are about 1meV larger than the photocurrent spectra. I could not reduce further the computed linewidth and simultaneously maintain the experimental splitting between two absorption peaks by further reducing either Γ_{ISB} or MIM cavity metal's losses. As we will see with the CMT data fitting in the next section, the photocurrent linewidth can be reduced by introducing the influence of the QCD's extractor stage.

With the obtained fitting parameters, I re-computed the field distribution $|E_z|^2$ in the optimized structure of QCD40 and QCD41 and compared them with the initial optimization. These simulations are depicted in Figure 4.32. $\omega_P = 8.5eV, \Gamma = 0.71eV$ are used for Au Drude model rather than Ordal's value [99]. The Γ_{ISB} is reduced from 12meV to 6.5meV for both QCD40 and QCD41. Other changes of dielectric functions at low temperature are also taken into account, but they do not modify significantly the field distribution. On the left are $|E_z|^2$ maps computed for optimal device in QCD40 and QCD41 (depicted respectively in Figure 4.32a and 4.32c), compared to the initial optimization for QCD41 (depicted in Figure 4.32e) with Ordal's values for Au and Γ_{ISB}=12meV.

Figures 4.32b, d, f on the right are $|E_z|^2$ profiles in the z direction, averaged over the whole period P, correspond respectively to the left figures a), c), e). Compared to the initial optimization computation in f), the $|E_z|^2$ enhancement in d) due to MIM cavity is reduced to about 4 in InAlAs barrier (rather than about 7 in f)) with updated Au dielectric function having a larger optical loss. The ENZ enhancement on the other hand is increased to about 4.8 rather than 2.8, thanks to the reduction of Γ_{ISB} from 12meV to 6.5meV.

With this updated version, the theoretical values of useful absorption $A_{z\,QW}$ are respectively 34% for QCD40 (N=5×$10^{17} cm^{-3}$) and 55% for and QCD41 (N=1×$10^{18} cm^{-3}$).

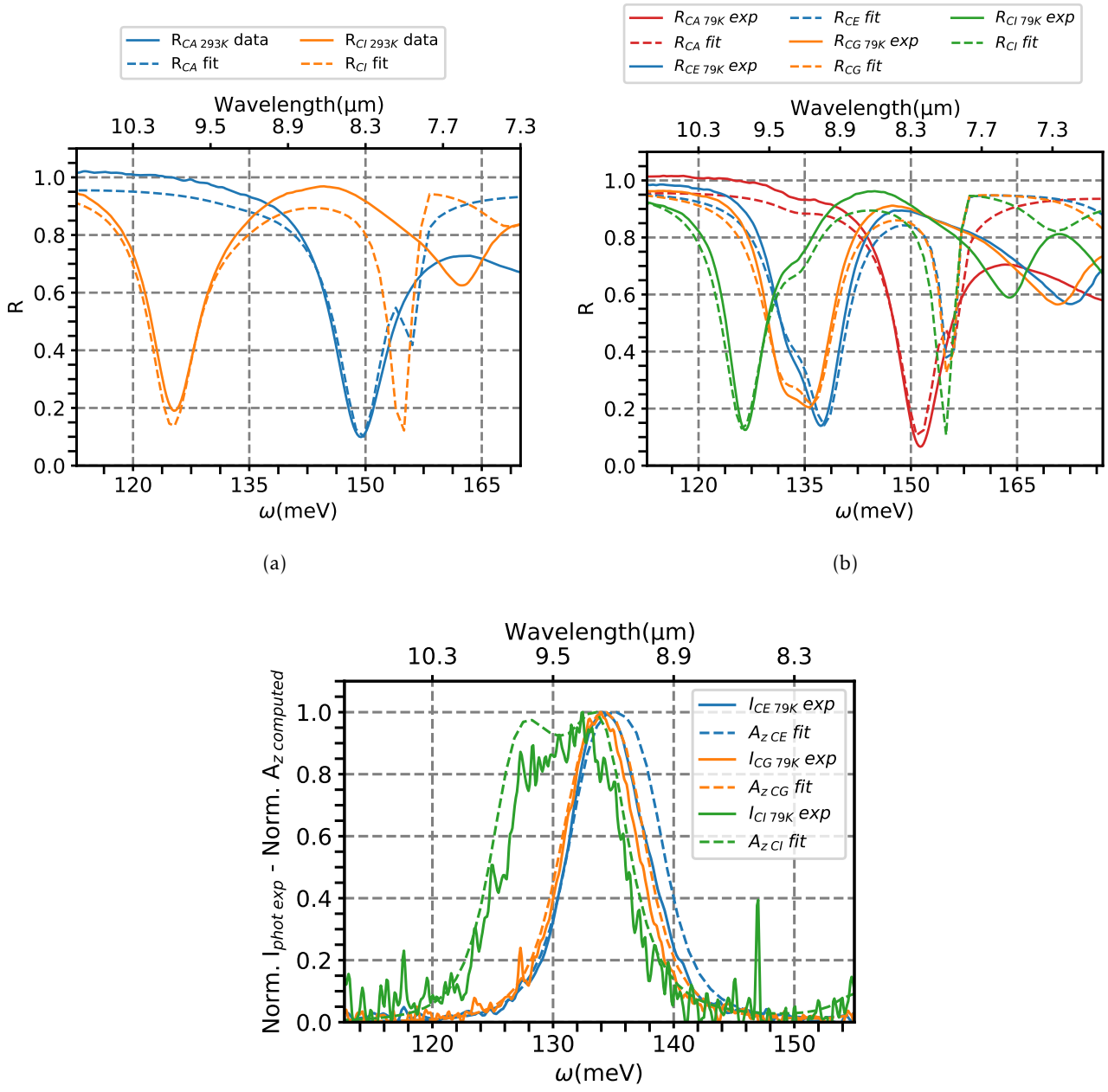

Figure 4.31 – Experimental spectra and simulated spectra (realized with Reticolo) of the sample QCD40-2-3: a) Reflectances at 293K. Parameters: Γ_{ISB}=12meV, $\omega_{0\,ISB}$=131.9meV ($\tilde{\omega}_{ISB}(\Gamma_{ISB} = 12meV) = 134.0meV$)), N=5×10$^{17}cm^{-3}$, $\epsilon_{\infty InGaAs}$(293K)=11.22, $\epsilon_{\infty InAlAs}(293K) = 10.24$, Au: Drude model with $\omega_P = 8.5eV, \Gamma = 0.71eV$, Ti: Drude model from Rakic's paper [107].
b) and c) Reflectances and photocurrents spectra at 79K. Parameters set similar to 293K's case, with Γ_{ISB}=6.5meV, $\tilde{\omega}_{ISB}(\Gamma_{ISB}$=6.5meV) = 135.5meV, $\epsilon_{\infty InGaAs}(79K) = 10.94$, $\epsilon_{\infty InAlAs}(79K) = 9.96$

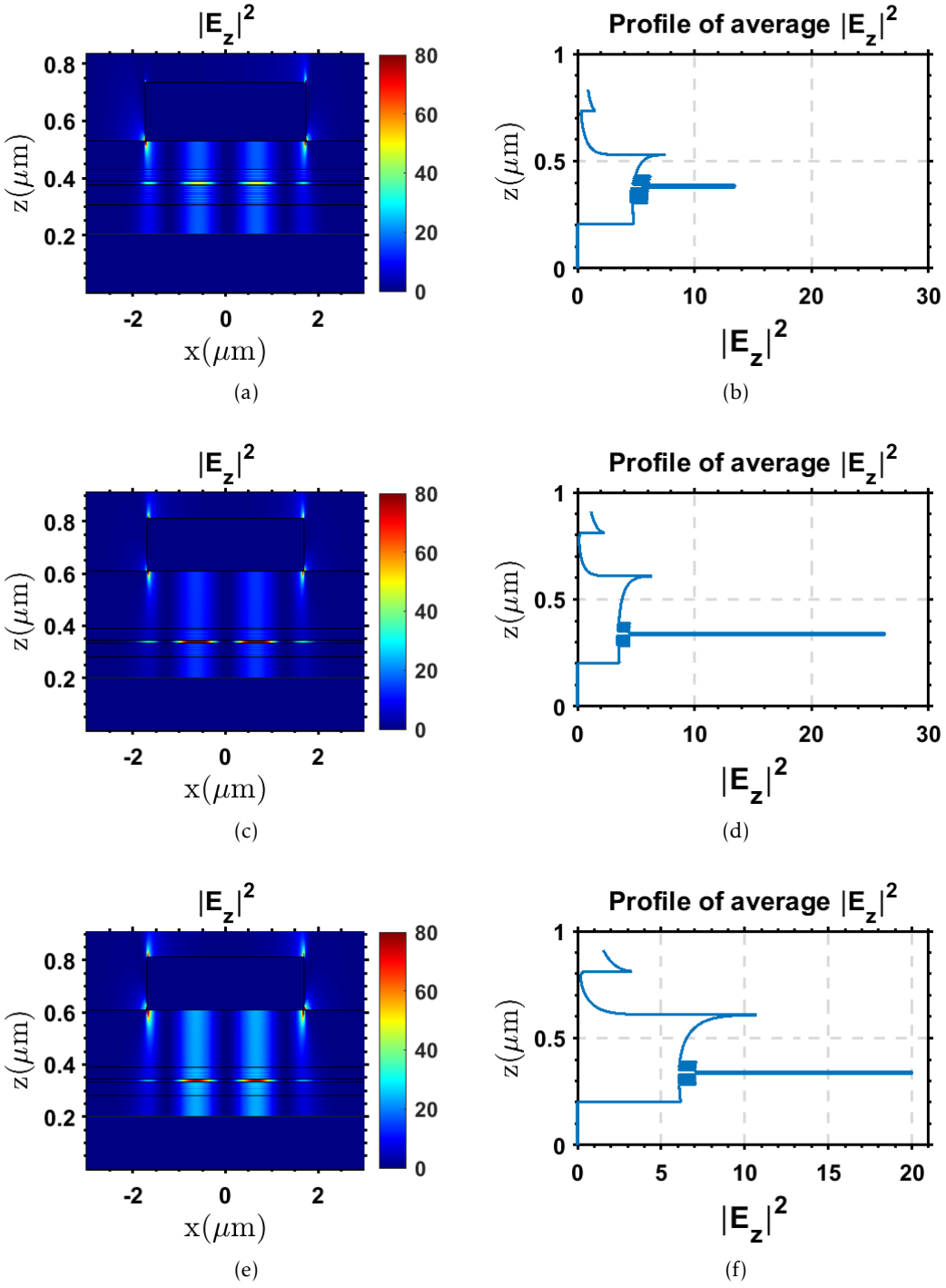

Figure 4.32 – Left: $|E_z|^2$ distributions. a) and c) are computed respectively for optimized structure of QCD40 and QCD41 with updated parameters of dielectric function of Au ($\omega_P = 8.5eV, \Gamma = 0.71eV$) and the ISB transition (Γ_{ISB}=6.5meV). e) is the initial optimization computed for QCD41, with Au dielectric function of Ordal and Γ_{ISB}=12meV.
Right: in b), d), f) are $|E_z|^2$ profiles in the z direction, averaged over the whole period P, corresponding respectively to the left figures a), c), e). Compared to the initial optimization computation in f), the $|E_z|^2$ enhancement in d) due to MIM cavity is reduced to about 4 in InAlAs barrier (rather than about 7 in f)) with updated Au dielectric function having a larger optical loss. The ENZ enhancement on the other hand is increased to about 4.8 rather than 2.8, thanks to the reduction of Γ_{ISB} from 12meV to 6.5meV. All computations are realized at 9μm.

4.5.1.2 Data fitting with Coupled Mode Theory

Our QCD system can be considered as two resonators with eigen frequencies ω_c (MIM cavity mode) and ω_{ISB} of the ISB transition. Their interraction is described by the light-matter coupling constant $\Omega=\frac{\omega_P}{2}\sqrt{f_w}$, where ω_P is the plasma frequency and f_w is the overlap factor between the cavity field and the active QW. The Rabi splitting is given by 2Ω, corresponding to the minimum splitting between the two polariton branches. The resonators have their losses factors: MIM cavity's radiative loss Γ_c, non-radiative loss γ_c and ISB transition non-radiative loss γ_{ISB} (Half width at half maximum, $2\gamma_{ISB}=\Gamma_{ISB}$ used in previous sections).

When ω_c, ω_{ISB}, Ω, Γ_c, γ_c, γ_{ISB} are known, the CMT allows to compute the absorption and reflectance spectra of the two-resonator system cavity-ISB transition. In reference [117], for photocurrent modeling, Lagrée et al. added one more mode (of frequency ω_E, loss γ_E and coupling term Ω_T with the ISB transition) to describe the interaction of the extractor stage of the QCD structure with the previous two-mode system, as illustrated in Figure 4.33, adapted from the same reference. The extractor's mode does not interact with the cavity mode and the introduction of this mode does not change the reflectance spectra compared to the result calculated with the two-mode system. Further details about the model can be found in this paper.

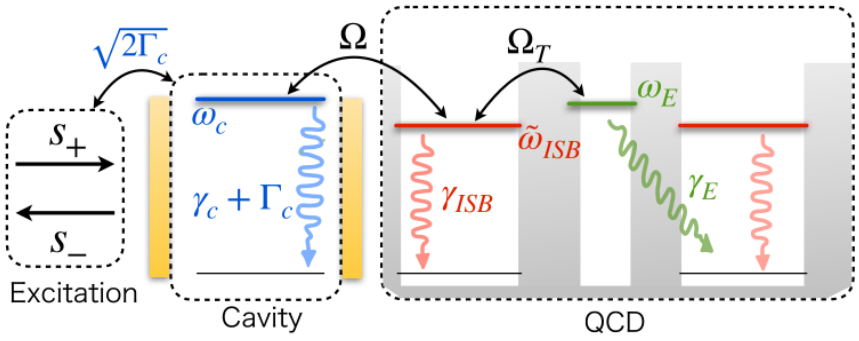

Figure 4.33 – Schematic of CMT with a three-resonator system in QCD, adapted from reference [117].

The data fitting process uses the python package Curve-fit. 4 parameters are supposed to be independent of temperature: ω_{ISB}, Γ_c, γ_c and ω_P (to compute Ω, in which f_w is supposed to be the same as geometrical overlap factor). As discussed in the Reticolo adjusment section, ω_c and γ_{ISB} are temperature dependent. We supposed that the optical index n and the damping factor γ_{ISB} vary linearly with temperature:

$$\omega_c = \frac{2\pi c}{\lambda_{res}} = \frac{2\pi c}{\frac{2n_{eff\,MIM}S}{3}} = \frac{3\pi c}{n_{eff\,MIM\,0}S.(1+T/T_0)} \tag{4.3}$$

$$\Gamma_{ISB} = \alpha T + \Gamma_{ISB\,0} \tag{4.4}$$

The fitting process of multiple devices' reflectance spectra at the same time is quite delicate. Indeed, the position of the MIM resonance is very sensitive to small variation of the strip width S. We used the experimental values of S extracted from SEM images. However a variation of 20-30nm is enough to significantly shift the resonance frequency and affects the fitting result, making a global fitting for the whole data set complex. This is not specific to CMT code but quite general for multiple parameters fitting with one of the parameters having a strong influence on the output. Small resonance details

tend to be ignored during the fitting process since their weight is small in the least square computation. Nevertheless, these fine details are what we are looking for in our case.

Instead of fitting the whole reflectance data set, I chose to fit only spectra of one device at various temperatures, then use the obtained parameters to compute the spectra of other device and compare them with the experimental data. By doing this, we can bypass small uncertainties on S values of different devices.

For sample QCD41-2-3, I fitted the dataset of *'CE'*, as illustrated in Figure 4.34a, with experimental reflectance in solid lines and computed curves in dashed lines. The fits match well with the experimental data. The fitted parameters are reported in Table 4.3 and are used to compute other devices's reflectance spectra on QCD41-2-3, using strip width S obtained from SEM images. We observe three groups of devices with different behaviors:

- *'CH'*, *'CI'*, *'CK'*: their reflectances spectra are reported in Figure 4.34c. Simulated curves show good agreement with experimental data.
- *'CA'*, *'CB'*, *'CC'*: their reflectances spectra are reported in Figure 4.35a. Simulated curves are all blueshifted compared to experimental data, and the shift increases from *'CC'* to *'CA'*. This behavior is also observed in QCD40-2-3 as will be shown in Figure 4.37. We attribute this behavior to the appearance of a diffraction mode as shown in Figures 4.31a and 4.31b around 150-170meV range. The interaction with the diffraction mode repels the MIM mode towards smaller ω than the expected ω of CMT. It is also interesting to notice that we do not observe this behavior in the Reticolo simulation: the simulated spectra of *'CA'* device of QCD40-2-3 both at room temperature and 79K with Reticolo match experimental peak position, whereas CMT fitting gives a peak shift for both QCD41-2-3 and QCD40-2-3. Indeed, Reticolo takes into account diffraction and dielectric function dispersion, whereas CMT ignores these details.
- *'CD'*, *'CG'*, *'CJ'*: their reflectance spectra are reported in Figure 4.34c. The simulated curves are blueshifted by about 5meV compared to experimental spectra. We attribute this bebavior to the defects during fabrication of *'CD'*, *'CG'*, *'CJ'* as stated in Figure 4.16b.

Figure 4.34b depicts the evolution of Γ_{ISB} as a function of temperature, varying from about 6meV to 10meV betwen 79K and 293K. These values are a bit smaller than the adjusted values with Reticolo.

Data fitting with other datasets of QCD41-2-3 are reported in Appendix (illustrated in Figure 43a for *'CG'* dataset fitting and in Figure 43b for the whole *'CE'*, *'CH'*, *'CI'*, *'CK'* datasets being fit together). The fitted parameters are reported in Table 4.3. All these fittings do not give a good matching for all the devices of QCD41-2-3, confirming that there are three groups of devices with different behavior as categorized above: first group includes *'CE'*, *'CH'*, *'CI'*, *'CK'*, second group includes *'CD'*, *'CG'*, *'CJ'* and third group includes *'CD'*, *'CG'*, *'CJ'*.

It's also noticeable that ω_P seems to be underestimated in these fittings. The value ω_P=49meV is expected with METIS's data for a doping N=1×$10^{18} cm^{-3}$. For *'CE'* dataset fitting, ω_P=33.5meV (corresponding roughly to N=5×$10^{17} cm^{-3}$). The fit with multiple devices *'CE'*, *'CH'*, *'CI'*, *'CK'* datasets even gives a smaller ω_P=30.4meV.

The Rabi splitting 2Ω is about 4.8meV for *'CE'* dataset fitting. 2Ω is about the same as $\frac{\gamma_C+\Gamma_C+\Gamma_{ISB}}{2} \sim$ 4.75 (with γ_C=2.2meV, Γ_C=1.3meV, Γ_{ISB}=6meV), at the limit of the strong coupling condition ($2\Omega > \frac{\gamma_C+\Gamma_C+\Gamma_{ISB}}{2}$) as stated in references [117,121]. Eventhough the plasma shift ω_P seems to be underestimated and so does the Rabi splitting in consequence, the strong coupling condition is satisfied, confirming that the devices of QCD41-2-3 operate at the beginning of the strong coupling regime between the ISB transition and the MIM mode.

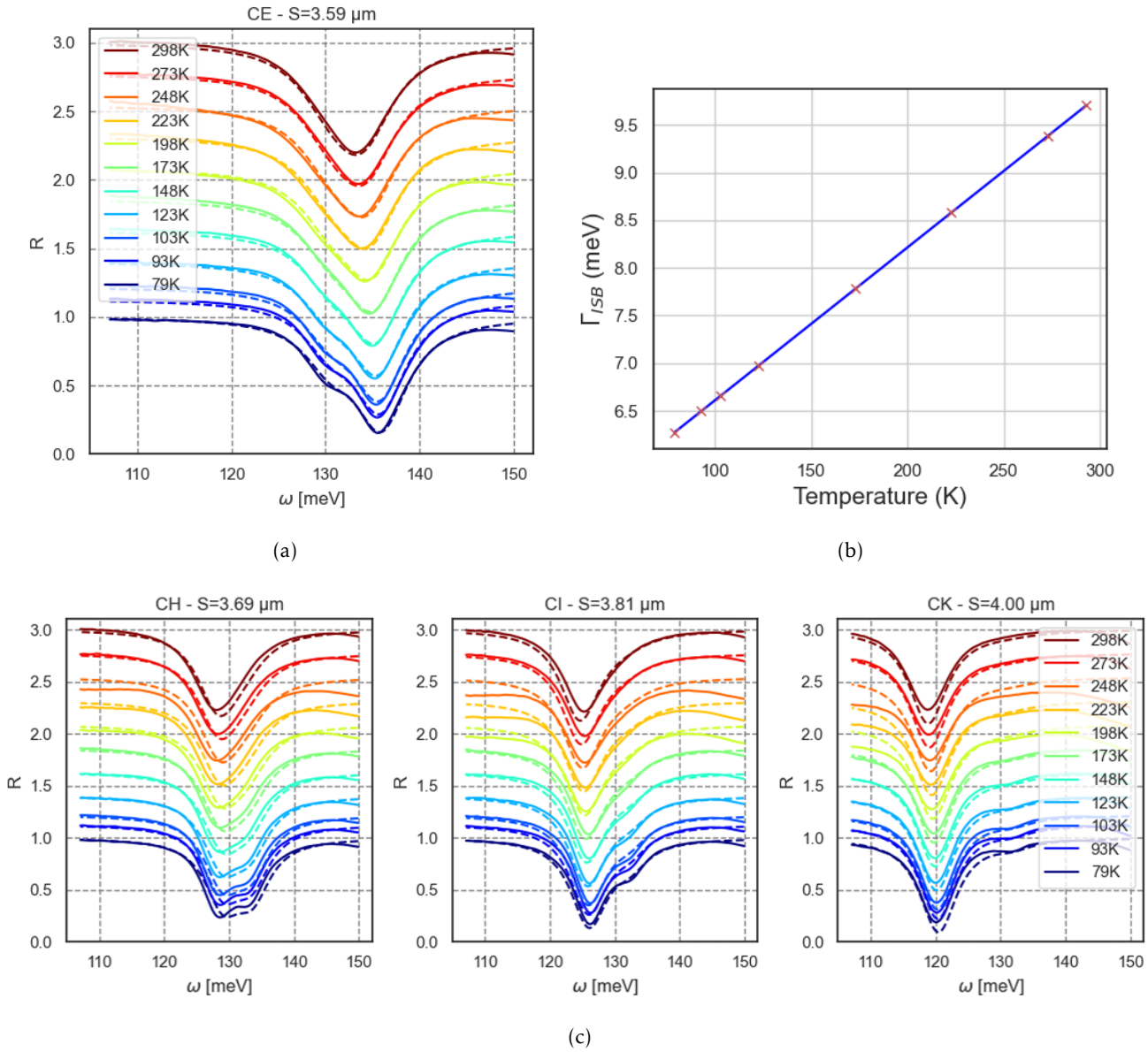

Figure 4.34 – a) Data fitting with CMT of reflectances with *'CE'* dataset of sample QCD41-2-3. b) Evolution of Γ_{ISB} as a function of temperature. c) The obtained parameters are used to compute the reflectance spectra of *'CH'*, *'CI'*, *'CK'*.

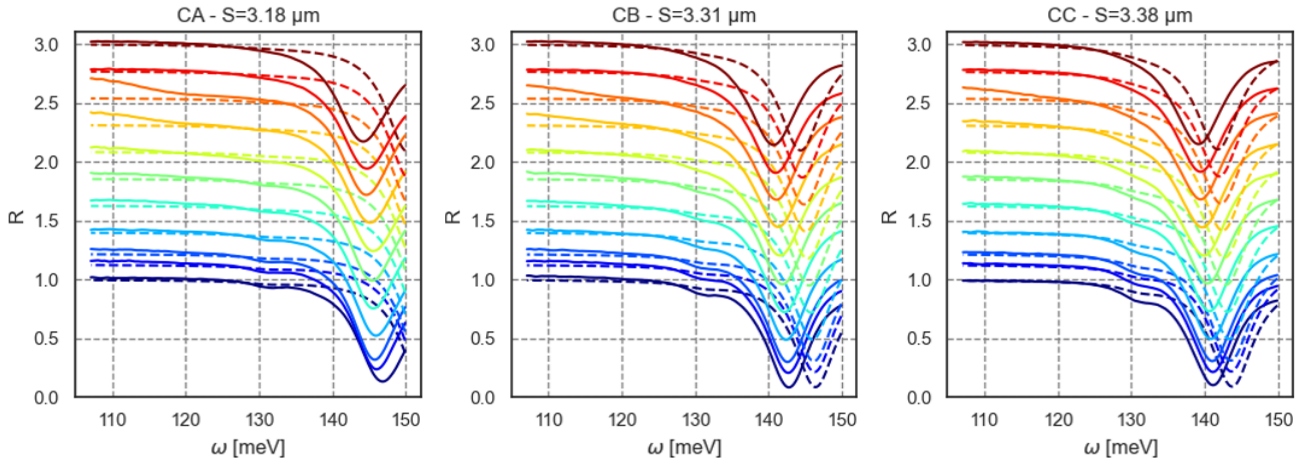

(a)

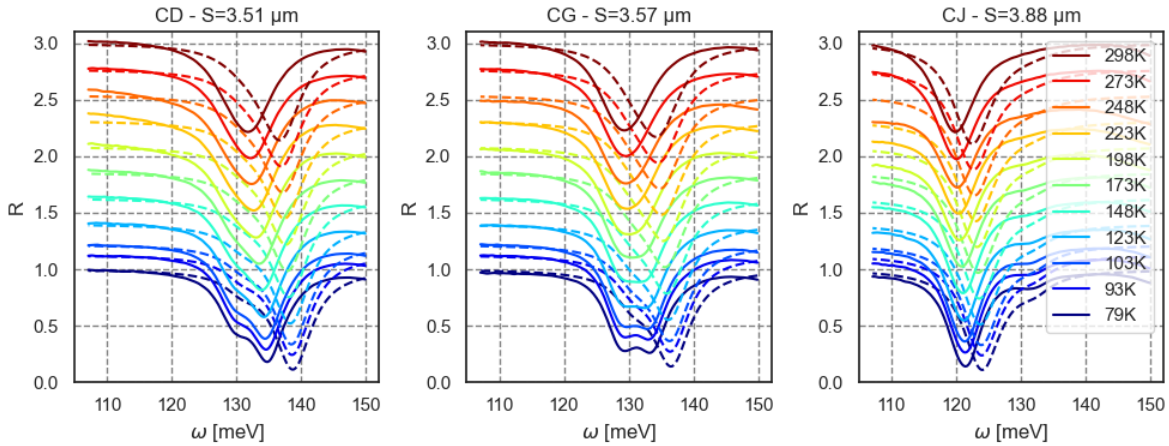

(b)

Figure 4.35 – The fitted parameters obtained with *'CE'* dataset fitting are used to compute the reflectance spectra of: a) *'CA'*, *'CB'*, *'CC'* and b) *'CD'*, *'CG'*, *'CJ'*. Solid lines: experimental data, dashed lines: simulated data with parameters from fit with *'CE'*.

	QCD41-2-3 CE fit	QCD41-2-3 CG fit	QCD41-2-3 CE, CH, CI, CK fit	QCD40-2-3 CG fit	QCD40-2-3 CE-CI fit
ω_{ISB} (meV)	127.2	125.8	127.8	130.6	132.4
ω_P (meV)	33.5	36.5	30.4	30.0	20.9
$\tilde{\omega}_{ISB}$ (meV)	131.6	131.0	131.4	134.0	134.0
Rabi splitting 2Ω (meV)	4.8	5.2	4.4	4.4	3
γ_C (meV)	2.2	1.9	2.5	2.3	2.7
Γ_C (meV)	1.3	1.2	1.2	1.3	1.3
$n_{eff\ MIM\ 0}$	3.825	3.942	3.828	3.886	3.869
$T_0(K)$	15510	14506	15704	19080	12005
α (meV.K^{-1})	1.118 e-05	1.107 e-05	7.881 e-06	8.033 e-06	5.653 e-07
$\gamma_{ISB\,0}$ (meV)	2.5	2.5	2.5	2.5	2.5

Table 4.3 – Table of results of CMT reflectance fit

Similar analysis is realized on sample QCD40-2-3. Figure 4.36 depicts the experimental reflectance spectra (solid line) compared to the fitted curves (dashed lines) realized with the *'CG'* device dataset. The fitted parameters are gathered in Table 4.3 and are used to compute the reflectance spectra of other devices, depicted in Figure 4.37. The agreement is quite good, except for smaller *S* (*'CA'*, *'CB'*). As in the case of QCD41-2-3, we attribute this difference to the appearance of a diffraction mode.

The value of fitted ω_P is about 30meV, matches with METIS's expected value for doping N=5×10$^{17}cm^{-3}$. Similar to the analysis of QCD41-2-3, the fitted parameters of QCD40-2-3 indicate the beginning of a strong coupling regime between the ISB transition and the MIM mode.

Data fitting with more other devices (from 'CE' to 'CI' of QCD40-2-3) are presented in Appendix 44. ω_P obtained in this fit is only 20meV, indicating the tendency of reducing ω_P when many devices' dataset are used in fitting.

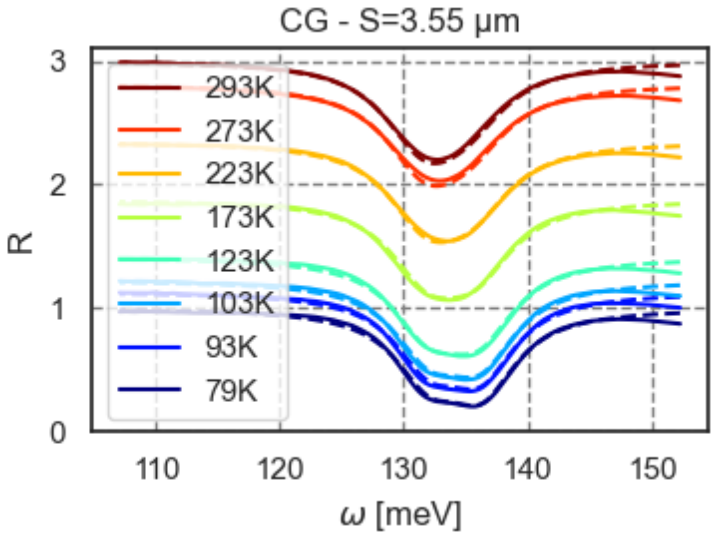

Figure 4.36 – Data fitting with CMT of reflectances with *'CG'* dataset of sample QCD40-2-3.

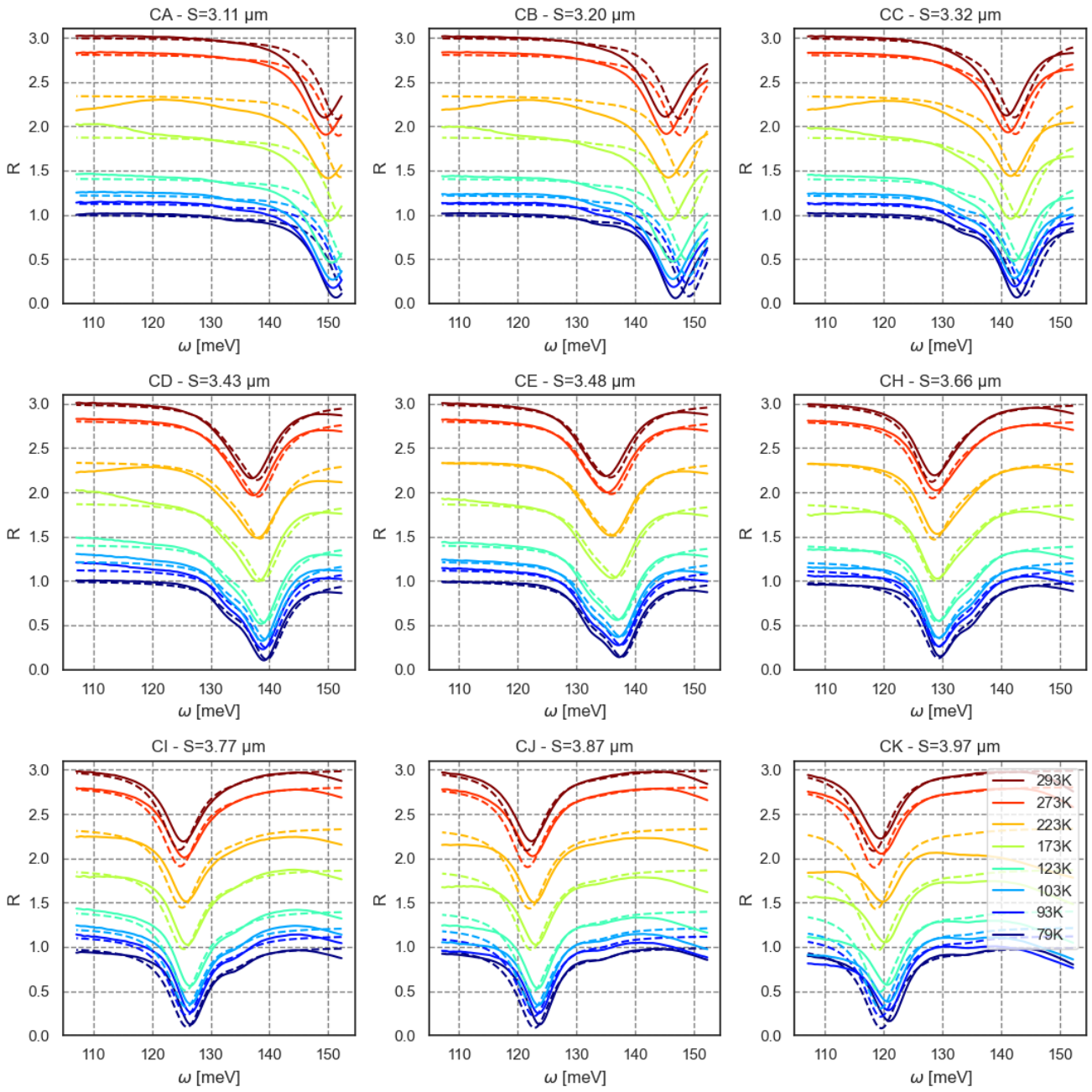

Figure 4.37 – The obtained parameters are used to compute the reflectance spectra of other devices. Solid lines: experimental data, dashed lines: simulated data with parameters from fit with *'CG'*.

The fitted parameters obtained with *'CG'* dataset are used to compute the photocurrent spectra, as illustrated in Figure 4.38. A third resonator with ω_E=132.6meV, Ω_T=2meV and Γ_E=8meV is added in the CMT model. The experimental spectra are in solid lines and the simulated ones are in dashed lines. The linewidths of these photocurrent spectra seem to match better to experimental data, as compared to a simple $A_{z\,QW}$ computation like in Reticolo computation.

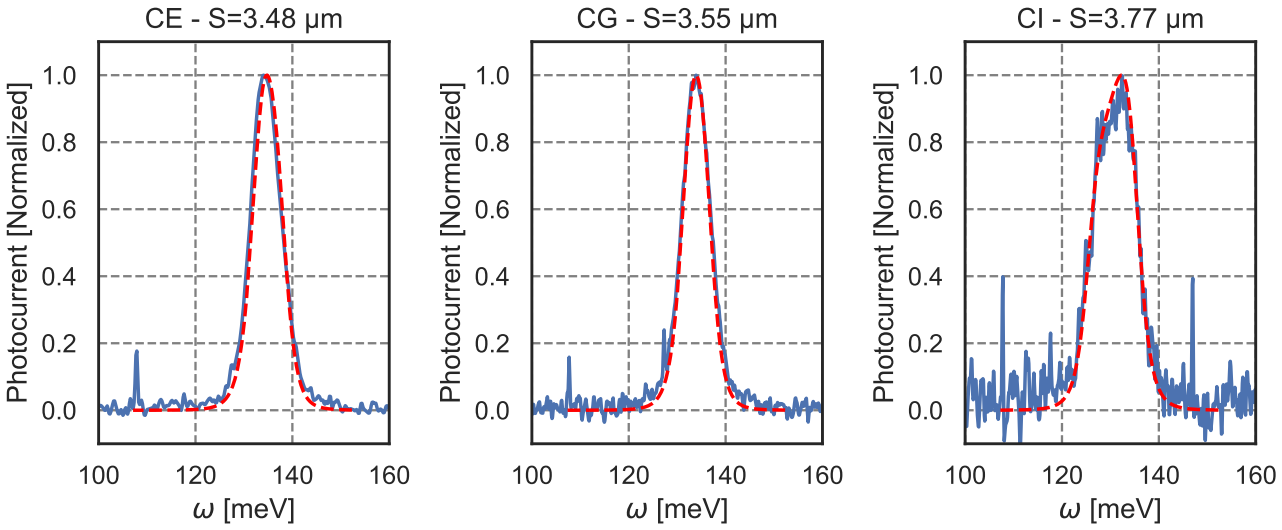

Figure 4.38 – Data fitting with CMT: experimental(blue curves) and simulated (red dashed curves) photocurrents of sample QCD40-2-3.

Finally, the relative amptitude of photocurrent peaks of different devices are computed and illustrated in Figure 4.39a. They are normalized to the maximum value of the *'CG'* device. These ampltidues are put together in Table 4.4 for comparison with normalized experimental amplitude of photocurrent in devices *'CD'*, *'CE'*, *'CG'*, and with $A_{z\,QW}$ computation by Reticolo. For comparison, Figure 4.39b depicts $A_{z\,QW}$ computed with Reticolo using fitted parameters from section 4.5.1.1. In terms of relative amplitudes, the CMT and Reticolo values are quite similar and overestimate a bit the amplitude of photocurrent in 'CD' and 'CE' compared to 'CG'. The result from CMT is closer to the experimental values.

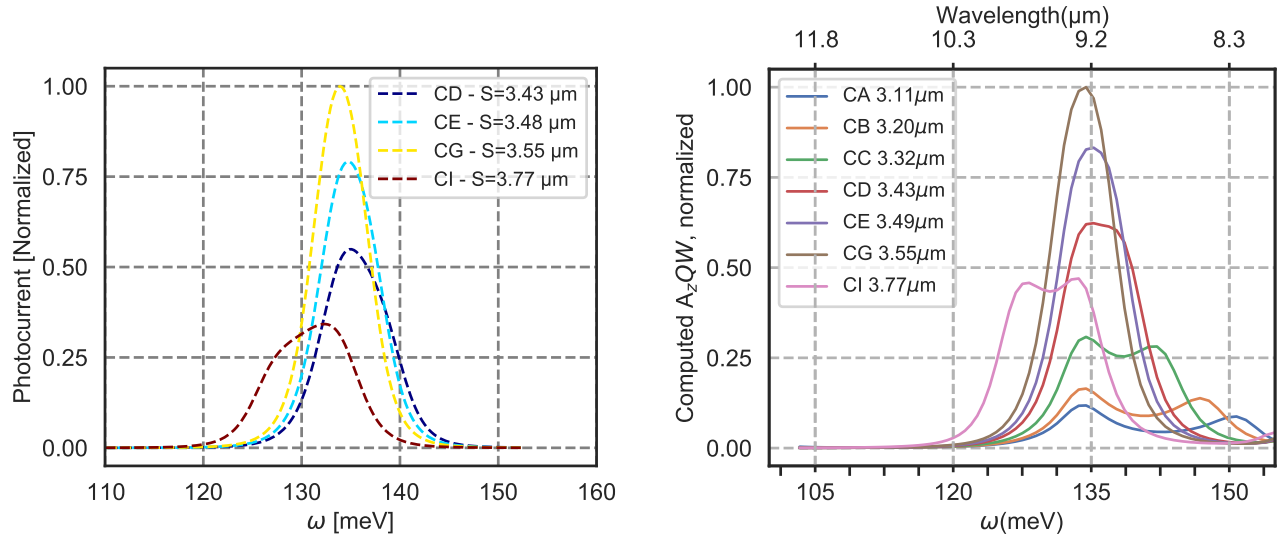

(a) (b)

Figure 4.39 – a) Computed photocurrent spectra with CMT, giving relative amplitudes between different devices. b) Computed useful $A_{z\,QW}$ for different devices with Reticolo, normalized to the maximum of $A_{z\,CG}$.

	CG	CE	CD	CI
$I_{ph\,exp\,norm}$	1	0.72	0.52	-
$\mathrm{Max}_{A_{z\,QW}\,norm}$ Reticolo	1	0.83	0.62	0.46
$\mathrm{Max}_{I_{CMT}\,norm}$ CMT	1	0.79	0.55	0.34

Table 4.4 – Sample QCD40-2-3: Values of normalized photocurrents $I_{ph\,exp\,norm}$ and normalized values of computed maxima of useful absorption A_z ($\mathrm{Max}_{Az\,norm}$ Reticolo) and maxima of the photocurrent spectra computed with CMT $\mathrm{Max}_{I_{CMT}\,norm}$.

4.5.2 Discussion on EQE low value

The EQE of this first generation of single-period ENZ-QCD is about 0.057%, about 300-400 times smaller than the expected value (16-26%, with $A_{z\,QW}$ being 34-55% and P_e=47%). We have not fully understood the reason for this striking difference yet. Nevertheless, some investigations are underway on:

- The electronic transport structure of single-periode QCD: CMT data treatment points out that the experimental value of $\tilde{\omega}_{ISB}$ is smaller than expected (about 131.6 for QCD40-2-3 and 134meV for QCD41-2-3 rather than 137.7meV). In case of QCD40-2-3, this value $\tilde{\omega}_{ISB}$ is smaller than the energy of the first extractor level (ω_E=132.6meV), whereas in initial design we would expect ω_E to be about 3meV smaller than ω_{ISB}. The full transport modelling of single-period QCD is under development at the moment at III-V lab and we expect to get further insights on the impact of such a change on the electron extraction probability P_e and the photocurrent.
- The contact layers used in both QCD structures are doped at $1{\times}10^{17}cm^{-3}$, relatively low compared to contact layers usually found in literature (typically $5{\times}10^{17}cm^{-3}$ - $5{\times}10^{18}cm^{-3}$). While a

low doping reduces optical loss, this doping was chosen near the lower boundary of the doping needed in contact layer in METIS and had not been used experimentally before, introducing some uncertainty in the model. A low doped contact layer induces series resistance that influences the detector's response.

- QCD's fabrication process is not optimized yet. The QCD40-2-3 sample has a non negligeable peripheral current contribution.
- We are also investigating if there is any problem with the opto-electrical characterization setup in term of optical flux and impedance matching. The low flux of the blackbody source and the introduction of different optics may induced error in flux estimation. The samples QCD40-2-1 and QCD41-2-3 have high impedance, up to 1-3MΩ, compared to the sample QCD40-2-3 with an impedance 100 time smaller. We will need to investigate if this difference has any consequence in terms of signal acquisition.

4.6 Chapter conclusion

In summary, in this chapter, I presented the simulation, experimental realization and characterizations of a single-period ENZ-QCD. This kind of device is expected to have a larger External Quantum Efficiency compared to multiple-period QCD, thanks to the reduction of the period number and the enhancement of useful absorption in a single quantum well due to the use of ENZ effect and optical cavity.

In terms of electromagnetic computation, we paid attention not to include the depolarization shift in the ISB dielectric function of the quantum well because this effect is already taken into account by boundary conditions in the Reticolo code. Our computation shows a clear enhancement of E_z field in the quantum well, where the MIM cavity accounts for an enhancement factor of about 5 and the ENZ effect multiplies this enhancement by a factor of about 1.6. The computation predicts a useful absorption of about 34-55% of the incident optical power. The electronic transport simulation realized by our colleagues predicts an Internal Quantum Efficieny of about 47-48%, leading to a theoretical value of EQE up to about 16-26%.

Experimentally, we observed a clear signature of the intersubband transition of a single active quantum well in the QCD structure by cryogenic FTIR reflectance measurement. The ISB absorption happens at 131meV (9.46μm) and 134meV (9.25μm) in two samples of different doping level, and a linewidth of about 6meV (FWHM) at 79K. A transition from weak coupling to strong coupling regime between the ISB transition and the MIM cavity mode is observed when the sample is cooled down from room temperature to 79K. We succeeded to measure the polarization-dependent photocurrent of QCD samples and their spectral responses. The photocurrent spectrum of the optimal device is centered at about 134meV (9.25μm) with a linewidth of about 6meV (FWHM) at 79K. By using two independent computation tools, Reticolo and CMT codes, we were able to reproduce a large set of experimental reflectance and photocurrent spectra. This agreement validates partially our computational method. However, the External Quantum Efficiency is estimated to be about only 0.057%, corresponding to a responsivity of about 4mA/W. This experimental value is about two order of magnitude smaller than simulation's predicted value. Further investigations need to be carried out for a better understanding of this difference.

General conclusion and perspectives

ENZ effect is a relatively new topic and has been studied actively since the last decade for its property to confine and enhance light field in highly sub-wavelength layers. The goal of my Ph.D. work is to apply the ENZ concept to mid-infrared optoelectronic devices traditionally limited by weak light-matter interaction.

In chapter 1, I introduced the ENZ effect its potential for nanophotonics. I discussed about the theory of the dielectric function ϵ and its different contributions: free charges, ISB transion and optical phonon that can be used to reach the ENZ regime. In the discussion about absorption of the Berreman mode in thin slab, we suggested a generalization of the plasma shift or depolarization shift notion to the three contributions to ϵ.

In chapter 2, I studied the dielectric function of InGaAs, our material of choice to realize the ENZ effect. I introduced different experimental methods to study parameters of the dielectric function: Van der Pauw Hall effect, FTIR, Raman. We also suggested applying a model with sum of gaussian lineshapes to describe the dielectric function of optical phonons in InGaAs. This model respects the Kramer Kronig relation, helps to avoid the problem of non physical negative ϵ'', found in literature's data. Angular dependent FTIR measurement in far IR of a 320nm-thick only InGaAs layer displays clear variations due to both TO and LO phonon, thanks to the detuned Salisbury screen configuration. The FTIR result is in good agreement with Raman measurement. This optical phonon study in InGaAs is subject of a paper ready for submission.

Chapter 3 focused on the study of an ENZ-EOM structure. The optical modulation is based on detuning an ENZ mode which is initially in strong coupling with a cavity mode, where the detuning consists in electron depletion with a voltage bias. I realized two kinds of structures, HEMT-like and MOSFET-like ENZ-EOM. Electromagnetic computation shows a strong confinement of light in the ENZ layer and a significant amplitude modulation (up to 90% in HEMT-like structure). Experimetnally, we observed a strong coupling regime in both structures, between ENZ mode and MIM cavity mode in HEMT-like structure, and with a third mode - ENZ optical phonon of SiO_2 insulator - in MOSFET-like structure. However, a significant electron depletion appears to be challenging in both structures, attributed mainly to unmastered interface conditions and too high doping level. Nevertheless, an optical modulation of about 5-10% of the reflectance (or 0.5-1.2dB in modulation depth) around 7.5μm is observed in the MOSFET-like structure, linked to the presence of thin SiO_2 layer. This observation possibly paves the way to study a new modulation mechanism which involves three modes coupling. Future work will be

focused on changing to new material systems of larger band gap for HEMT-like structrure and on exploring the three modes coupling modulation mechanism. Another path of study consists in application in the THz range of ENZ-EOM structure, where much lower doping level is required to reach the ENZ regime and thus the electron modulation should be less challenging.

The last chapter is devoted to the development and demonstration of a single-period ENZ-QCD. Electromagnetic computation indicates that ENZ effect combined with MIM cavity enhanced significantly the normal component of electric field in the quantum well, beneficial to ISB absorption. This enhancement leads to a useful absorption of about 34-55% of the incident optical power by a single quantum well, according to modelization of our experimental realization. Combined with the electronic transport modelling result, a theoretical value of the External Quantum Efficiency up to about 16-26% is expected. Experimentally, we observed a clear signature of the ISB transition of a single quantum well in the QCD structure, using cryogenic FTIR reflectance measurement. A transition from weak coupling to strong coupling regime between the ISB transition and the MIM cavity mode happens when the sample is cooled down from room temperature to 79K. We succeeded to measure the polarization-dependent photocurrent of QCD samples and their spectral responses. We were able to reproduce in good agreement a large set of experimental reflectance and photocurrent spectra, using two independent computation tools, validating partially our computational method in terms of spectral response. However, the expermiental EQE is estimated to be about 0.057% for this first generation ENZ-QCD, more than two order of magnitude smaller than computation's prediction. Future works should focus on mastering the fabrication process, studying the consequence of a smaller ISB energy than expected on the electronic transport, reviewing the experimental setup in terms of impedance matching and using a stronger IR source. The single-period ENZ-QCD structure is a complex system at the interface between optoelectronics and nanophotonics. Further investigations will offer interesting perspectives for both fundamental understanding and technological application.

Appendix

A Samples list of ENZ-EOM and control samples

Stacking of various samples from chapter 3 and 2 are reported here, from substrate to top. The thicknesses are nominal values.

Samples with grating:

HEMT-like ENZ EOM:

- TGB4545-6-1: Au 400nm / Ti 2nm / InP 50nm / InGaAs n-doped $1.24\times10^{19}cm^{-3}$ 25nm / InP 10nm / Ti 2nm / Au 200nm.
- TGB4545-2-1: Au 200nm / Ti 2nm / InP 50nm / InGaAs n-doped $1.24\times10^{19}cm^{-3}$ 25nm / InP 10nm / Ti 2nm / Au 200nm.

MOSFET-like ENZ-EOM:

- TGB4545-6-2: Au 400nm / Ti 2nm / InP 50nm / InGaAs n-doped $1.24\times10^{19}cm^{-3}$ 25nm / InP 10nm / SiO2 5nm ALD / Ti 2nm / Au 200nm.
- TGB4545-5-2: Au 400nm/ Ti 2nm / InP 50nm / InGaAs n-doped $1.24\times10^{19}cm^{-3}$ 25nm / InP 10nm /sputtered SiO2 15nm / Ti 2nm / Au 200nm

Test samples:

- H7739-3-1-1: Au 300nm / Ge 5nm / InGaAs n-doped $1\times10^{19}cm^{-3}$ 120nm / Ge 5nm / sputtered SiO2 5nm /Ge 5nm / Au 200nm
- H7739-3-2: Au 300nm / Ge 5nm /InGaAs n-doped $1\times10^{19}cm^{-3}$ 120nm / Ge 5nm / Au 200nm

Sample without grating for Berremann's absorption measurement:

TGB4545-2-3 : Au 200nm / Ti 2nm / InP 50nm / InGaAs n-doped $1.24\times10^{19}cm^{-3}$ 25nm / InP 10nm

B Fabrication processes

B.1 Ormostamp wafer bonding

The active stack is transfered on a Pyrex glass host substrate by Ormostamp bonding:

- The multilayer substrate is glued on a silicon wafer with wax (*Sticky wax*, soluble in hot tricloroethylene or *Crystal bond wax*, soluble in acetone) for easier handling.
- Plasma O_2 1 minute of both the sample and the Pyrex glass to improve the adhesion.
- Spin coating of Ormostamp solution on the multilayer surface (right after plasma O_2), speed 3000rpm, 2000rpm/s during 30s. Keeping the Pyrex glass on hot plate preheated at 120°C during spin coating.
- Inclining and slowly putting into contact the Pyrex glass with the multilayer sample in order to chase out all air bubles.
- Polymerization of Ormostamp under UV lamp (*Lightningcure LC5* Hamamatsu) at a power of 50mW during 20 minutes.
- Leaving the sample overnight for the polymer to relax.
- Removing wax in hot tricloroethylene 85°C (for Sticky wax) or acetone (for Crystal bond wax), leaving the sample bonded to the Pyrex glass.

B.2 EOM fabrication process

EOM InP substrate removal

The initial 500μm-thick InP substrate is removed by wet etching in HCl 37% (etch rate about 8μm/minute). Prior to this etching, it is recommended to protect the edges of the sample with wax to prevent lateral underetching. However, I found that the Ormostamp forms a thin line on the edges of the structure that already plays the protection role, so the wax protection is optional.

The etching stops when the InGaAs etch-stop layer is uncovered with a mirror-like aspect. Due to very high etching selectivity between InP and InGaAs, we can leave the etching 5 more minutes in order to remove completely InP from the surface for further homogeneous etching. The anisotropic etching of InP leaves 2 InP walls on the side of the sample that needs to be removed mechanically with a cutter prior to lithography steps.

The stop-etch layers (200nm InGaAs, 20nm InP, 10nm InGaAs) are removed by successively etching in $H_3PO_4/H_2O_2/H_2O$ 9v/3v/120v (etch rate about 100nm/minute) for InGaAs and in HCl 37% for InP. At this thickness of the multilayer on top of gold, we observe a color change highly dependent on the thickness of the multilayer. This is a good indicator of etching completion and allows a quick optical check of the etching homogeneity. Thanks to high selectivity, we are allowed to leave the etching to continue 10-20s after the etching time calculated from average etching rate. This is important to obtain homogeneous etching.

Level 1: Top Grating

The top grating is realized by lift-off process with AZ5214E resist in image reversal mode. We would like to realize a metal grating composing of strips of around 1μm by UV lithography (i-line of wavelength 365nm). On substrate transferred samples, this process can be quite challenging compared to the same process on a large silicon wafer. Indeed, our substrate transferred samples is not flat as ideal silicon wafer, the resist film is usually not homogeneous. Residues from InP walls and Ormostamp resist on the side of the sample are thick and pose serious problems if not removed completely. The sample is about 2x2cm^2, smaller than standard 2inches silicon wafer, so edge-beads' influence also reduces the resolution.
In order to achieve strip patterns of around 1μm:

- I removed carefully all the residues of InP walls and Ormostamps on the sample's side.
- I used a thin resist (spin-coated at 6000rpm, 2000rpm/s, 63s, baked at 125°C 90s to obtain about 900nm of thickness).
- AZ5214E can be used both as positive and negative resist. I removed the edge-beads with one extra lithography step in positive resist mode, consisting of edge exposure 30s, then development 2 minutes in MIF826. The exposed resist on the edges is removed after the development while the active surface is still covered with resist for the main lithography step. For thick edge-beads that are not completely removed after development, we used a Q-tip soaked with very little acetone to brush only the substrate edges.

These steps are indispensable to obtain high resolution patterns. They are followed by an exposure in vacuum contact mode with the grating mask during 5s (dose 50mJ/cm^2). The sample is baked at 125°C for 90s, then exposed in flood mode for 30s to realize image reversal process. It follow by a first development during 40s in MIF826 after which we can observe the development state of the resist and adjust the duration of a second development step. Usually this second step requires a prewetting of 30s in water and a further 15s of development in MIF826 to obtain good patterns' size.
The sample is treated by 1 minute plasma O_2 to remove resist residues, then deoxidized in HCl37%/H_2O 1v/9v during 1 minute, before a metalization with 2nm Ti and 200nm Au. The lift-off process is realized by leaving the sample in acetone for about 30 minutes to dissovle the resist, then firing strong acetone jets with help of a syringe to remove the resist. The sample is then kept in isopropanol (avoid drying) and observed under microscope to assure that the lift-off is realized correctly. Otherwise, we repeat the syringe operation many more times. This is an effective way to get a high success rate of lift-off. It is not recommended to soak the sample in acetone overnight because the edges of the bonding tend to peel off and the sample is fragilized.
This grating level is the first lithography step and also the most challenging one due to the need to obtain 1μm large strips. Following steps do not require high resolution so their processes are less demanding.

Level 2: QW Contact

Two contact pads are realized on the sides of each EOM device. They are posed in contact with the QW InGaAs layer, for the purpose of creating electron reservoirs where electrons can be evacuated to under bias. The process is quite similar to the grating level. A deoxidation step prior to resist spin-coating is necessary to remove native oxide and avoid underetch. The same process as the grating level is realized, but we dont need a thin resist film in this case, so the standard speed is used: 4000rpm, 2000rpm/s during 30s for a 1.4μm thick resist layer. The development time is increased to 90s to obtain a clear negative flank profile.
After the development and the plasma O_2 treatment, 10nm InP top barrier is etched away by a 'flash' etch of 3s in HCl 37%. Longer etching time tends to enlarge the underetch with the risque of touching the grating level (distanced by 2.5μm on the mask) and causing short-circuit. The deoxidation is crucial since native oxide of InP is etched faster than InP so the acid can penetrate easily under the resist and etch away unintended parts. I also tried to dilute the HCl 37% in H_3PO_4 at ratio 1v/3v in an attempt to reduce the etch rate and therefore the underetch. However, H_3PO_4 is highly viscous compared to HCl 37%, causing inhomogeneous etching in resist patterns and making the etching even more complex.
After this etching step, 5nm Ti and 200nm Au are deposited, following by the lift off process.

B.3 QCD fabrication process

QCD epitaxie files

Epitaxy files of QCD40 and QCD41 are given here below. The transport design was realized by Mathurin Lagrée and colleagues at III-V lab.

QCD40	Material	Thickness (Å)	Doping (cm^{-3})
1	InGaAs:Si	1000	1×10^{17}
2	InAlAs	26	-
3	InGaAs	88	-
4	InAlAs	28	-
5	InGaAs	72	-
6	InAlAs	29	-
7	InGaAs	63	-
8	InAlAs	29	-
9	InGaAs	56	-
10	InAlAs	29	-
11	InGaAs	50	-
12	InAlAs	31	-
13	InGaAs	45	-
14	InAlAs	33	-
15	InGaAs	41	-
16	InAlAs	33	-
17	InGaAs	39	-
18	InAlAs	31	-
19	InGaAs	7	-
20	InGaAs:Si	31.4	$6.4\times10^{11}cm^{-2}$
21	InGaAs	60.6	-
22	InAlAs	35	-
23	InGaAs:Si	85	5×10^{16}
24	InAlAs	35	-
25	InGaAs:Si	96	5×10^{16}
26	InAlAs	35	-
27	InGaAs:Si	107	5×10^{16}
28	InAlAs	35	-
29	InGaAs:Si	1000	1×10^{17}
30	InAlAs	2000	-
31	InGaAs	2000	-

Table 5 – Epitaxie file QCD40

QCD41	Material	Thickness (Å)	Doping (cm^{-3})
1	InGaAs:Si	1000	1×10^{17}
2	InAlAs	26	-
3	InGaAs	88	-
4	InAlAs	28	-
5	InGaAs	72	-
6	InAlAs	29	-
7	InGaAs	63	-
8	InAlAs	29	-
9	InGaAs	56	-
10	InAlAs	29	-
11	InGaAs	50	-
12	InAlAs	31	-
13	InGaAs	44	-
14	InAlAs	33	-
15	InGaAs	40	-
16	InAlAs	33	-
17	InGaAs	7	-
18	InGaAs:Si	31.4	$1.25\times10^{12}cm^{-2}$
19	InGaAs	62.6	-
20	InAlAs	35	-
21	InGaAs:Si	85	5×10^{16}
22	InAlAs	35	-
23	InGaAs:Si	96	5×10^{16}
24	InAlAs	35	-
25	InGaAs:Si	107	5×10^{16}
26	InAlAs	35	-
27	InGaAs:Si	1000	1×10^{17}
28	InAlAs	2000	-
29	InGaAs	2000	-

Table 6 – Epitaxie file QCD41

QCD etching process

The etch-stop layers used are 200nm InGaAs and 200nm InAlAs. Both materials are etched by H_3PO_4:H_2O_2:H_2O at similar rate. I adapted another selective etching process for InGaAs and InAlAs.

InAlAs at 52% of Al can be selectively etched from InGaAs in HCl:H_2O 3v:1v (etch rate non linear as a function of time). InGaAs can be selectively etched from InAlAs by citric acid solution:H_2O_2 1v:1v.

The citric acid solution is made of citric acid powder disolved in deionized water for the mass ratio 1:1 (endothermic reaction) about 1 hour before so that the solution is back to room temperature. The interface between InGaAs and InAlAs can have mix alloy which is not completely etched in citric:H_2O_2 1v:1v or HCl:H_2O 3v:1v. The etching of InAlAs by HCl:H_2O 3v:1v can be very inhomegeneous if we start the etching directly from this interface. To remove homegeneously the 200nm InAlAs etch-stop, I chose to etch by H_3PO_4:H_2O_2:H_2O during 20s from the InGaAs/InAlAs inerface, then finish with HCl:H_2O 3v:1v. In this way, the etching is much more homogeneous.

NLOF 2070 lithography process

The NLOF 2070 lithography process for thick negative photoresist was realized as followed:

- Dehydration 105°C 2min.
- Spin coating 4000rpm, 2000rpm/s, 30s (film thickness about 7μm).
- Baking at 105°C 90s.
- Edge bead removing by immersing just the glass substrate edges in AZ400K 15s per edge.
- Exposure 34s with negative mask, vacuum contact.
- Baking at 105°C, 90s.
- Development 60-180s in MF26.

SEM image of QCD40's cross section

Here below is the SEM image of QCD40's cross section:

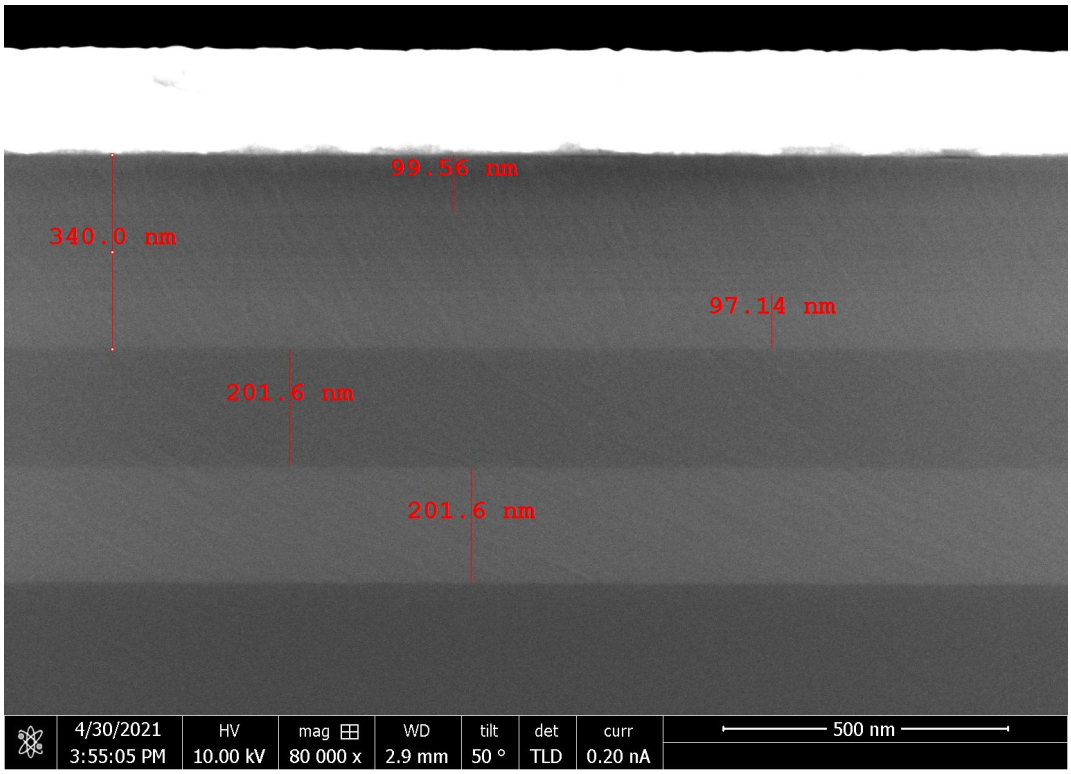

Figure 40 – SEM image of QCD40 substrate's cross section with Ti/Au/Ti/SiO_2/Ti on top.

C QCD's parasitic photocurrent spectrum

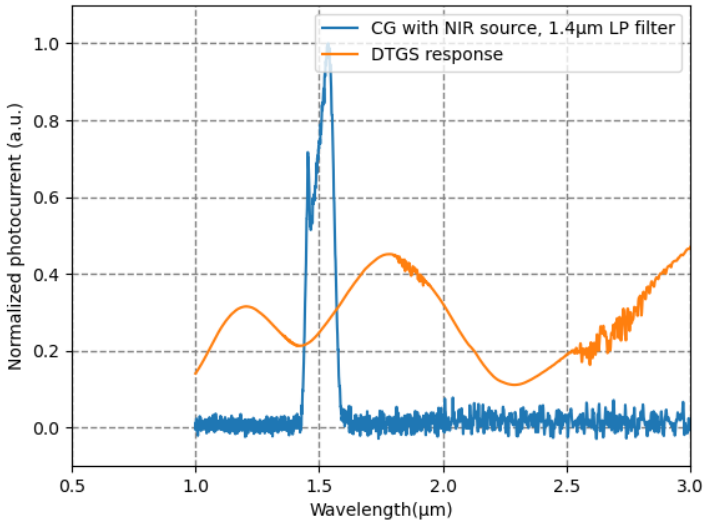

Figure 41 – Parasitic photocurrent spectrum in near-IR range. The signal is filtered with longpass filger 1.4μm to remove the laser signal of the FTIR.

D QCD's photon flux estimation

Let's consider the optical schematic presented in Figure 42. The experimental setup consists of a blackbody source with emitting surface limitted by a pinhole of radius R and surface S=πR^2. The pinhole is located at the focal point of a parabolic mirror which plays the role of collimating the beam. For simplicity, the collimator is represented by an equivalent lens of focal length F and diameter D. Let θ_0 be the angular aperture of the collimator. The collimated beam is re-focalized by a smaller lens of focal length f and diameter d. The detector (in square form) of size a and surface A=a^2 is positionned in the focal plan of the second lens. Let λ_0 and $\Delta\lambda$ be the detection wavelength and the optical bandwidth of the detector. The beam also passes through a polarizer, a filter and a cryostat's windows which introduce their transmission coefficients T_1 T_2 T_3 = T_{optics}. We would like to determine the photon flux impinging on the detector's surface A.

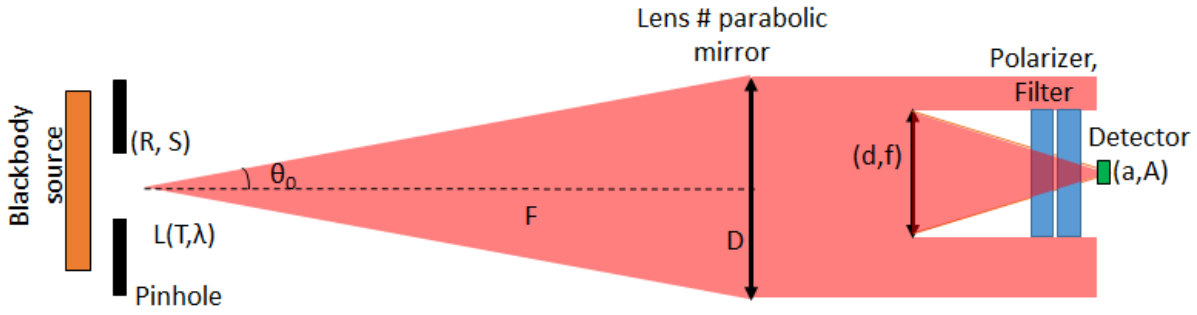

Figure 42 – Schematic of the optical system.

The blackbody and the pinhole together are considered as a lambertian source with isotropic spectral radiance L depending on the blackbody source's temperature T and the considered wavelength λ. The spectral radiance (in photon number) of a blackbody source is given by the Planck's law as follows:

$$L(T,\lambda) = \frac{2c}{\lambda^4}\left(exp\left(\frac{hc}{\lambda k_B T}\right) - 1\right) \tag{5}$$

The unit of the spectral radiance in photon number is $[s^{-1}.m^{-3}.sr^{-1}]$.

By integrating over the source's surface and the angular aperture of the collimator, the photon flux entering the collimator is given by:

$$\Phi_S = \int L(T,\lambda)d\lambda.dS.Cos\theta d\Omega \tag{6}$$

$$\Phi_S = \int L(T,\lambda).d\lambda.dS.Cos\theta.d\Omega \tag{7}$$

$$= S\int L(T,\lambda).d\lambda.\int_{\phi=0}^{2\pi}\int_{\theta=0}^{\theta_0} cos(\theta).sin(\theta).d\theta.d\phi \tag{8}$$

$$= \pi S sin^2(\theta_0)\int L(T,\lambda).d\lambda \tag{9}$$

A fraction of Φ_S is re-collected by the second lens and is focalized toward the detector, determined by the ratio of the lens's surface. The beam also passes by optics with certain transmission coefficients:

$$\Phi_{lens\,2} = \Phi_S \frac{d^2}{D^2}.T_{optics} \tag{10}$$

The pinholes used are large enough so that the image of the pinhole is larger than the detector's surface. The the photon flux impinging on the detector surface is determined by the ratio between detector surface and the surface of the pinhole's image: $\frac{A}{S}\frac{F^2}{f^2}$.

By condisering $\theta_0 \ll \pi$ (valid experimentally), we can simplify by having $\sin(\theta_0) \simeq \frac{D}{2F}$. After simplification, the flux impinging on the detector surface is given by:

$$\Phi_D = A\frac{\pi d^2}{4f^2}.T_{optics}.\int L(T,\lambda)d\lambda \tag{11}$$

Geometrical quantities are: R=2mm, F=0.762m, D=0.1m, f= 0.2m, d=0.05m, a=150μm, A=2.25×10^{-8}m^2. The spot size of the pinhole image is about 1.1mm in diameter. The blackbody temperature is 1373K. Our detector works with $\lambda_0 \sim 9.5\mu$m, $\Delta\lambda \sim 0.5\mu$m according to photocurrent spectrum of the device *'CG'* of QCD40-2-3, the integral of the spectral radiance gives $\int L(T,\lambda).d\lambda \sim 2\times10^{22}$ photons.m^{-2}.s^{-1}.sr^{-1}.

The transmissions of the polarizer, the filter and the cryostat's windows are respectivelyabout 0.7, 0.9, 0.8 according to manufacturers' information. We also take into account the TM polarization by dividing the flux by 2.

The photon flux in TM polarization is: $\Phi_{D\,TM} \sim 5.5\times10^{12}$ photons.s^{-1}. For an EQE=100%, the photocurrent is given by $I_{phot\ max}$=$\Phi_{D\,TM}$.e=0.88μA.

E QCD reflectance spectra fit with CMT

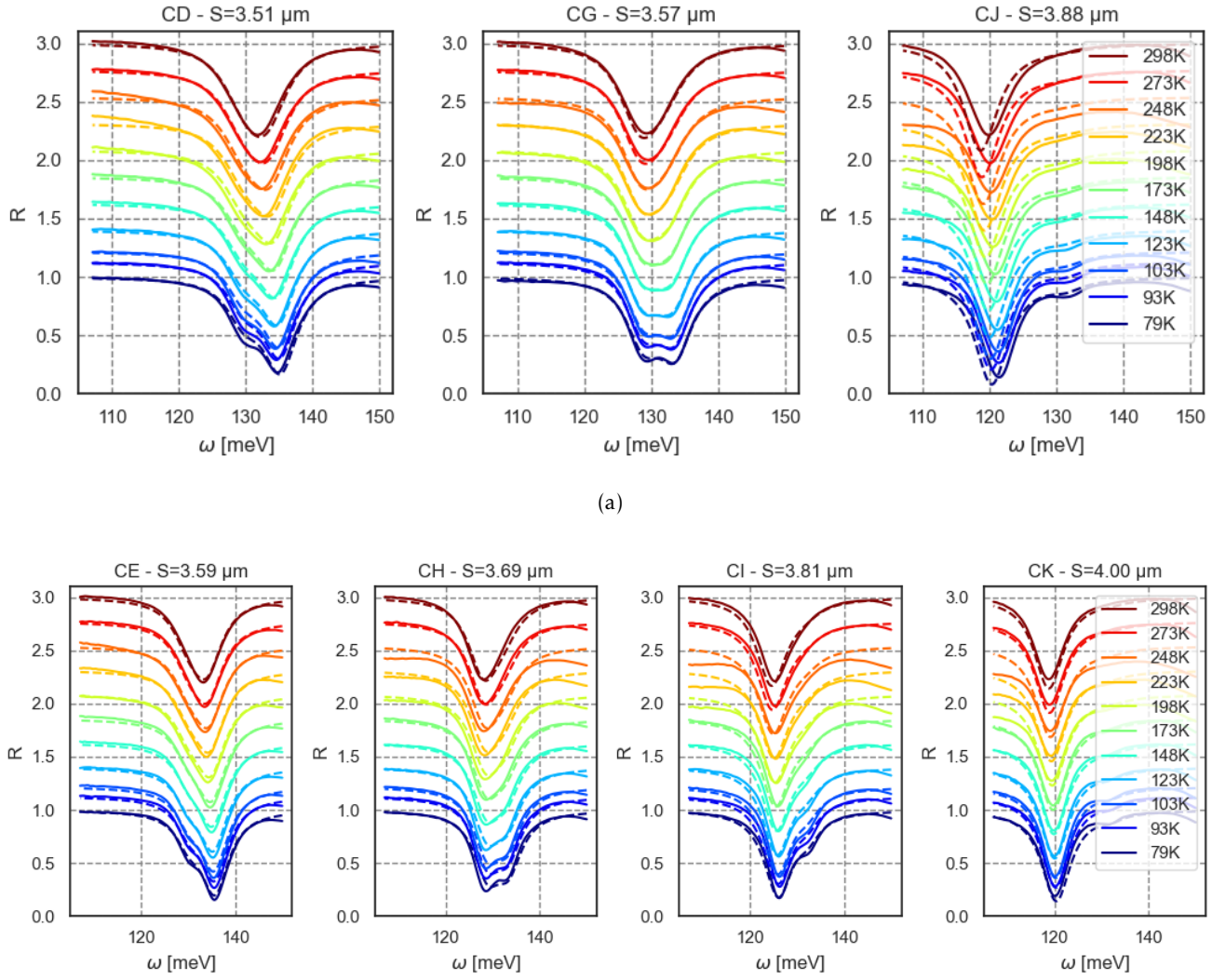

(a)

(b)

Figure 43 – Data fitting with CMT: Reflectances at various temperatures of sample QCD41-2-3. a)The fit is realized with *'CG'* dataset. b)The fit is realized globally with *'CE'*, *'CH'*, *'CI'*, *'CK'* dataset.

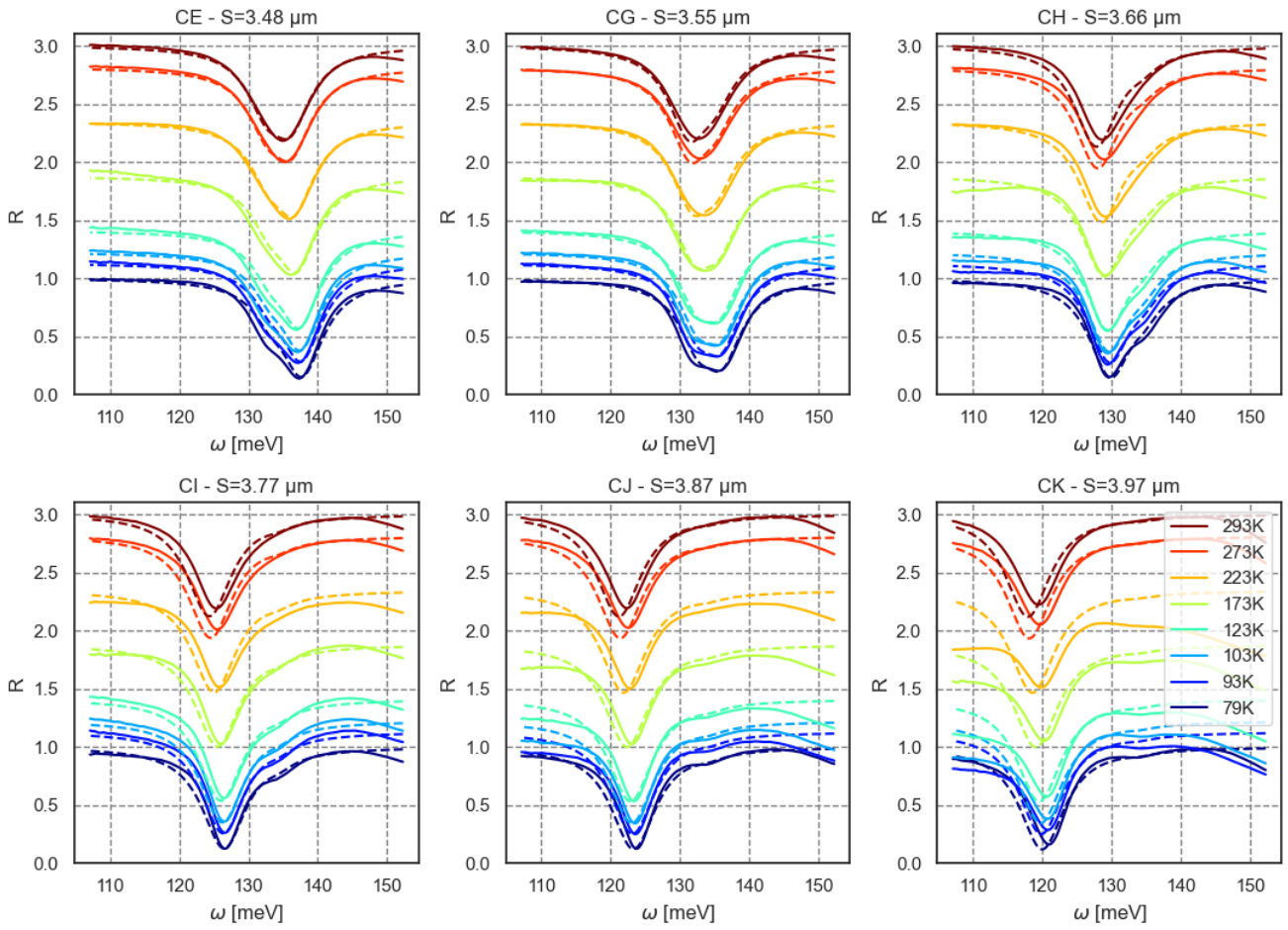

Figure 44 – Data fitting with CMT: Reflectances at various temperatures of sample QCD41-2-3. The fit is realized globally with *'CE'*, *'CG'*, *'CH'*, *'CI'* dataset.

Bibliography

[1] Shuren Hu, Marwan Khater, Rafael Salas-Montiel, Ernst Kratschmer, Sebastian Engelmann, William MJ Green, and Sharon M Weiss. Experimental realization of deep-subwavelength confinement in dielectric optical resonators. *Science advances*, 4(8):eaat2355, 2018. (Cited at page 12).

[2] KS Thyagarajan and Ajoy Ghatak. *Fiber optic essentials*, volume 10. John Wiley & Sons, 2007. (Cited at pages 13, 68).

[3] Stefano Pirotta, Ngoc-Linh Tran, Arnaud Jollivet, Giorgio Biasiol, Paul Crozat, Jean-Michel Manceau, Adel Bousseksou, and Raffaele Colombelli. Fast amplitude modulation up to 1.5 ghz of mid-ir free-space beams at room-temperature. *Nature communications*, 12(1):1–6, 2021. (Cited at pages 13, 71, 72, 72, 73, 119).

[4] Alexandre Delga. Quantum cascade detectors: A review. *Mid-infrared Optoelectronics*, pages 337–377, 2020. (Cited at pages 14, 123, 123, 124, 125, 125).

[5] What is the physical significance of Dielectric Constant or Relative Permittivity? https://shorturl.at/tzVZ7. (Cited at page 18).

[6] Mário Silveirinha and Nader Engheta. Tunneling of electromagnetic energy through subwavelength channels and bends using ε-near-zero materials. *Physical review letters*, 97(15):157403, 2006. (Cited at page 20).

[7] Stefan Enoch, Gérard Tayeb, Pierre Sabouroux, Nicolas Guérin, and Patrick Vincent. A Metamaterial for Directive Emission. *Physical Review Letters*, 89(21):1–4, 2002. (Cited at page 20).

[8] David A. Powell, Andrea Alù, Brian Edwards, Ashkan Vakil, Yuri S. Kivshar, and Nader Engheta. Nonlinear control of tunneling through an epsilon-near-zero channel. *Physical Review B - Condensed Matter and Materials Physics*, 79(24):1–5, 2009. (Cited at page 20).

[9] D. C. Adams, S. Inampudi, T. Ribaudo, D. Slocum, S. Vangala, N. A. Kuhta, W. D. Goodhue, V. A. Podolskiy, and D. Wasserman. Funneling light through a subwavelength aperture with epsilon-near-zero materials. *Physical Review Letters*, 107(13):1–5, 2011. (Cited at page 20).

[10] M. Zahirul Alam, Israel De Leon, and Robert W. Boyd. Large optical nonlinearity of indium tin oxide in its epsilon-near-zero region. *Science*, 352(6287):795–797, 2016. (Cited at page 20).

[11] Michael G Wood, Salvatore Campione, S Parameswaran, Ting S Luk, Joel R Wendt, Darwin K Serkland, and Gordon A Keeler. Gigahertz speed operation of epsilon-near-zero silicon photonic modulators. *Optica*, 5(3):233–236, 2018. (Cited at pages 20, 20, 70, 70, 71).

[12] Bokun Zhou, Erwen Li, Yunfei Bo, and Alan X Wang. High-speed plasmonic-silicon modulator driven by epsilon-near-zero conductive oxide. *Journal of Lightwave Technology*, 38(13):3338–3345, 2020. (Cited at pages 20, 20, 70, 70, 70).

[13] Ting S Luk, Salvatore Campione, Iltai Kim, Simin Feng, Young Chul Jun, Sheng Liu, Jeremy B Wright, Igal Brener, Peter B Catrysse, Shanhui Fan, et al. Directional perfect absorption using deep subwavelength low-permittivity films. *Physical Review B*, 90(8):085411, 2014. (Cited at page 20).

[14] Jin Xu, Jyotirmoy Mandal, and Aaswath P Raman. Broadband directional control of thermal emission. *Science*, 372(6540):393–397, 2021. (Cited at page 20).

[15] Nathaniel Kinsey, Clayton DeVault, Alexandra Boltasseva, and Vladimir M. Shalaev. Near-zero-index materials for photonics. *Nature Reviews Materials*, 4(December), 2019. (Cited at pages 20, 31, 31, 37).

[16] Erwen Li, Qian Gao, Ray T. Chen, and Alan X. Wang. Ultracompact Silicon-Conductive Oxide Nanocavity Modulator with 0.02 Lambda-Cubic Active Volume. *Nano Letters*, 18(2):1075–1081, 2018. (Cited at pages 20, 70).

[17] Xiaoge Liu, Kai Zang, Ju Hyung Kang, Junghyun Park, James S. Harris, Pieter G. Kik, and Mark L. Brongersma. Epsilon-Near-Zero Si Slot-Waveguide Modulator. *ACS Photonics*, 5(11):4484–4490, 2018. (Cited at pages 20, 70, 70).

[18] Iñigo Liberal and Nader Engheta. Near-zero refractive index photonics. *Nature Photonics*, 11(3):149–158, 2017. (Cited at page 21).

[19] Hyun-Joo Chang, Se-Heon Kim, Yong-Hee Lee, Emil P Kartalov, and Axel Scherer. A photonic-crystal optical antenna for extremely large local-field enhancement. *Optics express*, 18(23):24163–24177, 2010. (Cited at page 23).

[20] Paul Drude. Zur elektronentheorie der metalle. *Annalen der physik*, 306(3):566–613, 1900. (Cited at page 24).

[21] Tsuneya Ando, Alan B Fowler, and Frank Stern. Electronic properties of two-dimensional systems. *Reviews of Modern Physics*, 54(2):437, 1982. (Cited at pages 26, 40).

[22] M. Załużny and C. Nalewajko. Coupling of infrared radiation to intersubband transitions in multiple quantum wells: The effective-medium approach. *Physical Review B*, 59(20):13043–13053, may 1999. (Cited at page 26).

[23] Manfred Helm. The Basic Physics of Intersubband Transitions. In *Semiconductors and Semimetals*, volume 62, pages 1–99. Elsevier, jan 1999. (Cited at pages 26, 67).

[24] Emmanuel Rosencher and Borge Vinter. *Optoelectronics*. Cambridge University Press, 2002. (Cited at pages 26, 130).

[25] Mark Fox. Optical properties of solids, 2002. (Cited at pages 26, 27).

[26] Pierre Jouy. *Dispositifs quantiques en régime de couplage ultra-fort lumière-matière pour l'optoélectronique dans le moyen infrarouge*. PhD thesis, Paris 7, 2012. (Cited at pages 27, 73).

[27] Max Born, Kun Huang, and M Lax. Dynamical theory of crystal lattices. *American Journal of Physics*, 23(7):474–474, 1955. (Cited at page 30).

[28] Edward D Palik. *Handbook of optical constants of solids*, volume 3. Academic press, 1998. (Cited at pages 30, 63, 63, 86).

[29] WG Spitzer, D Kleinman, and D Walsh. Infrared properties of hexagonal silicon carbide. *Physical Review*, 113(1):127, 1959. (Cited at pages 30, 32).

[30] W Streyer, K Feng, Y Zhong, AJ Hoffman, and D Wasserman. Engineering the reststrahlen band with hybrid plasmon/phonon excitations. *MRS Communications*, 6(1):1–8, 2016. (Cited at page 32).

[31] A Kasic, M Schubert, S Einfeldt, D Hommel, and TE Tiwald. Free-carrier and phonon properties of n-and p-type hexagonal gan films measured by infrared ellipsometry. *Physical Review B*, 62(11):7365, 2000. (Cited at page 32).

[32] Edward Sachet, Christopher T Shelton, Joshua S Harris, Benjamin E Gaddy, Douglas L Irving, Stefano Curtarolo, Brian F Donovan, Patrick E Hopkins, Peter A Sharma, Ana Lima Sharma, et al. Dysprosium-doped cadmium oxide as a gateway material for mid-infrared plasmonics. *Nature materials*, 14(4):414–420, 2015. (Cited at page 32).

[33] Heinz Reather. Surface plasmons on smooth and rough surfaces and on gratings. *Springer tracts in modern physics*, 111:1–3, 1988. (Cited at page 34).

[34] Dror Sarid. Long-Range Surface-Plasma Waves on Very Thin Metal Films. *Physical Review Letters*, 47(26):1927–1930, dec 1981. (Cited at page 35).

[35] Pierre Berini. Long-range surface plasmon polaritons. *Advances in Optics and Photonics*, 1(3):484, 2009. (Cited at page 35).

[36] Simon Vassant, Alexandre Archambault, François Marquier, Fabrice Pardo, Ulf Gennser, Antonella Cavanna, Jean-Luc Pelouard, and Jean-Jacques Greffet. Epsilon-near-zero mode for active optoelectronic devices. *Physical review letters*, 109(23):237401, 2012. (Cited at pages 35, 36, 36, 71, 71).

[37] Simon Vassant, Jean-Paul Hugonin, Francois Marquier, and Jean-Jacques Greffet. Berreman mode and epsilon near zero mode. *Optics express*, 20(21):23971–23977, 2012. (Cited at pages 35, 37, 37, 37).

[38] Salvatore Campione, Igal Brener, and Francois Marquier. Theory of epsilon-near-zero modes in ultrathin films. *Physical Review B - Condensed Matter and Materials Physics*, 91(12):1–5, 2015. (Cited at pages 35, 35, 35, 36).

[39] Junghyun Park, Ju-Hyung Kang, Xiaoge Liu, and Mark L Brongersma. Electrically tunable epsilon-near-zero (enz) metafilm absorbers. *Scientific reports*, 5(1):1–9, 2015. (Cited at pages 36, 71, 72, 72, 78, 119).

[40] Thierry Taliercio, Vilianne Ntsame Guilengui, Laurent Cerutti, Eric Tournié, and Jean-Jacques Greffet. Brewster "mode" in highly doped semiconductor layers: an all-optical technique to monitor doping concentration. *Optics Express*, 22(20):24294, 2014. (Cited at page 37).

[41] Vladimir Moiseevich Agranovich. *Surface polaritons*. Elsevier, 2012. (Cited at page 37).

[42] Mathias Schubert. *Infrared ellipsometry on semiconductor layer structures: phonons, plasmons, and polaritons*, volume 209. Springer Science & Business Media, 2004. (Cited at page 37).

[43] B Harbecke, B Heinz, and P Grosse. Optical properties of thin films and the berreman effect. *Applied Physics A*, 38(4):263–267, 1985. (Cited at pages 38, 39).

[44] Benjamin Askenazi. *Du couplage ultra-fort lumière-matière: nouvelle Ingénierie de Métamatériaux Térahertz*. PhD thesis, Sorbonne Paris Cité, 2015. (Cited at page 39).

[45] L J Van Der Pauw. A method of measuring the resistivity and Hall coefficient on lamellae of arbitrary shape, 1958. (Cited at page 42).

[46] John G Webster. *The Measurement, Instrumentation, and Sensors: Handbook*. Springer Science & Business Media, 1999. (Cited at page 43).

[47] Chandrasekhara Venkata Raman and Kariamanikkam Srinivasa Krishnan. A new type of secondary radiation. *Nature*, 121(3048):501–502, 1928. (Cited at page 45).

[48] Sidney Perkowitz. *Optical characterization of semiconductors: infrared, Raman, and photoluminescence spectroscopy*. Elsevier, 2012. (Cited at page 46).

[49] Tobias Ruf. *Phonon Raman scattering in semiconductors, quantum wells and superlattices*. 1997. (Cited at page 46).

[50] DA Long. The raman effect: a unified treatment of the theory of raman scattering by molecules. 2002. *West Sussex, England: John Wiley & Sons Ltd*, 2002. (Cited at page 46).

[51] JA Steele, Pascal Puech, and Roger A Lewis. Polarized raman backscattering selection rules for (hhl)-oriented diamond-and zincblende-type crystals. *Journal of Applied Physics*, 120(5):055701, 2016. (Cited at pages 46, 47).

[52] T Co Damen, SPS Porto, and B Tell. Raman effect in zinc oxide. *Physical Review*, 142(2):570, 1966. (Cited at page 47).

[53] BB Varga. Coupling of plasmons to polar phonons in degenerate semiconductors. *Physical Review*, 137(6A):A1896, 1965. (Cited at page 47).

[54] Andrés Cantarero. Raman scattering applied to materials science. *Procedia Materials Science*, 9:113–122, 2015. (Cited at page 48, 48).

[55] RL Lachance and L Rochette. Non-linearity correction of ftir instruments. In *Fifth Workshop of Infrared Emission Measurements by FT-IR. ABB Bomem. Québec City, Canada*, 2000. (Cited at page 50).

[56] RO Carter III, NE Lindsay, and D Beduhn. A solution to baseline uncertainty due to mct detector nonlinearity in ft-ir. *Applied spectroscopy*, 44(7):1147–1151, 1990. (Cited at page 50).

[57] Limin Shao and Peter R Griffiths. Correcting nonlinear response of mercury cadmium telluride detectors in open path fourier transform infrared spectrometry. *Analytical chemistry*, 80(13):5219–5224, 2008. (Cited at page 50).

[58] RP Lowndes. Influence of lattice anharmonicity on the longitudinal optic modes of cubic ionic solids. *Physical Review B*, 1(6):2754, 1970. (Cited at page 52).

[59] François Gervais and Bernard Piriou. Anharmonicity in several-polar-mode crystals: adjusting phonon self-energy of lo and to modes in al2o3 and tio2 to fit infrared reflectivity. *Journal of Physics C: Solid State Physics*, 7(13):2374, 1974. (Cited at page 52).

[60] NL Rowell, G Yu, DJ Lockwood, and PJ Poole. Phonons in in 0.53 ga 0.47 a s/i n p (100) superlattices by infrared reflectance. *Physical Review B*, 68(16):165320, 2003. (Cited at page 52).

[61] G Yu, NL Rowell, DJ Lockwood, and PJ Poole. Infrared dielectric response function of strained in 1- x ga x as/inp epilayers. *Applied physics letters*, 81(12):2175–2177, 2002. (Cited at page 52).

[62] ZV Popović, Andrés Cantarero, J Camacho, A Milutinovi, O Latinovi, and L González. Raman scattering and infrared reflectivity in [(inp) 5 (in 0.49 ga 0.51 as) 8] 30 superlattices. *Journal of Applied Physics*, 88(11):6382–6387, 2000. (Cited at page 52).

[63] DJ Lockwood, G Yu, NL Rowell, and PJ Poole. Optical phonons via oblique-incidence infrared spectroscopy and their deformation potentials in in 1- x ga x as. *Journal of applied physics*, 101(11):113524, 2007. (Cited at page 52).

[64] R Brendel and D Bormann. An infrared dielectric function model for amorphous solids. *Journal of applied physics*, 71(1):1–6, 1992. (Cited at page 52).

[65] D De Sousa Meneses, G Gruener, M Malki, and P Echegut. Causal voigt profile for modeling reflectivity spectra of glasses. *Journal of non-crystalline solids*, 351(2):124–129, 2005. (Cited at pages 52, 60).

[66] D De Sousa Meneses, M Malki, and P Echegut. Structure and lattice dynamics of binary lead silicate glasses investigated by infrared spectroscopy. *Journal of non-crystalline solids*, 352(8):769–776, 2006. (Cited at page 52).

[67] J Orosco and CFM Coimbra. On a causal dispersion model for the optical properties of metals. *Applied optics*, 57(19):5333–5347, 2018. (Cited at page 52, 52).

[68] Rei Kitamura, Laurent Pilon, and Miroslaw Jonasz. Optical constants of silica glass from extreme ultraviolet to far infrared at near room temperature. *Applied optics*, 46(33):8118–8133, 2007. (Cited at pages 52, 99).

[69] Tatiana Amotchkina, Michael Trubetskov, Daniel Hahner, and Vladimir Pervak. Characterization of e-beam evaporated ge, ybf 3, zns, and laf 3 thin films for laser-oriented coatings. *Applied optics*, 59(5):A40–A47, 2020. (Cited at pages 54, 57).

[70] Robert L. Olmon, Brian Slovick, Timothy W. Johnson, David Shelton, Sang Hyun Oh, Glenn D. Boreman, and Markus B. Raschke. Optical dielectric function of gold. *Physical Review B - Condensed Matter and Materials Physics*, 86(23):1–9, 2012. (Cited at pages 57, 59, 116, 157).

[71] IF Chang, SS Mitra, JN Plendl, and LC Mansur. Long-wavelength longitudinal phonons of multimode crystals. *physica status solidi (b)*, 28(2):663–673, 1968. (Cited at page 57).

[72] Thomas P Pearsall. *GaInAsP alloy semiconductors*. Wiley, 1982. (Cited at page 59).

[73] WK Metzger, MW Wanlass, LM Gedvilas, JC Verley, JJ Carapella, and RK Ahrenkiel. Effective electron mass and plasma filter characterization of n-type ingaas and inasp. *Journal of applied physics*, 92(7):3524–3529, 2002. (Cited at page 59, 59).

[74] U Wiesner, J Pillath, W Bauhofer, A Kohl, A Mesquida Küsters, S Brittner, and K Heime. In-plane effective masses and quantum scattering times of electrons in narrow modulation-doped ingaas/inp quantum wells. *Applied physics letters*, 64(19):2520–2522, 1994. (Cited at page 59).

[75] Gregory Quinchard. *Détecteur infrarouge hétérodyne à cascade quantique*. PhD thesis, Université de Lille, 2021. (Cited at pages 59, 60, 60, 73, 76, 76, 89, 89, 124, 124, 125).

[76] Ngoc Linh Tran. *Mid-Infrared Intersubband Polaritonic Devices*. PhD thesis, université Paris-Saclay, 2020. (Cited at pages 67, 73, 75).

[77] Graham T Reed, G Mashanovich, F Yand Gardes, and DJ Thomson. Silicon optical modulators. *Nature photonics*, 4(8):518–526, 2010. (Cited at page 68).

[78] Tze-Wei Yeow, KL Eddie Law, and Andrew Goldenberg. Mems optical switches. *IEEE Communications magazine*, 39(11):158–163, 2001. (Cited at page 69).

[79] Boston Micromachines. Mems grating modulator. `https://bostonmicromachines.com/mems-grating-modulator`, 2021. (Cited at page 69).

[80] SungWon Chung, Makoto Nakai, and Hossein Hashemi. Low-power thermo-optic silicon modulator for large-scale photonic integrated systems. *Optics express*, 27(9):13430–13459, 2019. (Cited at page 69).

[81] Ke Liu, Chen Ran Ye, Sikandar Khan, and Volker J Sorger. Review and perspective on ultrafast wavelength-size electro-optic modulators. *Laser & Photonics Reviews*, 9(2):172–194, 2015. (Cited at pages 69, 69, 70).

[82] Zhaolin Lu, Wangshi Zhao, and Kaifeng Shi. Ultracompact electroabsorption modulators based on tunable epsilon-near-zero-slot waveguides. *IEEE Photonics Journal*, 4(3):735–740, 2012. (Cited at page 70).

[83] Nima Dabidian, Iskandar Kholmanov, Alexander B Khanikaev, Kaya Tatar, Simeon Trendafilov, S Hossein Mousavi, Carl Magnuson, Rodney S Ruoff, and Gennady Shvets. Electrical switching of infrared light using graphene integration with plasmonic fano resonant metasurfaces. *Acs Photonics*, 2(2):216–227, 2015. (Cited at page 71, 71).

[84] Y. Todorov, L. Tosetto, J. Teissier, A. M. Andrews, P. Klang, R. Colombelli, I. Sagnes, G. Strasser, and C. Sirtori. Optical properties of metal-dielectric-metal microcavities in the THz frequency range. *Optics Express*, 18(13):13886, 2010. (Cited at pages 73, 75, 76, 77, 77).

[85] Charlie Koechlin, Patrick Bouchon, Fabrice Pardo, Jean-Luc Pelouard, and Riad Haïdar. Analytical description of subwavelength plasmonic mim resonators and of their combination. *Optics express*, 21(6):7025–7032, 2013. (Cited at pages 73, 76).

[86] Ludivine Emeric. *Antennes optiques à nanogap alimentées électriquement, interactions entre optique et transport électronique*. PhD thesis, Université Paris-Saclay (ComUE), 2019. (Cited at pages 73, 76, 89).

[87] Yanko Todorov and Christophe Minot. Modal method for conical diffraction on a rectangular slit metallic grating in a multilayer structure. *Journal of the Optical Society of America A*, 24(10):3100, 2007. (Cited at page 75).

[88] Hyounggwan Woo, Arifur R Khan, Hirokazu Masui, Mengu Cho, Takehiro Miyakawa, and Tatsuhito Fujita. Discharge observation on antenna surface radiating high-power microwaves in simulated space environment. *TRANSACTIONS OF THE JAPAN SOCIETY FOR AERONAUTICAL AND SPACE SCIENCES, AEROSPACE TECHNOLOGY JAPAN*, 12:11–19, 2014. (Cited at page 77).

[89] Takashi Mimura, Satoshi Hiyamizu, Toshio Fujii, and Kazuo Nanbu. A new field-effect transistor with selectively doped gaas/n-alxga1-xas heterojunctions. *Japanese journal of applied physics*, 19(5):L225, 1980. (Cited at page 78, 78).

[90] Dae-Hyun Kim and Jesus A Del Alamo. Logic performance of 40 nm inas hemts. In *2007 IEEE International Electron Devices Meeting*, pages 629–632. IEEE, 2007. (Cited at page 78).

[91] T Enoki, K Arai, A Kohzen, and Y Ishii. Ingaas/inp double channel hemt on inp. In *LEOS 1992 Summer Topical Meeting Digest on Broadband Analog and Digital Optoelectronics, Optical Multiple Access Networks, Integrated Optoelectronics, and Smart Pixels*, pages 14–17. IEEE, 1992. (Cited at page 78).

[92] M Wojtowicz, R Lai, DC Streit, GI Ng, TR Block, KL Tan, PH Liu, AK Freudenthal, and RM Dia. 0.10 μm graded ingaas channel inp hemt with 305 ghz f t and 340 ghz f max. *IEEE Electron Device Letters*, 15(11):477–479, 1994. (Cited at page 78).

[93] Zhang Renping, Yan Wei, Wang Xiaoliang, and Yang Fuhua. Fabrication and characterization of high performance algan/gan hemts on sapphire with silicon nitride passivation. *Journal of semiconductors*, 32(6):064001, 2011. (Cited at page 78).

[94] Jean Paul Hugonin and Philippe Lalanne. Reticolo software for grating analysis. *arXiv preprint arXiv:2101.00901*, 2021. (Cited at page 81).

[95] Patrick Bouchon, Charlie Koechlin, Fabrice Pardo, Riad Haïdar, and Jean-Luc Pelouard. Wideband omnidirectional infrared absorber with a patchwork of plasmonic nanoantennas. *Optics letters*, 37(6):1038–1040, 2012. (Cited at page 81).

[96] Hung-Ling Chen, Andrea Cattoni, Romaric De Lépinau, Alexandre W Walker, Oliver Höhn, David Lackner, Gerald Siefer, Marco Faustini, Nicolas Vandamme, Julie Goffard, et al. A 19.9%-efficient ultrathin solar cell based on a 205-nm-thick gaas absorber and a silver nanostructured back mirror. *Nature Energy*, 4(9):761–767, 2019. (Cited at page 81).

[97] Armande Hervé, Jérémie Drévillon, Younes Ezzahri, Karl Joulain, Domingos De Sousa Meneses, and Jean-Paul Hugonin. Temperature dependence of a microstructured sic coherent thermal source. *Journal of Quantitative Spectroscopy and Radiative Transfer*, 180:29–38, 2016. (Cited at page 81).

[98] Gérard Granet. Reformulation of the lamellar grating problem through the concept of adaptive spatial resolution. *JOSA A*, 16(10):2510–2516, 1999. (Cited at page 81).

[99] Mark A Ordal, Robert J Bell, Ralph W Alexander, Larry L Long, and Marvin R Querry. Optical properties of fourteen metals in the infrared and far infrared: Al, co, cu, au, fe, pb, mo, ni, pd, pt, ag, ti, v, and w. *Applied optics*, 24(24):4493–4499, 1985. (Cited at pages 83, 84, 85, 86, 86, 116, 131, 159).

[100] Snider Gregory. 1d poisson code. `https://www3.nd.edu/~gsnider/`, 2021. (Cited at page 86).

[101] Christine H Tsau, S Mark Spearing, and Martin A Schmidt. Characterization of wafer-level thermocompression bonds. *Journal of microelectromechanical systems*, 13(6):963–971, 2004. (Cited at page 89).

[102] JS Huang and CB Vartuli. Scanning transmission electron microscopy study of au/zn/au/cr/au and au/ti/pt/au/cr/au contacts to p-type ingaas/inp. *Journal of applied physics*, 93(9):5196–5200, 2003. (Cited at page 89).

[103] GG Roberts and KP Pande. Electrical characteristics of au/ti-(n-type) inp schottky diodes. *Journal of Physics D: Applied Physics*, 10(10):1323, 1977. (Cited at page 95, 95).

[104] D Subba Reddy, M Bhaskar Reddy, N Nanda Kumar Reddy, V Rajagopal Reddy, et al. Schottky barrier parameters of pd/ti contacts on n-type inp revealed from ivt and cvt measurements. *Journal of Modern Physics*, 2(03):113, 2011. (Cited at page 95).

[105] DF Bezuidenhout, KD Clarke, and R Pretorius. The optical properties of yf3 films. *Thin Solid Films*, 155(1):17–30, 1987. (Cited at page 98).

[106] DF Bezuidenhout and R Pretorius. The optical properties of evaporated y2o3 films. *Thin Solid Films*, 139(2):121–132, 1986. (Cited at page 98).

[107] Aleksandar D Rakić, Aleksandra B Djurišić, Jovan M Elazar, and Marian L Majewski. Optical properties of metallic films for vertical-cavity optoelectronic devices. *Applied optics*, 37(22):5271–5283, 1998. (Cited at pages 116, 157, 160).

[108] P Dollfus, M Mouis, and R Castagné. Dimensionnement et performances potentielles des misfet à hétérojonction. *Revue de physique appliquée*, 24(1):65–69, 1989. (Cited at page 119).

[109] Antoni Rogalski. History of infrared detectors. *Opto-Electronics Review*, 20(3):279–308, 2012. (Cited at page 121).

[110] Antony Rogalski. Hgcdte infrared detector material: history, status and outlook. *Reports on Progress in Physics*, 68(10):2267, 2005. (Cited at page 122).

[111] BF Levine, KK Choi, CG Bethea, J Walker, and RJ Malik. New 10 μm infrared detector using intersubband absorption in resonant tunneling gaalas superlattices. *Applied physics letters*, 50(16):1092–1094, 1987. (Cited at page 122, 122).

[112] Daniel Hofstetter, Mattias Beck, and Jérôme Faist. Quantum-cascade-laser structures as photodetectors. *Applied Physics Letters*, 81(15):2683–2685, 2002. (Cited at page 123).

[113] Laure Gendron, M Carras, Agnes Huynh, V Ortiz, C Koeniguer, and V Berger. Quantum cascade photodetector. *Applied physics letters*, 85(14):2824–2826, 2004. (Cited at page 123).

[114] Benedikt Schwarz, Peter Reininger, Andreas Harrer, Donald MacFarland, Hermann Detz, Aaron M Andrews, Werner Schrenk, and Gottfried Strasser. The limit of quantum cascade detectors: A single period device. *Applied Physics Letters*, 111(6):061107, 2017. (Cited at pages 124, 124, 125, 125, 126, 148, 150).

[115] Shen-Qiang Zhai, Jun-Qi Liu, Feng-Qi Liu, and Zhan-Guo Wang. A normal incident quantum cascade detector enhanced by surface plasmons. *Applied Physics Letters*, 100(18):181104, 2012. (Cited at page 124).

[116] A Buffaz, A Gomez, M Carras, L Doyennette, and V Berger. Role of subband occupancy on electronic transport in quantum cascade detectors. *Physical Review B*, 81(7):075304, 2010. (Cited at pages 148, 150).

[117] Mathurin Lagrée, Mathieu Jeannin, Grégory Quinchard, Oussama Ouznali, Axel Evirgen, Virginie Trinité, Raffaele Colombelli, and Alexandre Delga. Direct polariton-to-electron tunneling in quantum cascade detectors operating in the strong light-matter coupling regime. *arXiv preprint arXiv:2110.08060*, 2021. (Cited at pages 157, 157, 162, 162, 163).

[118] Mathieu Jeannin, Thomas Bonazzi, Djamal Gacemi, Angela Vasanelli, Lianhe Li, Alexander Giles Davies, Edmund Linfield, Carlo Sirtori, and Yanko Todorov. Absorption engineering in an ultra-subwavelength quantum system. *Nano letters*, 20(6):4430–4436, 2020. (Cited at page 157).

[119] Daniele Palaferri. *Antenna resonators for quantum infrared detectors and fast heterodyne receivers*. PhD thesis, Sorbonne Paris Cité, 2018. (Cited at page 157).

[120] Mario Bertolotti, Victor Bogdanov, Aldo Ferrari, Andrei Jascow, Natalia Nazorova, Alexander Pikhtin, and Luigi Schirone. Temperature dependence of the refractive index in semiconductors. *JOSA B*, 7(6):918–922, 1990. (Cited at page 158).

[121] DS Dovzhenko, SV Ryabchuk, Yu P Rakovich, and IR Nabiev. Light–matter interaction in the strong coupling regime: configurations, conditions, and applications. *Nanoscale*, 10(8):3589–3605, 2018. (Cited at page 163).